UNIVERSITAT DE
BARCELONA

Understanding the transport mechanism of BBB peptide shuttles: THRre and MiniAp-4 as case studies

Cristina Fuster Juncà

Programa de doctorat de Química Orgànica

Understanding the transport mechanism of BBB peptide shuttles: THRre and MiniAp-4 as case studies

Cristina Fuster Juncà

Tesis doctoral dirigida per:

Dra. Meritxell Teixidó Turà

IRB Barcelona

Programa de química i biología estructural

Dra. Macarena Sánchez Navarro

IRB Barcelona

Programa de química i biología estructural

Tutor:

Prof. Ernest Giralt Lladó

Universitat de Barcelona

Facultat de Química - Departament de Química Inorgànica i Orgànica

Barcelona, 2019

You cannot hope to build a better world without improving the individuals. To that end, each of us must work for our own improvement.

Marie Curie

CONTENTS

ABBREVIATIONS

aa	amino acid
ACN	acetonitrile
AcOH	acetic acid
AMT	adsorptive-mediated transcytosis
Apo	apolipoprotein
ATP	adenosine triphosphate
AuNP	gold nanoparticle
BBB	blood-brain barrier
BBBCM	cell-based BBB model
Boc	*tert*-butoxycarbonyl
BSA	bovine serum albumin
cF	carboxyfluorescein
cy5	cyanine-5
CMT	carried-mediated transport
CNS	central nervous system
COSY	correlation spectroscopy
CPP	cell-penetrating peptide
CSF	cerebrospinal fluid
CTX	chlorotoxin
CuAAC	copper-catalysed azide-alkyne cycloaddition
Da	dalton
Dap	2,3-diaminopropionic acid
DCM	dichloromethane
DIEA	*N*,*N*-diisopropylethylamine
DIC	diisopropylcarbodiimide
DMEM	Dulbecco's modified eagle medium
DMF	dimethylformamide
DMSO	dimethylsulfoxide
dSTORM	direct stochastic optical reconstruction microscopy
DTT	D,L-dithiothreitol
EDC	*N*-(3-dimethylaminopropyl)-*N'*-ethylcarbodiimide hydrochloride

EDTA	ethylenediaminetetraacetic acid
EGF	epidermal growth factor
EGFR	epidermal growth factor receptor
ELISA	enzyme-linked immunosorbent assay
eq	equivalent
ESI	electrospray ionization
FBS	fetal bovine serum
Fmoc	9-fluorenylmethoxycarbonyl
HEPES	4-(2-hydroxyethyl)piperazine-1-ethanesulfonic acid
HOAt	1-hydroxy-7-azabenzotriazole
HPLC	high performance liquid chromatography
HPLC-MS	high-performance liquid chromatography with mass spectrometry detection
HSQC	heteronuclear single quantum coherence spectroscopy
KD	dissociation constant
ICP	inducing-coupled plasma
GFP	green fluorescent protein
GM1	monosialotetrahexosylganglioside
IAA	iodoacetamine
i.v.	intravenous
LAT	large neutral amino acid transporter
LDL	low-density lipoprotein
LDLR	low-density lipoprotein receptor
LY	Lucifer yellow
mAb	monoclonal antibody
MeOH	methanol
MS	mass spectrometry
MW	molecular weight
nAChR	nicotinic acetylcholine receptor
NaPi	sodium phosphate
NHS	N-hydroxysuccinimide
NMR	nuclear magnetic resonance

NOE	nuclear Overhauser effect
NOESY	nuclear Overhauser effect spectroscopy
NP	nanoparticle
PAGE	polyacrylamide gel electrophoresis
PAMPA	parallel artificial membrane permeability assay
Papp	apparent permeability
PBS	phosphate-buffered saline
PDA	photodiode array
PEG	polyethylene glycol
PFA	paraformaldehyde
PK	pharmacokinetics
PyBOP	1H-benzotriazol-1-yloxytris(pyrrolidino)phosphonium
QDot	quantum dot
RH	Ringer HEPES
RMT	receptor-mediated transcytosis
RNA	ribonucleic acid
ROI	region of interest
RT	room temperature
SAW	surface acoustic wavelength
SD	standard deviation
SDS	sodium dodecylsulfate
SEC	size exclusion chromatography
SPPS	solid-phase peptide synthesis
STD	saturation transfer difference
TBTU	O-(benzotriazole-1-yl)-1,1,3,3-tetramethyluronium tetrafluoroborate
tBu	$tert$-butyl
TCEP	tris(2-carboxyethyl)phosphine
TEER	transendothelial electrical resistance
TEM	transmission electron microscopy
TFA	trifluoroacetic acid
Tf	transferrin
TfR	transferrin receptor

TIS   triisopropylsilane

TJ   tight junction

TOCSY   total correlation spectroscopy

tR   retention time

Trt   trityl

UPLC   ultra-high performance liquid chromatography

UPLC-MS   ultra-high performance liquid chromatography with mass
                spectrometry detection

UV   ultraviolet

Proteinogenic amino acids

A
Ala
L-Alanine

C
Cys
L-Cysteine

D
Asp
L-Aspartate

E
Glu
L-Glutamate

F
Phe
L-Phenylalanine

G
Gly
L-Glycine

H
His
L-Histidine

I
Ile
L-Isoleucine

K
Lys
L-Lysine

L
Leu
L-Leucine

M
Met
L-Methionine

N
Asn
L-Asparagine

P
Pro
L-Proline

Q
Gln
L-Glutamine

R
Arg
L-Arginine

S
Ser
L-Serine

T
Thr
L-Threonine

V
Val
L-Valine

W
Trp
L-Tryptophan

Y
Tyr
L-Tyrosine
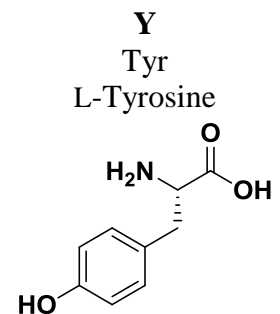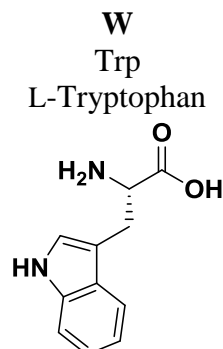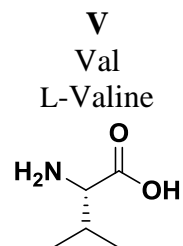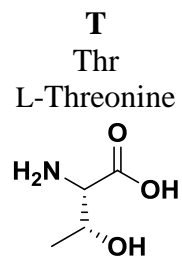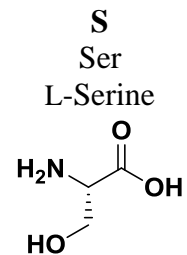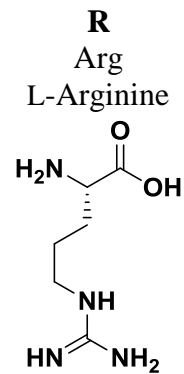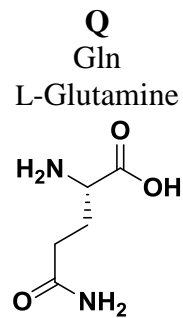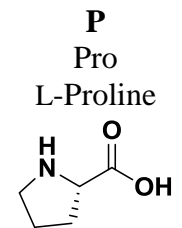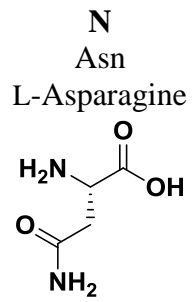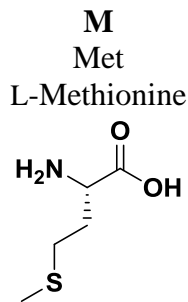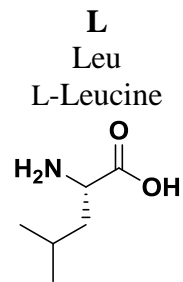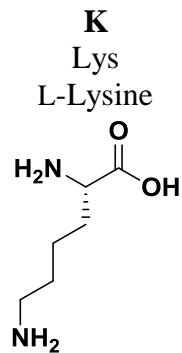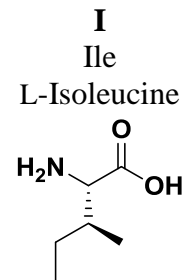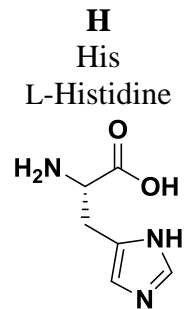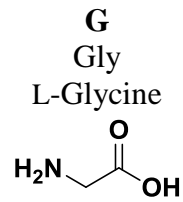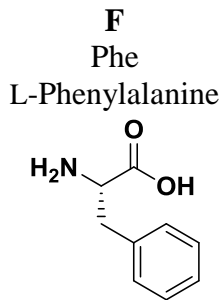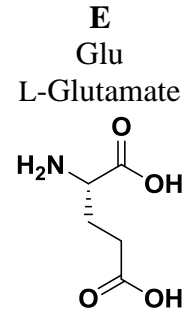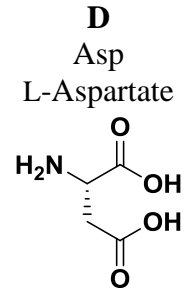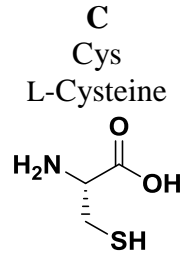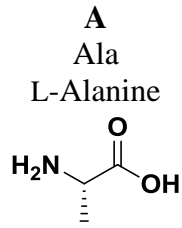
Protecting groups
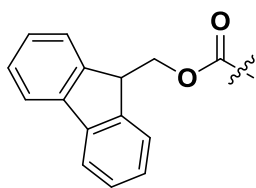
Fmoc

9-fluorenylmethoxycarbonyl

*t*Bu

tert-butyl

Boc
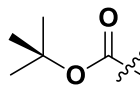
tert-butoxycarbonyl
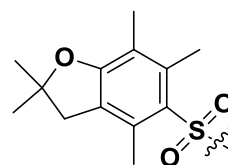
Pbf

2,2,4,5,7-pentamethyldihydro benzofurane-5-sulfonyl
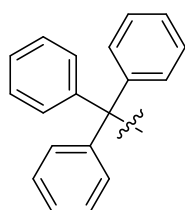
Trt

Trityl
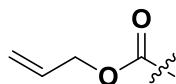
Alloc

Allyloxycarbonyl
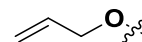
OAl

Allyl

Coupling reagents and additives
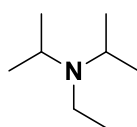
DIEA

N,N-diisopropylethylamine
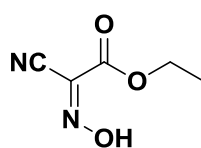
Oxyma

ethyl cyano-glyoxylate-2-oxime

DIC
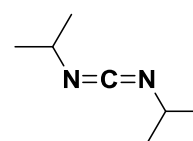
diisopropylcarbodiimide

EDC
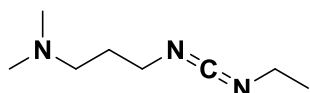
N-(3-dimethylaminopropyl)
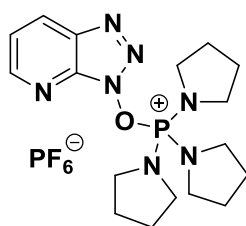
PyBOP

1H-benzotriazol-1-yloxytris

(pyrrolidino)phosphonium

hexafluorophosphate
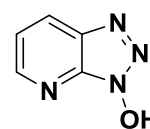
HOAt

1-hydroxy-7-

azabenzotriazole
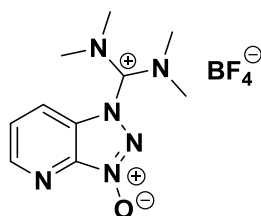
TBTU

O-(benzotriazol-1-yl)-1,1,3,3-
tetramethyluroniumtetrafluoroborate
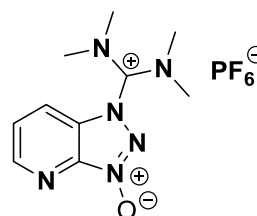
HBTU

O-(benzotriazol-1-yl)-1,1,3,3-

Tetramethyluroniumhexafluorophosphate

Non-proteinogenic amino acids and other functional groups
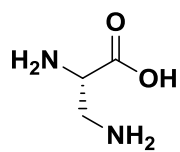
Dap

diaminopropionic
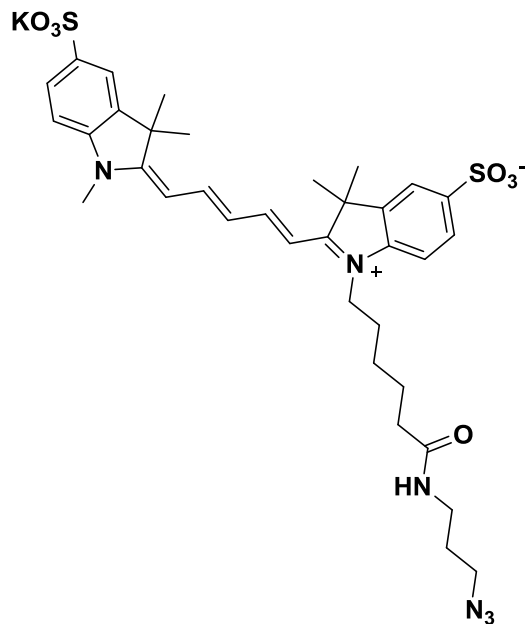
Cy5

cyanine5
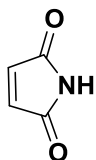
Mal

maleimide

cF
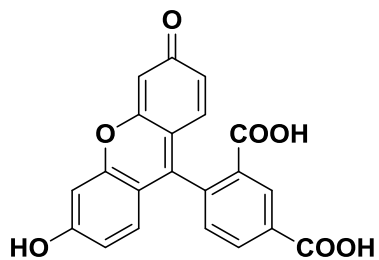
carboxifluorescein

Resins
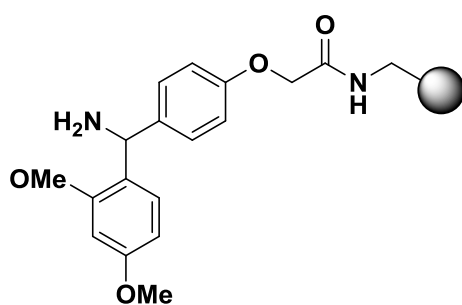
RinkAmide-Chemmatrix resin
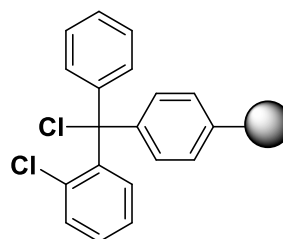
2-chlorotrityl resin
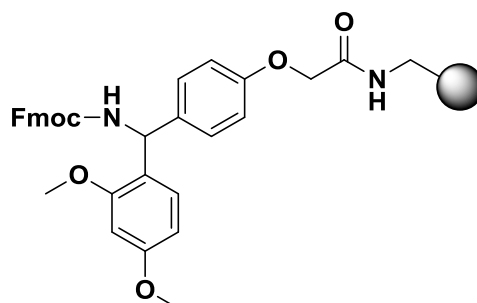
RinkAmide resin Pro-Tide

INTRODUCTION

Aging in the first world population results in an increase in central nervous system (CNS) related disorders. The list of diseases that require direct treatment into the brain tissue is long and diverse: it includes Alzheimer's and Parkinson's disease, psychiatric illnesses such as bipolar disorder and schizophrenia, brain tumors and even some aspects of obesity. It is estimated that in the world, one out of four people will suffer a disease related to the CNS during their lifetime. Also, some studies point that by 2020, the population older than 65 years old will have increased around 50% and the cost of just Alzheimer's disease could reach half a trillion US dollars.

For all these reasons, the neuropharmaceutical market has an urgent need to develop new therapeutics to treat these disorders as it would improve the well-being of many people and also reduce the health economic costs. However, most of the designed compounds are not effective due to their inability to enter the brain and reach their target in therapeutically relevant amounts. In more detail, more than 98% of low molecular weight drugs and almost 100% of large molecule drugs cannot penetrate the brain due to a formidable obstacle, namely the blood-brain barrier (BBB).[1-2] The BBB is a metabolic and transport barrier that isolates the brain from the rest of the body. One of the main characteristics is the presence of tight junctions (TJs) between endothelial cells, which are responsible for the restricted transport across this barrier.

For many years different approaches have been studied in order to improve the transport of these compounds from the blood stream to the cerebral parenchyma. These approaches can be divided in two groups: invasive and non-invasive. Some invasive approaches include direct administration to the brain, however they have been discarded due to the high risk of brain damages. In the case of non-invasive approaches, we can find the so-called BBB-shuttles, molecules that can translocate other compounds in an efficient-safe manner. This concept includes proteins, Trojan horse antibodies and peptides with the ability of transporting a cargo without affecting the integrity of the barrier.[3] Over the last decade, peptide BBB-shuttle have emerged as a potential tool to overcome the BBB, as they offer considerable advantage in front the classical antibodies and proteins such as low risk of immunogenicity, ease of synthesis and characterization and a lower cost of production.

In this introduction, we will give an overview of the BBB, the different brain delivery approaches and the BBB-shuttles described until now. Then, we will move to describe the different transport mechanism displayed by these shuttles. Finally, we will described different tools in order to assess the BBB penetration of shuttle-cargo compounds.

Based on this knowledge, in the present thesis we will explain our attempts to understand the transport mechanism of two well-known BBB-shuttles, THRre and MiniAp-4.

1.1 - The blood-brain barrier

The brain is a complex organ which controls a wide variety of complex functions, thus being necessary the presence of robust barriers to control the transport to the brain parenchyma. There are three described barriers that regulate the homeostasis within the brain: the arachnoid barrier, the blood-cerebrospinal fluid barrier (BCSFB) and the blood-brain barrier (*Figure 1*). The arachnoid barrier has some efflux transporters that reduce the number of molecules which pass through the plasma membrane into the cytosol. The BCSFB is established by choroid plexus epithelial cells which have a secretory function and produce also the cerebrospinal fluid (CSF).[4]
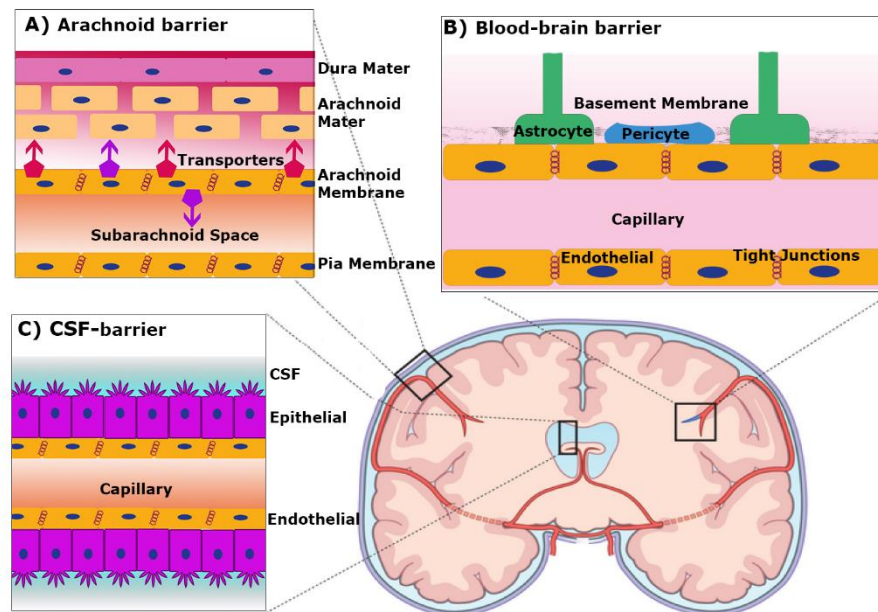
Figure 1. Representation of the three different barriers in the brain. A) The arachnoid barrier showing endothelial cells and efflux pump transporters, B) The BBB constituted of endothelial cells. C) The CSF barrier formed by epithelial and endothelial cells. Adapted from McCully *et al.*[5]

The BBB is formed by 650 km of brain capillaries with a total surface of 20 m^2 approximately, being 1000-fold larger than the blood-CSF interface.[6] However, it is the main obstacle in the development of new drugs for the CNS. The BBB is a high selective permeable barrier that isolates the brain from the rest of the body, regulating brain homeostasis. It controls the transport of endogenous and exogenous compounds by controlling their efflux and metabolism in the brain.[7] It is a dynamic, interactive and adaptable monolayers of cells mainly formed by endothelial cells which interact with other cell types such as pericytes and astrocytes.[8-9] Pericytes embrace the brain capillaries and seem to contribute to the maintenance, development and regulation of BBB meanwhile, the astrocytes are crucial for the induction and perservation of the endothelial barrier. The endothelial cells form a restrictive cell-to-cell due to the presence of tight junctions (TJs), which are intricate nets of trans-membrane and cytoplasmic proteins such as claudins or occludins, and adherens junctions (AJs). These TJs together with an absence of macropinocytotic vesicles and intracellular fenestrae, difficult the pass of several compounds.[10]
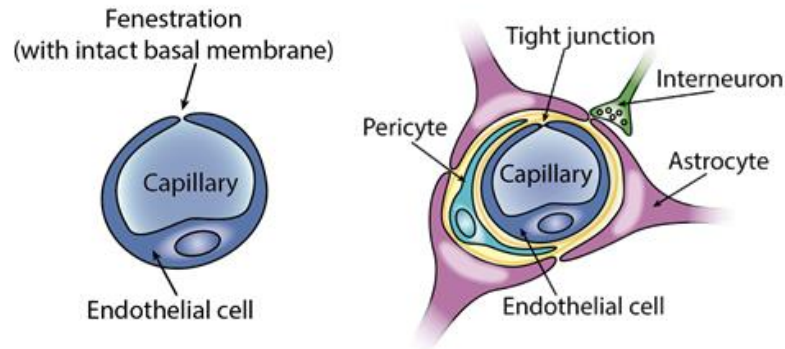
Figure 2. Difference between a capillary from a non-neuronal tissue and a brain capillary.

Although the brain is protected by the presence of the BBB, this organ is not completely isolated as it requires essential nutrients, ions and hormones to perform its normal functions.

In general, transport across the BBB can be classified into: (a) paracellular for aqueous compounds; (b) transcellular lipophilic diffusion; (c) carrier-mediated transport; (d) receptor-mediated transcytosis; (e) adsorptive-mediated transcytosis (*Figure 3*).
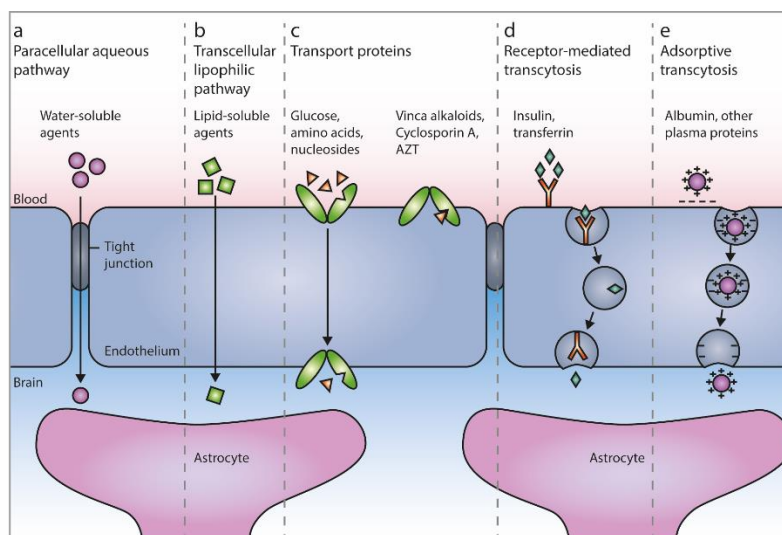
Figure 3. Main routes for molecular traffic across the BBB. Adapted from Abbott *et al.*[11]

The first two mentioned pathways are considered passive diffusion while the other three involved active transcytosis. The diffusion pathways are non-saturable and spontaneous transport processes limited to lipid-soluble molecules with a molecular weight under 600 Da. Small molecules can be modified in order to increase their lipophilicity and subsequently enhance their permeability, however, this modifications cannot be applied to peptides and proteins due to their inherent hydrophilicity and large size.

Carrier-mediated transport is an energy-dependent mechanism and one of the main entry route of nutrients. It consists of a substrate recognition, such as glucose, amino acids or nucleosides among other substances by a specific carrier protein. As this type of mechanism is saturable and competitive, any drug intended for this type of route will have to compete with the native nutrient for the service of the carrier.

In the case of receptor-mediated transcytosis, the substance is recognized by a receptor overexpressed in the membrane, followed by the internalization and further release of the ligand into the brain. One well-studied case is the complex formed by the transferrin and the transferrin receptor, which is overexpressed in the brain capillaries and regulates the uptake of free iron in biological fluids.[12] Finally, cationic substances, which interact with the negative charged parts of the cell membrane, enter the brain by absorptive-mediated transcytosis, an energy-dependent mechanism.

1.2 - Drug delivery to the brain

Drug delivery to the brain can be achieved by either invasive, pseudo-invasive, or non-invasive strategies (*Figure 4*).
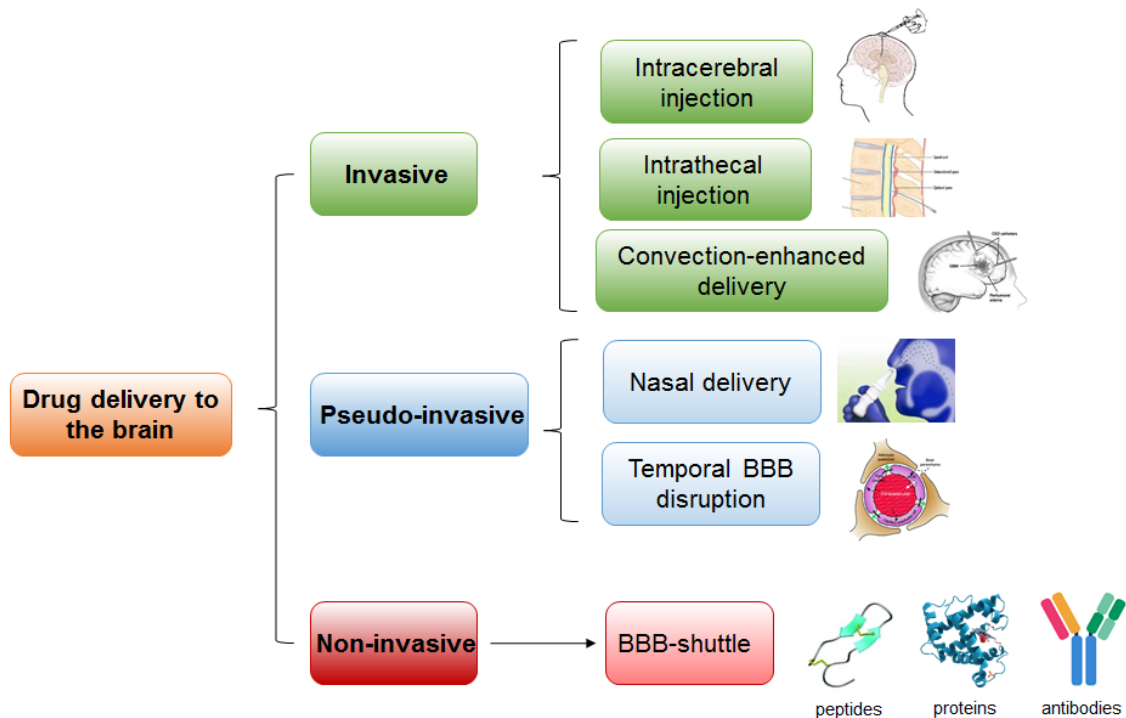
Figure 4. Scheme of the different drug delivery to the brain strategies classified in order of invasiveness.

The invasive strategies are the most direct and effective for drug delivery into the brain, however, these approaches requires drilling a hole in the cranium of the patient, thus involving a high risk of brain damage and infection. The delivery of the drug can be done by intracerebral injection, intrathecal injection or convection-enhanced delivery. The first one implies the direct administration of the drug into the brain which is usually used for local delivery as the diffusion in brain tissue is slow and significant distribution in the whole brain is not possible.[13] The intrathecal administration consists of an injection into the spinal canal to reach the CSF and it is usually used in anesthesia procedures or pain management. Finally, the convection-enhanced delivery consists of a catheter implanted in the brain which is connected to a pump through which the drug is distributed *via* bulk flow.[14-15]

In the case of pseudo-invasive strategies, nasal delivery and temporal disruption strategies are the most common. In the case of nasal drug delivery system, the drug moves through the olfactory epithelium, being the therapeutic amounts that reach the target areas very low.[16] The temporal disruption strategy consist of the co-injection of the drug and a solvent, which causes a temporal breakdown of the barrier. Compounds as mannitol, ethanol, dimethysulfoxide or detergents such as sodium dodecyl sulphate (SDS) have the capacity to disrupt the BBB.[17–19] Other methods such as high-dose free fatty acid, intracarotid acid pH injection or focused ultrasound (FUS), have been described to have the ability to open the BBB reversibly.[20–22] The last one has been reported that may cause brain damage.[23] Although these techniques allow the reach the brain, they imply a

momentarily exposure to neurotoxic, endogenous and exogenous compound found in plasma, thus being not totally safe.

The non-invasive approaches would permit the administration of drugs through intravenous, oral or transdermal administration without causing damage. Taking advantage of the rich vascularity of the brain, intravenous administration would be the ideal one, as the total brain capillary length is estimated to be 650 km, with capillaries encasing every brain cell.[24] For this reason, brain delivery through the BBB hold great potential. An extensively used approach to overcome the BBB is to use BBB-shuttles, compounds with the capacity to carry another cargo which is not able to cross itself via either active or passive diffusion.[25-26] The concept of BBB-shuttle was first described by William M. Pardridge in 1986 which a strategy for fusion protein delivery was proposed.[27] The first successful attempts relied on cationized albumin, which presented low brain selectivity, and then to IgGs against transferrin and insulin receptors.[28-29] In the subsequent years until nowadays, this field have grown enormously and plenty of new BBB-shuttles have appeared, some of which are currently in clinical trials. Antibodies, proteins and peptides are some of the compounds that have been used as "shuttles". However, the production and characterization of antibodies and proteins is challenging and expensive. In the case of peptides, which combine the specificity of biologics and the low cost of small drugs, the production and characterization is easier and have low immunogenicity.[30] In addition, there is the possibility of applying a non-natural modifications and of introducing functional groups for the conjugation to a wide variety of cargos such as nanocarriers or proteins. Although they have been undervalued in pharmaceutical chemistry because of their low resistance to proteolytic degradation, many ways to overcome this problem have emerged such as the use of non-natural or D-amino acids, cyclization or *N*-methylation.

The approach of peptide shuttles was introduced in a work done by Schwarze and co-workers in 1999, in which they reported the capacity of a fragment from the HIV TAT protein to deliver β-galactosidase into the brain and other organs.[31] Few years later, in 2007 Kumar *et al*. reported how a peptide derived from rabies virus glycoprotein (RGV) was able to bind and transduce siRNA to neuronal cells *in vitro*. In the same period of time, Angiopep-2 was reported as potential BBB-shuttle, being able to transport different antitumor drugs such as paclitaxel or doxorubicin.[32–34] This peptide has reached clinical trials phase II, thus proving the great potential of peptide BBB-shuttles as safety drug delivery systems.

1.3 - Transport mechanism of different BBB-shuttles

1.3.1 - Passive transport mechanism

Passive transport mechanism can be classified in passive diffusion and paracellular which are non-energy dependent.

Passive diffusion is a type of non-saturable transport process that only small lipophilic molecules with a molecular weight between 400-600 Da use.

Some BBB-shuttles have been developed in order to enhance the transport of some compounds across the BBB via passive diffusion. For example, diketopiperazines (DKPs) and *N*-methylphenyl-rich peptides were developed in our laboratory.[35–37] DKPs have the capacity to transport dopamine and baicalin across an *in vitro* BBB model. The BBB model is an artificial membrane permeability assay (PAMPA) which is the most used BBB model for passive diffusion.[38] Another family is the *N*-methylated phenylalanine-rich peptides which have been described to transport small cargoes such as L-dopa, 4-aminobutanoic acid (GABA), nipecotic acid (Nip) and aminolevulinic acid (Ala) in the same model. However these peptides showed poor water solubility, for this a new family of phenylproline peptides were developed.[39]
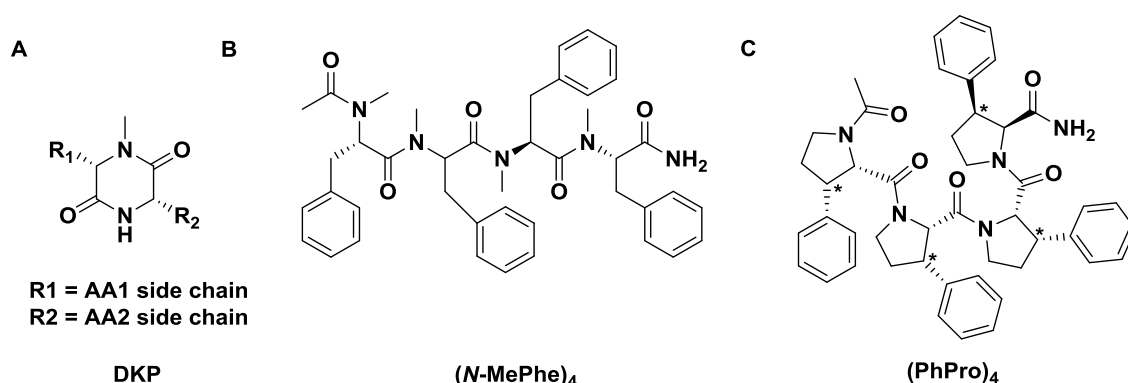
Figure 5. Chemical structure of peptide shuttles that cross the BBB via passive transport mechanism. (A) DKP, (B) (*N*-MePhe)₄, (C) (PhPro)₄. *indicates racemic *cis*-3-phenylproline.

Paracellular diffusion have been evaluated as an alternative route for drug delivery as it has been studied its capacity to increase skin and intestinal permeability. Peptides derived from E-cadherin, such as HAV6, have been describe to open the AJs in a reversible manner and also increase the uptake of two small molecules, gadolinium-diethylenetriaminepentaacetate (Gd-DTPA) and camptothecin-glutamate (CPT-Glu)[40-41].

1.3.2 – Active transport mechanisms

Carried-mediated transport (CMT)

CMT is a type of saturable mechanism in which some specific transport proteins are involved. These transport proteins provide essential nutrients and endogenous compounds to the brain such as the glucose or some cationic amino acids.[42] Several approaches have

tried to modify the structure of a given drug to resemble the native substrate of transporter, however some activity problems may appear after the modification. One option would be to link the drug to a substrate of a given transporter. For example, Bonina *et al.* proved how tyrosine, which uses the large neutral amino acid transporter (LAT1), was able to transport Nip *in vivo*.[43] Also, it was described the capacity of tyrosine and glucose to shuttle ketoprofen, a propionic acid class of nonsteroidal anti-inflammatory drug.[44-45]
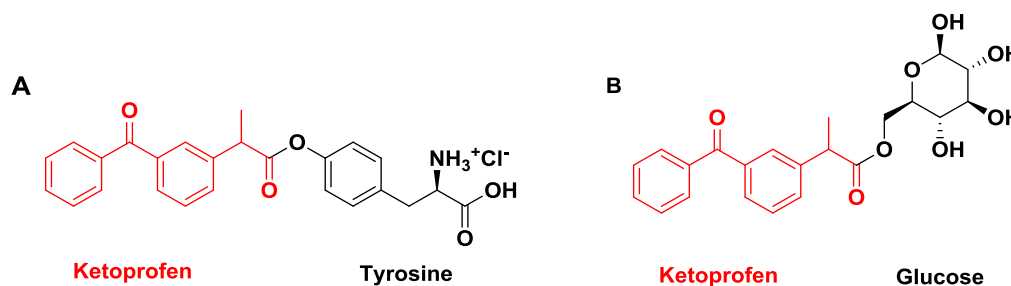
Figure 6. Tyrosine (A) and glucose (B) have been used as a BBB-shuttle to deliver ketoprofen (red) to the brain.

Absorptive-mediated transcytosis (AMT)

Cationic compounds and cell penetrating peptides (CPPs), such as TAT, penetratin and oligoarginine use this type of mechanism to overcome the BBB.[46–48] Also, cationized albumin and histone have been described to use this mechanism.[28-49] Compared to other types of mechanisms, AMT does not involve any type of membrane receptors. It consists of the interaction of a given compound with the negative charges of the plasma membrane surface area, such as proteoglycans.[50] Some of this CPPs have also the capacity to cross the BBB, thus being a good opportunity to transport a cargos across the barrier. Schwarze *et al.* described how a TAT was able to transport β-galactosidase protein in mice after intraperitoneal injection.[31] Also, it was described how TAT conjugated NPs enhance the transport of ritanovir, a pharmaceutical drug for the treatment of HIV infection.[51]

As this type of mechanism is non-carrier dependent, the use of CPPs as BBB-shuttles is not limited to small cargoes, however the transport is actively down-regulated in the BBB to protect the brain from non-specific exposure to cationic compounds.

BBB-shuttle	Sequence	Proposed mechanism	Main cargoes
TAT (47-57)	YGRKKRRQRRR-NH$_2$	AMT	Protein NPs
Penetratin	RQIKIWFQNRRMKWKKGG	AMT	Doxorubicin
Oligoarginine	RRRRRRRR (R$_8$) RRRRRRRRRR (R$_{10}$) RRRRRRRRRRRR (R$_{12}$)	AMT	Protein

			Gd-DTPA
HAV6	Ac-SHAVSS-NH$_2$	AMT	CPT-Glu

Table 1. Examples of BBB-shuttling by absorptive-mediated transcytosis. In the case of oligoarginine peptides, there is a representation of some of peptides used.

Receptor-mediated transcytosis (RMT)

Although there are a wide variety of receptors present on the BBB, only some of them accomplish the essential properties to become attractive for brain delivery purposes such as the capacity to mediate transcytosis or high expression in the luminal side of the brain.

Next, different receptor will be explained with their main characteristics and some BBB-peptide shuttle which use such receptor to cross the BBB.

Low-density lipoprotein receptor

The low-density lipoprotein receptor (LDLR) family is a cell surface glycoproteins which function is to control the uptake of cholesterol-carrying lipoprotein particles into cells. The receptor binds low-density lipoprotein particles (LDLs), which are primary carriers of cholesterol in the blood at the cell surface and release them in the endosome where the pH is lower. The family of LDLR includes over 7 members, however only the parent LDLR and the lipoprotein receptor-related protein 1 (LRP1) and 2 (LRP2) have been used for drug delivery to the CNS.[52-53]

ApoB or ApoE are two peptides based on natural ligand proteins which target this family of receptors showing good transport capacities for brain delivery.[54-55] Angiopep-2, which was identified by sequence alignment of aprotinin with other human proteins having a Kunitz domain, also interacts with LRP1.[56] This peptide has shown its ability to carry small drugs, proteins, nanoparticles and DNA into the CNS.[57–60] Also, there is one peptide described to target the LDLR family that does not derive from a natural protein, Peptide-22, which was discovered by Malcor *et al*. by phage display against the extracellular domain of a human LDLR.[61] This peptide was able to carry PLGA-PEG NPs across the BBB *in vitro* and *in vivo*.[62]

BBB-shuttle	Sequence	Proposed mechanism	Main cargoes
Angiopep-2	TFFYGGSRGKRNNFK	LRP1	Small drugs DNA/RNA NPs
Angiopep-2 *retroenantio*	yeektfnnrkgrsggyfft	LRP1	NPs

ApoB (3371-3407)	SSVIDALQYKLEGTTRLT RKRGLATALSLSNKFVE GS	LDLR LRP2	Protein
ApoE (159-167)₂	(LRKLRKRLL)₂	LDLR LRP1 LRP2	Protein NPs
Peptide-22	Ac-C(&)MPRLRGC(&)-NH₂	LDLR	NPs

Table 2. Examples of BBB-shuttling by receptor-mediated transcytosis. Nomenclature of cyclic peptides (&) is based on Spengler *et al.*[63]

Transferrin receptor

The transferrin receptor (TfR) is a transmembrane protein which function is to mediate the cellular iron uptake by binding and internalizing diferric transferrin.[64] Holo-Tf binds to TfR on the cell surface which is enters the cells via clathrin-mediated endocytosis. The acidic pH of the endosome leads to protein conformational changes that provoke the release of iron form transferrin. The apo-Tf and TfR both return to the cell surface where they dissociate at neutral pH.[65] Two TfRs have been described: TfR1 and TfR2, this last presenting 25-fold lower affinity for Tf and mainly express in the liver.[66] TfR is expressed practically in all cell types in the body, including brain capillaries.[67] Also, it has received a lot of attention in drug delivery due to its overexpression in cancer cells.[68-69] One way to target the brain can be achieved using Tf as BBB-shuttle. It was reported how a Tf conjugated to a horseradish peroxidase (HRP) was uptaken in BBB endothelial cells *in vitro*, however due to saturation of TfR in physiological conditions and high concentrations of Tf in plasma, this approach presents important limitations,[70] since it could lead to alterations in iron homeostasis. To overcome this problem, a good option would be the development of vectors that do not overlap with the same binding site of Tf. Two examples are the murine monoclonal antibody (mAb) OX-26 and the rat mAb 8D3, which their capacity to carry a variety of cargoes *in vivo* have been reported.[71–76] The main disadvantage of these antibodies is that they do not bind the human TfR, thus blocking this technology for human applications. The preparation of humanized antibodies is complex and can lead to a loss of affinity for the target receptor.[77]

Genentech and Hoffman-La Roche developed an antibody fragment to the TfR as a potential BBB-shuttle. They demonstrated that the monovalent binding mode to the TfR efficiently transcytoses across the BBB and can be released from the receptor, while the bivalent binding mode leads to lysosome sorting.[78]

A possible alternative for Tf or mAb for targeting human TfR is the use of peptides, which in addition to their relatively low molecular weight, show low cytotoxicity and immunogenicity.[79] Different peptides as THR, B6, T7 or CRT have been reported to undergo transcytosis through this receptor.[80–82] Prades, *et al.* reported a retroenantio version of THR (THRre), which presented better stability against proteases and an

enhancement shuttling capacity, being able to transport quantum dots *in vitro* and *in vivo*.[83]

BBB-shuttle	Sequence	Proposed mechanism	Main cargoes
OX-26	-	TfR1	Vasoactive intestinal peptide analogue (VIPa) Chitosan nanoparticles EGF Radiolabeled $A\beta^{1-40}$
8D3	-	TfR1	β-galactosidase Liposome carrying β-galactosidase
B6	GHKAKGPRK	TfR1	NPs
T7	H-HAIYPRH-NH$_2$	TfR1	RNA
CRT	C(&)RTIGPSVC(&)	TfR1	Virus
THR	H-THRPPMWSPVWP-NH$_2$	TfR1	RNA NPs
THRre	H-pwvpswmpprht-NH$_2$	TfR1	Small drugs NPs

Table 3. Examples of BBB-shuttling by receptor-mediated transcytosis. Nomenclature of cyclic peptides (&) is based on Spengler *et al.*[63]

Insulin receptor

Insulin receptor (IR) is a transmembrane receptor that belongs to the large class of tyrosine kinase receptors which are important regulators of cell differentiation, growth and metabolism.[84] The IR plays a key role in the regulation of glucose homeostasis. It consists of two α subunits and two β subunits which are joined by a disulfide bridge to form a cylindrical structure. The *in vivo* application of insulin as a BBB-shuttle is limited for the large amount of endogenous insulin in the blood stream, as it happens with Tf.

A murine mAb against human IR (mAb-HIR) was found to carry across the BBB in adult Rhesus monkey a brain derived neurotrophic factor (BDNF), a neurotrophin which does not cross the BBB.[85] Another example is the fusion of the α-L-iduronidase (IDUA) to the mAb-HIR, which improved the transport of across the BBB in monkeys.[86]

13

Nicotinic acetylcholine receptor

The nicotinic acetylcholine receptor (nAChRs) are ligand-gated ion channel that are regulated by the binding of neurotransmitter acetylcholine. They are found throughout the CNS, and exist diverse subtypes composed as pentamers with unique combinations form at least seventeen (α1-α10, β1-β4, γ, δ, ε) genetically different subunits.[87] The binding of the endogenous (acetylcholine) or exogenous (nicotine) agonists to the receptor cause an opening of the ion channel, thus allowing the pass of cations such as Na^{2+}, Ca^{2+} or K^+ through the cell membrane. This receptor is widely express in brain endothelium, thus making it an attractive target for BBB-shuttles.

A 29 amino acid peptide derived from rabies virus glycoprotein (RVG) was described to inhibit the binding between the snake venom toxin α-bungarotoxin to the nAChR.[88] Kumar *et al*. proved the potential of this peptide to deliver a small interfering siRNA into the CNS.[89] In another studies, it have been confirmed the high potential of this sequence for gene delivery using polylysine dendrigraft, polyethylenimine or PAMAM dendrimers.[90–93] Also, a study reported by Fu *et al*. demonstrated how a peptide derived from RVG was able to deliver proteins with different molecular weight and pI into the brain *in vivo*.[94] Zhan *et al*. took advantage of some snake neurotoxins for the nAChR to develop two new BBB-shuttles: KC2S and [L]CDX based on *Ophiophagus hannah* toxin b and *Bungarus candidus* candotoxin respectively, which showed NP accumulation in mouse brain.[95-96] The same group developed a retroenantio version of [D]CDX peptide, which showed better transport properties due to its stability against proteases, however the affinity for the receptor was 5-fold lower than the original peptide.[97]

BBB-shuttle	Sequence	Proposed mechanism	Main cargoes
RVG29	YTIWMPENPRPGTPCDIFTNSRGKRASNG	nAchR	RNA/DNA NPs
KC2S	YTKTWC(&)DGFC(&)SSRGKRIDLG	nAChR	NPs
[L]CDX	FKESWREARGTRIERG	nAChR	NPs
[D]CDX	greirtgraerwsekf	nAChR	NPs

Table 4. Examples of BBB-shuttling by receptor-mediated transcytosis. Nomenclature of cyclic peptides (&) is based on Spengler *et al.*[63]

Leptin receptor

Leptin is a 16 kDa protein hormone secreted by adipocytes into the blood stream. Barrett *et al.* identified a fragment of leptin, from position 61-90, that could be used as potential BBB-shuttle as it presented an equivalent brain-plasma ratio as leptin.[98] The same sequence was used by Liu *et al.* been modified with a PEGylated poly-L-lysine dendrigraft for brain-targeted gene delivery.[99]

Glutathione

Glutathione (GSH) is the peptide comprised of three amino acids (cysteine, glycine and glutamic acid) present in most mammalian which plays a role in detoxification of intracellular metabolites. First, it was reported the capacity of GSH to deliver L-dopa, dopamine and adamantamine *in vitro* and *in vivo*.[100-101]

More recently, G-Technology®, which consist of PEGylated nanoliposomes targeted with GSH loaded with small drugs, have shown great results for the treatment of multiple sclerosis and cancer, being currently in Phase I/IIa (ClinicalTrials.gov ID: NCT01386580, NCT01818713, NCT02048358). Two of the great advantages of this formulation is that is not necessary to modify the drug and that a wide range of compounds that can be applied, including biologics.[102-103]

Further studies needs to be done in order to elucidate the transcytosis mechanism of GSH, as it is known that many transporters mediate its influx and efflux, some of them mainly express in the CNS.[102]

Gangliosides

Protein transporters are not the only way to achieve a certain degree of selectivity in the transcytosis across the BBB. Gangliosides are molecules composed of a glycosphingolipid with one or more sialic acids linked on the sugar chain. It have been reported the ability of gangliosides to facilitate intracellular traffic in polarized cells, thus being a potential strategy across cell barriers.[104-105]

Peptide G23, which was found by phage display biopanning against G_{T1b} and GM1, showed to have the capacity to transport nanocarriers across the BBB and provide a targeting effect, thus being a potential BBB-shuttle.[106-107]

1.4 - Assessing BBB transport in cellular models

Several models have been developed to assess the transport across the BBB. They can be classified as *in silico*, *in vitro* and *in vivo* models. The *in silico* models have gained popularity in development of new drugs as they are cheaper and less time-consuming than the experimental data through *in vitro* and *in vivo* models. Some *in silico* models for passive diffusion of small molecules have been described although they are not completely reliable.

Over the years, *in vivo* models have been used to obtain total brain concentrations and the pharmacokinetics (PK) and pharmacodynamics (PD) properties of a given compound. This type of experiments are the most reliable ones to assess brain penetration ability, however due to the huge number of generated molecules by computational, they not adequate for the first stages of development.[108] Also, their high cost, technical complexity and ethics protocols are main drawbacks of these types of assays. Therefore, *in vitro* models are the preferred choice to assess transport across the BBB, as they have a lower cost and a relatively high-throughput, thus being ideal models to optimize BBB permeability.

These models can be classified in non-cellular (passive diffusion) and in cellular-based models (endocytosis BBB models and cell-based BBB transport models).

1.4.1 – Passive diffusion BBB models

The PAMPA assay, which was developed by Kansy *et al.*, is the most used model to evaluate the passive permeability or permeability of apolar compounds across a biological barrier such as the BBB or the gastro-intestinal barrier.[38] It consists of two compartments, the donor and the acceptor, which are separated by a multilayer of lipids on an artificial membrane (*Figure 7*). At the beginning of the experiment, the drug is added into the donor compartment while the acceptor is drug-free. After a certain time, the amount of drug is measured in both compartments.
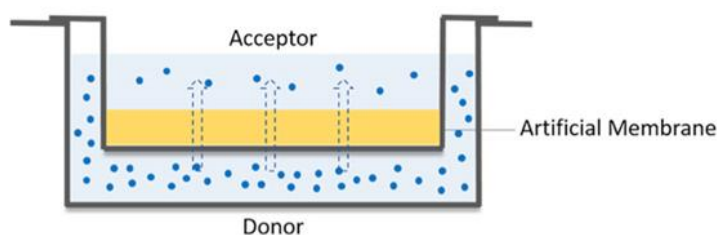
Figure 7. Scheme of PAMPA model

The permeability (P_e) can be calculated using the following equation:

$$P_e = \frac{-2183}{t} Log \left(1 - \frac{2C_A(t)}{C_D(t_0)} \right) \cdot 10^{-6}$$

Where t is the running time, $C_A(t)$ is the concentration of the compound in the acceptor well at a given time (t), and $C_D(t_0)$ is the compound concentration in the donor well before running the PAMPA assay. The units of the P_e are cm·s^{-1}.

Also, taking into account just the concentration of the compound at t_0 and at time t, the transport percentage (T) can be obtain following the formula:

$$T(\%) = \frac{C_A(t)}{C_D(t_0)} \cdot 100$$

1.4.2 – Endocytosis BBB-models

Cell cultures are not use as BBB models as they cannot estimate precisely the permeability across the BBB. The most common experiments consist of the incubation of a compound in a specific cell line and after a certain period of time, quantify the uptake in different techniques such as flow cytometry or confocal microscopy. Two of the most common cell lines used for BBB studies are b.End3 and hCMEC/D3.[109] The first one is an immortalized mouse brain endothelial cell line which express tight junctions proteins such as zonula occludes ZO-1, ZO-2, occludins and claudin-5, thus maintaining the BBB characteristics and being an attractive cell line as a model of the BBB.[110] The hCMEC/D3 is a human cerebral microvascular endothelial cell line which also express different junction-associated proteins such as claudin-3,-5, occluding and ZO-1,-2.[111]

As they are simple models, they can be used in preliminary studies in order to elucidate the mechanism of endocytosis. These types of experiments are useful as internalization is the first step towards transcytosis.

A molecule to internalize into cells via endocytosis can take different pathways of entry.
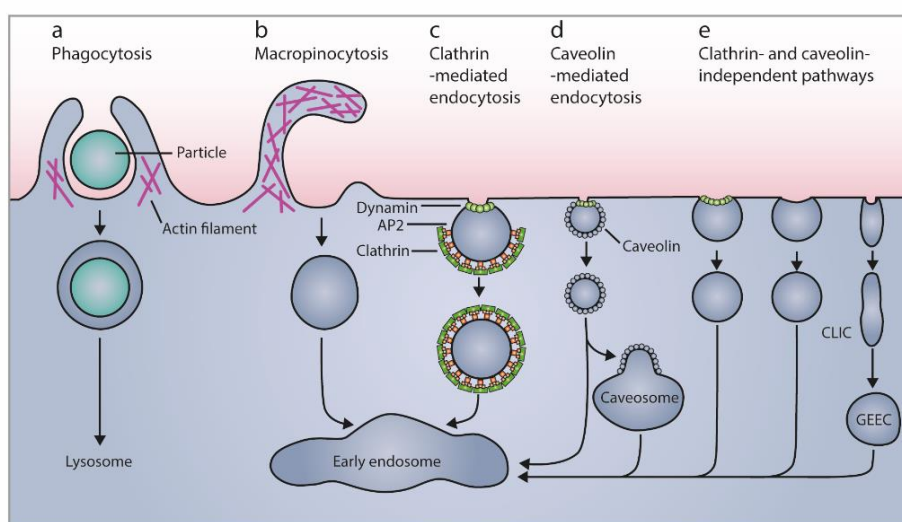
Figure 8. Different pathways of entry into cells. Adapted from Mayor *et al.*[112]

Phagocytosis and micropinocytosis are two actin-dependent endocytic mechanisms where the formed vesicles are much larger compared to other routes. While large compounds such as bacteria are taken inside the cell by phagocytosis, growth factors and

fluid use a micropinocytosis pathway. As it have been mentioned before, the BBB does not present these type of entry mechanisms.

Endocytosis produces small membrane vesicles (60-120 nm) that transport cargo molecules from the cell membrane to the cytoplasm. These cargo molecules are transmembrane proteins involved in different physiological processes such as cell signaling, cell adhesion and nutrient uptake among others. This transmembrane proteins have their extracellular ligands. It have been described many endocytic pathways of internalization, however clathrin mediated endocytosis is the major endocytic route of entry.[113]

This endocytic pathway is named due to one key component, the clathrin protein, which is responsible for the formation of clathrin-coated vesicles.[114] However, more than 50 other proteins have been described to contribute to the vesicle formation.[115-116] Adaptor proteins (AP) are another major component of the vesicles which form a second layer between the membrane and clathrin. Its function is to trap different transmembrane proteins, such as transport receptors, and attach them inside the vesicle to the soluble molecules that they transport. Each adapter protein is specific to a series of transport receptors, thus having a variety of different transport receptors and transported molecules. Clathrin mediated endocytosis is a key process in vesicular trafficking which implies transport of different molecules, such as proteins, hormones, metabolites and even viruses inside the cell. The endocytic part of the cycle begins in the regions where the clathrin-coated depressions occupy around 2% of the total area of the membrane and, within a minute of being formed, are invaginated inside the cell, separating of the membrane forming clathrin-coated vesicles.
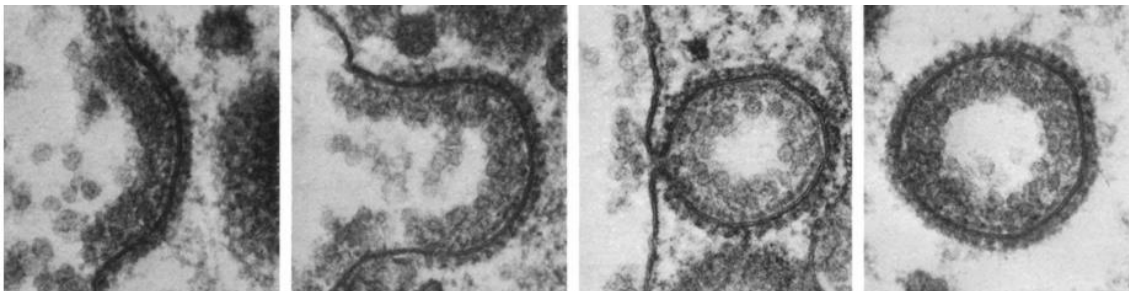
Figure 9. Electromicrograph of the formation of clathrin-coated vesicles in the plasma membrane. Adapted from Perry and Gilbert.[117]

When a vesicle coated with clathrin is being formed, soluble cytosolic proteins, including dynamin, a GTPase of 100 kDa, are assembled to form a ring around the neck of each of the vesicles. Dynamin contains a $PI(4,5)P_2$ binding domain, which binds to membrane proteins, and a GTPase domain that regulates the frequency of vesicle separation from the membrane.

The dynamin ring recruits other proteins in order to destabilize the lipid bilayers and thus separate it from the membrane.
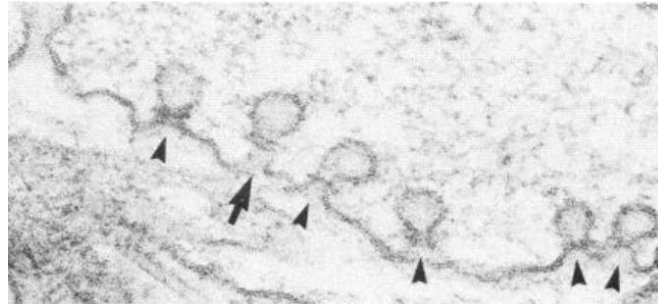
Figure 10. Electromicrograph of several clathrin invaginations on the plasma membrane with a dynamin ring around the neck of the vesicle. Adapted from Koenig *et al.*[118]

In most mammalian cells, clathrin coated vesicles are responsible for the uptake of macromolecules from the extracellular fluid. This process is called receptor-mediated endocytosis. In this process, macromolecules bind to membrane receptors that are accumulated in the coated depressions and enter the cell as a receptor-macromolecule complex. Each ligand is specific to a receptor, for example, cholesterol is transported to the blood attached to low-density lipoproteins (LDL). When a cell needs cholesterol, it produces LDL-accepting proteins that are directed to the plasma membrane. Once there, the LDL receptors are inserted into the depressions coated with clathrin and capture any LDL molecule. After clathrin shell is detached, the vesicles release their content in the early endosomes, where due to their low pH, a separation between the receptor and the ligand occurs. Afterwards, the LDL proteins are transported to the late endosomes where the cholesterol esters are hydrolyzed giving rise to free cholesterol. The receptors are instead recycled to the membrane for reuse, while the LDL are transported to lysosomes and follow a degradation pathway.

The transferrin receptor follows a route similar to that of the LDL receptor, but in this case, the ligand is also recycled. As we explained above, iron-loaded transferrin (holo-Tf) binds to the transferrin receptors in the plasma membrane. Once they reach the early endosomes, iron is released there and the transferrin-receptor complex is recycled back to the plasma membrane.[119]

The following figure shows transferrin and LDL trafficking. Both are internalized inside the cell via clathrin-mediated endocytosis. LDL, which follows a degradation pathway, are preferentially targeted to the dynamic endosomes, while the recycling transferrin is non-selectively delivered to all endosomes and enriched in the larger, static ones. Zuang and co-workers identified two populations of early endosomes: the dynamic which matures faster towards late endosomes and the static which matures much slower.[120] The experiment consist of the staining using two GTPase markers: fluorescently-labeled Rab5 and Rab7, which are mainly present in early and late endosomes respectively.[121]

The transferrin-receptor complex can return back to the cell membrane using a fast route which implies being directly transported to the cell membrane or through a slower route that involve being trafficked first to recycling endosomes before returning to the surface.[122] a co-localization of fluorescently labeled Tf with Rab11, a GTPase marker

within recycling compartments, has been described thus confirming that Tf is delivered to the recycling compartment from early endosomes.[123]
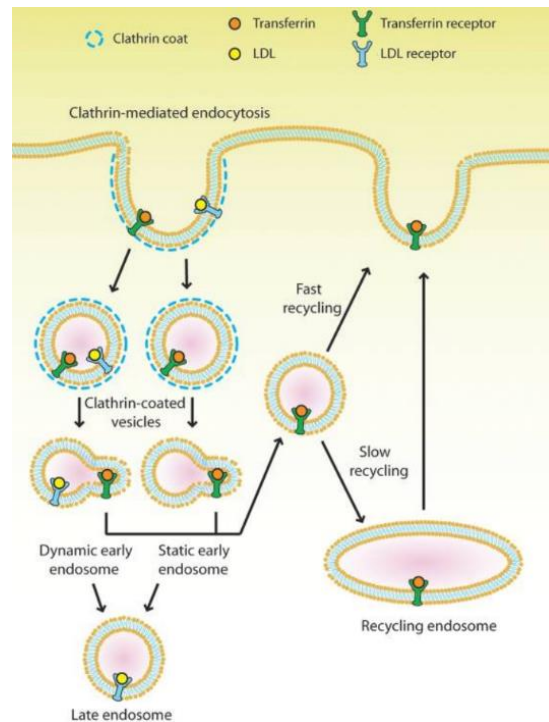
Figure 11. An overall of transferrin and LDL trafficking. Both use a clathrin-dependent endocytic mechanism to internalize from the cell membrane to the cytoplasm. Adapted from Mayle *et al.*[119]

Other receptors, such as the epidermal growth factor receptor (EGFR), which binds members of the epidermal growth factor family (EGF family), is accumulated in the cell membrane only when it is bound to EGF. It follows a degradation pathway in the lysosomes, instead of a recycling route.[124]

However, not all pinocytic vesicles are coated with clathrin. There are clathrin independent (CI) pathways in which also vesicle formation occurs. Caveolae-mediated endocytosis is the best characterized dynamin dependent CI pathway. Caveolae are flask-shaped invaginations of 50-80 nm in the cell membrane that express caveolin, cholesterol and sphingolipids.[125-126] There are three homologous genes of caveolin expressed in mammalian cells: cav1, cav2 and cav3, which encode caveolin-1, caveolin-2 and caveolin-3 21 kDa proteins respectively.[127] Caveolins are synthesized as monomers and transported to the Golgi complex as oligomers. The presence of these oligomerized caveolins leads to a change in the morphology on the membrane, thus forming the caveolae.

Figure 12. Electromicrograph (A) and (B) of caveolae located in the plasma membrane of a fibroblast. Adapted from Rothberg *et al.*[128]

1.4.3 - Cell-based BBB transport models

As it has been explained previously, isolated cells cannot mimic all the BBB properties and *in vivo* models represent high cost for preliminary screening of compounds, for this reason, *in vitro* BBB cellular models were developed in order to mimic the entire journey from the blood to the brain parenchyma. Despite of the efforts, none of these models meets all the requirements.[129] A BBB model should present different features such as reproducibility, display a restrictive paracellular pathway and physiologically architecture, expression of typical BBB transporters and ease of culture.

A recent model developed Prof. Cecchelli's laboratory has been used in the present thesis.[130] This model consists of a human brain capillary endothelial cells derived from pluripotent stem cells co-culture with bovine pericytes on a semi-permeable membranes of a transwell. After six days of culture, the endothelial cells become polarized and comply most characteristics of the BBB such as the TJs, expression of efflux pumps, proteolytic activity, among other.

When the model is seeded, for the first three days, the permeability of endothelial cells decreases until day 4 when it reaches a stationary phase which can be maintained at least for 20 days. At day 6, endothelial cells show a low permeability value to Lucifer Yellow, similar to other BBB models.[131] Also, they express transcripts of efflux transporters such as P-glycoprotein (P-pg), multidrug resistance proteins (MRP) and breast cancer resistance protein (BCRP). In addition, they express receptors which have been described that are expressed in the BBB, such as the TfR, LRP-1 or the receptor for advanced glycation end products (RAGE).
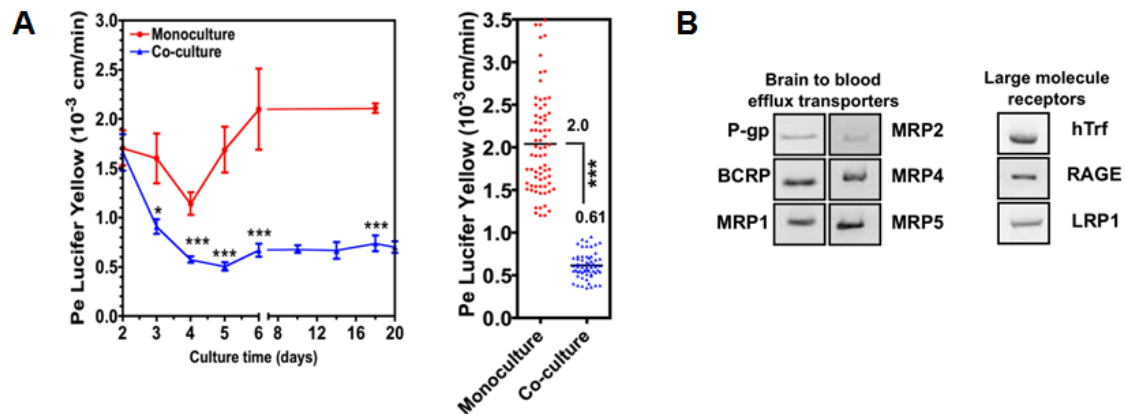
Figure 13. (A) Paracellular permeability of Lucifer Yellow (LY) in an endothelial cells monolayer either cultured alone or with pericytes. (B) Gene expression of efflux transportes and large molecule receptors in endothelial cells co-cultured for pericytes after 6 days. Adapted from Cecchelli *et al.*[130]

Also, endothelial cells showed an expression of ZO-1, occluding, JAM-A, claudin-1, claudin-5 at cell-cell contact.
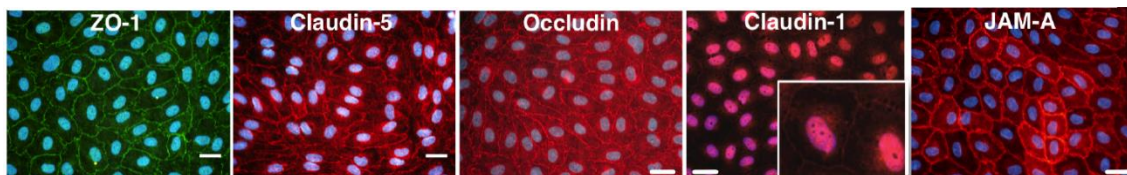
Figure 14. Expression of BBB marker proteins seen by immunofluorescence staining. Adapted from Cecchelli *et al.*[130]

Once the endothelial cells are differentiated, the transwell are placed in new culture plates without the pericytes in order to perform the transport assay.
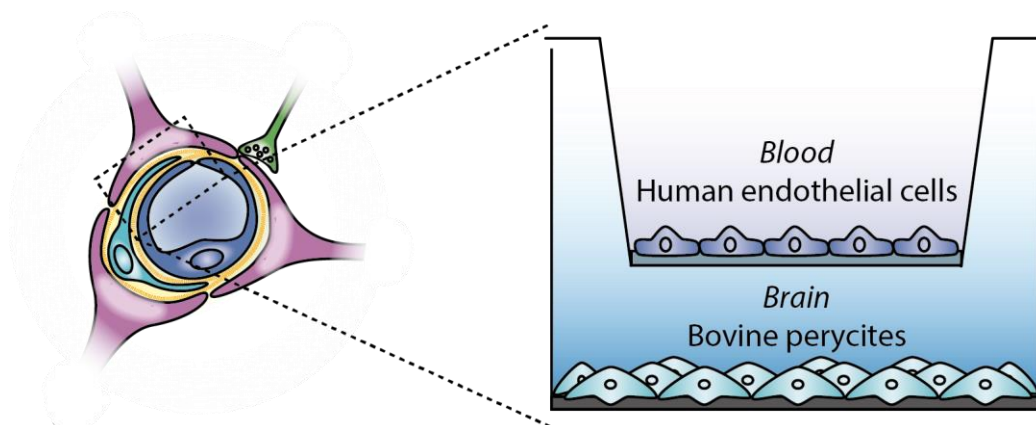
Figure 15. *In vitro* BBB cellular model representation formed by two compartments: the upper contains human endothelial cells which are co-culture with bovine perycites placed in the lower compartment.

A known concentration of a compound solution is placed in the donor compartment which represents the blood stream. After a certain period of time, the amount of compound in the acceptor compartment, which represents the brain, is analysed. In order to confirm the formation of the TJs, a known concentration of LY is add as an internal control in each

well. The analysis can be performed in different ways depending on the nature of the compound, for example peptides are quantified by UPLC, UPLC-MS or fluorescence intensity while proteins can be quantified by ELISA, fluorescence intensity or gamma counter in the case that the proteins had been radiolabelled previously.

In our group, this model have been used in order to validate different described BBB-shuttles such as THRre[83], MiniAp-4[132], Mini-CTX3[133] and SGV[134].

The apparent permeability (Papp) of peptides is calculated using the following formula:

$$Papp = \frac{Q_A(t)}{t} \cdot \frac{1}{A} \cdot \frac{V_D}{Q_D\,(t_0)}$$

Where Q_A and Q_D are the amount of compound in the acceptor at time t or in the donor at time zero, respectively. A is the area of the membrane in cm^2 and V_D is the volume in the donor compartment. The units of the Papp are cm·s^{-1}.

Also, taking into account just the amount of compound at a given time in the acceptor wells and the amount of compound in the donor wells at the beginning of the experiment, the transport percentage can be calculated using the following formula:

$$T(\%) = \frac{Q_A(t)}{Q_D(t_0)} \cdot 100$$

Also, the permeability can be expressed as the relative permeability to the parent compound, as it can be a clear way to see an improvement, for example in optimizing studies of a given peptide.

1.5 - Perspectives

Due to an aging of the population, the probability to suffer a disease related to the CNS have increased significantly, thus having an increase on the demand for adequate treatments. As it has been explained, one of the main problem that pharmaceutical industries face is the delivery of potential compounds to the brain in therapeutically relevant amounts due to the presence of the BBB which presents a tight layer of endothelial cells. Since 1986, when W. Pardridge described the concept of antibodies that could act as Trojan horses, the field of drug delivery to the brain have progressed enormously. Over the last 30 years, many approaches have emerged in order to improve the first described shuttles. Peptides offer some advantages compared to antibodies and proteins, as the low cost of production, the ease of conjugation to a wide variety of cargoes and their low immunogenicity and cytotoxicity. However, development of new BBB-shuttles with higher features such as transport or stability is still required. Most of the developed peptide BBB-shuttle present a low metabolic stability, for this reason an increase of the protease-resistance is needed in order to enhance the brain permeability. Another important need is to understand better the BBB composition in order to take advantage of some receptors that it express, thus designing potential peptide BBB-shuttles to target them, as for now, receptor-targeting is good approach in order to design new BBB-shuttles.

The development of a universal BBB-shuttle, which could transport all kind of cargoes with the same yield would be of great interest. Even more relevant, would be to have the capacity to distribute cargoes along specific brain regions, as different brain diseases affect different parts of the br

OBJECTIVES

This PhD thesis has been structured around two BBB-shuttles developed in our laboratory during the past years: THRre and MiniAp-4.

1 –The first goal of this thesis was to study in detail THRre and its interaction with the transferrin receptor by different techniques.

In order to accomplish the first objective, the following secondary aims were established:

- To validate the binding interaction between THR and THRre with the transferrin receptor by different biophysical techniques.
- To elucidate the binding site to the receptor by photocrosslinking.
- To study the pharmacokinetic properties of THRre *in vitro* and *in vivo*.

2 – The second goal of this thesis was to understand the mechanism by which MiniAp-4 crosses the BBB.

The following secondary aims were proposed to reach the second objective:

- To study the *cis/trans* ratio conformation of a range of MiniAp-4 analogues by high-field NMR techniques, with the aim to identify if there is a direct relation between the conformation population and the transport across a cell-based BBB model.
- To verify that MiniAp-4 is able to carry large cargoes as quantum dots across a cell-based BBB model and compare it with a well-known BBB-shuttle as ApoE.
- To elucidate the mechanism by which this peptide crosses the BBB by photocrosslinking

RESULTS AND DISCUSSION

THR and THRre

Introduction

A work reported by Lee, *et al*. described a screening of peptide epitopes specific for cell surface receptors as the human transferrin receptor (hTfR) using phage display.[81] This technique was discovered by G.P. Smith in 1985 and has become a widely used technique for study of protein-protein, protein-peptide and protein-DNA interactions.[135-136] It consists of a phage, a virus that infects bacterial cells, which connect protein with genetic information that encodes them. Two sequences, THRPPMWSPVWP and HAIYPRH, were identified as potential peptides that bind the human TfR in a different binding site from the transferrin. The transferrin receptor is expressed in different cell types, however in the brain microvasculature there is high expression of this receptor where it delivers the iron, thus being a possible gateway to the CNS.[12-137] In addition, an overexpressing of this receptor is found in the BBB compared to other receptors as the low-density lipoprotein receptor.[138] The main problem of THR is that, as it is form by natural amino acids, it is rapidly metabolized by serum proteases, thus having a half-life *in vitro* of 30 minutes.[83] For this reason, Prades, *et al*. developed its retroenantio version, THRre (pwvpswmpprht), where the sequence was reversed and the stereochemistry of all amino acids were changed (from L- to D- amino acids). This retroenantio version have similar topochemical characteristics and similar three-dimensional arrangement despite the inversion of the amide bond. THRre showed high stability against proteases, as D- amino acids are no recognized by them. In addition, THRre showed a capacity to transport a variety of cargoes *in vitro* and *in vivo*.[83]
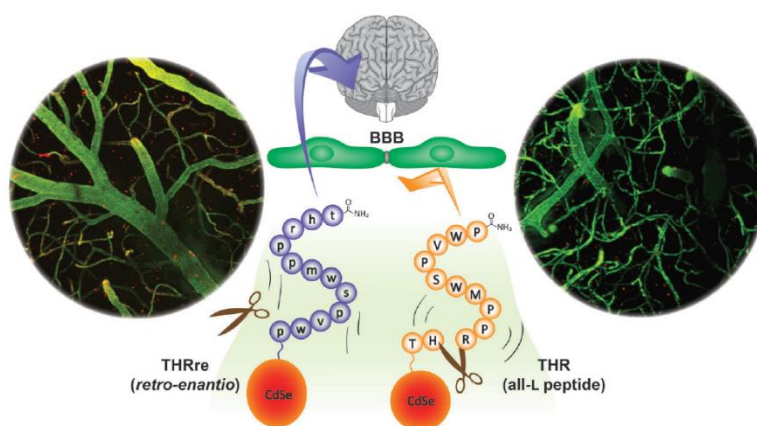
Figure 16. Protease-resistant THRre is able to transport quantum dots into the brainparenchyma. Adapted from Oller-Salvia *et al.*[139]

The main objective of this chapter was to study in detail THRre. First, we wanted to validate the interaction of THR and THRre with the TfR by nuclear magnetic resonance (NMR) spectroscopy. After, we studied more in detail the validated interaction by quantifying the strength of such binding. To this end, we used isothermal titration calorimetry (ITC) and sensor acoustic wavelength (SAW), a biophysical technique with the same basis of surface plasmon resonance (SPR). Moreover, by a photocrosslinking approach, we wanted to elucidate the binding site to the receptor. Finally, during my stay in Prof. Tetsuya Terasaki's laboratory at Tohoku University, we were able to study the pharmacokinetic properties of THRre *in vitro* and *in viv*

Biophysical characterization of the THR and THRre interaction with the transferrin receptor

Saturation Transfer Difference NMR (STD-NMR)

NMR has emerged as a powerful tool to identify and characterize protein-ligand interactions in solution under near physiological conditions.[140] It allows the study of very weak interactions (i.e. mM range), for which other techniques are often unsuitable.[141] However, the sensitivity is still too low to solve a variety of cutting-edge biological problems in solution, especially those that involve viscous samples, very large biomolecules or aggregation-prone systems that need to be kept at low concentration.[42] There are two ways to study protein-ligand interactions by NMR: from the perspective of the protein or from the perspective of the ligand.

One of the most commonly used ligand-based NMR approaches is the saturation transfer difference (STD). This technique allows the use of reduced amounts of protein with a relative easy implementation. The STD-NMR experiment is based on the rapid exchange of bound and free ligand that occurs in weak interactions (K_D values from 10^{-8} to 10^{-3} M)[142]. Assuming that the protein [P] has a single binding site for the ligand [L], the reversible binding can be described as:

$$[P] + [L] \leftrightarrow [P\text{-}L]$$
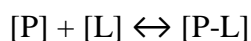
In the typical STD experiment, the protein is selectively saturated. Saturation is then transferred from the protein to any bound ligand and, for reversible interactions, to the free form of the ligand after complex dissociation. The accumulation of free saturated ligand causes an attenuation of their NMR signals. The signal attenuation could be only a few percent of the original size of the signal and may be difficult to appreciate. For this reason, the STD spectrum takes the difference between two experiments acquired in parallel, the *on*-resonance and the *off*-resonance. In the *on*-resonance experiment, the protein is selectively saturated by irradiating at a region of the spectrum that only contains protein resonances, usually at 0 to -1 ppm, where some methyl signals of folded proteins resonate and there is a minimal risk of ligand excitation..[143] For the off-resonance experiment, the typically range of irradiation frequencies is about 50 ppm, in which no protein or ligand resonances are perturbed. The resulting difference between the two spectra gives only the signals of the ligand(s) that have experienced saturation transfer from the protein *(Figure 17)*. The intensity of a given STD signal (I_{STD}) will be the difference between its intensity in the off- (I_o) and on-resonance (I_{SAT}) spectra ($I_{STD} = I_o - I_{SAT}$). Those ligand protons that are in close contact with the protein will receive the highest degree of saturation and it could be qualitatively assumed that they will also exhibit the strongest STD signals. Therefore, comparing the relative STD effects (100 x I_{STD}/I_o) it is possible to identify the chemical groups of the ligand molecule that are important for the interaction.

37
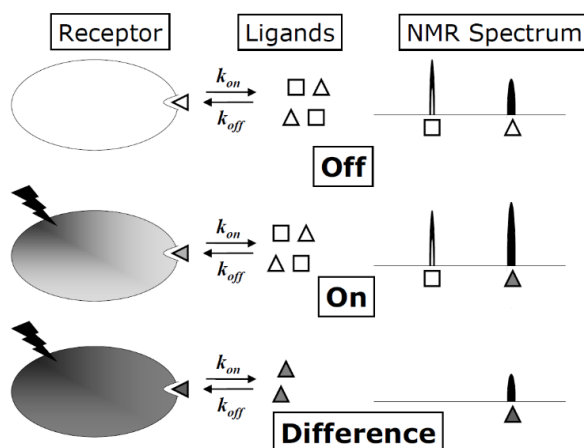
Figure 17. Schematic representation of the STD experiment. Image from Krishnan V V. *Current Analytical Chemistry*, 2005, *1*, 307–320.[144]

The objective was to prove the interaction of THR and THRre with the transferrin receptor (TfR) by STD-NMR with the help of Dr. Jesús García. To this end, we performed STD NMR for both peptides and compare them with a scrambled version of THR (PWRPSHPVWMPT) as control.[81]

For all the experiments, TfR and peptides were dissolved in 30 mM phosphate buffer, 0.05% NaN$_3$, D$_2$O at pH 7. In order to identify the residues that presented STD effects, we used the assignment previously done by Arranz *et al*.[145] However, due to the severe spectral overlap in the aliphatic region (from 1.5 to 5 ppm), we only could unambiguously identify the methyl groups of valine and threonine residues and the aromatic protons of the histidine and tryptophan residues.

In all figures three different spectrums are shown: the STD spectrum, which corresponds to the *off* minus the *on* spectrum signals, the *off*-resonance and a STD without protein used as a control.

In the case of study of TfR-THR, the concentrations used were 3 µM and 480 µM respectively. The presence of signals in the STD spectrum confirms the interaction between the peptide and the receptor. The methyl groups of the L-Val residue presented a STD effect of 3-3.5% while for L-Thr was 1.2%, suggesting that the L-Val residue is in closer spatial proximity with the protein than the L-Thr. For aromatic residues, the STD effect were 6-6.3% and 8-13% for L-His and L-Trp respectively, however the STD effect could be in some cases, overestimated. The strongest STD effects in the L-Trp protons when compared to L-His, as well in the methyl groups of L-Val compared to L-Thr suggest that the *C*-terminal region of the THR peptide is responsible of the interaction with the receptor *(Table 5) (Figure 18)*.

The following table shows the STD effects (%) for the three peptides:

Residue	δ, ppm	STD (%) THR (**TH**RPPM**W**SP**VW**P)	STD (%) THRre (p**wv**ps**w**mpprh**t**)	STD (%) THR scrambled (**P**WRPSHP**VW**MP**T**)
Val	0.8	3-3.5	6.5	1.7
Thr	1.1	1.2	3.2	1.2
His	7.015	6.3	8.3	3.3
	7.8	6	9.7	3.7
	7.1	8.8	14	5.4
	7.15	8.8	14	5.8
Trp	7.25	10	16	4.9
	7.45	13	12-13	6.8
	7.50	8	9.7	4.7

Table 5. Comparison of the STD effects (%) for THR, THRre and THR scrambled peptides. STD effects were estimated by the following equation: STD (%) =100 x I_{STD}/I_o. The chemical shifts (δ) correspond to an average for the three peptides. In the case of the Trp, values correspond to W7 and W11 for THR, W2 and W6 for THRre and W2 and W9 for THR scrambled peptides.
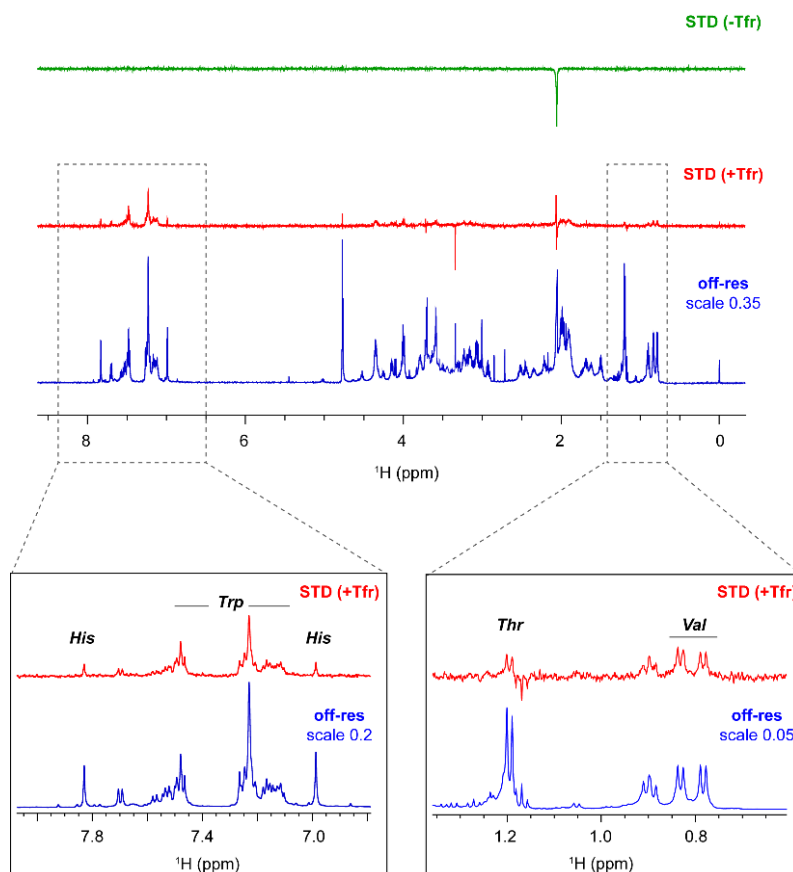
Figure 18. STD spectrum for THR-TfR study. In zoom, aliphatic and amide region in order to see differences between *off* resonance and STD spectrums.

In the case of TfR-THRre experiments, the concentrations used were 5.5 µM and 550 µM respectively, obtaining similar results as THR. In this study, higher STD effects for D-Val and D-Thr were observed, obtaining a STD effect of 6.5 and 3.2% respectively. The aromatics residues, D-His and D-Trp, presented a higher STD effect, ranging from 8-8.3% for the histidine to 10-16% for the tryptophan, suggesting that in this case the interaction site is in the *N*-terminal sequence of the peptide (*Table 5*) (*Figure 19*).
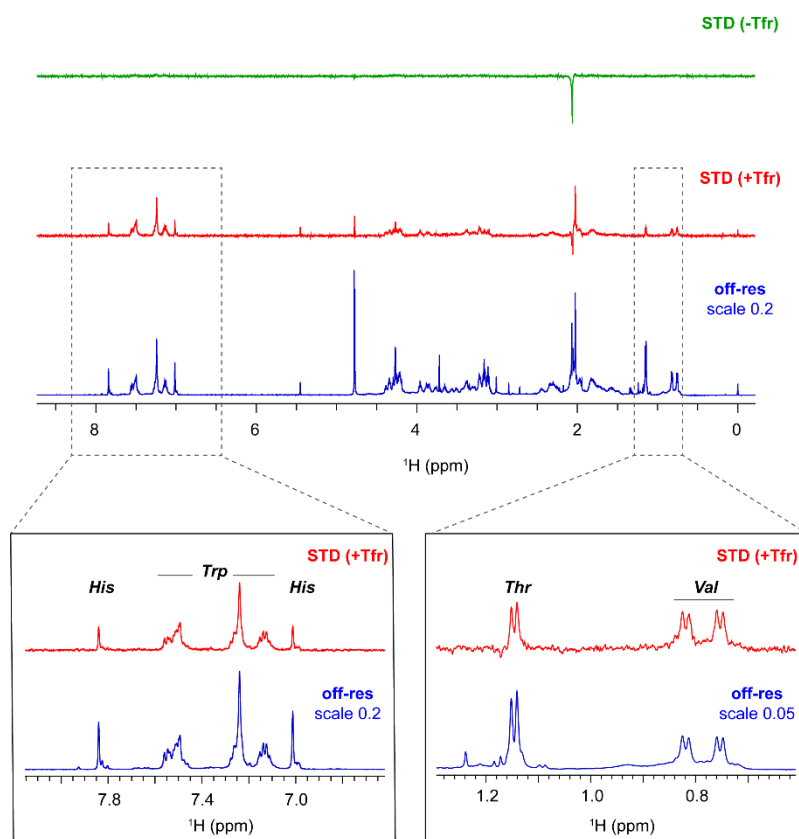
Figure 19. STD spectrum for THRre-TfR study. In zoom, aliphatic and amide region in order to see differences between *off* resonance and STD spectrums.

Both peptides showed higher STD effect values at the region where the two tryptophan residues are located, implying that this region is closer to the receptor in the bound form when, the saturation transfer takes place.

Finally, we wanted to compare the obtained results with the scrambled version of THR, which has been reported that it does not compete for the same binding region as THR.[81] In this case, all STD effects were approximately half lower than THR and THRre (*Table 5*), obtaining almost negligible values for the L-Val and L-Thr and values around 3.3-6.8% for His and Trp, reinforcing the idea of a selective interaction between the receptor and the peptide.

We could confirm the interaction of THR and THRre with the receptor, however, as these analyses are semi quantitative, a direct relation between the percentage of STD and K_D values cannot be set. Higher STD effects for the region where tryptophan are located

could be observed, suggesting that this part of the sequence is responsible for the interaction with TfR.

Isothermal titration calorimetry (ITC)

ITC records the change in temperature of a protein solution upon titration with a ligand.[146] It is a robust physical technique which allows to determine the thermodynamic parameters of interactions in solution. It is usually used to study the interaction between small molecules to larger ones such as proteins. In a single experiment, ITC measures the association constant (K), stoichiometry (n), the enthalpy change (ΔH^O) of binding. The entropy change (ΔS^O) of the reaction, as is related to the Gibbs free energy of binding (ΔG^O), can be easily calculated from the following relationship: $\Delta G^O = -RT\ln K = -T\,\Delta S^O$. During a biomolecular interaction event, the formation of non-covalent interactions (van der Waals contacts, hydrogen bonds, salt bridges, etc.) at the interface, together with the reorganization of nearby water molecules, often results in heat exchange. ITC is the only approach that directly measures heat exchange during complex formation at a constant temperature and it provides useful information about the forces (enthalpic or enthropic) that drive the interaction process.
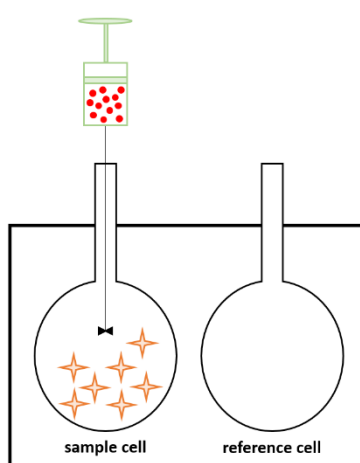
Figure 20. ITC instrument consists of a stirring syringe, a sample cell and a reference cell.

The most commonly used isothermal titration calorimeters are based on a cell feedback network which measures the differential heat effects between a sample and a reference cell which contains the buffer in which the sample is dissolved (*Figure 20*). In the first injections the analyte binds to the ligand, resulting in endothermic or exothermic signal. As the concentration of analyte increases in the sample cell, the ligand becomes saturated until no heat is evolved or absorbed. After, the heats can be plotted versus the concentration of the analyte injected obtaining a binding curve. After applying the appropriate binding model into the obtained curve, all the thermodynamic parameters can be obtained. The binding affinities that can be measured by this technique are between 10^{-9} and 10^{-3} M.

As we have explained, STD results proved the interaction between the TfR and THR or THRre. The next step was measuring this interaction by ITC. To this end, the first step was to measure the constant of affinity of the TfR with its natural ligand, the holo-Tf and see if there was a correlation between the reported values ($K_D \approx 1$nM). For this, we followed the work by Bou-Abdallah and Terpstra in which the interaction between the TfR and different types of transferrin were studied in detail.[147]

In our experiment, the holo-Tf was titrated (16 injections of 3 µL at 100 µM) into a solution containing 12 µM of TfR, both samples dissolved in the same buffer. As we can see in the *Figure 21*, at each ligand injection, a heat is absorbed and decreases gradually

due to the saturation of the binding site of the receptor. By fitting the data, a K_D value of 38 ± 10.78 was obtained for the Tf-TfR interaction, very similar to the reported values.[147] This experiment was repeated at least 3 times obtaining similar results.
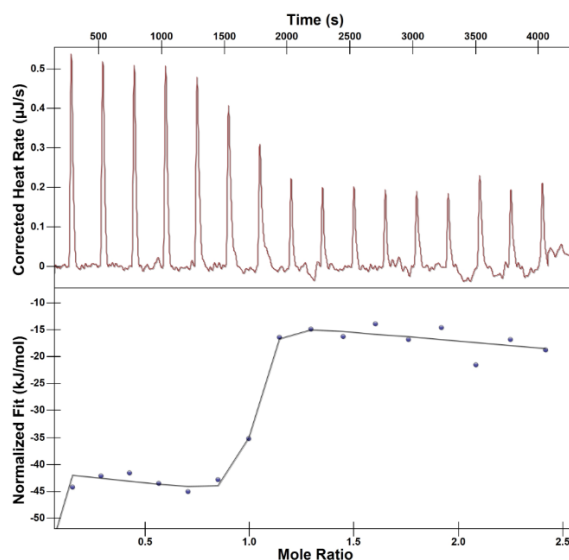
Figure 21. The top panel show the raw calorimetric data obtained for 16 automatic injections (3 μL) of holo-Tf. The area under the peaks was integrated and plotted against the molar ratio of holo-Tf to TfR.

Once the interaction of the TfR with holo-Tf was validated, we evaluated its interaction with our two peptides of interest, THR and THRre.

In the case of THR peptide, the TfR, at 12 μM, was titrated with a solution of 5mM of the peptide. The binding isotherm did not show saturation plateau, indicating a weak binding to the protein. Even though, after fixing the stoichiometry of the interaction to 1 and fitting the data to a single binding site model, a K_D value of 0.72 mM could be obtained. The ΔH and ΔS were -271.6 kJ·mol⁻¹ and -850.9 J·(mol·K)⁻¹ respectively (*Figure 22*).

Figure 22. The top panel show the raw calorimetric data obtained for 16 automatic injections (3 μL) of holo-Tf. The area under the peaks was integrated and plotted against the molar ratio of THR to TfR. The solid line represents the best fit of the experimental data to a single site binding model.

However, for THRre, it was not possible to obtain a K_D value, even at a high concentration as 5 mM. With the obtained isotherm, NanoAnalyze software was not able to fit the data.

Also, we tried to increase the concentration of THRre in solution, however it could not be done due to solubility problems.

	K_D	ΔH, (kJ·mol^{-1})	ΔS, (J/(mol·K))	n
Holo-Tf	38 ± 10.78	-33.16 ± 3.05	32.75 ± 13.08	0.9 ± 0.05
THR	0.72	-850	-271.6	1
THRre	Interaction could not be measured			

Table 6. Thermodynamic binding parameters for holo-Tf, THR and THRre.

With our results in hand, we could conclude that maybe ITC is not the ideal technique to study the interaction between the transferrin receptor and THR and THRre peptides due to their low affinity. For this reason, we decided to move to another biophysical technique as SAW, which lower affinity constants can be measured in order to obtain better results.

Surface acoustic wave (SAW)

As an alternative biophysical method, we used a surface acoustic wave (SAW) device. SAW sensors are reported to be extremely useful for the analysis of real-time binding events of biomolecules at high sensitivity. This technique requires one binding component to be immobilized on a sensor chip surface, which serves as the recognition element of a specific ligand, while the other binding component is flowed over the sensor surface in buffer solution. A binding interaction is detected using an acoustic method that measures small changes in the amplitude and phase of the acoustic waves as they progress through the sensor surface (*Figure 23*).
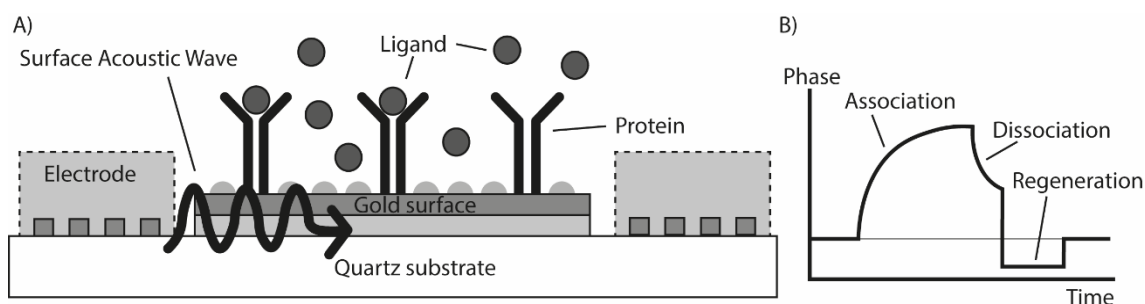
Figure 23. Schematic representation of A) a SAW biosensor and B) representation of a theoretical sensogram of the association and dissociation events.

One of the main drawback is that once the immobilization takes place, the part of the element that is in contact with the surface gets inaccessible to interact with the ligand. For this reason, different coating of the chip can be assessed to have all the binding sites of the molecule available for the interaction.[148]

SAW sensors allow the use of label-free ligands, from small molecules to peptides and proteins, which will interact with an immobilized partner at the surface of the chip. First, a solution of the ligand passes over the immobilized compound. If there is an interaction

between these two, an increment of mass over the sensor surface occurs, leading to a change of the phase of the acoustic wave. Analysis of this data gives the association rate constant (K_{obs}). After a certain time, the ligand solution is replaced by a dissociation buffer (usually containing a high concentrations of salts at a low or high pH) to disrupt the interaction between the ligand and the immobilized partners, thus regenerating free protein. Analysis of this part gives the dissociation rate constant (K_{off}).

The affinity of the interaction can be calculated with the following formula:

$$K_D = \mathrm{K_{off}} / \mathrm{K_{on}}$$

Where the K_{on} is the association rate constant of the interaction and can be calculated knowing the concentration of the ligand.

The surface of the chip that we used in our experiments was coated with a 2D monolayer of *16*-mercaptohexadecanoic acid. First, we tried to immobilize our protein directly on the SAM chip via carbodiimide chemistry. After, a capping of the unreacted NHS-esters is performed with a solution of 1M of ethanolamine-hydrochloride at pH 8.5 in order to reduce the undesired further immobilization (*Figure 24*).
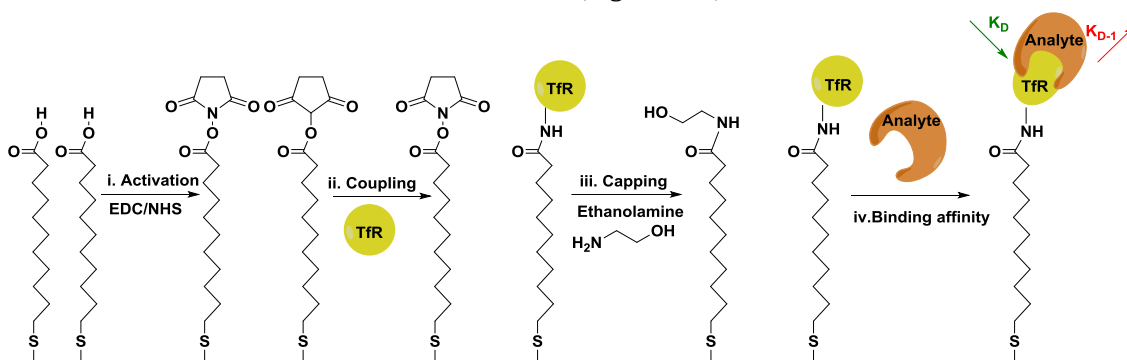
Figure 24. Scheme of i) the activation of carboxylic groups of SAM by EDC/NHS; ii) coupling of a TfR via carbodiimide chemistry iii) capping of unreacted NHS-esters with ethanolamine hydrochloride iv) affinity binding of the analyte.

After several unsuccessful attempts to obtain a good interaction between the expressed TfR and its natural ligand, the holo-Tf, we hypothesized that the receptor was immobilized by its interaction site. For this reason, we decided to design a new TfR construct bearing a His$_6$-tag at its *N* terminal, in order to have all the sites of the protein accessible for the interaction once the receptor is immobilized on the chip surface. For this purpose, we add an extra step during the activation of the chip surface. After the activation of the carboxylic group with EDC and NHS, after we injected a solution of tris-NTA amine, followed by a 0.5 mM solution of NiCl$_2$. The NTA-amine react with the activated carboxylic acids and helps to chelate the Ni^{2+}, which has a high affinity for His$_6$-tag. After the coupling of the His$_6$-tag protein, an EDC/NHS step followed by a capping is performed in order to crosslink the lysine of the protein (*Figure 25*).
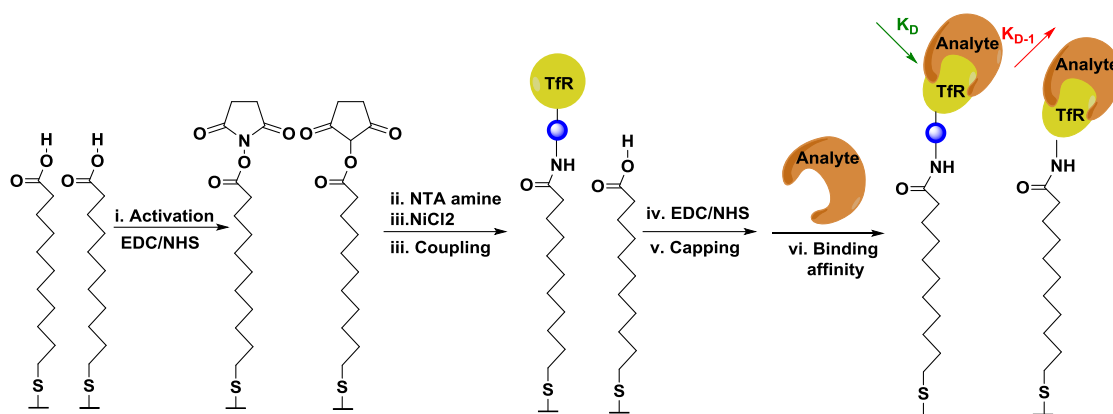
Figure 25. Scheme of i) the activation of carboxylic groups of SAM by EDC/NHS; ii) tris-NTA amine iii) NiCl₂ iv) Coupling of the His₆-tag TfR; iv-v) crosslink of the lysine residues of the TfR; vi) affinity binding of the analyte.

The holo-Tf was injected from 100 nM to 20 μM in 50 mM Pipes (pH 7.5), 150 mM NaCl, 0.005% (v/v) P20 and flown over immobilized TfR. To disrupt the holo-Tf-TfR interaction the same running buffer was supplemented with a high concentration of 0.5 M of $MgCl_2$. Changes in the amplitude and the phase of the acoustic wave report on the mass loading of the chip, allowing the quantification of the binding events. Binding curves were analyzed by using the Origin Pro 7.5 software, and pseudo-first order kinetics (k_{obs}) were determined by busing the FitMaster software, from which K_D values were calculated by linear regression *(see Materials and methods, SAW experiments)*.

The measured K_D value for TfR-Tf interaction was 3.38 ± 0.35 μM, similar to the reported values (*Figure 26*).[147]
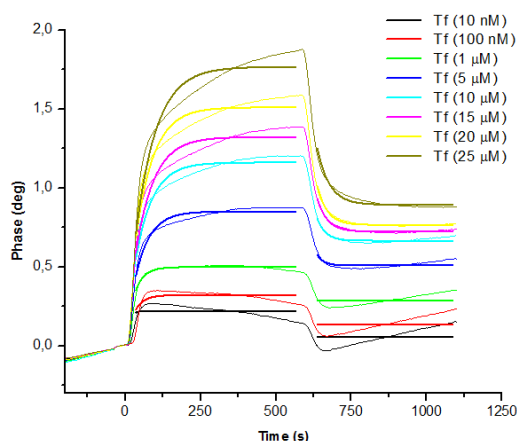
Figure 26. SAW sensogram of Tf injected at a range of concentrations from 10nM to 25 μM. N=3. Significant changes were not observed between replicates.

After validating the control interaction, our two peptides of interest, THR and THRre, were studied. The range of concentration for THR was from 7.8 μM to 2M, obtaining a K_D value of 0.97 ± 0.06 mM. In the case of THRre, the injected concentration moved from 250 μM to 4 mM, however, the Origin program was no able to calculate the K_D value. Higher concentrations of the peptide could not be injected due to solubility

problems. For this reason, we hypnotized that the K_D value is higher than 4 mM (*Figure 27*).
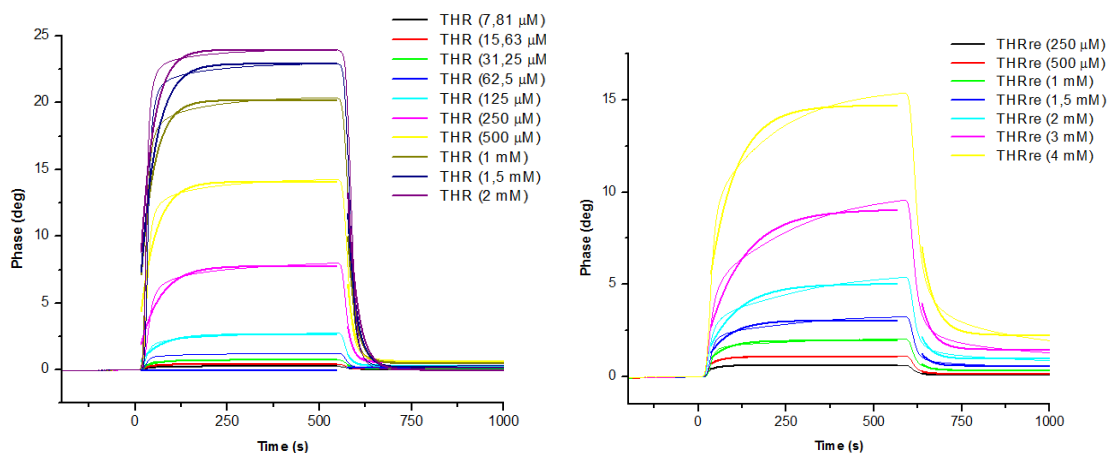
Figure 27. SAW sensograms of THR (left) and THRre (right). N=3. Significant changes were not observed between replicates.

In order to validate the assay, we performed a negative control measuring the interaction of DRG3 peptide (FGQKASS) with the TfR. This peptide that recognizes specifically the dorsal root ganglions (DRG) neurons, the most affected in Friedreich's ataxia.[149] In this case, DRG3 was injected in a range of concentrations from 125 µM to 2 mM (*Figure 28*).
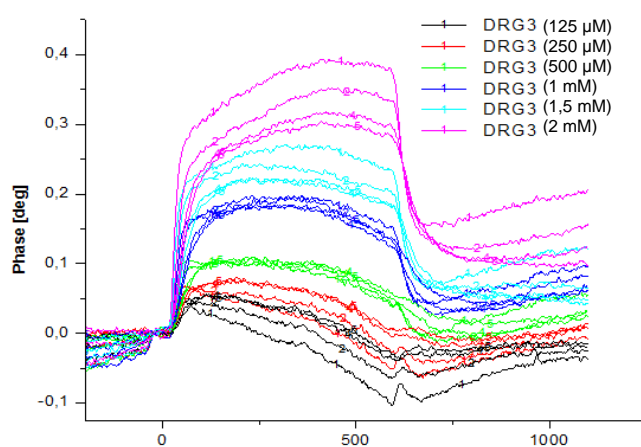
Figure 28. SAW sensograms of DRG3 injected at a range of concentrations from 125 µM to 2 mM. N=3. Significant changes were not observed between replicates.

As it was expected, no interaction between the TfR and this peptide was observed, not even at higher concentrations. To rule out the degradation of the receptor, holo-Tf was injected obtaining again similar values as the reported ones. With our results in hand, we could confirm the interaction of THR and THRre with the TfR. However, the measured constant of dissociation was weak for THR and we could not calculate it for THRre. The results are in agreement with the calorimetry experiments suggesting a feeble interaction between both peptides and TfR. these two different techniques are not the most suitable to study this kind of interaction.

In conclusion, we have probed the affinity of THR and THRre for the TfR by NMR spectroscopy. After, we quantified the interaction by ITC and SAW. In the case of THR, similar results for ITC and SAW were obtained, however the K_D value was low ($\approx$1 mM). In the case of THRre, it was not possible to obtain a K_D value by ITC neither by SAW technique, suggesting that the interaction with the receptor is weaker than the one of the

parent peptide, as is normal in these type of constructs. Wei, *et al*. reported two works in which they described how retroenantio versions of L-CDX and Angiopep-2 peptides, which target the nicotine acetylcholine receptor (nAChR) and the low density lipoprotein related protein 1 receptor (LRP-1) respectively, presented lower binding affinities for the corresponding receptor than the parent peptide.[97-150]

Photocrosslinking as a tool to elucidate the THR/THRre-TfR binding site

Discovered over sixty years ago by Westheimer *et al*.[151] photoaffinity labeling has evolved significantly, although its principle remains unchanged. Photoaffinity labeling requires the use of a photoactivable inert group, which upon light binds irreversibly to the biological target. This photoirradiation leads to the formation of highly reactive species such as nitrene, carbene or diradical, which rapidly form a covalent bond between the photoprobe and the biological target.

In general, aromatic azides, aliphatic and aromatic diazirines and benzophenones are used as photoreactive groups in photoaffinity labeling.[152-153] When one have to choose between one of them for a particular case study, it is important to consider their advantages and disadvantages. For example, aryl azides are small and can be easily incorporated into a ligand; however, its maximum absorption wavelength is below 300 nm, which can induce considerable damage to biological systems upon irradiation. Diazirines are more stable than azides upon different conditions, nevertheless their synthesis can be difficult and long. Finally, benzophenones are excited between 350-360 nm like diazirines; however, due to their bulkiness, the interaction between the photoprobe and the biological target can be hampered. In addition, benzophenone sometimes need a long period of irradiation that can be a risk for non-specific labeling.[154]

In order to facilitate the isolation of the photolabeled products, the addition of a tag, such as a biotin or a fluorophore, is widely used (*Figure 29*).
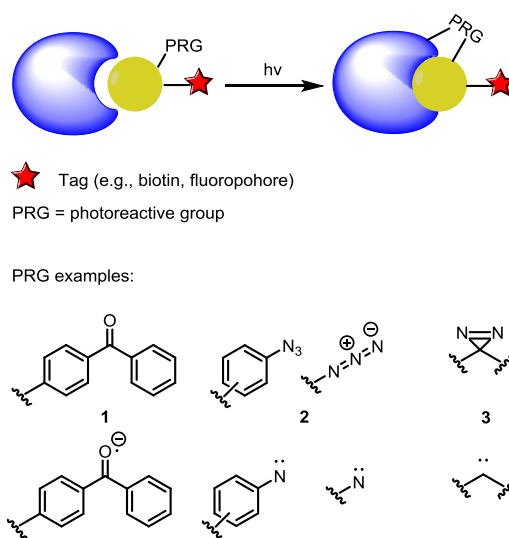
Figure 29. Schematic representation of photoaffinity labeling conjugation. A probe (yellow) contains a photoreactive group (PRG) (1: benzophenone, 2: aromatic azide and arylazide, 3: diazirine; with their respective radical versions) and a tag (red) (e.g. biotin, fluorophore) and upon irradiation a covalent is formed with the biological target (blue).

The aim of this chapter was to elucidate the binding site of THR and THRre to the transferrin receptor. As it has been explained in the introduction, these two BBB-shuttles cross the BBB using the transferrin receptor via receptor-mediated trancytosis.[81-83]

In the previous STD experiments, we confirmed the interaction of these two peptides with the transferrin receptor, thus we designed two photoreactive versions mutating one of the tryptophan residues for a non-natural commercial amino acid bearing a benzophenone

moiety, a 4-benzoylphenylalanine (Bpa), obtaining two photoreactive versions for each peptide. The peptides were synthetized by SPPS using the standard Fmoc/*t*Bu conditions and Bpa was coupled using 4 eq of TBTU and 8 eq of DIEA. The peptides were obtained in good yield and their synthesis did not present any additional difficulties.

Once we had synthetized and purified the peptides, we move to the crosslinking experiment. First, to assess the correct folding and activity of the expressed TfR, ITC with the holo-Tf was performed at the same conditions described previously *(see Materials and methods, ITC experiments)*.

Time course experiment

TfR and photoreactive peptide were incubated at 4ºC at a 1:1 ratio and irradiated at different time points at 365 nm. Kinetic analysis of a 1:1 protein:peptide mixture was performed in order to demonstrate time-dependent production of the crosslinked TfR-peptide complex.

Transferrin receptor and Bpa-peptide were mixed at 12 μM each, incubated for 20 minutes in the dark to allow binding and then irradiated after selected times (0.5, 1, 2, 5, 10, 20, 30, 40, 50 and 60 minutes). After UV exposure, samples were diluted with 2x loading buffer, electrophoresed and analyzed by WB (*Figure 30*).
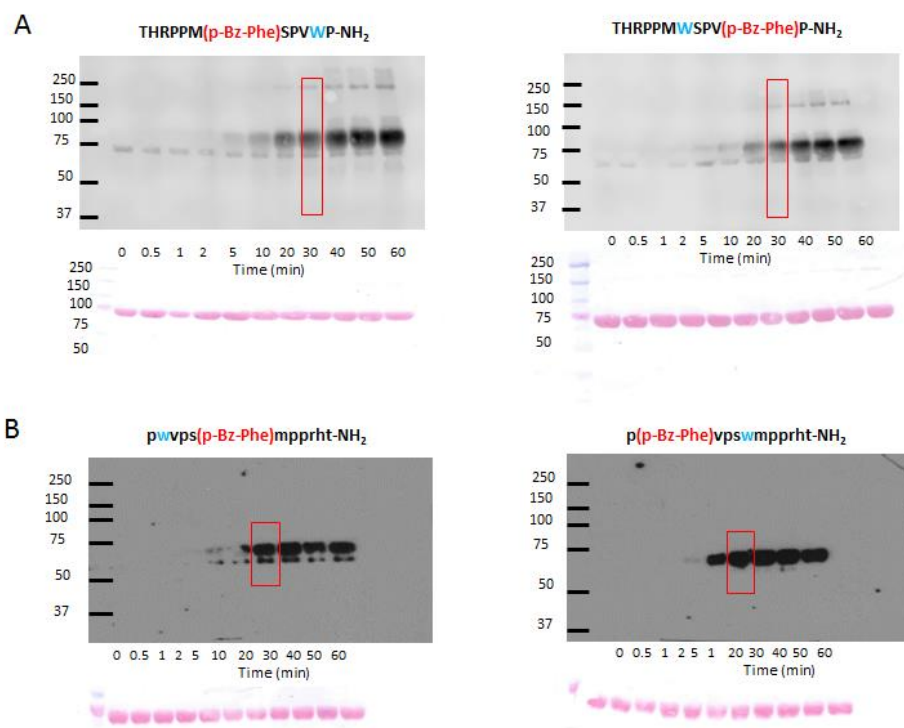
Figure 30. WB analysis (up) and ponceau staining (down) of time course for UV-dependent crosslinking of THR (A) and THRre (B) upon UV irradiation. N=3. No significant changes were observed between replicates.

For all four peptides, we clearly validate a time-dependent relation as over time a clear band around 80 kDa appears that corresponds to the crosslinked product. For further experiments, 30 minutes was selected as an optimal time for obtaining a photocrosslinked product.

Characterization of the THR/THRre-TfR photocrosslinked product and elucidation of their binding site

The next step was the characterization of the THR and THRre photocrosslinked product. Two approached were attempted, first analysis of the intact mass of the complex and second, analysis of the tryptic digested complex in order to elucidate the binding site region of the peptide to the receptor using mass spectrometry techniques. Recent studies in MS have facilitated the study of protein-ligand interactions, allowing the detection and characterization of individual conformational states of protein complexes.[155]

The analysis of the intact mass proved to be challenging. In first place, the analysis of the starting receptor was unsuccessful until we decide to deglycosilate the sample with PNGaseF to facilitate its detection.

We performed the experiment using the already optimized conditions: TfR and Bpa-peptide were pre-incubated in the dark at 12 μM and then irradiated for 30 minutes at 365 nm. After that, the mixture was filtrated through a MidiTrapG25 column in order to eliminate the unreacted peptide. Then in order to isolate the biotinylated products, an affinity purification step was carried out incubating the mixture with Dynabeads™ MyOne™ Streptavidin T1 overnight at 4ºC was performed followed by the elution with biotin protocol (*see Materials and methods, Streptavidin magnetic beads protocol*). Unfortunately, it was not possible to obtain the intact mass of the photocrosslinked product.

For the elucidation of the binding site, same protocol was used, however after elution step with biotin, a deglycosilation step followed by SDS-page. After, digestion of the band was carried out and analyzed by nano-LC-MS/MS. The searches for crosslinked peptides were performed with StavroX software and run against a fasta database, which contained two entries: user protein and expected crosslinked peptide. Due to unexpected delays on the MS analysis, results are still pending.

Pharmacokinetic studies of THRre and analogues

This chapter corresponds to our collaboration with Prof. Tetsuya Terasaki's laboratory at Tohoku University in Sendai, Japan. His research group is focused on absolute proteomics and its application to BBB research. During my stay in his laboratory, I had the opportunity to work with Sadanori Toba, a master student whose master's project was based in the study of the pharmacokinetic properties of two BBB-shuttles, THRre and MiniAp-4, *in vitro* and *in vivo*.

Quantitative targeted absolute proteomics (QTAP)

Proteomics consists of the characterization of a complete set of proteins that are present in cells, organ, organism or another type of biological system. For the last years, several advances in mass spectrometry and global proteomics have enabled the identification of proteins in biological samples in a single analysis.[156–158] However, with global proteomics is not possible to detect low-abundance proteins due to the high background noise. For these reason a new generation of proteomic methods named quantitative targeted absolute proteomics (QTAP) has been developed in order to determine the absolute protein expression levels of target protein in biological materials by liquid chromatography-linked tandem mass spectrometry (LC-MS/MS). The targeted peptides are quantified by selected/multiple reaction monitoring (SRM/MRM) in the MS/MS device, using a triple quadrupole (QqQ) to achieve highly selective and sensitive quantifications.

The QqQ consists of Q1 and Q3 chambers which are mass filters of the parent and daughter ions respectively, and a Q2 chamber in which the peptide is fragmented by N_2 gas. (*Figure 31*) Each combination of a Q1 and Q3 is a SRM/MRM transition.
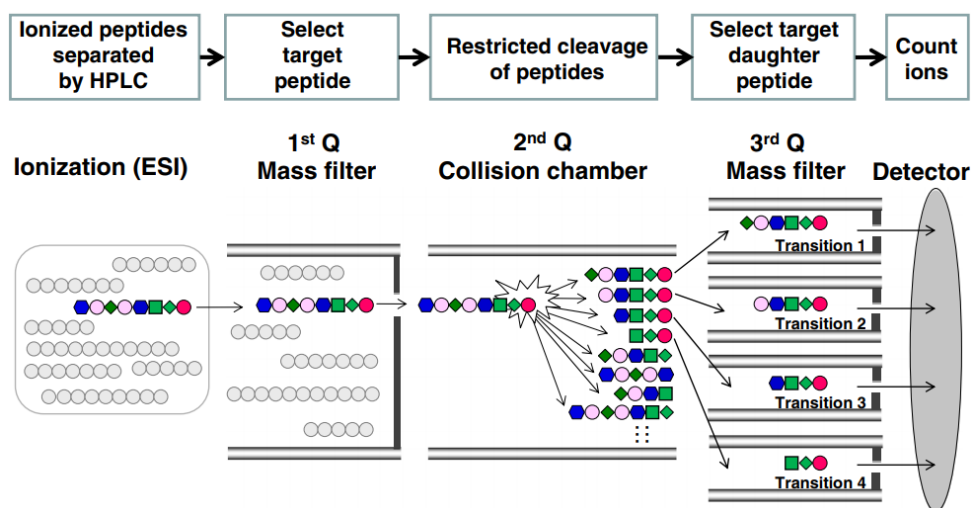
Figure 31. Principle of peptide selection by selected/multiple reaction monitoring (SRM/MRM) mode of triple quadrupole mass spectrometry (QqQ MS). Adapted from Uchida *et al.*[159]

However, this technique has some limitations such as the length of the selected peptide which has to be no longer than 8-10 amino acids for the QqQ MS analysis.[159]

As a general overview, the workflow of a QTAP consists of one first step of the selection of the targeted protein or peptide that one wants to quantify. After, it is necessary to synthesize the isotopically labeled versions that will be used as an internal standard (IS).

Then a calibration curve using a mixture of unlabeled peptides and a fixed amount of labeled followed by the sample preparation. Finally, the LC-MS/MS is performed in order to calculate the protein/peptide level in the biological samples.

Previous results

As I mentioned, the main objective of our collaboration was to study the pharmacokinetic (PK) properties of THRre *in vitro* and *in vivo*.

For that, the initial experiments, carried out by Sadanori Toba, aimed to prove the interaction between THRre and the transferrin receptor. For that we used the human cerebral microvessel endothelial cells line (hCMEC/D3) which is widely used for *in vitro* studies as it mimics the BBB.[111] This cell line express claudins and occluding, which are necessary for the tight junctions.

To this end, THRre was co-incubated at 1 µM with 1 mg/mL of holo-Tf (diferric) and apo-Tf (non-ferric) for 15 minutes in hCMEC/D3 cell line. Moreover, holo-Tf was pre-incubated for 30 minutes at 1 mg/mL in order to decrease the density of transferrin receptor in the cell membrane. (*Figure 32*). To better understand this plot, first we need to explain what exactly means the Cell/Medium ratio (CM). This concept can be defined as:

$$CM = \frac{\text{peptide concentration in cells } (\frac{\text{fmol}}{\text{µL}})}{\text{peptide concentration in medium } (\frac{\text{fmol}}{\text{µg protein}})}$$
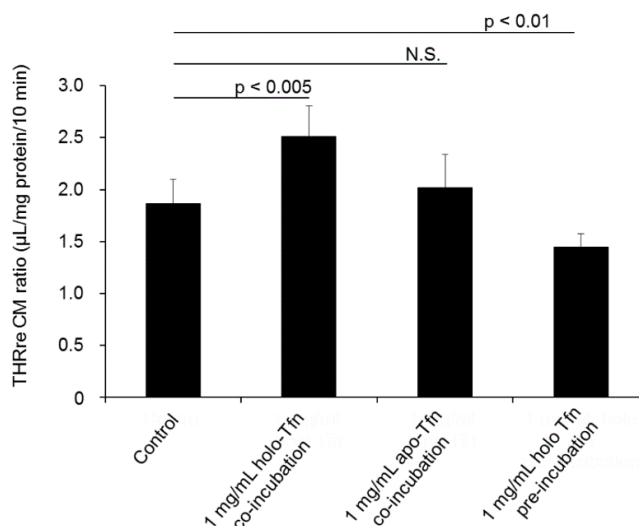
Figure 32. Effect on the uptake of THRre in the presence of apo-Tf and holo-Tf in hCMEC/D3 cells. Each bar represents the mean ± SD. N=5. P value was obtained from Student's t-test. N.S: no significance differences observed.

As it can be observed in the above figure, the internalized THRre amounts were influenced by the presence of the holo-Tf (iron loaded) but not for the apo-Tf (non-iron), confirming that THRre interacts with the human TfR.

We next evaluated the use of an endocytosis inhibitor, chlorpromazine (CZPZ), a cationic amphipathic drug that inhibits clathrin-mediated endocytosis. Transferrin, which is the natural ligand for the TfR, is known to internalize through a clathrin-mediated endocytosis, so a decrease in the uptake of THRre would lead to reconfirm the interaction between such peptide and the TfR. After a 10 minutes pre-incubation of the hCMEC/D3 cells in ECF buffer (0.12 M NaCl, 25 mM NaHCO$_3$, 3 mM KCl, 0.4 mM K$_2$HPO$_4$, 10 mM glucose, 1.4 mM CaCl$_2$, 10 mM HEPES), 50 μM solution of CPZ was added for 30 minutes, followed by the addition of a 1 μM solution of THRre for 10 minutes at 37°C (*Figure 33*).
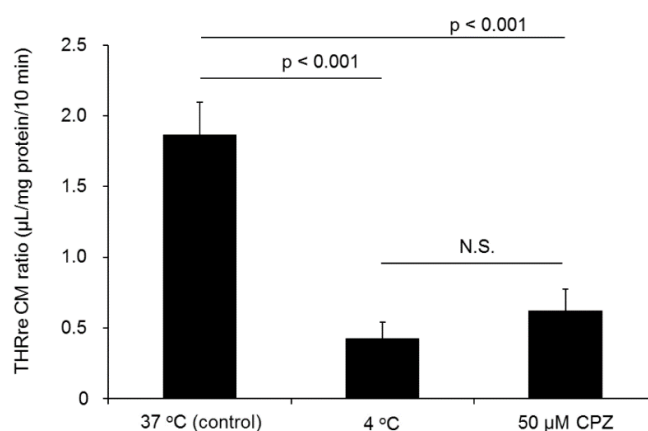
Figure 33. THRre uptake inhibition at 4°C and in a presence of chlorpromazine inhibitor. Each bar represents the mean ± SD. N=5. P value was obtained from Student's t-test. N.S: no significance differences observed.

The addition of the CPZ produces a significant decrease on the THRre uptake, decreasing more than 50% the CM ratio value, implying the involvement of clathrin-mediated endocytosis pathway in the internalization of THRre inside the cells.

We next, evaluated the PK of THRre *in vivo* (mice and rats). 500 nmol/kg and 250 nmol/kg of THRre were administrated in mice (male, 8 weeks) and Wistar rats (male, 8 weeks) respectively. Blood samples were drawn from same jugular vein at (0, 5, 10, 15, 30 minutes and 1, 2, 3, 4 and 5 hours).

In order to obtain the PK values of THRre, data was fitted by MMLTI program using the two-compartment model which considers that the body is divided in two parts: the central which consists of the blood and well perfused organs (e.g. liver or kidney) and the peripheral which corresponds of tissue where the distribution of the drug is slower.[160] In this approach the following equation is used: $C_{p(t)} = ae^{-\alpha t} + be^{-\beta t}$ in which a, b, α and β are called Hybrid Constants.
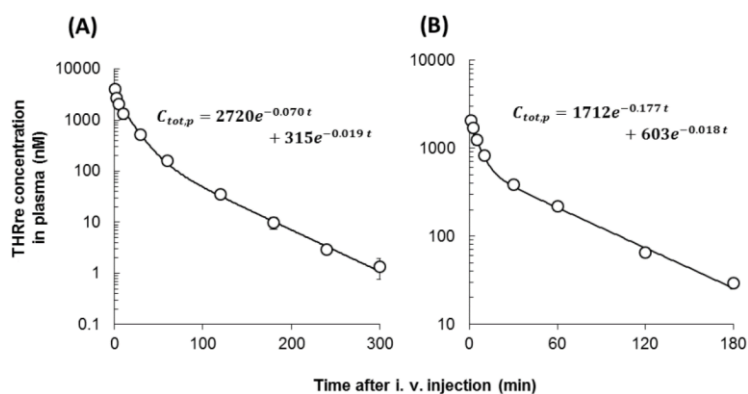
Figure 34. THRre plasma concentration versus time curve in mice (A) and rats (B). Each point represents the mean ± SD. N=3.

The following table show the parameters obtain using a MMLTI program, a program developed by Yamaoka *et al.* widely used in pharmacokinetic studies.[161] In the following table, we can see the different parameters obtained. As we mentioned, A, B, α and β are the Hybrid Constant. The volume of distribution at steady state (V_{dss}), represents how a compound is distributed to the actual blood and tissue volume and the relative binding to protein in these spaces. The total clearance (CL_{tot}) describes the rate at which compound is removed from the systematic circulation per unit time. As it can be observed in the table, the THRre values where compared with inulin, a polysaccharide used as an extracellular fluid marker.

Parameter	Mice		Rat	
	THRre	Inulin[162]	THRre	Inulin
A (pmol/mL)	2720 ± 786		1712 ± 125	
α (min^{-1})	0.070 ± 0.015		0.177 ± 0.039	
B (pmol/mL)	315 ± 87		603 ± 49	
β (min^{-1})	0.019 ± 0.001		0.018 ± 0.001	
V_{dss} (mL/kg)	240 ± 43	181 ± 62	257 ± 7	219 ± 24
CL_{tot} (mL/min/kg)	9.15 ± 1.02	11.3 ± 1.5	5.65 ± 0.19	6.47 ± 0.24

Table 7. A, α, B and β were calculated from MMLTI program. Each value represents the mean ± SD. N=3.

Also, the permeability values for THRre where compared with two different monoclonal antibodies, RI7 and OX-26, which recognizes the transferrin receptor.

	PS value (µL/g brain)	
	Mice	Rat
THRre	16.6 x 10^{-3}	16.6 x 10^{-3}
[^{125}I]-RI7 (anti-murine TfR mAb)[163]	1,2	
[^{3}H]-OX-26 (anti-rat TfR mAb)[164]		1,56
^{99}Tc-Albumin[165]		9,72 x 10^{-3}

Table 8. PS value of THRre in mice and in rats. Comparison with TfR monoclonal antibody and albumin.

500 nmol/kg and 250 nmol/kg of THRre were injected in mouse and in rat in order to obtain the permeability values. The BBB permeable clearance of THRre obtained was 1/100 compared to an anti-TfR antibody and only 1.7 times higher than albumin which is known as a non-permeable marker protein.[165]

Evaluation of time dependency uptake of THRre

hCMEC/D3 cells were pre-incubated with warm ECF buffer for 15 minutes followed by the incubation of 1 µM solution of THRre in RH buffer at different time point (0, 2.5, 5, 10, 20 and 30 minutes) at 4ºC or 37ºC. At selected time points, cells were washed with sodium acetate buffer at pH 3.5 in order to remove the peptide from the cell surface. After obtaining the cell homogenates for all the conditions, peptide concentration was quantified using a micro LC-Qtrap. *Figure 35* represents the CM ratio values over time, observing an increase in the uptake at 37ºC and non at 4ºC.
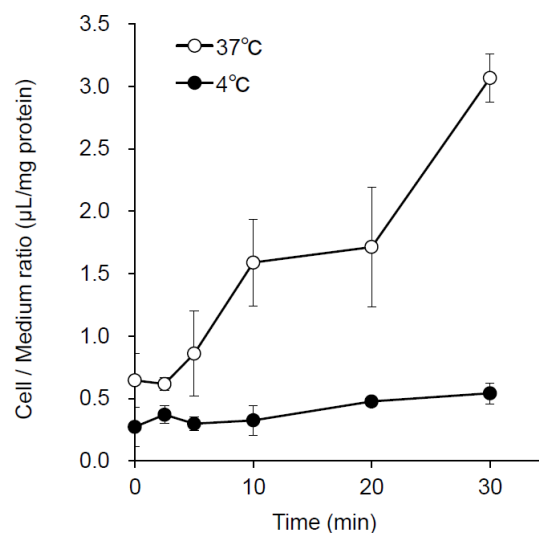

Figure 35. Uptake time course of THRre at 4ºC and 37ºC in hCMEC/D3 cells. Concentration in cell homogenate was quantified by micro LC-Qtrap 5500. All data represent mean ± SD. N=3.

Also, it was confirmed that THRre does not bind to a plasma protein higher than 12 kDa, as the recovery of such peptide after a centrifugal filtration with a dialysis filter of 12-14 kDa was closed to 100% at different plasma concentrations by LC-MS/MS analysis.

The problem was that after centrifugal filtration through with a 3.5 kDa membrane cut-off, no recover of the peptide was obtained. This lead us to hypothesize that THRre aggregates somehow, for these reason, we decided to study the behavior of such peptide with different cargoes, as what is actually important is if the peptide with a cargo aggregates.

Study of different THRre analogues

With our previous results where after filtration through a membrane of 3.5 kDa no peptide was recovered, we hypothesize that maybe THRre aggregates. For this reason, first we design and synthesized six different analogues containing different cargoes. On one hand, DRG1 (SPGARAF) and DRG2 (DGPWRKM) were chosen as peptide cargoes. These peptides were discovered by phage display and targeted the root dorsal ganglions neurons in mice, which are the most affected in Friedreich's ataxia.[149] On the other hand, we decided to use L-Dopa as a small size cargo. L-Dopa is a pro-drug of dopamine used in Parkinson's disease which is transported to the brain by the large natural amino acid transporter (L1) in competition with ten naturally occurring large neutral amino acids.[166-167] In order to increase the solubility and stability, we also prepared the PEGylated versions with a $(PEG)_3$ as a spacer of all analogues.[168]

For the THRre-G-DRG1 and THRre-G-DRG2, a glycine residue was used as a spacer in order to facilitate the synthesis. In addition, for these two peptides an extra step of tryptic digestion was required in order to reduce the sequence for the further analysis by the QTAP technique as a length of 8-10 aa is ideal for the detection.[159] We have to take into account that before the LC injection, it is necessary to perform the desalination of all the samples by GL tips (*see Materials and methods*).

The first step was the optimization of Q1 and Q3 values for the parent peptide and all analogues. All peptides were detectable unless the THRre-G-DRG1, THRre-G-DRG2 and THRre-$(PEG)_3$-DRG2.

	Channel	Q1	Q3
	1		301
THR	2	497.3	491.6
	3		688.3
THRre-G-DRG1	1	559.0	284.1
THRre-$(PEG)_3$-DRG1	1	793.7	284.1
	2	595.6	254.2

	3		268.2
	1		371.0
L-Dopa-THRre	2	557.3	497.3
	3		554.3
	1		353.1
LDopa-(PEG)$_3$-THRre	2	625.1	371.1
	3		509.3

Table 9. m/z channel of Q1 or Q3 represent singly, doubly or triply charged product ions of THR and the detectable THRre analogues.

To rule out that the fact of not being able to detect the DRG2 peptides was the oxidation of the methionine, we performed the direct infusion of the two peptides at 5 and 10 µM, however, the non-oxidized form peak was the majority one. Therefore, maybe the length (18 aa even after trypsin step) or the sequence were not ideal to be detected by this technique.

After, a calibration curve was done. For that, a range of concentrations of the peptides from 5 to 200 nM in 0.1% FA were injected. A fixed amount of isotopically labeled peptide, heavy-THRre, was added in each sample, to be used as internal standard. This isotopically labeled version (pw*Vpswmpprht) contains a L-Val residue in which all the carbon has been substituted for ^{13}C, therefore increasing the molecular weight 5 Da. With this experiment the limit of quantification (LOQ) for each peptide was calculated:

	LOQ (fmol/injection)
THR	2.03
THRre	4.2
THRre-G-DRG1	415
THRre-(PEG)$_3$-DRG1	55.6
L-Dopa-THRre	115
L-Dopa-(PEG)$_3$-THRre	9.50

Table 10. Peptide QTAP limit of quantification.

Evaluation of peptide aggregation by filtration dialysis

In order to study the hypothesized aggregation of THRre, we decided to study the recovery of such peptides after a centrifugal filtration though a membrane with a cut-off of 6-8 kDa. Peptides were dissolved in RH at 5 µM and centrifuged for 2 hours at 5400g through the membrane. The obtained solution was diluted 1/10 in H$_2$O with 0.1% FA and injected at the LC-MS/MS in order to calculate the recovery.

	Donor (µM)	Acceptor (µM)	Recovery (%)
THRre		2.21	44.1 ± 3.3
THR		2.39	47.7 ± 11.3
THRre-(PEG)$_3$-DRG1	5	0.14	2.82 ± 0.41
L-Dopa-THRre		1.5	29.9 ± 4.3
L-Dopa-(PEG)$_3$-THRre		2	39.8 ± 4.2
THRre (12-14 kDa)		4.22	84.5 ± 8.5

Table 11. Peptide recovery percentages of THR, THRre and all the detectable analogues quantified by micro LC-Qtrap 5500. All data represent mean ± SD. N=4.

The peptides with the highest recovery were THR, THRre and L-Dopa-(PEG)$_3$-THRre analogue. The dialysis through a 12-14 kDa membrane was performed as a positive control. Results suggested that THRre behaves similar when L-Dopa is the cargo, while for the PEG-DRG1 analogue, the recovery is almost 0%.

Quantification of peptide uptake using hCMCE/D3 cell line

After, we decided to calculate the CM ratio of all the detectable peptides by measuring its internalization in hCMEC/D3 cells. For this, peptides were incubated at 0.5 µM for 15 minutes in the presence 0.1% w/v of BSA and 0.1 mg/mL of holo-Tf. BSA and holo-Tf were used to avoid non-specific binding to the cell surface plate and to stimulate endocytosis respectively. After and in order to remove peptide in the cell membrane, 3 cycles of washing of the cells were performed in sodium acetate buffer at pH 3.5.[169]

Finally, concentrations of each peptide were quantified, however for THR and L-Dopa conjugates, concentrations in cell homogenate were under the LOQ, thus being not possible to calculate the CM ratio. In the case of THRre-(PEG)$_3$-DRG1 analogue, it was not possible to obtain a linear standard calibration curve ($R^2 < 0.95$).

	CM ratio (µL/mg protein)
THRre	1.17 ± 0.41
THR	< 1.94
THRre-(PEG)$_3$-DRG1	$R^2 < 0.95$
L-Dopa-THRre	< 17.6
L-Dopa-(PEG)$_3$-THRre	< 2.60

Table 12. Cell/Medium ratio of THR, THRre and the cargo peptides. All data represent mean ± SD. N=3.

Competition experiment of THRre and all analogues

In order to study if THRre and all synthesized analogues bind to the same binding site of the TfR, we designed and performed a competition experiment, in which each peptide was co-incubated with THRre. To this end, a solution of 5 µM of THR or THRre analogues was co-incubated in hCMEC/D3 cells with 0.5 µM of THRre in RH in the presence 0.1% w/v of BSA and 0.1 mg/mL of holo-Tf at 37ºC for 15 minutes.

As *Figure 36* shows, all the peptides except for PEGylated-DRG2 analogue decreased the uptake of THRre, suggesting that there is a competition during the internalization, suggesting that they share the same binding site. In the case of, PEGylated-DRG2 maybe due to its tridimensional structure, there is no competition while for the L-Dopa as it is a small cargo, the CM ratio significantly decreased.
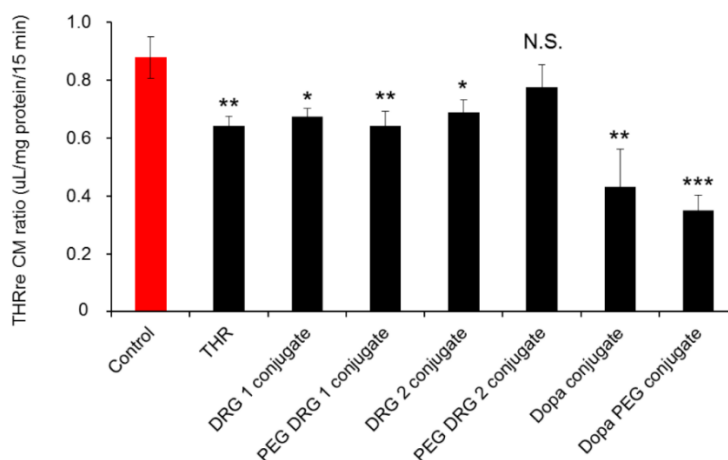
Figure 36. Competition experiment between of THRre with all analogues. Concentration in cell homogenate was quantified by micro LC-Qtrap 5500. All data represent mean ± SD. N=3.

Comparison of holo-Tf and THRre uptake

As it has been reported and probed in this present thesis, THRre crosses the BBB by interacting with the TfR. For this reason, we wanted to compare the holo-Tf and THRre uptake amounts in hCMEC/D3 cells as they targeted the same receptor.

	Protein amount (fmol/µg protein)	CM ratio (µL/mg protein)
TfR	2.69 ± 0.22	-
Holo-Tf	4.65 ± 0.29	8.10 ± 0.61
THRre	0.59 ± 0.21	1.17 ± 0.41

Table 13. On one column, comparison of protein amounts of holo-Tf, TfR and THRre in hCMEC/D3 cells. In right column, comparison of CM ratio of holo-Tf and THRre. All data represent mean ± SD. N=3.

The transferrin receptor amount quantified in hCMEC/D3 cells was 2.69 ± 0.22 fmol/µg protein, similar to the reported values (3.83 ± 0.31 fmol/µg protein) by Ohtsuki *et al.*[138] The amount of THRre quantified in cells was significantly lower than Tf, being actually 8 times lower. When we compare the CM ratios of Tf and THRre, a huge difference can be observed, however it is normal as Tf is the natural ligand for the receptor.

In summary, we have been able to obtain different PK parameters *in vitro* and *in vivo*, however the PS values obtained, together with the V_{dss} and CL_{tot}, suggested that the internalization of this peptide is low, validating all the data obtained by biophysical studies and photocrosslinking

MiniAp-4

Introduction

Venoms contain highly bioactive and selective components and have traditionally been used to treat a variety of pathologies. Recently, advances in analytical techniques have allowed the discovery of a number of bioactive compounds, some of which have found clinical applications. One such example is BLZ-100, a chlorotoxin venom analogue used as an imaging agent for cancer.[170] Among their many applications, venoms have showed potential to reach the CNS, however most of these substances reach the brain through the bloodstream causing an inflammation to the BBB, which facilities unspecific paracellular diffusion.[171] The best known venoms are from snakes, scorpions and spiders, although many venoms from other animals have been studied. Nevertheless, only a small number of compounds related to venoms have been described to penetrate the BBB and reach the brain by crossing the barrier without causing damage.[172]

Among the few peptide animal toxins that have been reported, apamin and chlorotoxin are the most widely studied. The use of venoms as source of BBB-shuttles has previously been validated with the development of MiniAps family inspired in apamin. Apamin is a 18-mer peptide derived from bee (*Apis mellifera*) venom and known to cross the BBB and blocks calcium-mediated potassium channels.[173] In our laboratory, a set of apamin analogues were designed and synthesised in order to optimise the parent peptide. The first cyclic minimised version of apamin with improved BBB transport properties was MiniAp-3, however, its serum stability was limited ($t_{1/2}$= 2.8 h).[174] In order to obtain a cyclic peptide of the same size of MiniAp-3, aspartic (D) and diaminopropionic acid (Dap) were selected to form a lactam bridge, leading to obtain MiniAp-4, which had a dramatically increased proteolytic stability ($t_{1/2}$ >24h). MiniAp-4 was obtain as the lead candidate due to its resistance to serum proteases, its efficiency to deliver various cargoes across a HBBBCM and to be considerably less toxic and immunogenic than apamin (*Figure 37*).[132] Also, MiniAp-4 is able to deliver a fluorophore into the brain parenchyma of mice upon *i.v* injection. Previous experiments using PAMPA and Caco-2 assays point to an active transport mechanism.[174]
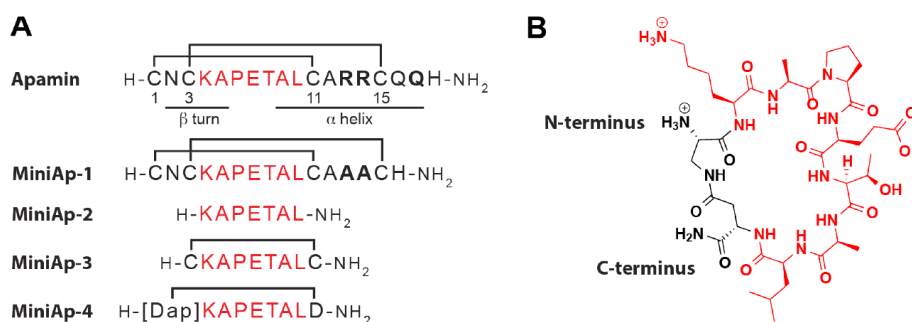
Figure 37. MiniAp family inspired in apamin. A) Sequences represented with one-letter code. B) Molecular structure of MiniAp-4. (From Oller-Salvia et al. 2016)[132]

The good properties of MiniAp-4 were attribute the good stability against proteases. It is well established that proline residues can introduce conformational diversity as a result of *cis/trans* isomerization of the Xaa-Pro tertiary peptide bond.[175] MiniAp-4 showed a remarkable 1:1 *cis/trans* Ala-Pro conformer population, however the role of this noticed feature was not clear.

Evaluation of proline cis-trans ratio as tool to fine-tune transport

In this chapter, our main goal is to analyse how the proline conformational states may influence the transport and stability of MiniAp-4 and a set of analogues with different point mutation at the *C-* or *N-* terminal.

Their Ala-Pro *cis/trans* population ratio was quantified by NMR spectroscopy and their proteolytic stability was evaluated in different mediums. After, BBB transport was assessed using a human cell-based BBB model (HBBBCM).

Design and synthesis of analogues

The first MiniAp-4 analogues were designed to evaluate the relevance of the position and chirality of the amino acids forming the lactam bridge. To this end, the *C-* and *N-* terminus were swapped (analogue **1**) and the natural aspartic acid (D) was mutated to the corresponding D-amino acid (d) (analogue **2**). A direct relation between the replacements of some residues by their D-version has recently been reported to be related to an improvement in the cell permeability of polar cyclic peptides.[176]

We then evaluated the structural constraints imposed by the cycle by changing the length of the lactam bridge. In this regard, *cis/trans* isomerism was examined in the sequence X(&)KAPETALZ(&), with the X and Z amino acids forming the lactam bridge chosen from a set of positively (Dap**,** Dab**,** Orn, and Lys) and negatively (Asp and Glu) charged residues differing in the length of the side chain (analogues **3**-**6**). Finally, the proline was mutated to 5,5-dimethylproline (dmP) (analogue **7**) to study whether the *cis* proline conformer could be blocked, as it is well-established that dmP induces a shift in *cis/trans* equilibrium towards the *cis* form as a result of steric hindrance caused by the two methyl groups (*Figure 38*).[177]
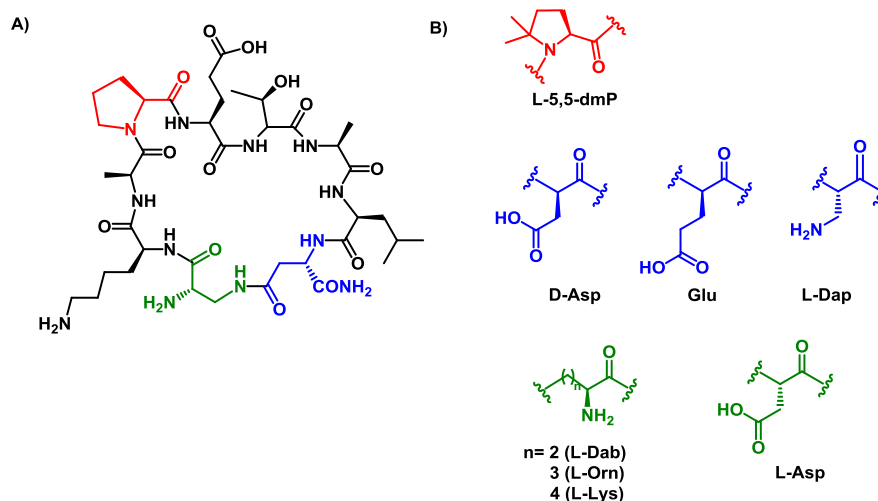
Figure 38. A) MiniAp-4 structure showing the different point mutations at the *C-* (blue) or *N-* (green) terminus and also at the proline residue (red). B) Chemical structure of the amino acids used to generate the MiniAp-4 analogues.

All peptides were synthesized using standard Fmoc/*t*Bu SPPS and Rink AmideChemMatrix resin was used to provide an amide at the *C*-terminal in analogy to MiniAp-4. Oxyma (3 eq.) and DIC (3 eq.) were used as coupling reagents for the

elongation steps, and UPLC-MS was used to confirm completion of the couplings. In the case of analogue **7**, the correct incorporation of Ala was hampered due to the steric hindrance of the two methyl groups of the preceding proline. After several attempts using different coupling reagents, including HOAt and PyBOP, we found that the best option was to increase the number of equivalents of Oxyma and DIC to 5, together with an increase in the reaction time to 16 hours. The amino acids involved in the lactam bridge formation were orthogonally protected. In the case of Dap, Dab, Orn and Lys, amines were protected with an Alloc group to prevent their acylation, which would lead to the formation of undesired branched peptides. Asp and Glu carboxylic acids were protected in form of allyl esters.[178] Removal of these two protecting groups was carried out with tetrakis(triphenylphosphine)palladium(0) in the presence of phenylsilane, followed by the removal of palladium traces with a solution of sodium diethyldithiocarbamate. For the formation of the lactam bridge standard coupling conditions, such as PyBOP (4 eq.), HOAt (12 eq.), and DIEA (12 eq.), were used and UPLC-MS was used to confirm the cyclization. After all syntheses were completed, peptides were cleaved from the resin, purified by preparative HPLC, and conveniently characterised by UPLC and UPLC-MS.

NMR studies

With the peptides in hand, we analysed their conformational behaviour and their *cis/trans* population ratio by NMR (600 MHz). Complete sequence-specific assignments were obtained using a combination of 2D homo- (TOCSY, ROESY) and hetero-nuclear (^{1}H ^{13}C HSQC) NMR experiments (performed by Dr. Monica Varese). The *cis* and *trans* conformers were identified on the basis of the chemical shift difference between ^{13}C$_\beta$ and ^{13}C$_\gamma$ from proline residues and from identification of diagnostic NOE connectivities between specific proline protons and the H$_\alpha$ of the Pro-preceding residue.[179]

Similar to what was reported for MiniAp-4, the analysis of structure-based NMR parameters such as ^{13}C$_\alpha$ chemical shifts and ^{3}J$_{\alpha NH}$ coupling constants did not suggest a defined secondary structure for either the *cis* or *trans* conformers of the peptides studied in this work. In addition, only sequential ROE connectivities were observed in the ROESY spectra, further indicating that these peptides do not exhibit a unique and well-defined secondary structure.

Swapping of the amino acids involved in the lactam bridge (analogue **1**) and changing the chirality of the *C*-terminal residue of MiniAp-4 (analogue **2**) had little effect on the *cis/trans* population ratio, although both modifications slightly reduced the *cis* content from 50% in MiniAp-4 to 45% and 43% in analogue **1** and **2**, respectively.

Similarly to MiniAp-4, in which the lactam bridge is formed by 5 bonds (z = 5), analogues **4** (z = 7) and **6** (z = 6) showed equally populated *cis* and *trans* conformers (*Table 14*); whereas analogue **3** (z= 6), resulting from the replacement of Dap by Dab, deviated slightly from this trend, showing 45% of the *cis* rotamer. Analogue **5**, which differed from MiniAp-4 only in the replacement of Dap by Lys, the latter extending the side chain in three bonds (z = 8), showed a moderate decrease in the population of the *cis* isomer (37%). These results suggest that changes in the length of the lactam bridge have only modest or

no effects on the conformation of the prolyl amide bond. In the MiniAp-4 sequence, an increase in the length of the lactam up to 2 bonds (z = 7) did not have a significant effect on the *cis*/*trans* ratio when compared with the parent peptide. In contrast, for longer lactam bridges (analogue **5**, z = 8), a moderate decrease in the population of the *cis* rotamer was observed, most probably related to the lower structural constraints on this longer cyclic peptide. Finally, we examined the effects of replacing the natural proline residue of MiniAp-4 with the proline analogue dmP. This amino acid is known to favour the *cis* conformation of the peptidyl-prolyl bond as a result of the increased steric hindrance of the two bulky methyl groups at the C_δ position of the dmP residue.

	n	m	z	Ratio *cis*/*trans*
MiniAp-4	1	1	5	50:50
1	1	1	5	45:55
2	1	1	5	43:57
3	2	1	6	45:55
4	3	1	7	50:50
5	4	1	8	37:63
6	1	2	6	50:50
7	1	1	5	83:17

Table 14. Description of MiniAp-4 peptide analogues and summary of the relative population of *cis* and *trans* rotamers. Number of methylene groups in the side chain of the *N*- (**n**) and *C*-terminal (**m**) amino acids and number of bonds in the lactam bridge (**z**). Quantification of Pro *cis*/*trans* population was done by NH amide peak integration in 1D ^{1}H-NMR spectra acquired at 298 K.

Two distinct sets of resonances, with relative populations of 85% and 15%, were observed in the NMR spectra of analogue **7** (*Figure 39*).
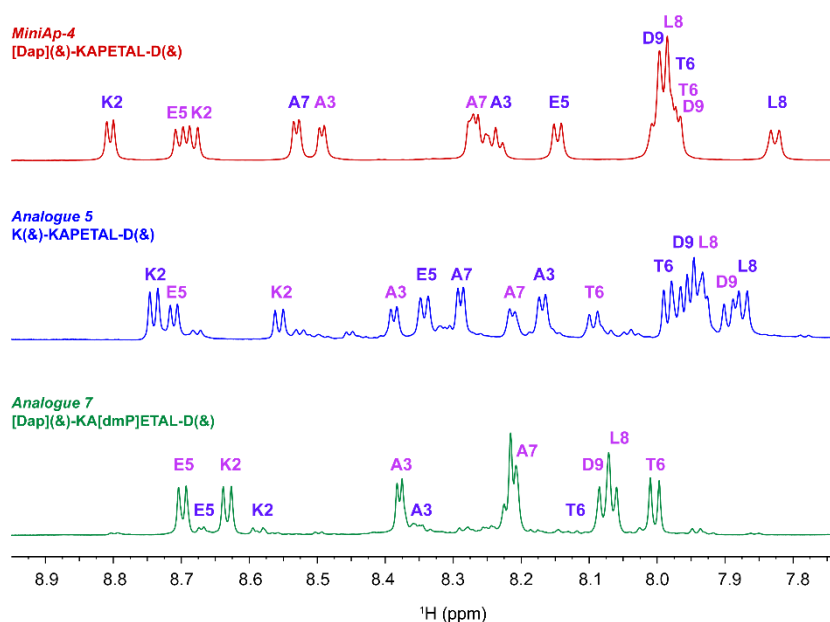
Figure 39. Comparison of the amide region of the 1D ¹H NMR spectra of MiniAp-4 (red), analogue **5** (blue) and analogue **7** (green). The amide resonances of the *trans* (purple) and the *cis* (pink) conformers are labelled.

The predominant species was identified as the *cis* Xaa-Pro bond conformer on the basis of a strong ROE cross-peak between the H_α of Ala and the H_α of dmP and between the $H_{\varepsilon3}$ of dmP and the NH amide proton of E5 (*Figure 40*). In contrast, the complete NMR elucidation of the minor species, which we assumed corresponds to the *trans*-rotamer, could not be achieved due to the low intensity and overlapping of the signals, which hindered the detection of the diagnostic NOE cross-peaks between H_α of Ala and the $H_{\varepsilon3}$ of dmP.

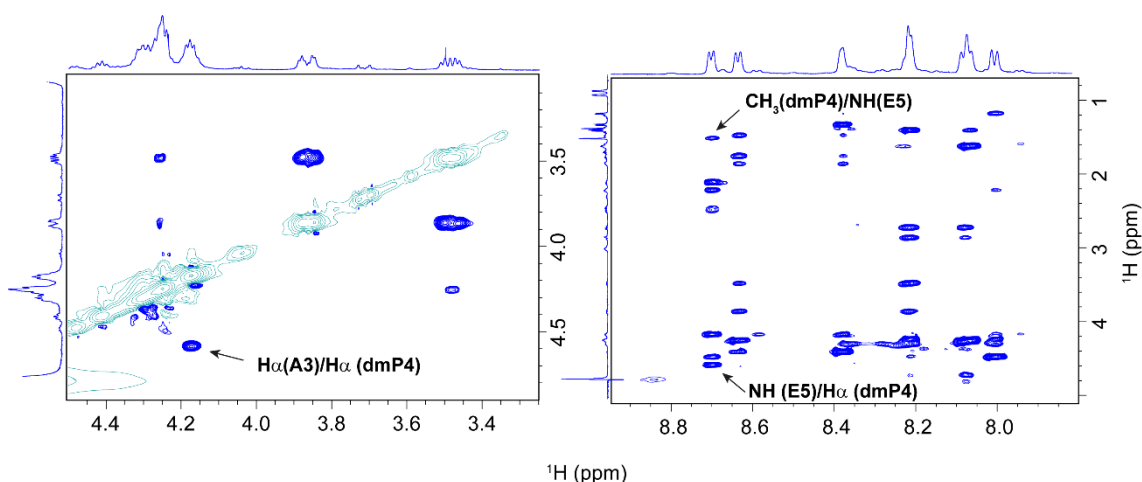**Figure 40.** Expanded regions of 2D ROESY spectrum of analogue **7** (Dap(&)KAdmPETALD(&)) in 90:10% H_2O:D_2O, at 298 K pH 2.5. Characteristic sequential ROE cross-peak observed between the H_α of dimethyl Proline and the H_α of the preceding alanine residue (right panel) confirmed that the *cis* rotamer was the major specie.

Stability studies

Due to the excellent stability that MiniAp-4 showed against human serum, we decided to test its stability in three different media: pepsin, rat plasma and pancreatin, in order to find an aggressive media in which MiniAp-4 was degraded.

Rat plasma was chosen as it is reported to be more aggressive than human plasma.[180] We also used two widely used mediums to predict oral bioavailability of compounds with high proteolytic activity: pepsin, an aspartic endoproteinase isolated from pig gastric mucosa, and pancreatin, a mixture of enzymes composed by trypsin, chymotrypsin, and elastase produced by the exocrine cells of the porcine pancreas.[181]

Angiopep-2, a 19-mer BBB-shuttle peptide that targets the LPR-1, was used as a control in the stability assays with pepsin and pancreatin, while in the rat plasma experiment, benfluoriex and verapamil were used as positive and negative control of degradation, respectively.[32] Quantification of the peptide degradation was done by UPLC in the case of pepsin and rat plasma, whereas UPLC-MS was needed for the pancreatin assay since some components of the media masked MiniAp-4 detection.

No degradation was observed in a 24 h incubation in pepsin and rat plasma, which implies that the half-life is longer than this timeframe (*Figure 41a*). This high biostability is extraordinary for a peptide containing mostly natural amino acids, pointing towards the compact structure imposed by the cycle as the main responsible. In addition, when we tested the stability in 1% of pancreatin, results showed that almost 50% of the peptide was still intact after 4 h, while Angiopep-2 was completely degraded after 10 min of incubation. Due to the excellent stability on MiniAp-4, we decided to test only the two analogues with notable differences in *cis/trans* isomer population, **5** and **7**, with 37:63 and 83:17 respectively, in order to see if there was any correlation with peptide stability. Interestingly, analogue 5 was totally degraded after 2 hours of incubation, which could be attributed to a loss of the cycle constrain and the presence of a natural L-Lys residue instead of the non-natural Dap. However, analogue **7** showed similar stability values to MiniAp-4, suggesting that the high stability of the parent peptide is given by its compact structure and the presence of a non-natural amino acid (*Figure 41b*).
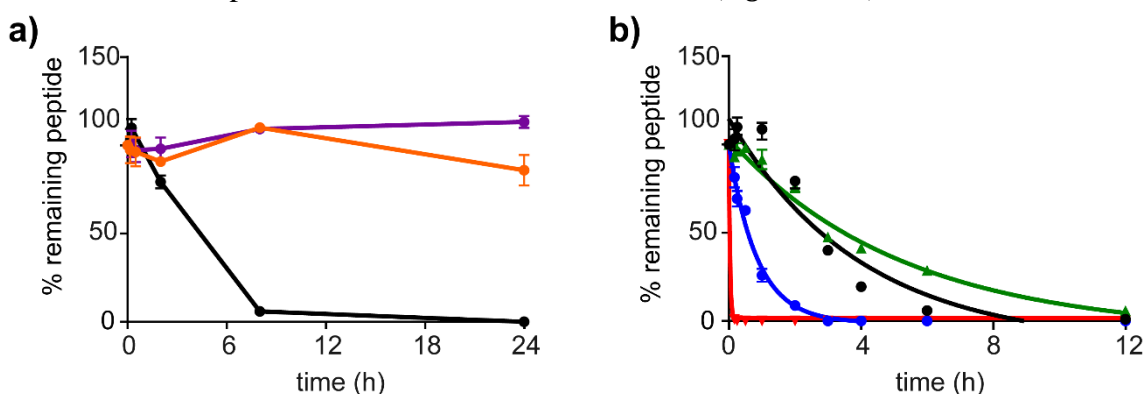

Figure 41. a) Stability of MiniAp-4 in pepsin (purple), rat plasma (orange) and pancreatin 1% (black). b) Comparison of the stability of MiniAp-4 (black), analogue **5** (blue), analogue **7** (green) Angiopep-2 (red) in pancreatin 1%. Peptide stability was monitored by UPLC (a) and UPLC-MS (b). N=3. Data are expressed as the mean ± standard deviation (s.d.).

Human based BBB cellular model

Chirality, sequence, shape, and net charge, among others, have been considered key parameters on permeability across biological barriers.[182] Transport was assessed using an *in vitro* human BBB cell-based model that consists of a monolayer of human endothelial cells derived from pluripotent stem cells that are co-cultured with bovine pericytes. Under culture conditions, the endothelial cells grow polarized, resembling some of BBB properties due to the presence of tight junctions between the cells and the expression of receptors and efflux pumps.[130] This model has been widely validated and the permeability of a great variety of compounds is similar to that obtained *in vivo*.[174]

The peptides were added to the donor compartment at 200 µM, and their recovery in the acceptor compartment was quantified by UPLC. All compounds were assayed in the presence of Lucifer Yellow, which was added in each well as internal standard of the monolayer quality. Importantly, the permeability of Lucifer Yellow of the analogues assayed was below the threshold considered for membrane integrity ($15 \cdot 10^{-6}$ cm·s^{-1}), indicating that none of the peptides were toxic or caused transient opening of the BBB.

In the case of analogues **1** to **7**, the apparent permeability was comparable to that of MiniAp-4 (*Figure 42, Table 15*).
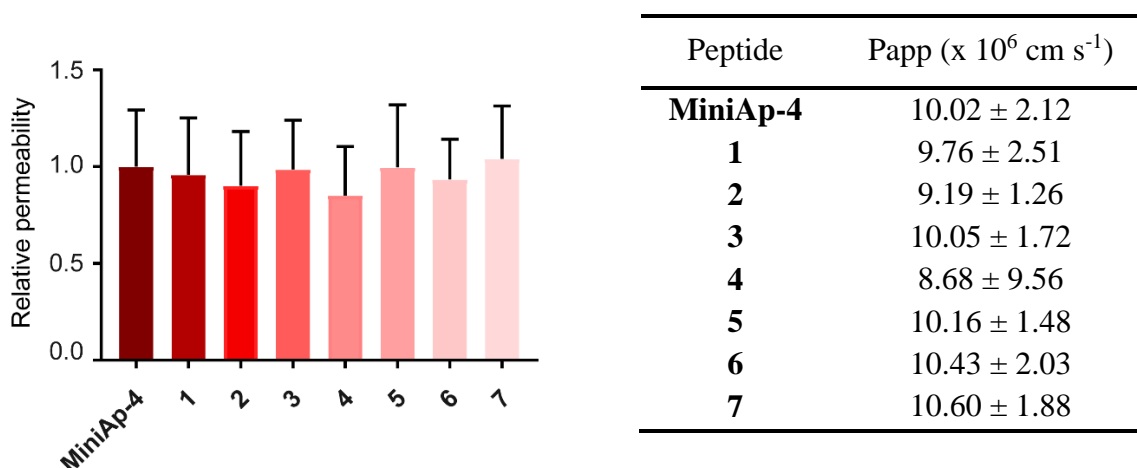

Peptide	Papp (x 10^6 cm s^{-1})
MiniAp-4	10.02 ± 2.12
1	9.76 ± 2.51
2	9.19 ± 1.26
3	10.05 ± 1.72
4	8.68 ± 9.56
5	10.16 ± 1.48
6	10.43 ± 2.03
7	10.60 ± 1.88

Figure 42. Relative permeability of all analogues compared to the parent peptide. N=3. Transport was measured using a human-based cellular BBB model and quantified by UPLC. Data are expressed as the mean ± standard deviation (s.d.). **Table 15.** Apparent permeability of MiniAp-4 and its analogues across the human cell-based BBB model. N=3. Transport was measured by UPLC. Data are expressed as the mean ± standard deviation (s.d.).

Although, this permeability is remarkable for a peptide, this result suggests that proline conformation is not linked to the transport across a cellular model, as we previously hypothesized. However, the complexity of the assay impedes the evaluation of the influence of subtle chemical changes in the apparent permeability of the compounds tested. Therefore, we conjugated the parent peptide and analogue **7** to a small cargo as carboxifluorescein (cF) since previous reports showed the capacity of both MiniAp-1 and

MiniAp-4 to carry it.[174] In that way, conjugated **8** (cF-MiniAp-4) and **9** (cF-analogue**7**) were evaluated in the human BBB cell-based model under the same conditions that MiniAp-4 and **7**.

As previously reported, the transport of MiniAp-4, was not affected by the presence of the small cargo (relative permeability conjugate 8: MiniAp-4 = 0.88). However, conjugate **9** displayed an improved permeability (relative permeability conjugate 9:7 = 1.51) suggesting that transport properties may be superior compared to MiniAp-4 for this type of cargoes (*Figure 43*).
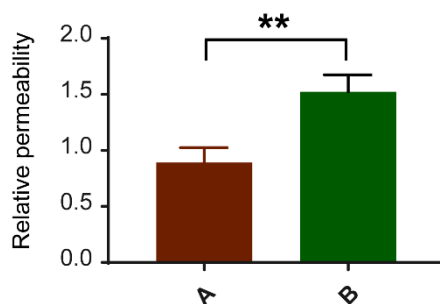

Figure 43. A and B correspond to the relative permeability values of conjugates **8** and **9** compared to MiniAp-4 and analogue **7** respectively. N=3. Data are expressed as the mean ± standard deviation (s.d.).

Internalization study using AiryScan microscopy

In order to probe the capacity to internalize inside cells of the parent peptide and the best candidate (analogue **7**), their cF conjugated versions were incubated at 100 μM in b.End3 cells for 1 hour at 37 °C. After, cells were washed twice with PBS and media was added to perform live imaging. Hoescht was used as a marker for cell nuclei and cell mask for membrane staining. As *Figure 44* shows orthogonal projections, which gives 3D information from 2D images, confirming the internalization of conjugate **8** and **9**.
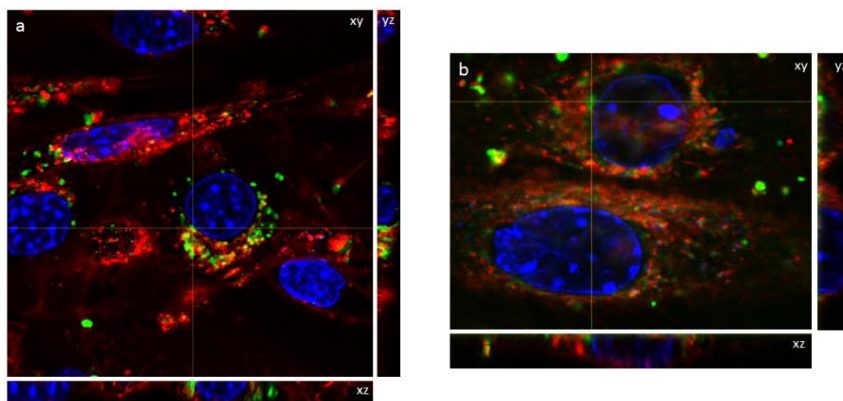

Figure 44. Airy scan processed images with orthogonal projections of the internalization of (a) conjugate **8** or (b) conjugated **9** in b.End3 cells after 1 hour incubation. CF-labeled peptides are shown in green, cell mask in red and cell nuclei (Hoechst staining) in blue.

After, cells were fixed with 4% of PFA for at least 20 minutes at RT. *Figure 45* represents the acquired images for conjugated 8 (a) and conjugated 9 (b).
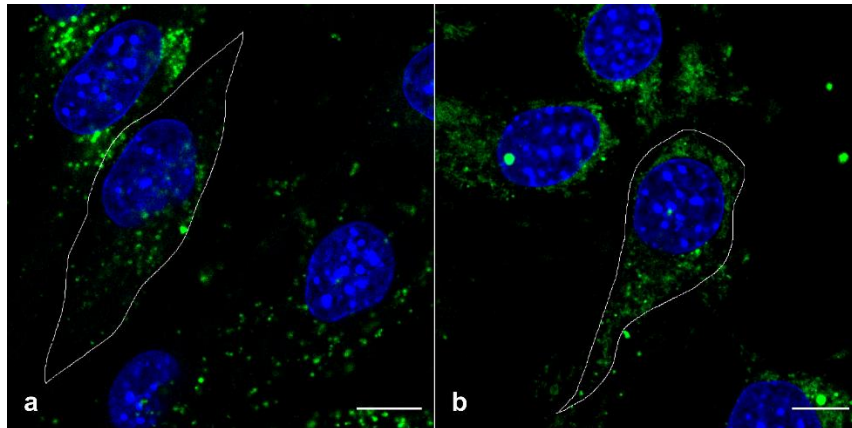
Figure 45. Internalization of (a) conjugate **8** or (b) conjugated **9** in b.End3 cells after 1 hour incubation. CF-labeled peptides are shown in green and cell nuclei (Hoechst staining) in blue. Single-plane images presented were acquired with AiryScan. Cell membrane outlines shown in white. Scale bars represent 10 μm.

This images confirm the ability of a these two BBB-shuttles to improve the permeability of a cargo that is not able to enter the brain unaided. Altogether, these results confirm that MiniAp-4 displays privileged stability and transport properties and we believe that the transport mechanism of this optimized version of MiniAp-4 BBB-shuttle deserves further attention.

Quantum dots as a tool to study the BBB-shuttle uptake

Quantum dots (QD) are fluorescent semiconductor nanoparticles with unique optical properties suitable for multiplexed *in vitro* and *in vivo* imaging.[183-184] For many years, several studies have been focused on the improvement of their coating, biocompatibility, surface modification, targeting specificity, as well as other important features as toxicity and applicability.[185]

QDs can be used in place of traditional organic dyes as they have a strong resistance to chemical degradation and photobleaching over long periods of times, allowing the acquisition of images with good contrast and good signal intensity. Most QDs are brighter than other organic dyes due to their high extinction coefficient ($0.5-5 \times 10^{-6} \, M^{-1} \, cm^{-1}$) and high quantum yields.

Excitation-emission matrix analysis has shown that QDs always emit the same wavelength of light no matter what excitation wavelength is used.[186] For this reason, multiple QDs with different emission spectra can be simultaneously visualized using a single excitation source (*Figure 46*). The fluorescence signal of each QD can be individually analyzed as the emission spectrum of each QD is narrow, in order to achieve multiplexed imaging.
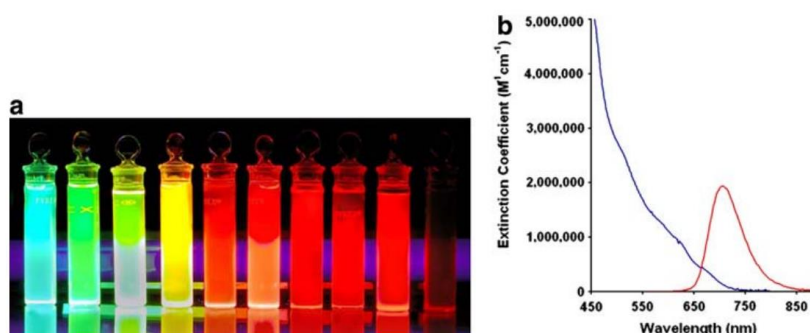

Figure 46. (A) a series of QDs of different core size and emission wavelength. (B) representative excitation (blue) and emission (red) spectra of QDs.

For all these reasons, research based on QDs has become a powerful tool in fields such as molecular and cell biology, molecular imaging or medical diagnostics.

Conjugation to quantum dots

First, we decided to work with QD605-COOH following the work that Dr. Roger Prades performed in our laboratory, in which the capacity of THRre to transport NPs using 2-photon microscopy was proved.[83] The conjugation of the peptide with the QDs was carried out using EDC to activate the carboxylic group, followed by the reaction of this activated group with the *N*-terminus of the peptide in PBS (*Figure 47*).
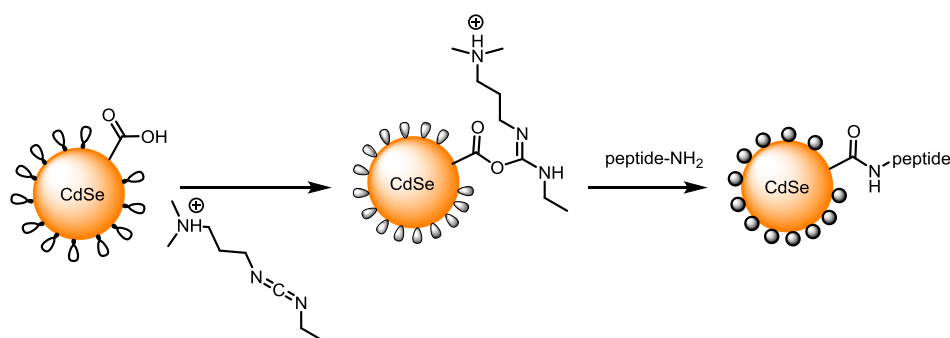
Figure 47. Modification of QD-COOH.

Several attempts were performed without successful results. We observed that these QDs precipitated when they were mixed in PBS. Therefore, we decided to work with PEGylated QDs. In this sense commercial PEGylated QDs (QDot605-PEG-NH$_2$), used previously in our group to prove the capacity of MiniAp-4 to carry them across a HBBBCM, were selected.[132] Also, the stability of these type of QDs is excellent as they showed no sign of aggregation even after 1 month (*Figure 48*).
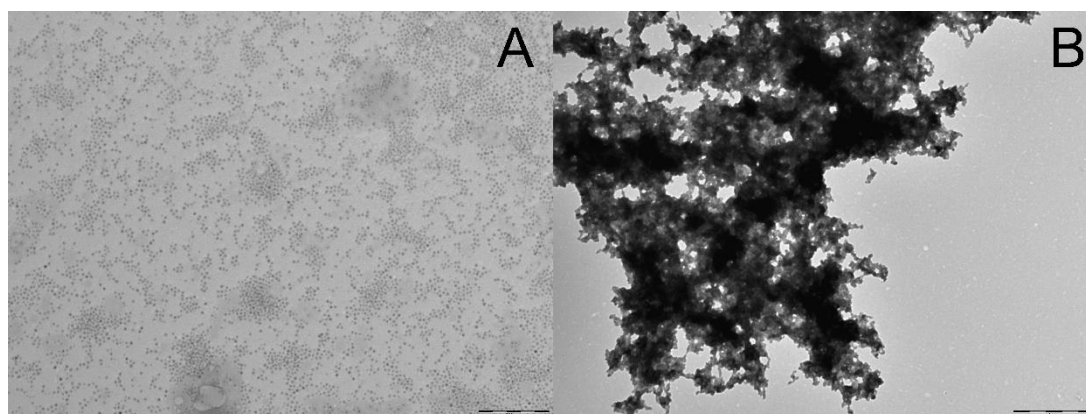

Figure 48. TEM micrographies showing stability of QDot605-PEG-NH$_2$ (A) and aggregation in PBS of QDot605-COOH (B). (Scale bar=100 nm).

The protocol established by Cai and co-workers is based on the modification of the QDs with a linker containing maleimide moiety and a carboxylic acid activated as *N*-hydroxysuccinimide ester (*Figure 49*).
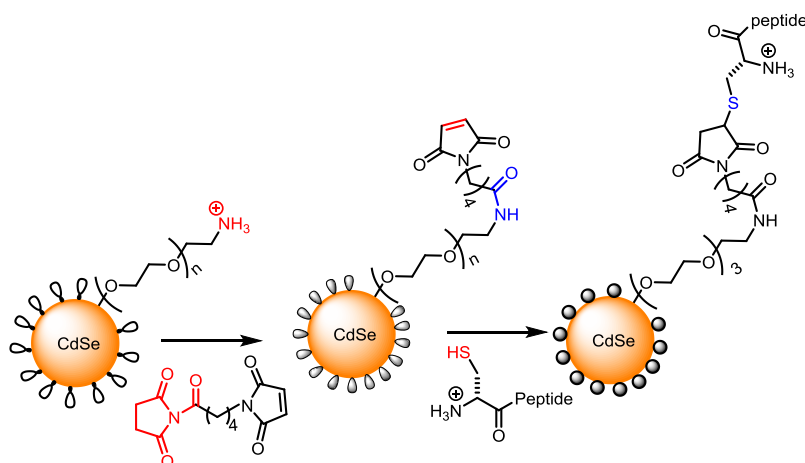

Figure 49. Modification of QD-PEG-NH$_2$ with a peptide containing a Cys at the *N*-terminus.

After the addition of the maleimide, the cys-peptide is incorporated via thiol-maleimide chemistry. A peptide containing a cysteine could then be linked to the maleimide through a Michael addition. This approach would permit the use of peptides with more than one amine, as MiniAp-4, as it is known that thiols react 1000-times faster than amines.[187]

After conjugation, the sample was fully characterized by UV, zeta potential and analysis of amino acids. All together allow the determination of the concentration of the peptide sample and the number of peptides copies incorporated per QD.

To gain further insight into the transport mechanism of MiniAp-4, we used the prepared nanoparticles as a model to study internalization assays in bEnd.3 cells as a first step of trancytosis.[110] This is an immortalized mouse brain endothelial cell line used as a BBB model, as it presents high levels of tight junctions proteins such as claudin-5.[188] It is a simpler model than the *in vitro* BBB cellular model, but can give us more insight into the mechanisms involved in the endocytosis of the peptides.

Our objective was to quantify internalization based on fluorescence intensity of MiniAp-4 conjugated QDs and compared it with a well-known BBB-shuttle as ApoE ((LRKLRKRLL)$_2$), a peptide derived from apoliprotein E that shows high efficiency in transporting proteins into the CNS.[54]

It was not possible to compare the internalization of MiniAp-4 to THRre and Angiopep-2, due to the lower number of copies obtained every time that we performed the conjugation of these peptides.

To analyze the experiments, we used two widely known techniques: confocal microscopy and flow cytometry. Confocal microscopy was chosen as it is a good technique to obtain in real time images in a short period of time, however, the quantification analysis is long and difficult to perform. Flow cytometry typically provides good statistics as a large number of cells can be evaluated very quickly, however, it is not possible to obtain information about the localization of the nanoparticles inside the cell.

Quantification of QD internalization by confocal microscopy

Our first objective was to confirm the internalization of conjugated NPs into b.End3 cells by confocal microscopy. For this purpose, naked (-3.4 ± 0.179 mV), MiniAp-4 (180 copies, -3.2 ± 0.375 mV) and ApoE (105 copies, -1.31 ± 0.206 mV) decorated QDs were incubated at 100 nM for 2 hours. After, cells were washed twice with PBS to remove the excess of particles that did not internalize and cell medium was added. Then, cells were imaged *in vivo*. Cells mask was used in order to stain the cell membrane and distinguish between inside and outside the cell.

As seen in *Figure 50*, ApoE and MiniAp-4 conjugated QDs internalize into brain endothelial cells, with a clear increase in the uptake for the ApoE modified nanoparticles with respect to MiniAp-4 ones. The distribution of the nanoparticles were homogenous along the cytoplasm. In order to see if the QDs were in the lysosomes, we add a LysoTracker up to a final concentration of 50 nM, however, no co-localization could be observed.
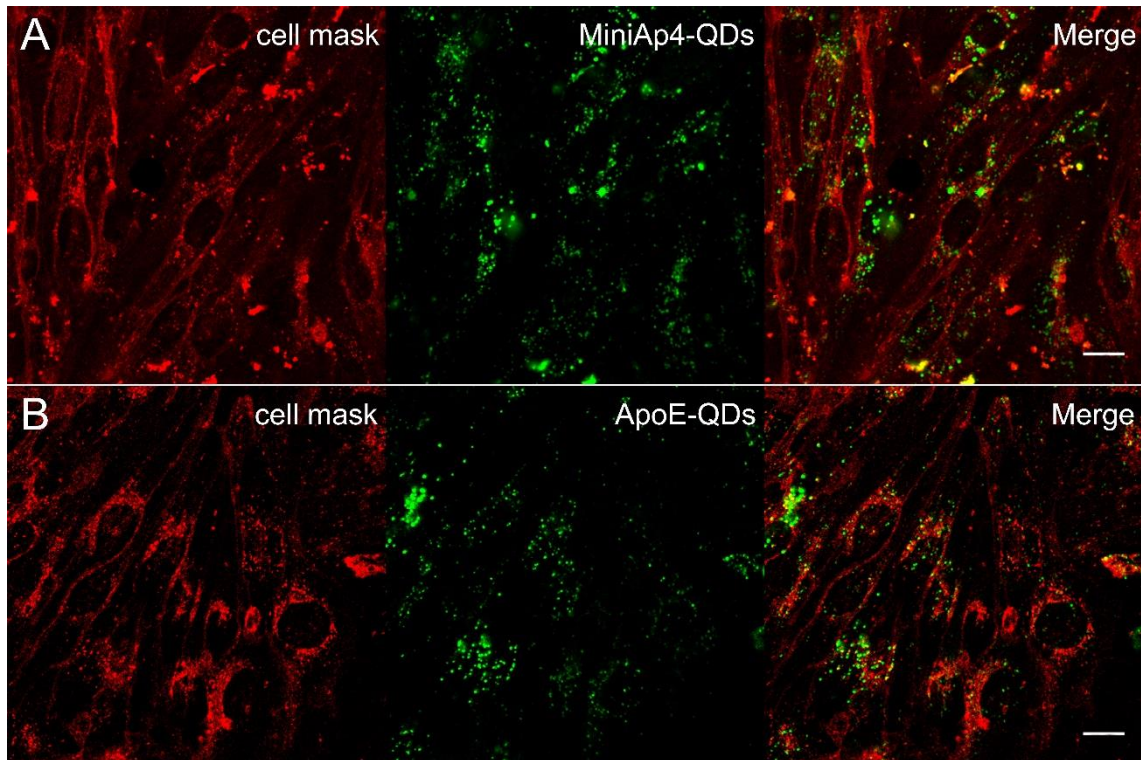
Figure 50. Confocal fluorescence microscopy images of b.End3 cells after 2 hours of incubation with ApoE-QDs (A) and MiniAp-4 (B) at 37 ºC in RH pH 7.4. Cell mask is shown in red and conjugated QDs in green. (Scale bar=15 µm).

Also, naked QDs were evaluated as control in order to see if any internalizaiton was observed. To our surprise, naked QDs internalizes into the cells. In this case, the distribution of the naked NPs were along the cytoplasm, and we could not appreciate differences with the modified ones.
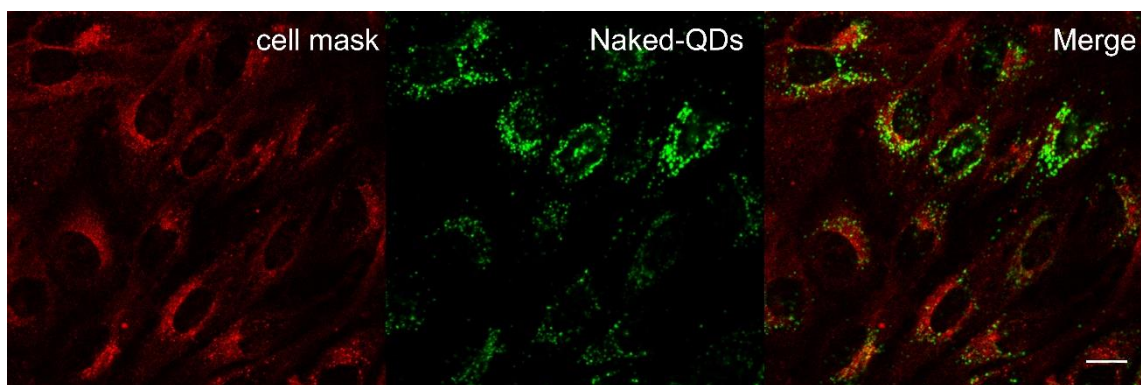

Figure 51. Confocal fluorescence microscopy images of b.End3 cells after 2 hours of incubation with naked NPs at 37 ºC in RH pH 7.4. Cell mask is shown in red and naked QDs in green. (Scale bar=15 µm).

After, we decided to quantify the uptake of the conjugated NPs over time with subsequent digital image analysis in order to study differences between conditions. With the help of the Advanced Digital Microscopy facility at IRB, we programmed a macro in order to distinguish between the background and sample intensities. In more detail, we set a threshold for the cell mask and QDs intensities, thus obtaining two sets of areas. After, a ratio between the area of the cell mask and the area of the QD inside the cell was

86

calculated in order to quantify the internalization of the NPs; the higher the ratio, the higher the internalization. For this purpose, naked (-4.6 ± 0.5 mV), MiniAp-4 (102 copies, -4.72 ± 0.36 mV) and ApoE (95 copies, -1.86 ± 0.31 mV) decorated QDs were incubated at 100 nM for 1, 2 and 8 hours. After, cells were washed twice with PBS to remove the non-internalized NPs and cell medium was added in order to perform *in vivo* imaging. For each conditions, an average of 5 to 10 images were taken and analyzed with the macro (*Figure 52*). ApoE conjugated QDs displayed the highest internalization, however, naked NPs internalized more than the MiniAp-4 conjugated ones, suggesting that maybe MiniAp-4 is not the ideal BBB-shuttle to carry cargos as quantum dots in uptake experiments.
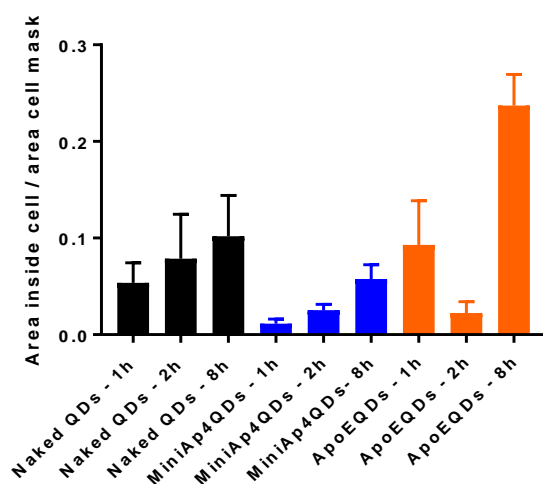

Figure 52. Quantification of the QD internalization. Area inside cell/area cell mask ratio quantified by confocal microscopy. N=5-10. Data are expressed as the mean ± standard deviation (s.d.).

However, in the case of ApoE conjugated NPs at 2 hours, a decreased of internalization was observed. This experiment was repeated two times observing in both cases this trend.

Quantification of QD internalization by flow cytometry

Flow cytometry is a powerful tool for the analysis of multiple individual cell parameters from heterogeneous cell populations. This technique is used in different multicolor applications for biology or functional studies as well as a broad range of research applications including: proliferation studies, fluorescent protein, and cell counting among others. Thousands of cells per second pass one by one through one or more laser beams in a flow cytometer, which measure scattered lights at several angles and fluorescence emissions. Some of them are also capable of analyzing cell volume by electrical impedance variation. Three parts constitute a flow cytometer: first, the fluidic system permits hydrodynamic focusing; second the excitation source and optical emission systems from the wavelength filters to the detectors constitute the optical part and finally the electronic system digitalizes the signal to be analyzed with specific software.

In order to analyse MiniAp-4 modified QDs, we used the same controls that for the confocal microscopy experiments: ApoE conjugated QDs as a positive control of internalization and naked QDs as negative control of internalization.

The internalization experiments were performed by incubating the conjugated and the naked QDs with bEnd.3 cells. After, several washings were performed in order to remover an excess of nanoparticles followed by the evaluation of peptide uptake using flow cytometry.

First, different times of incubation were selected, in order to obtain a good signal without damaging the cells, as we could observed cell death at longer times of incubation.

MiniAp-4 and ApoE peptides were conjugated and characterized as before, obtaining 59 copies (-3,1 ± 0.215 mV) and 47 copies (-1.6 ± 0.387 mV), respectively. Also, the zeta potential values obtained were compared with the naked ones (-3.7 ± 0.198 mV) in order to see a difference in the surface charge. The zeta potential of the ApoE conjugated NPs were significantly positive than the naked ones due to all the positive charge residues that ApoE contains. In the case of MiniAp-4 ones, the zeta potential were slightly positive, as MiniAp-4 net charge is zero.

All three QDs (naked, MiniAp-4 and ApoE) were incubated for different times: 30 minutes, 2 hours and 4 hours at 100 nM. In addition, cells without nanoparticles were analyzed in order to discard autofluorescence of such cells. (*Figure 53*)
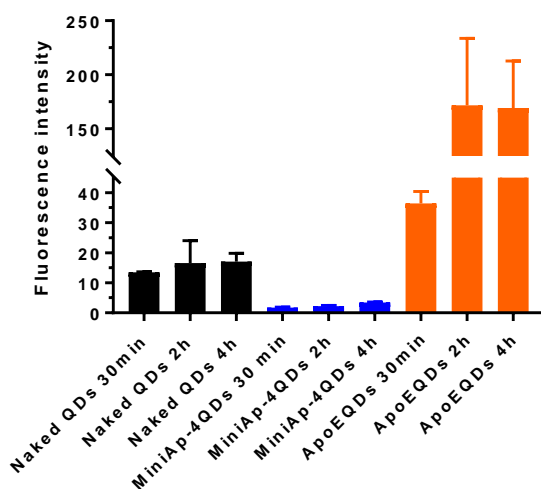

Figure 53. Fluorescence intensities measured with a flow cytometer. N=3. Data are expressed as the mean ± standard deviation (s.d.).

As it was expected, for ApoE-QDs, an increase of the fluorescence intensities is observed, concluding that this peptide is able to carry across this cells a large cargoes such as quantum dots. In the case of MiniAp-4, as we observed with the confocal microscopy experiments, it seems that MiniAp-4 conjugated nanoparticles internalizes less than the naked ones. This suggest that quantum dots behave differently than small cargos as carboxifluorescein. Dr. Benjamí Oller observed an increase in the transport of large

cargoes by MiniAp-4 in human cell-based BBB model.[132] The difference of the experimental set up between both models could explain these difference in behavior.

In conclusion and with two results obtain from different techniques, we can confirm that ApoE is the best shuttle to transport QDs inside brain endothelial cells. In the case of MiniAp-4, these type of NPs are not the best ones to study its transport across the BBB, and maybe other type of cargos such as small fluorophores could be a better choice

Elucidation of the mechanism of
internalization

The BBB transport mechanism of MiniAp-4 is still unknown, however Dr. Benjamí Oller proposed a caveolin mediated mechanism after studying the internalization of MiniAp-4 conjugated to a carboxifluorescein in the presence or absence of two inhibitors: chlorpromazine and filipin III. The first one is known to affect clathrin-dependent internalization meanwhile the other inhibits selectively caveolae-mediated endocytosis. Results showed how uptake was significantly reduced by filipin III but not chlorpromazin suggesting two important things: the transport of this peptide was at least partially due to an endocytic pathway and secondly that the mechanism was mediated by caveolae rather than clathrin.[174]

As we have explained, one of the main objectives of the present thesis is to understand the mechanism of internalization of MiniAp-4. As previous results showed a preference for caveolae pathway rather than clathrin, we decided to use controls of caveolin and clathrin endocytic pathways, cholera toxin and transferrin, respectively.

Cholera toxin (CT) is a protein secreted by the bacterium *Vibrio cholerae*, responsible for the diarrhea in cholera infection.[189] In 1886, Robert Koch assumed that the symptoms caused by the bacterium could be due to some poison produced by the organism, however it was not confirmed until 1959 by Sambhu Nath De.[190] This toxin consist of one subunit A and 5 identical subunits B, denoted as AB_5. The A subunit (28 kDa) has enzymatic activity and it is the responsible of the toxicity.[191] The homopentameric B subunit (CTB_5) consists of five 11 kDa monomers (CTB) which binds the GM1, a monosialoganglioside widely distributed on the plasma membrane surface of various animal epithelial cells.[192-193] The CTB-subunit (CTB) binds very tightly to GM1 with a K_D reported values in the range of 5 pM to 1 nM based on SPR and on-cell binding measurements.[194]

Cholera toxin can enter the cell by different endocytic pathways. Different studies suggested that the main mechanism of internalization of the CT was caveolae-mediated endocytosis due to the abundance of the ganglioside GM1 in caveolae.[195] However, other studies described how CT can internalize in cells by clathrin-dependent.[196-197] For example, a work done by Torgersen and co-workers, described how uptake of CT by caveolae was a minor pathway in Caco-2 cells.[196] Nevertheless, different cell lines have different membrane compositions, thus affecting the contribution of different endocytic pathways. Another work by Massol *et al*. describes how CT uses also a non-caveolar and non-clathrin-mediated pathway.[198]

In the other hand, transferrin is an iron-binding protein of 80 kDa that contains two specific binding sites for Fe(III). First, the iron-loaded Tf, the holo-Tf, binds the transferrin receptor and internalizes into the cells by clathrin-mediated endocytosis.[199] Involving lower pH, salt and an identified chelator, iron is released from the holo-Tf in the endosome. After, apo-Tf is subsequently directed to recycling endosomes to be taken back to the cell surface.[119]

Inhibition of the endocytosis

Dynamin is required for the formation of clathrin-coated vesicles in endocytosis as for uptake of ligands through caveolae. It is a multidomain protein of 100 kDa approximately, which is responsible for endocytosis. The best two characterized isoforms are dynamin 1 and 2. In order to see if the internalization of MiniAp-4 was dynamin-dependent, we used a specific dynamin inhibitor, dynasore.[200] The MiniAp-4 endocytosis was also compared with the CTB, which is a specific marker of a dynamin dependent endocytosis. b.End3 cells were pre-incubated with 100 μM of dynasore for 15 minutes at 37 °C and then cy5_MiniAp-4 and Alexa555-CTB were added and further incubated for 1 hour. AiryScan microscopy images showed an inhibition of the endocytosis of both probes and some accumulation at the cell membrane, probing that the internalization of MiniAp-4 is dynamin-dependent.
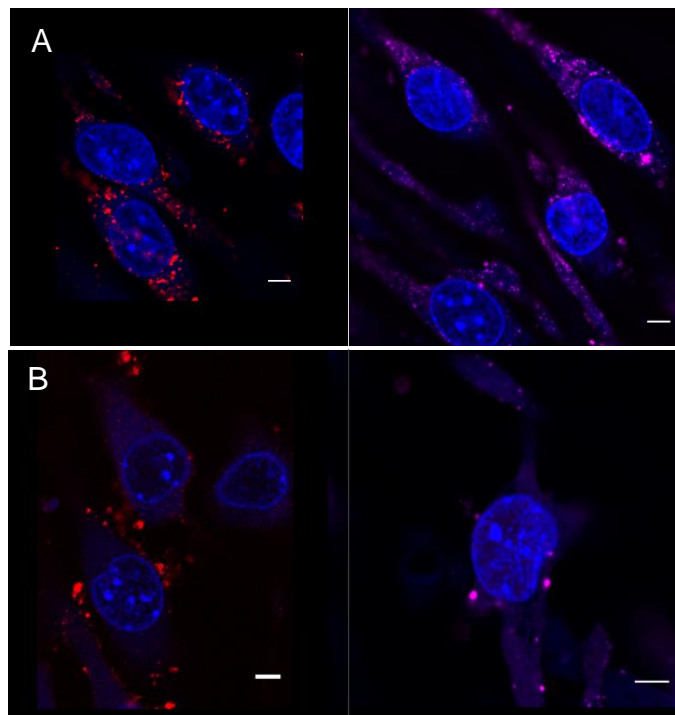

Figure 54. Microscope images of b.End3 cells co-incubated with Alexa555-CTB (red) at 20 μg·mL^{-1} and 100 μM of cy5_MiniAp-4 (magenta) for 1 hour at 37 °C A) control experiment B) pre-incubation of 100 μM of dynasore inhibitor. Cell nuclei are stained with Hoescht (blue) (Scale bar=5 μm).

Co-localization studies to understand the endocytosis mechanism

In order to understand different biological processes, quantitative co-localization analysis using fluorescent microscopy has been described as an efficient approach to compare the subcellular distribution of two fluorescently labeled molecules.

The concept of co-localization can be understood as the co-occurrence of two probes (the spatial overlap) and the correlation (the co-distribution in proportion within and between structures).

In order to quantify these parameters several coefficients have been proposed. First, the Pearson's correlation coefficient (PCC) described the linear regression of intensities of two probes, having values from -1 to 1.[201] The following formula represents the PCC value for a giving image consisting of red and green channels:

$$PCC = \frac{\sum_i (R_i - \overline{R}) \times (G_i - \overline{G})}{\sqrt{\sum_i (R_i - \overline{R})^2 \times \sum_i (G_i - \overline{G})^2}}$$

where R_i and G_i refers to the intensity values of the red and green channels of a pixel i, respectively, while the $\overline{R}$ and $\overline{G}$ correspond to the average value intensities across all the image. PCC values of 1 and -1 mean the intensities of two images are linearly or inversely related to one another respectively and 0 for no correlation. However, due to the difficulty to interpret negative correlation values, Manders' overlapping/correlation coefficients (MCC or MOC) were developed.[202] The MOC coefficient are based on PCC removing for the mathematical equation the average intensities, thus removing the possibility to obtain negative values:

$$MOC = \frac{\sum_i (R_i \times G_i)}{\sqrt{\sum_i R_i^2 \times \sum_i G_i^2}}$$

The coefficients vary from 0 to 1, meaning no co-localization and totally overlapping of the images respectively. Two MCC values were described: M1 and M2 in order to understand the fraction of one probe that colocalizes with the other and vice versa.
Both PCC and MCC have strengths and shortcomings, therefore they should be chosen depending on the nature of the image (*Scheme 1*).
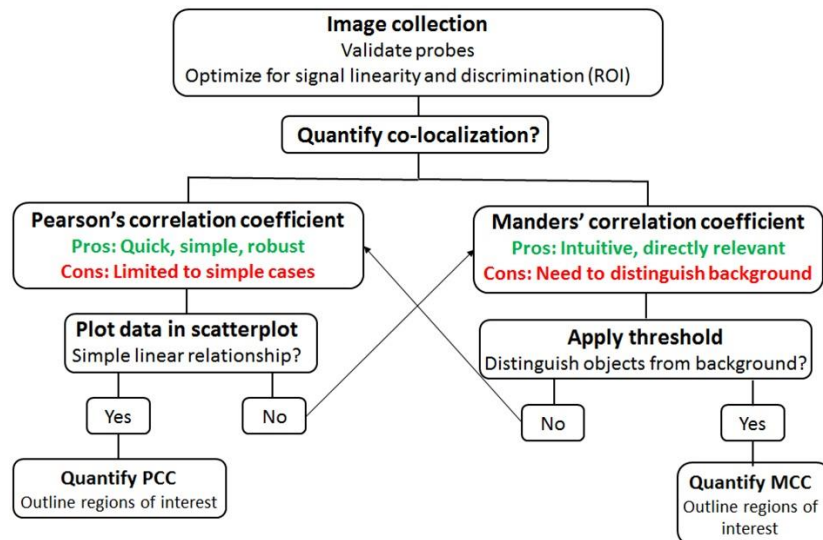
Scheme 1. Schematic of a general co-localization workflow

For our case of study, we decided to use the MCC to quantify the co-localization as it was easier to interpret the MCC coefficient rather than the PCC and we could distinguish between the labeled structures and the background in our acquired images.

Once we confirm that the internalization of MiniAp-4 was dynamin-dependent, we decided to perform co-localization studies of cyanine5_MiniAp-4 conjugated with Alexa488-Tf and Alexa555-CTB. To this end, cy5_MiniAp-4 was co-incubated at 100 µM in RH with Alexa488-Tf (50 µg/mL) and Alexa555-CTB (20 µg/mL) for 1 hour at 37 ºC, following the work done by Pujals *et al.*[203] Using an implemented software package in ImageJ called JACoP *(Just Another Co-localization Plugin)*, we were able to obtain the M1 and M2 coefficient values that strictly measures the co-occurrence independent of signal proportionality and correspond to the fraction of one probe overlapping with the other.

Figure 55 shows the M1 and M2 values, being M1 the fraction of cy5_MiniAp-4 overlapping to CTB or Tf and M2 the other way around. As the plot shows, co-localization with the two probes were observed, suggesting that maybe MiniAp-4 uses both endocytic pathways to enter the cells, however, a significant higher co-localization values were observed for CTB, meaning that maybe the main route of entry is caveolin dependent.
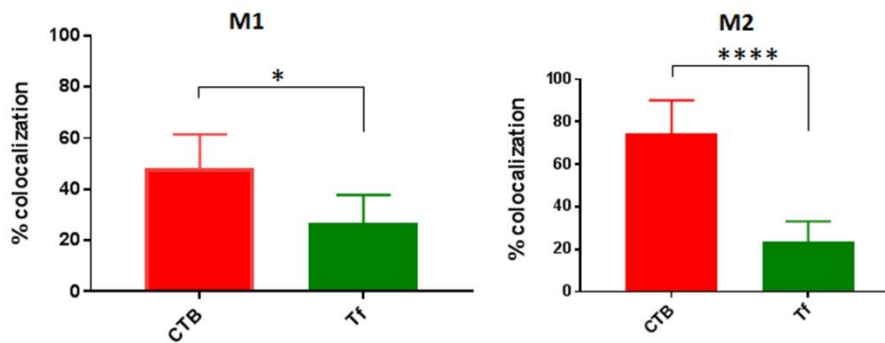

Figure 55. Co-localization values of cy5_MiniAp-4 with CTB and Tf. The co-localization values are expressed as the mean ± standard deviation (s.d.). N=5.

The following figure show representative images for this experiment. It can be observed co-localization of the peptide with the two probes, CTB and Tf, however, the co-localization of MiniAp-4 and CTB is stronger as most of the dots colocalize, obtaining almost a yellow staining for the merge image.
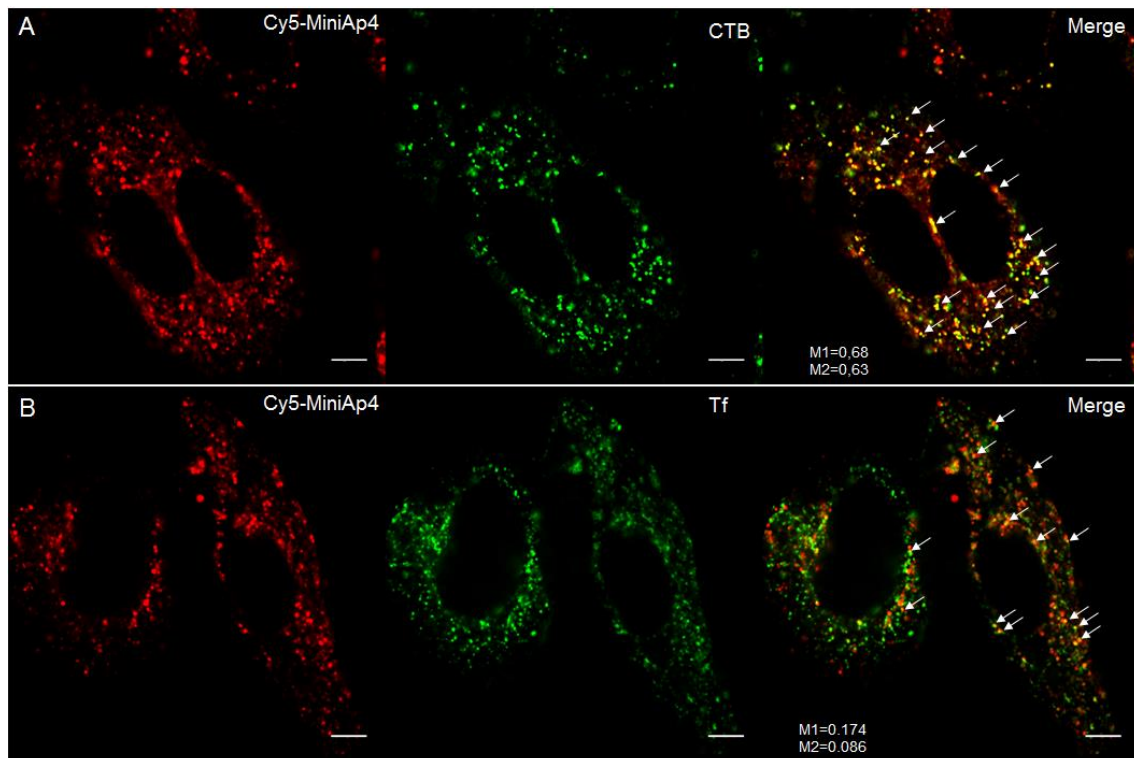
Figure 56. Microscope images of b.End3 cells co-incubated with 100 μM of cy5_MiniAp-4 (red) and A) AlexaFluor555-CTB (green) at 20 μg·mL^{-1} or B) AlexaFluor488-Tf (green) at 50 μg·mL^{-1} and 37 °C in 5% CO_2 for 1 h. (Scale bar=5 μm). Arrows indicate a few examples of co-localization between probes. M1 - Manders' coefficient M1 (Cy5_MiniAp-4 overlapping with Tf or CTB); M2 - Manders' coefficient M2 (CTB or Tf overlapping with Cy5_MiniAp-4).

With this results in hand, we decided to evaluate the co-localization at different time points (5, 15, 30 and 60 minutes) for both controls in order to see differences. In the case of CTB, no significant differences were observed over time, obtaining high MCC values for all time points, all of them higher than 35%. *Figure 57* shows a representative selection of images for this experiment.
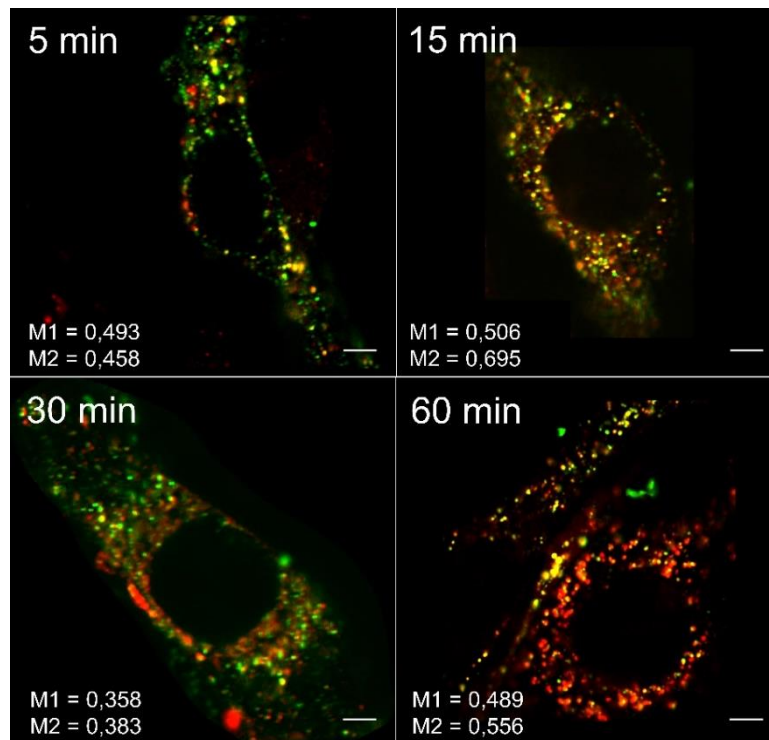
Figure 57. Co-localization of Cy5_MiniAp-4 (red) with Alexa555-CTB (green) at different time points at 37 $^\circ$C in 5% CO_2. Respective time points are indicated in the upper right corners. (Scale bar=5 μm). M1 - Manders' coefficient M1 (Cy5_MiniAp-4 overlapping with CTB); M2 - Manders' coefficient M2 (CTB overlapping with Cy5_MiniAp-4).

In the case of transferrin, some co-localization of cy5_MiniAp-4 with Tf could be detected, however the Manders' coefficients were lower (*Figure 58*).
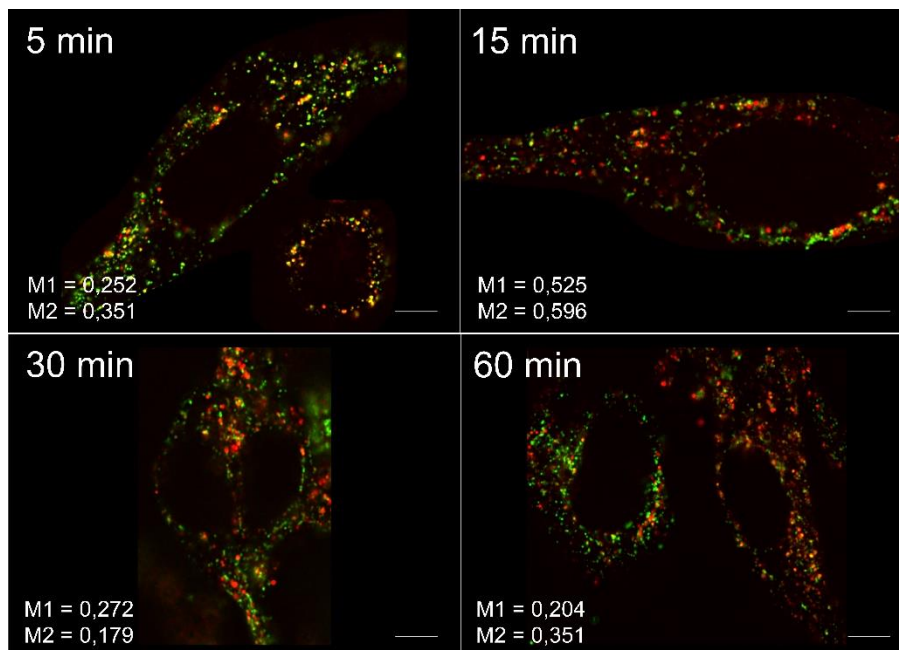

Figure 58. Co-localization of Cy5_MiniAp-4 (red) with Alexa488-Tf (green) at different time points at 37 $^\circ$C in 5% CO_2. Respective time points are indicated in the upper right corners. (Scale bar=5 μm). M1 - Manders' coefficient M1 (Cy5_MiniAp-4 overlapping with Tf); M2 - Manders' coefficient M2 (Tf overlapping with Cy5_MiniAp-4).

With these results in hand, we can hypothesize that this peptide uses both dependent and independent clathrin mediated endocytic pathways to enter the cells. However, we can also hypothesize that due to its clear high co-localization with CTB, that the main entry pathway route it is through caveoles.

Also, in order to confirm the previously obtained results, we performed direct stochastic optical reconstruction microscopy (dSTORM) with the help of Dra. Sílvia Pujals at the Institute for Bioengineering of Catalonia (IBEC). dSTORM is a technique of single molecule super-resolution imaging compatible with many conventionally used fluorophores that allows to visualize cellular structures with a resolution of 20 nm approximately.[204] It consists of the induction of hundreds cycles of activation (on-state), imaging and off-state, enabling the construction of super-resolution images from single-molecule events.[205] The photocycling is enhanced by the removal of oxygen, due to the susceptibility of cyanine dyes to irreversible oxidation and the addition of a thiol such as β-mercaptoethylamine.[206-207] Super-resolution images (*Figure 59*) confirmed the co-localization of cy5_MiniAp-4 to CTB, while almost non co-localization with Tf was observed.
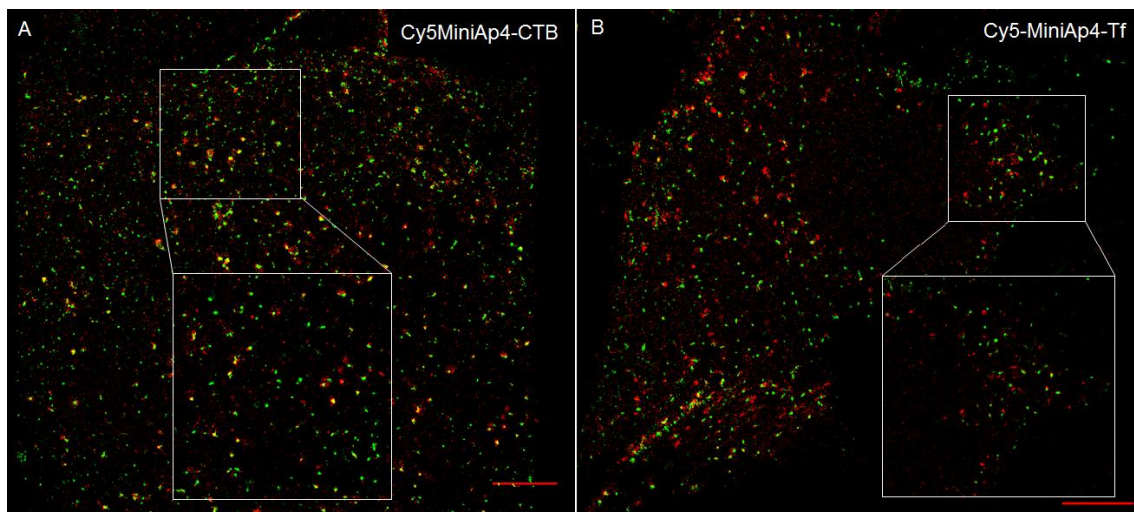

Figure 59. Super-resolution dSTORM images of b.End3 cells co-incubated with 100 μM of cy5_MiniAp-4 (red) and (a) AlexaFluor555-CTB (green) at 20 μg·mL^{-1} or b) AlexaFluor488-Tf (green) at 50 μg·mL^{-1} and 37 $^{\circ}$C in 5% CO_2 for 1 h. (Scale bar=5 μm).

In order to confirm our hypothesis, the three dyes were co-incubated in order to observe co-localization between them (*Figure 60*). Once again, clear co-localization between the MiniAp-4 and CTB was observed (pink), as well as a weaker overlapping with Tf. In addition, we could confirm that CT also uses a clathrin-dependent pathway to enter the cells, as it co-localized with the Tf (M1=0.09, M2=0.102).
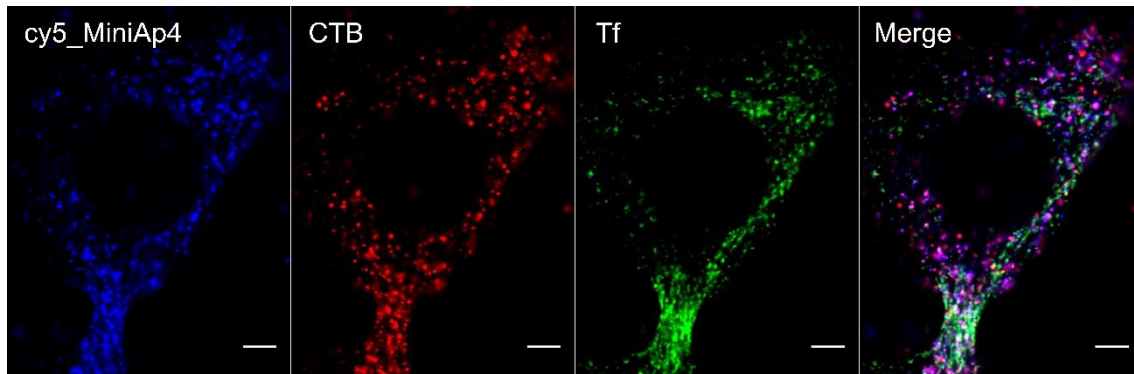
Figure 60. Microscope images of b.End3 cells co-incubated with 100 μM of cy5_MiniAp-4 (blue), AlexaFluor555-CTB (red) at 20 μg·mL^{-1} and AlexaFluor488-Tf (green) at 50 μg·mL^{-1} and 37 ºC in 5% CO_2 for 1 h. (Scale bar=5 μm).

To further study the route of entry, we decided to measure co-localization of the cy5_MiniAp-4 and Alexa555-CTB with specific antibodies related with subcellular structures involved in endocytosis. In that way, we selected a marker for early endosomes (early endosome antigen 1), for caveolin endocytic pathway (anti-caveolin-1), for late endosomes (anti-Lamp3) and for Rab7 a protein which regulates the vesicle traffic from early to late endosomes and from late endosomes to lysosomes (anti-Rab7).

Our first attempt was to quantify the co-localization of MiniAp-4 and CTB with an antibody that stain the caveolin pathway, anti-caveolin1.
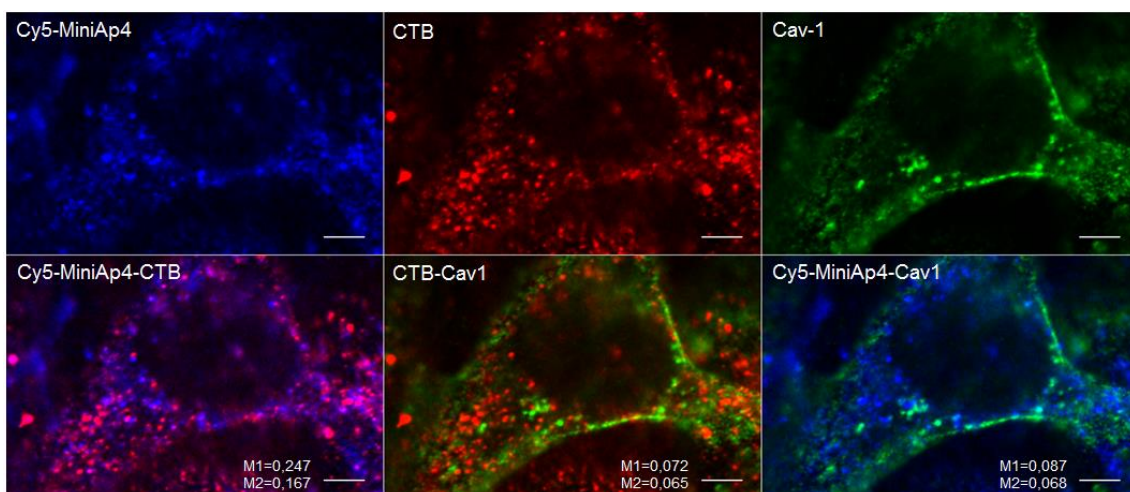

Figure 61. Co-localization of cy5_MiniAp-4 and Alexa555-CTB with Cav-1 marker. b.End3 cells were co-incubated with 100 μM of cy5_MiniAp-4 (blue), Alexa555-CTB (red) at 20 μg·mL^{-1} for 45 minutes at 37 ºC in 5% CO_2. (Scale bar=5 μm). Manders' coefficient M1 and M2 indicate the overlapping one probe to the other.

As *Figure 61* shows, the MCC values for the overlapping of cy5_MiniAp-4 and CTB with the caveolin marker were low. This can be related to the antibody used for this experiment. In the market there are many of these antibodies commercialized and it seems that the one used was not the ideal one.

100

For the early endosomes, co-incubation of MiniAp-4 peptide and CTB was performed for 5 minutes. With this time of incubation, the two probes should be on the membrane and in the early endosomes.
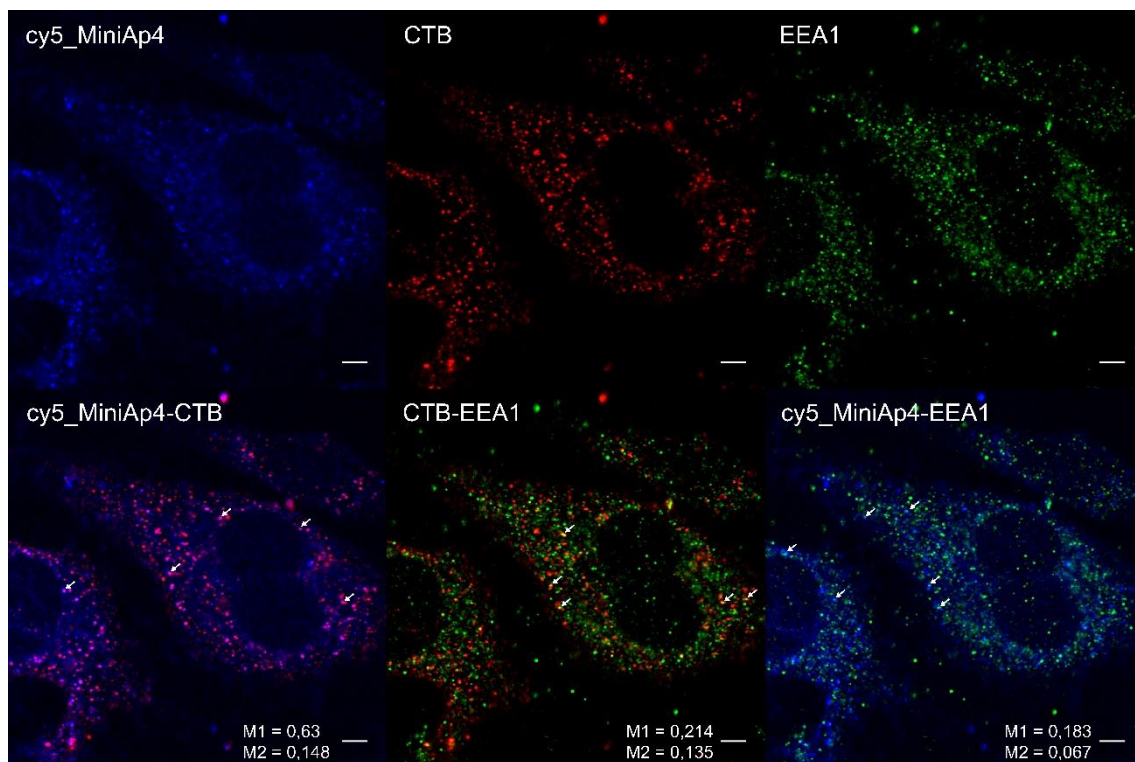

Figure 62. Co-localization of cy5_MiniAp-4 and Alexa555-CTB with EEA-1 marker. b.End3 cells were co-incubated with 100 µM of cy5_MiniAp-4 cy5_MiniAp-4 (blue), Alexa555-CTB (red) at 20 µg·mL^{-1} for 5 minutes at 37 °C in 5% CO_2. (Scale bar=5 µm). Manders' coefficient M1 and M2 indicate the overlapping one probe to the other.

In the case of Lamp3 and Rab7, co-incubation of cy5_MiniAp-4 and CTB were done for 5 minutes, obtaining low MCC values as it was expected. However, we repeated the experiment with a longer time of incubation, 45 minutes. At this time point, we could confirm the co-localization of the CTB with the two markers with high MCC values. For our peptide, some co-localization could be observed, however it was not as high as our control.
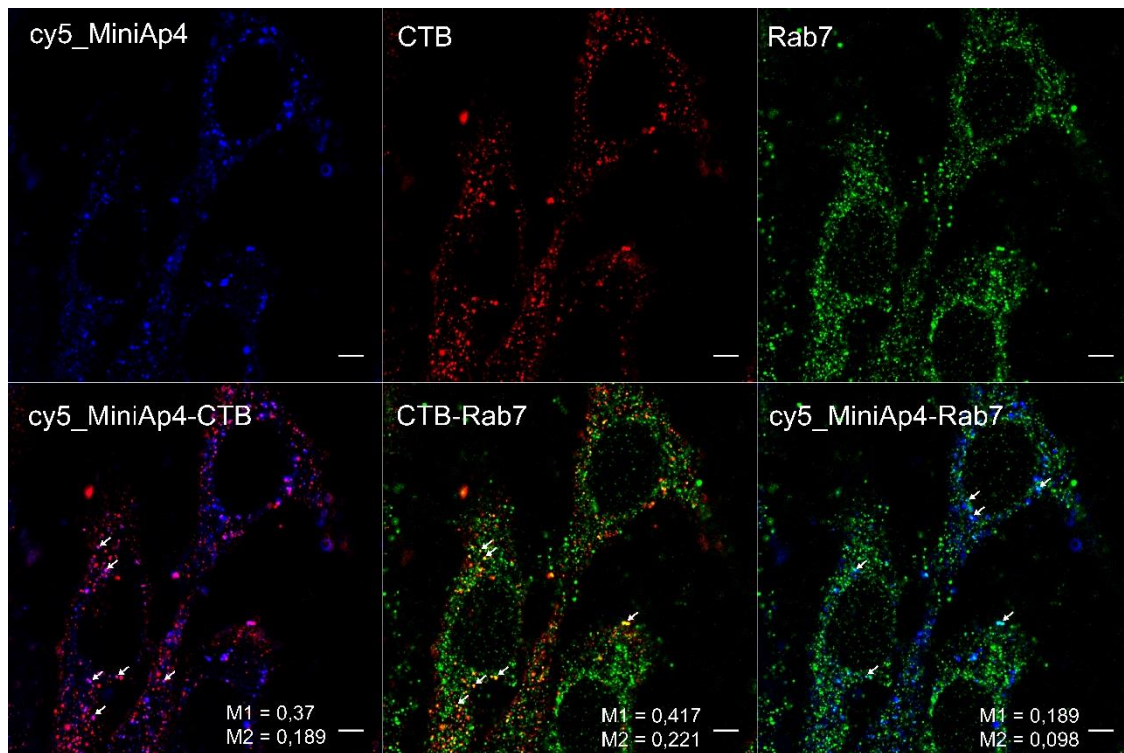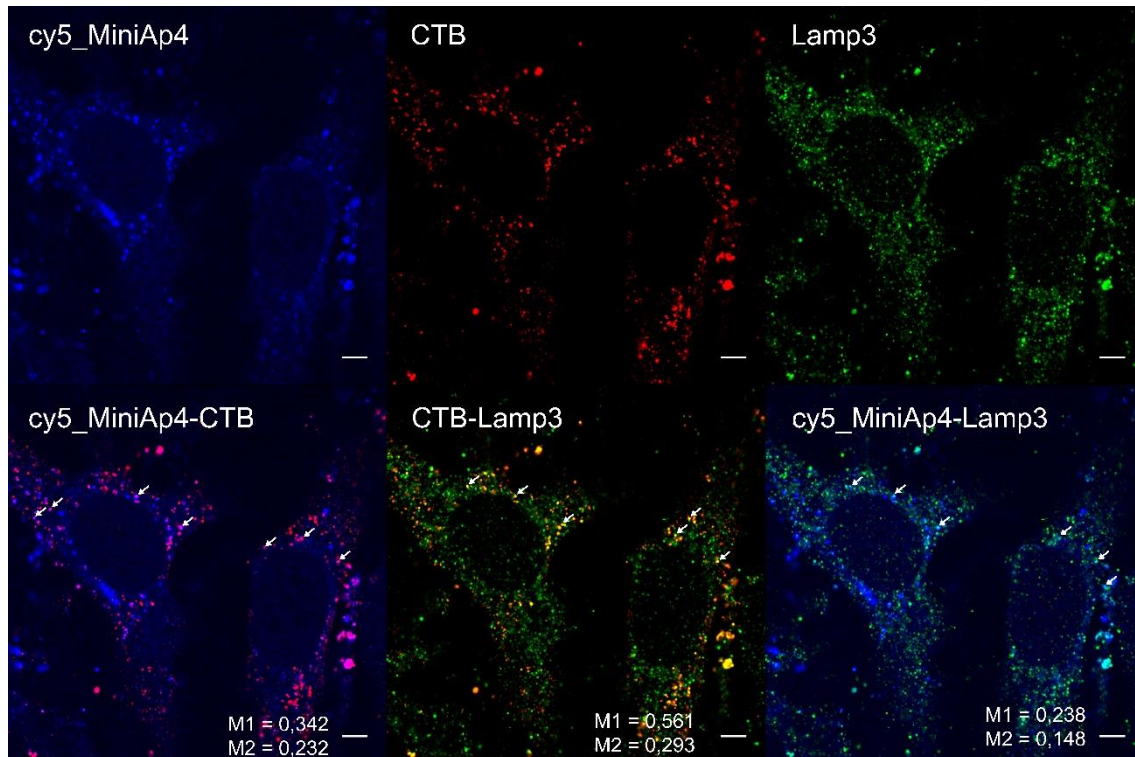
Figure 63. Co-localization of cy5_MiniAp-4 and Alexa555-CTB with Rab7 marker. b.End3 cells were co-incubated with 100 µM of cy5_MiniAp-4 (blue), Alexa555-CTB (red) at 20 µg·mL^{-1} for 45 minutes at 37 °C in 5% CO_2. (Scale bar=5 µm). Manders' coefficient M1 and M2 indicate the overlapping one probe to the other.

Figure 64. Co-localization of cy5_MiniAp-4 and Alexa555-CTB with Lamp3 marker. b.End3 cells were co-incubated with 100 µM of cy5_MiniAp-4 (blue), Alexa555-CTB (red) at 20 µg·mL^{-1} for 45 minutes at 37 °C in 5% CO_2. (Scale bar=5 µm). Manders' coefficient M1 and M2 indicate the overlapping one probe to the other.

In conclusion, with all these results, we can confirm that MiniAp-4 uses an endocytic pathway to enter in brain endothelial cells. Also, our co-localization experiments suggests that MiniAp-4 uses both endocytic routes of entry: the clathrin-dependent and the caveolin, being this last one the majority one. Moreover, it is possible that MiniAp-4 goes first to early endosomes and then to the late ones, thus partially following an endocytic degradation pathway.

Further experiments would need to be done in order to understand the route that MiniAp-4 takes once is internalized inside the cells. One good possible experiment would be to study the co-localization with an anti-GM1 antibody as we have previously mentioned how CTB binds GM1. Another would be to quantify the co-localization of cy5_MiniAp-4 with anti-clathrin and anti-caveolin, in order to see higher MCC values for caveolin. Also, in order to discard the recycling pathway, quantify the co-localization of cy5_MiniAp-4 with anti-Rab11 and compare it with transferrin would be a good option in order to discard it.

We have to take into account that in all these experiments we have studied the endocytosis of cy5_MiniAp-4, however performing the same experiments in the BBB model, which mimics better the BBB properties, we could study the entire transcytosis of such peptide.

Photocrosslinking studies to study the mechanism of internalization

As it has been explained in the first chapter, photocrosslinking consists of the modification of a ligand with a photoreactive group, which upon irradiation generates reactive species that covalently bind to the ligand its target.[151] This modification can be used to identify amino acid residues at protein-protein interactions, to study protein-ligand interactions, to isolate or identify unknown enzymes, among other studies. Once the crosslinked reaction has occurred, the product can be purified and then analyzed by various techniques methods.[208]

The use of photoreactive amino acids was first described by Thiele and co-workers in 2005. In this work, they designed isoleucine, methionine and leucine containing a diazirine group such that the corresponding tRNA recognized and incorporated them into a protein replacing the natural amino acids.[209] In our project we wanted to study the mechanism by which MiniAp-4 crosses the BBB incorporating a photoreactive amino acid in the sequence. To this end, a photoreactive analogue was designed and synthesized exchanging the L-proline for a L-photo-proline following the work described by Van der Mijden *et al.*[210]

In the case of the study of a protein-ligand interaction, the photoreactive group has to be small as possible in order to generate a suitable mimic of the original ligand. Our photoreactive amino acid contained a diazirine group at position 4 of the pyrrolidine ring, which is one of the most versatile photolabile groups due to its small size, efficiency and irreversibility after the formation of a reactive carbene upon irradiation at 350 nm.[211-212] One of the most significant feature of carbenes is its ability to form rapidly a covalent bond with the nearest molecule through C-C, C-H, O-H and X-H (X=heteroatom) in a short exposure of UV light and its rapidity to be quenched by reacting with H_2O unless they react with other surrounding molecules.[213-214]

Scheme 2 shows the synthesis of the Fmoc-L-photoproline from the L-*trans*-4-hydroxyproline, commercially available. First, the oxidation of the alcohol was performed using chromic acid in diluted sulfuric acid (Jones oxidation) leading the corresponded ketone **1,** which could be confirm by the appearance of a peak around 210 ppm in the ^{13}C NMR spectrum corresponding to the carbonyl group. Then, the formation of the diaziridine from the ketone was performed followed by the oxidation to a diazirine using iodine in the presence of Et$_3$N. In this step, also ^1H and ^{13}C NMR was performed in order to follow the reaction by the disappearance of the 210 ppm peak. Finally, the last step was the exchange of the Boc for a Fmoc group, which was confirm by ^1H NMR spectrum, obtaining new peaks around 7 ppm. Although the preparation steps for product **2** and **3** were repeated several times in order to increase the amount of product obtained, low overall yields were accomplished. The obtained Fmoc-photoproline was stable under acid and basic conditions, therefore it could be incorporated using standard solid-phase Fmoc/*t*Bu peptide chemistry.
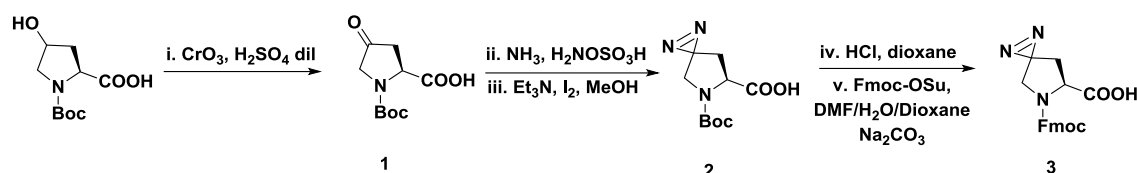
Scheme 2. Synthesis of Fmoc-L-photoproline.

In addition, we incorporated a biotin tag at the *N* terminal of the peptide in order to facilitate the further isolation of the fragments that have been covalently bound to the photo-peptide after photocrosslinking.

The first experiment designed consisted on the incubation of photo-MiniAp-4 with b.End3 cells followed by irradiation at 365 nm in order to form covalent bonds between our photoreactive peptide and the adjacent proteins. After, lysis of the cells followed by purification with magnetic beads is performed in order to obtain only the biotinylated fragments. Then, SDS-page followed by tryptic digestion of the protein bands with trypsin is perform to do bottom-up proteomics analysis (*Scheme 3*).
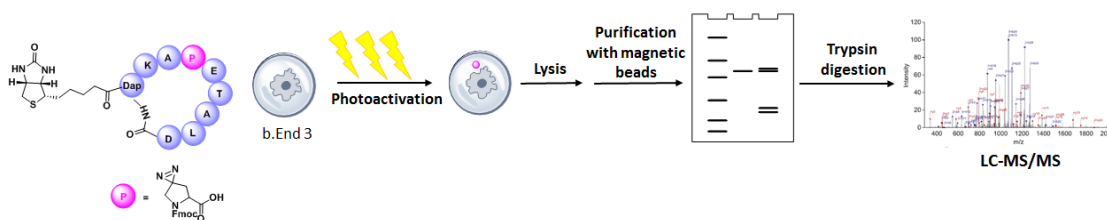
Scheme 3. Workflow of photocrosslinking experiment for MiniAp-4.

In our first attempt the photoreactive peptide was incubated with the cells at two different concentrations (1 µM and 10 µM) during 15 minutes at 4°C followed by 5 minutes irradiation at 365 nm. After adding lysis buffer, cells were sonicated in order to break the cells. Several cycles of centrifugation were performed in order to obtain the cell pellets which were mixed with Dynabeads™ MyOne™ Streptavidin T1 and incubated at 4 °C overnight in order to purify the biotinylated fragments. The first problem faced was the elution of the biotinylated fragments from the streptavidin beads. As it is well-known, streptavidin-biotin complex is one of the strongest binding partners occurring in nature and is far beyond the normal protein-ligand binding strength, therefore, the release of the biotin fragments from the beads can be hampered by this intense interaction.[215-216] The elution of biotinylated proteins sometimes requires harsh conditions and which are often incompatible in downstream processing, for this reason, digestion of the proteins on the beads is another possibility but it can lead to undesirable released peptides that may difficult the further analysis.[217-218] In order to optimize the elution conditions we applied four different described elution protocols: urea, ethanol, glycine and biotin.[219-220] For that, we repeated the experiment varying only the elution conditions. WB of all samples were performed in order determine the best conditions. As a control for biotin detection, a biotin-lysozyme conjugate was used (≈15 kDa).
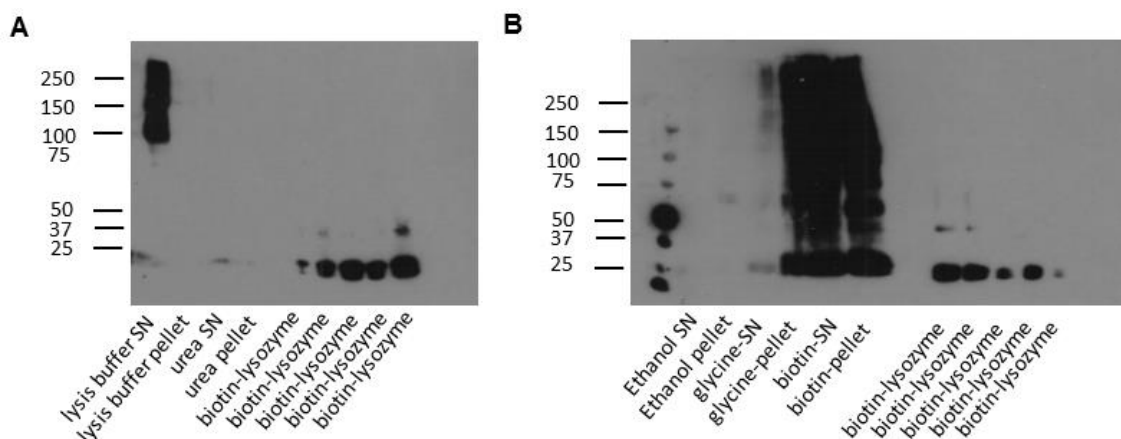
Figure 65. A) WB with lysis buffer elution and urea protocol. B) WB with ethanol, glycine and biotin elution for supernatant (SN) and pellet. Controls were performed using different concentrations of a biotin-lysozyme conjugate.

In brief, 20 µg of protein, both pellet and supernatant, were incubated with streptavidin magnetic beads in the presence of a known amount of biotin-lysozyme protein. The elution of the biotinylated proteins was followed by on-bead tryptic digestions and quantification of lysozyme by LC-MS/MS. Although the elution with biotin probed to be the most efficient method, as shown in *Figure 65*, the recovery of lysozyme was only of a 17%. For this reason, we decided to design a new protocol with a cleavable linker, which would allow the separation of the labelled proteins without eluting the biotin from the beads.

Cleavable linker strategy

In recent years, many cleavable linkers have been developed as an effective tool to break chemical bonds between two molecular entities also being compatible with the biological molecules and systems. These cleavable linkers need to have some desirable characteristics such as compatibility with bio-orthogonal reagents, the mild cleavage conditions and high yields of elution. Reduction/oxidation sensitive, photocleavable, nucleophile/electrophile sensitive are some linkers examples that can be classified depending on their cleavage conditions required.[221]
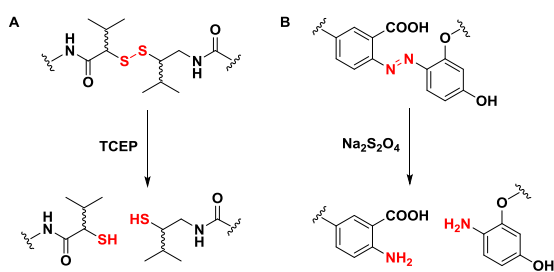

Scheme 4. Cleavage of a disulfide bridge (A) and an azo compound (B) by TCEP and sodium dithionite respectively.

In the group of the reduction sensitive linkers, there are two main subgroups: the azo compounds and the disulfide bridges. Azo compounds which are chemically stable in physiological conditions, are cleaved in mild conditions using sodium dithionite, obtaining two aniline moieties via an electrochemical reduction mechanism and allowing the use of reducing agents such as tris(2-carboxyethyl)phosphine (TCEP) or

dithiothreitol (DTT).[222] Optimized azo-based cleavable linkers were recently described to isolate endogenous protein complexes in non-denaturing conditions.[223] Disulfide bridges can be rapidly and easily cleaved under mild reducing conditions like TCEP or DTT. Although disulfide bridges have been used in a wide range of applications, they are unstable upon nucleophilic and electrophilic reagents, leading to thiol exchange and non-specific cleavage upon intracellular conditions. In the field of proteomics, the cleavage of the disulfide bridge might also trigger the reduction of disulfide bridges present in proteins, which generally play an important role in maintaining protein structure, thus changing the structure of such proteins.

With all this information in hand and considering the limitations of our system, we decided to use a disulfide bridge as a linker. To this end, our first step was first to synthetize a photo-MiniAp-4 with a disulfide bridge and a biotin. After the irradiation and further lysis of the cells, the cell lysates would be incubated in streptavidin magnetic beads and the reduction of the linker would be carried out using DTT and iodoacetamine (IAA). Proteomic analysis would be performed in order to identify the obtained fragments *(Scheme 5)*.
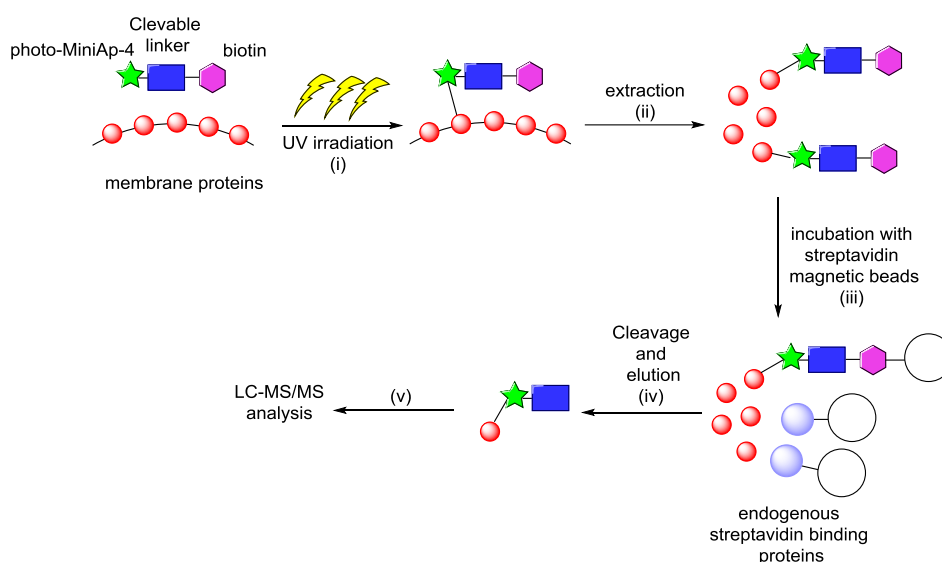
Scheme 5. Experimental scheme of protein identification. (i) Cell-surface proteins that interact with MiniAp-4 are crosslinked using a photoreactive analogue. (ii) Lysis of the cells. (iii) Incubation with Dynabeads™ MyOne™ Streptavidin T1 beads. (iv) Cleavage. (v) Analysis by LC-MS/MS of the eluted proteins.
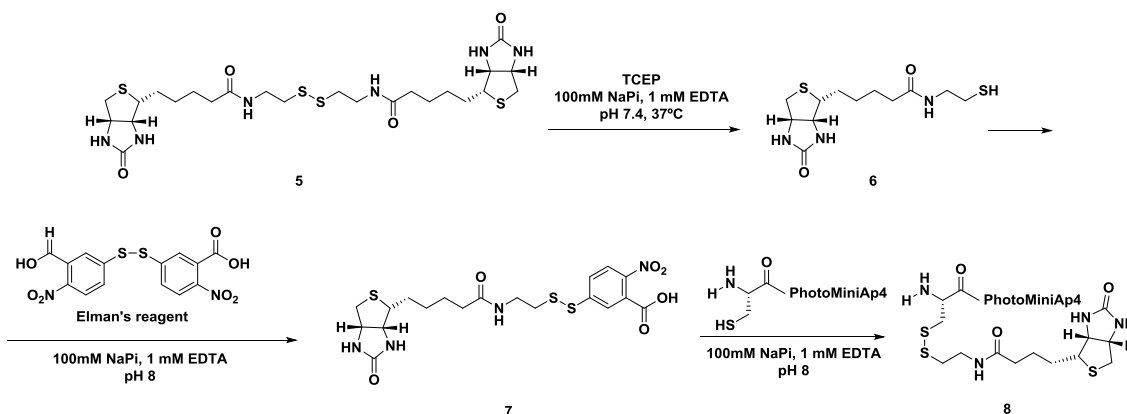
Synthesis

The first step of the activation of the carboxylic acid of the biotin to a *N*-hydroxysuccinimyl ester. This compound was reacted with cysteamine to yield compound **5**.The reaction was followed by UPLC and UPLC-MS and DIEA was added several times until no traces of the starting material were detected. After, the reduction of the disulfide bridge was carried out with TCEP and the thiol was activated with Elman's reagent *(Scheme 6).* Again, the reactions were followed with UPLC and UPLC-MS and the crude product **7** was purified by preparative HPLC.
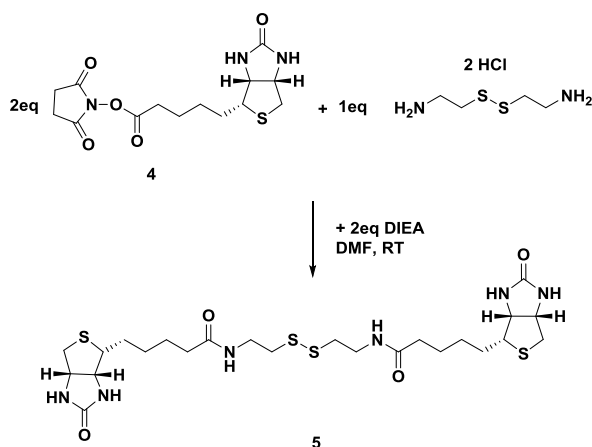
Scheme 6. Synthesis of compound **5**

The final step of the reaction was the formation of the disulfide bridge between compound **7** and the photoreactive version of MiniAp-4 containing a cysteine residue at the *N*-terminal. Product **8** was purified by preparative HPLC and characterized by UPLC and UPLC-MS.

Scheme 7. Schematic route for the synthesis of photo-MiniAp-4 with a cleavable linker and a biotin moiety (**8**).

Subcellular localization of crosslinked MiniAp-4

In order to demonstrate if there is a crosslinking reaction between the photoproline residue and the membrane proteins, we decided to examine the subcellular localization of the crosslinked peptide by AiryScan microscopy. To do this, 100 µM of cy5_photoMiniAp-4 were incubated 30 minutes at 4ºC in b.End3 cells, after the solution was removed and RH buffer was add. Then, cells were irradiated for 1 minute at 365 nm, followed by two washing steps. Finally, cells were fixed with a solution of 4% of PFA at least for 15 minutes at RT. As *Figure 66* shows, some signal that corresponds to the peptide seems to

be on the cell membrane however, as we did not acquire a bright field image, is difficult to confirm it.
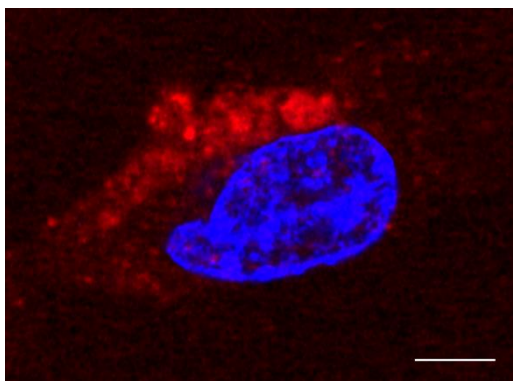

Figure 66. Microscope image of b.End3 cells co-incubated with 100 μM of cy5-photoMiniAp-4 (red) and irradiated at 365 nm for 1 minute. Cell nuclei are stained with Hoescht (blue). (Scale bar=5 μm). Single-plane images presented were acquired with AiryScan.

Photocrosslinking experiment

In order to get further insights into MiniAp-4 transcytosis mechanism we performed an UV triggered photocroslinking experiment. For that, b.End3 cells were treated with 10 μM of compound **8** at 4ºC for 30 minutes followed by 1 minute irradiation at 365 nm for crosslinking reaction. A mock experiment was carried out in parallel without peptide. The experiment was performed at 4ºC in order to slow the cell metabolism down. The cells were irradiated at 10 cm distance since we had observed that shorter distance leads to cell death. After irradiation, the cell membrane pellets were mixed with Dynabeads™ MyOne™ Streptavidin T1 and incubated at 4 ºC overnight. After several washes of the beads, elution was performed by cleavage of the disulfide bridge with DTT followed by alkylation with IAA. The last step was the protein digestion of the eluted proteins using trypsin. The digested proteins were subjected to LC-MS/MS analysis. After analysis of the sample, 238 possible interactor proteins were identified. Of note, only 39 were membrane related proteins. Most of the other proteins were nuclear, although other localization were found. Most of the obtained proteins were related with the TJs and AJs, such as Cadherin-5 and vinculin respectively. Also, some cytoskeleton proteins were found which are known to be implicated in endocytosis and transcytosis processes. Importantly, proteins related with clathrin-mediated and caveolin-dependent endocytosis like Clatrhin heavy chain 1 and caveolin 2 were found.
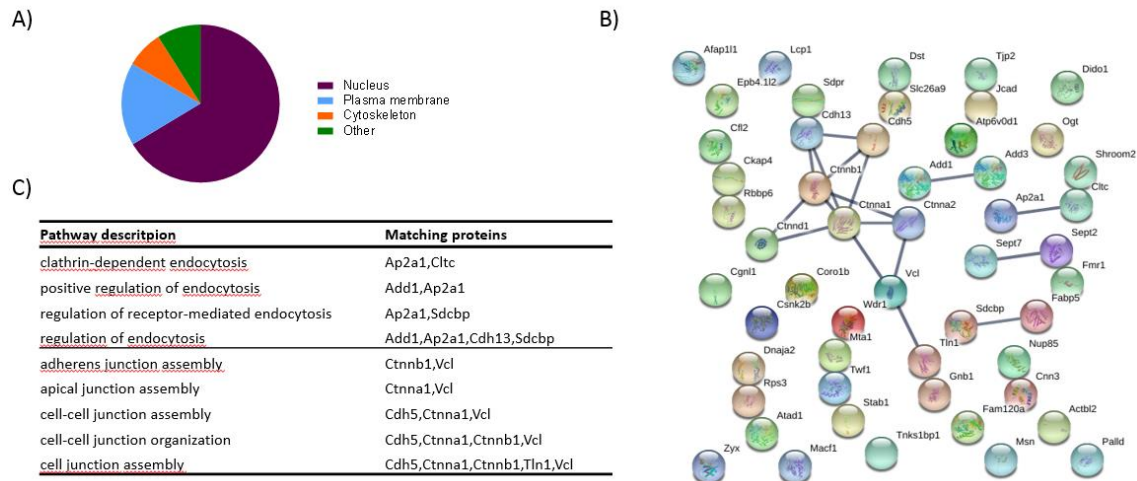
Figure 67. A) Sector diagram of all obtained proteins classified by their cellular localization. B) The STRING network view. Line between the proteins indicate the various types of interaction evidence described. Protein name corresponds to the gene. C) Ob

In order to better understand the pathways in which MiniAp-4 was involved we submitted the list of proteins related to the plasma membrane and the cytoskeleton for STRING (*Search Tool for the Retrieval of Interacting Genes/Proteins*) analysis. This software comprises a biological database, which predict protein-protein interactions from a wide variety of source including experimental data, computational prediction methods among others, allowing the identification of protein networks.[224]

STRING analysis suggested different relation between cadherins (Cdh5, Cdh13) and catenins proteins (Ctnna1, Ctnna2, Ctnnb1 and Ctnnd1). The family of cadherin proteins (Cadherin 5, 13) play an important role in intracellular junctions in endothelial cells, while the association between catenins to cadherins produces a complex which is linked to the actin filament network, which are important for cadherins cell-adhesion properties. Also vinculin, which is an actin filament binding protein have been reported to interact with cadherin family. Another two proteins related to actin were found as potential interactors, alpha and gamma adducin, which are membrane-cytoskeleton associated proteins that promotes the assembly of the spectrin-actin network.

Also, it reported a relation between the adaptor protein complex 2 (AP-2) and clathrin heavy chain 1 protein, both of them involved in clathrin-dependent endocytosis. These two obtained proteins reinforce the results obtained in the previous section (*see Elucidation of the mechanism of internalization*), where we proved that MiniAp-4 use a clathrin-dependent mechanism and a caveolin/lipid raft pathways. Also, one of the potential interaction obtained was the Caveolae-associated protein 2, which act as a scaffolding protein within caveolar membranes.

Gene	Protein name	Localization	T mean	1/FC
Tln1	Talin-1	Plasma membrane and cytoskeleton	31	0
Ctnna1	Catenin alpha-1	Plasma membrane and cytoskeleton	26,67	0.09
Ctnnb1	Catenin beta-1	Plasma membrane, cytoskeleton and nucleus	25,33	0.22
Vcl	Vinculin	Plasma membrane, cytoskeleton, and adherens junction	14	0
Add1	Alpha-adducin	Plasma membrane and cytoskeleton	9,33	0
Sept2	Septin-2	Plasma membrane and cytoskeleton	8,67	0
Cdh5	Cadherin-5	Plasma membrane and cell junction	8,33	0.24
Cltc	Clathrin heavy chain 1	Cytoskeleton, peripheral membrane protein and coated pits	7	0
Sdcbp	Syntenin-1	Plasma membrane, extracellular region or secreted, nucleus and cytosol	6,67	0
Ctnnd1	Catenin delta-1	Plasma membrane and nucleus	6	0
Ap2a1	AP-2 complex subunit alpha-1	Plasma membrane, peripheral membrane protein and coated pits	4	0
Sept7	Septin-7	Cytoskeleton	3.64	0
Add3	Gamma-adducin	Plasma membrane and cytoskeleton	3,33	0
Fabp5	Fatty acid-binding protein 5	Plasma membrane, extracellular region or secreted and nucleus	2,67	0
Cdh13	Cadherin-13	Plasma membrane	2,33	0
Ctnna2	Catenin alpha-2	Plasma membrane, cytoskeleton and nucleus	2	0

Table 16. Protein interactors found after LC/MS-MS analysis divided by protein name, cellular localization, sample spectral counts mean (T mean) and 1/FC coefficient which corresponds to coefficient between the control and the sample spectra counts mean. Protein found to interact are highlighted with the same color.

Table 16 shows all proteins which STRING database found a relationship, ordered from the highest to lowest T mean, which is the average of spectral counts of the sample which is a semiquantitative approach to measure the protein abundance in a sample however, it has some limitations.[225] Another value is the inverse of FC which is the coefficient between the average spectral counts of the control and the sample.

Although these experiment gives a list of potential interactor proteins, it would be necessary to repeated at least twice in order to see if similar results are obtained. Once we have a list of potential proteins, RNAi-mediated knockdown experiments combined with the use of inhibitors, could revealed how MiniAp-4 internalizes in cells.

CONCLUSIONS

Conclusions of the first objective: study in detail THRre and its interaction with the transferrin receptor by different techniques.

1. We could confirm the interaction of THR and THRre to the TfR by STD NMR. Both peptides showed higher STD effect values at the region where the two trypthofan residues are located, suggesting that this region is closer to the receptor when the saturation transfer occurs.

2. The dissociation constant could be calculated only for THR peptide by SAW and ITC obtaining a value around 1 mM. K_D value could not be obtained for THRre implying a weaker interaction with the receptor.

3. Different pharmacokinetic parameters of THRre were obtained confirming the low affinity for the receptor.

4. The two photoreactive versions of THR and THRre showed a time couse UV dependency, however we could not elucidate the binding site to the receptor, maybe due to their weak affinity.

Conclusions of the second objective: understand the mechanism by which MiniAp-4 crosses the BBB.

1. Seven different analogues of MiniAp-4 were designed and synthesized by SPPS and their *cis/trans* proline ratio conformation was measured by NMR. After assessing all peptides in a HBBBM, no significant differences were observed between alaogues. However, the analogue which presented an 85% of *cis* conformation showed better transport capacities for a small cargo as carboxifluorescein.

2. We could confirm the uptake of conjugated QDs to MiniAp-4, however, naked NPs internalize as well, implying that these type of NPs were not ideal for these type of studies.

3. MiniAp-4 uses a dynamin dependent endocystosis mechanism to internalize in b.End3 cells as its uptake was inhibid when it was co-incubated with dynasore. In addition, with different co-localization studies we could confirm that MiniAp-4 uses a clathrin dependent and independent mechasim to internalize in b.End3 cells and it follows a degradation pathway once inside the cell.

4. A photocrosslinking strategy was designed using a synthesized biotinylated photo-reactive analogue. After mass spectrometry analysis, different potential membrane proteins were obtained, however, further experiments needs to be done in order to confirm it.

MATERIALS AND METHODS

Solvents, reagents and basic instruments

All the reagents employed were from Sigma-Aldrich unless otherwise specified. Other providers for the most common reagents used are included in the following table:

Commercial supplier	Reagents and solvents
Amersham Biosciences	lysozyme
Amesham Pharmacia	western blotting detection kit
Applied GL Biochem	1-hydroxy-7-azabenzotriazole (HOAt)
ATCC	b.End3 cells
BioRad	Precision Plus ProteinTM Dual Xtra Prestained Protein Stand.
Biotechrabbit	Tris-NTA amine
CEM	RinkAmide ProTide resin
Corning Costar	Transwells bovine model (0.33 cm^2; pore size 0.4 μm)
	Transwells human model (1.13 cm^2, pore size 0.4 μm)
	12-well and 24-well cell culture-treated plates, BD matrigel
	growth factor reduced matrix, 100 mm diameter Petri Dish
GE-Healthcare	NAP-5 desalting columns, PD-10 desalting columns
GL Science Inc	GL-GC, GC-SBD tips
Innoprot	endothelial cells medium (ECM)
Iris Biotech GMBH	2-chlorotrityl chloride resin
	All amino acids except otherwise specified, TBTU
KaliChemie	trifluoroacetic acid (TFA)
Lumiprobe	cyanine5 NHS ester
MatTek Corporation	MatTek glass-bottom culture dishes
Merck	copper sulfate ($CuSO_4$)
Millipore	EBM-2 medium, hCMEC/D3 cells
Novabiochem	benzotriazoL-1-y L-oxytripyrrolidinophosphonium hexafluorophosphate (PyBOP), *N*-hydroxisuccinimide (NHS)
Scharlau	dichloromethane (DCM), dimethylformamide (DMF), MeOH, tert-butylmethylether
SDS	acetone, ACN, toluene
PCAS BioMatrix Inc.	ChemMatrix® resin

Thermofisher Tecn.	Dynabeads™ MyOne™ Streptavidin T1
	Qdot™ 605 ITK™ Carboxyl Quantum Dots
	Qdot™ 605 ITK™ Amino (PEG) Quantum Dots

Peptide synthesis and characterization

Solid-phase peptide synthesis (SPPS)

All peptides were synthesized using Fmoc/*t*Bu solid phase peptide synthesis (SPPS) manually or using an automated microwave synthesizer. Syntheses were performed in a 250 μmol-scale using several solid supports depending on the requirements of the synthesis. Peptide elongation and other manipulations were done in 20 mL polypropylene syringes with a polypropylene porous disk. Solvents and soluble reagents were eliminated under vacuum filtration. Washings between synthetic steps were done with DMF (5 x 30 s) and DCM (5 x 30 s) using 10 mL of solvent/g resin each time. During couplings the mixture was allowed to react with intermittent manual stirring.

Protected L- and D-amino acids used were the following unless otherwise specified: Fmoc-Ala-OH, Fmoc-Cys(Trt)-OH, Fmoc-Asp(*t*Bu)-OH, Fmoc-Glu(*t*Bu)-OH,Fmoc-Gly-OH, Fmoc-His(Trt)-OH, Fmoc-Lys(Boc)-OH, Fmoc-Leu-OH, Fmoc-Met-OH, Fmoc-Asn(Trt)-OH, Fmoc-Pro-OH, Fmoc-Gln(Trt)-OH, Fmoc-Arg(Pbf)-OH, Fmoc-Ser(*t*Bu)-OH, Fmoc-Thr(*t*Bu)-OH, Fmoc-Val-OH,Tyr(*t*Bu)-OH, Fmoc-Trp(Boc)-OH.

Solid supports

Several resins were used depending on the peptide:
- RinkAmide-ChemMatrix® resin (substitution of 0.52 mmol/g): manual SPPS
- 2-Chlorotrytil resin (substitution of 1.6 mmol/g): manual SPPS
- RinkAmide ProTide resin (substitution of 0.6-0.8 mmol/g): automated SPPS

Initial conditioning of the resin

All peptides with an *N*-terminal amide were synthesized on ChemMatrix® with a substitution of 0.4-0.6 mmol/g.

Treatment	Reagent
Washing	MeOH (5 x 30 s)
Washing	DMF (5 x 30 s)
Washing	DCM (5 x 30 s)
Washing	DCM 1% TFA (2 x 10 min)
Washing	DCM (5 x 30 s)
Washing	DCM 5% DIEA (2 x 10 min)

| Washing | DCM (5 x 30 s) |
| Washing | DMF (5 x 30 s) |

All peptides with an *N*-terminal carboxylate were synthesized on 2-chlorotrityl chloride resin.

Treatment	Reagent
Washing	DCM (5 x 30 s)
Washing	DMF (5 x 30 s)
Washing	DCM (5 x 30 s)
Coupling	0.8 eq Fmoc-aa-OH, 0.8 eq Oxima, 0.8 eq DIC
Capping	MeOH (1mL / g resin), 15 min
Washing	DCM (5 x 30 s)
Washing	DMF (5 x 30 s)
Washing	DCM (5 x 30 s)

General protocol for peptide chain elongation

Amino acids were coupled onto the growing chain following the methodology described below (*Table 17*). Briefly, the resin was washed several times and the temporary protecting group was removed using a solution of 20% piperidine in DMF. After washing the resin again, the amino acid and coupling reagents were added and left to react for 20-60 min. Finally, after the washings of the resin from the reagents and by-products, the coupling control was carried out by the ninhydrin or chloranil test.

Operation	Reagents	No treatments	Time, min
	DMF	3	0.5
Washing	DCM	3	0.5
	DMF	3	0.5
Deprotection	20% piperidine / DMF	3	1 x 1 min
			2 x 10 min
Coupling control	Ninhydrin or chloranil test	1	3 or 5
	DMF	3	0.5
Washing	DCM	3	0.5
	DMF	3	0.5
Coupling	Fmoc-aa-OH	1	20-60

	Coupling reagents in DMF		
	DMF	3	0.5
Washing	DCM	3	0.5
	DMF	3	0.5
Coupling control	Ninhydrin or chloranil test	1	3 or 5

Fmoc group removal

The Fmoc group was removed by treating the resin with a solution of 20% piperidine in DMF (10 mL/g resin, 1 x 1 min and 2 x 10 min). After deprotection, the resin was washed with DMF (5 x 30 s), DCM (5 x 30 s) and again DMF (5 x 30 s).

Fmoc group quantification/resin loading capacity

In order to know the degree of functionalization, the Fmoc adduct, formed during removal of the Fmoc group with piperidine, can be quantified with UV-Vis spectroscopy.
The Fmoc removal and washing steps solution were collected in a volumetric flask and diluted with DMF. Part of this solution was used to measure the absorption at 300 nm. Loading (f) was calculated using the following formula:

$$f = \frac{A \cdot V}{\varepsilon \cdot m \cdot b}$$

where A_{300} is the measured absorbance at 300 nm, V the volume of the flask, ε is the molar extinction coefficient of Fmoc at 300 nm (7800 $M^{-1}cm^{-1}$), l is the path length of the cuvette and m the weight of the resin.

Coupling methods
Manual synthesis

Several coupling methods were used depending on the amino acids involved. Method 1 was used as the default method, while Method 2 was used for milder couplings. Method 3 was used for long couplings and cyclization.

Method 1

Treatment	Reagents
Washing	DMF (5 x 30 s)
Coupling	3 eq Fmoc-Aa-OH, 3 eq TBTU, 6 eq DIEA in DMF (30-40min)
Washing	DMF (5 x 30 s), DCM (5 x 30 s), DMF (5x 30s)

Method 2

Treatment	Reagents
Washing	DMF (5 x 30 s)
Coupling	3 eq Fmoc-Aa-OH, 3 eq OximaPure®, 3 eq DIC in DMF (30-45 min or o/n)
Washing	DMF (5 x 30 s), DCM (5 x 30 s), DMF (5x 30s)

Method 3

Treatment	Reagents
Washing	DMF (5 x 30 s)
Coupling	4 eq Fmoc-Aa-OH, 4 eq PyBOP, 12 eq DIEA in DMF (45-60 min)
Washing	DMF (5 x 30 s), DCM (5 x 30 s), DMF (5x 30s)

Automated microwave-assisted peptide synthesis using Liberty Blue

The protected amino acid (0.2 M in DMF), DIC (0.5 M in DMF), Oxyma (1 M in DMF) and HOBt (1M in DMF) were added to the reaction vessel. The mixture was allowed to react for 2 min with a microwave potency of 170 V (90°C). The solvents were removed by filtration, and the resin was washed with DMF (3 x 30 s). For His the maximum temperature was reduced to 50°C. The removal of the Fmoc group was performed with piperidine (20% in DMF) or piperazine (10% in NMP/EtOH [9/1]) for 1 min.

Monitoring of couplings and deprotection

Colorimetric tests were used in the manual syntheses after each deprotection to verify Fmoc removal and after each coupling to know if the new protected amino acid had been successfully coupled. These tests are based on the detection of primary and/or secondary amino groups.

Kaiser or ninhydrin test

The ninhydrin test is based on the specific color of ninhydrin upon reaction with a primary aliphatic amino acid.[226] To perform this test, an aliquot of dried but DCM solvated resin was placed in a glass tube. Then, 6 drops of reagent A and 2 drops of reagent B were added and the tube was heated at 110°C for 3 min. A yellow/orange colour indicates a negative test, whereas a blue/purple coloration of the beads and/or the solution indicates a positive results, thereby indicative that a second coupling is needed.

Reagent A: Two solutions are needed. First solution: 40 g of phenol are dissolved in 10 mL of absolute ethanol. Second solution: 65 mg of KCN in 100 mL of water is prepared

and mixed with 100 mL of freshly distilled pyridine. Each solution is stirred with 4 g of Amberlite MB-3 resin for 45 minutes and filtered. Finally the two solutions are mixed. **Reagent B:** 2.5 g of ninhydrin are dissolved in 50 mL of absolute ethanol. This solution must be protected from the light.

Chloranil test

The presence of the secondary amino group of Pro can be detected using the chloranil test.2 An aliquot of dried but DCM solvated resin was placed in a glass tube. Then, 20 μL of the chloranil solution and 200 μL of acetone were added and after 5 min at RT the test was completed. A yellow/orange color indicates that the test is negative whereas a blue/green color of the solution and/or the beads was not quantitative.

Mini-cleavage of the resin

Few beads of dried but DCM solvated resin were transferred into an Eppendorf with 300 μL of cleavage solution (95% of TFA, 2.5% H_2O and 2.5% of TIS) for 15-30 minutes. After evaporating the solution with N_2, the resin was dissolved in H_2O/ACN (1:1) and injected at the UPLC-MS.

Cleavage from the resin/side-chain deprotection

After the deprotection of the *N*-terminus of the last amino acid, the resin was washed several times with DMF and DCM and dried by suction for 15 minutes. The dried resin was transferred to a 50 mL falcon and the peptides were cleaved from the resin using the appropriate cleavage mixture. The peptide was left to react for 2-4 h using enough solvent to allow a good swelling of the resin. All the cocktails incorporated a high percentage of TFA with the presence of scavengers to capture the cleaved protecting groups and avoid side reactions, such as H_2O, TIS. The following cleavage cocktails used are:

Cocktail A: TFA:H2O:TIS (95:2.5:2.5) [Standard cocktail]
Cocktail B: TFA:H2O:TIS (90:5:5) [For peptides containing Cys]

Work –up

After cleavage of the peptides, the solvent was evaporated applying a current of N_2. Cold *tert*-butyl methyl ether was added to precipitate the peptide and eliminate non-peptidic impurities, followed by the centrifugation of the mixture (4ºC, 3500 rpm, 10 min). The supernatant liquid was decanted and the process was repeated three times.
After that, the peptides were dissolved in a mixture 1:1 of H_2O:ACN with 0.1% TFA and lyophilized.

Lactam bridge formation

MiniAp-4 and its analogues were synthesized by Fmoc/*t*Bu solid-phase peptide synthesis using regular protected amino acids Fmoc-L-Asp(OAll)-OH and Fmoc-L-Dap(Alloc)-OH. Before the deprotection of the final Fmoc group, Allyl and Alloc groups were

removed using tetrakis(triphenylphosphine)palladium(0) (0.2 eq) and phenylsilane (5 eq) in DCM. Three treatments for 15 min were performed and the deprotection was assessed by the ninhydrin test and mini-cleavage with UPLC-MS analysis.

Cyclization was achieved with two reactions (2h and overnight) with PyBOP (4 eq), HOAt (12 eq) and DIEA (12 eq). The completion of the reaction was assessed through a mini-cleavage and UPLC-MS analysis. Finally the Fmoc group was removed using 20% piperidine in DMF.

Preparation of Fmoc-L-Dopa-OH

Fmoc-L-Dopa-OH was prepared according to the procedure described by Sever *et al*. L-Dopa (2.5 g, 12.7 mmol) was dissolved in a mixture of dioxane (36.8 mL) and a 10% Na_2CO_3 solution (36.8 mL) and stirred in an ice bath 10 min prior to the addition of Fmoc-Cl (3.29 g, 12.7 mmol), which was done over 50 min. The reaction was stirred for 4 h on an ice bath and 25h at room temperature. The cream colored suspension was added to a separation funnel and washed with *tert*-butyl methyl ether (3 x 100 mL). The aqueous layer was cooled on an ice bath and acidified to pH 3 using 6 M HCl. This aqueous solution was added to a separation funnel and extracted with ethyl acetate (3 x 100 mL). Ethyl acetate layers where combined, washed with brine (3 x 100 mL), and dried with anhydrous Na_2SO_4. Solvent was removed under vacuum to yield Fmoc-L-Dopa-OH as a light brown and fluffy solid.

(3g, 7.1 mmol, 56% yield) of a light brown and fluffy solid purity by UPLC: >98%, (t_R=1.742 min). Mcal (g/mol): 419.1, MS found $[M+H]^+$: 420.

^{1}H NMR (400 MHz, DMSO-d_6) δ 8.71 (d, J = 17.2 Hz, 2H), 7.86 (d, J = 7.5 Hz, 2H), 7.68 – 7.57 (m, 3H), 7.39 (td, J = 7.5, 3.6 Hz, 2H), 7.29 (q, J = 7.8 Hz, 2H), 6.70 – 6.57 (m, 2H), 6.49 (dd, J = 8.0, 2.0 Hz, 1H), 4.22 – 4.09 (m, 3H), 4.10 – 3.97 (m, 1H), 2.87 (dd, J = 13.9, 4.6 Hz, 1H), 2.67 (dd, J = 13.8, 10.2 Hz, 1H), 2.06 (d, J = 6.0 Hz, 1H).

L-Dopa coupling

Fmoc-L-Dopa-OH (4 eq), PyBOP (4 eq) and HOAt (12 eq) were sequentially added to the peptide-resin in DMF, followed by DIEA (12 eq). The mixture was allowed to react with intermittent manual stirring for 90 min. The solvent was removed by filtration, and the resin was washed with DMF (5 x 30 s) and DCM (5 x 30 s). The extent of coupling was checked by the appropriated colorimetric test.

Disulfide bridge formation in solution

Ellman test

This test allows the determination of free thiols in solution or in a polymer that is compatible with aqueous medium. The reagent was prepared on the day of the assay by dissolving 40 mg of 5,5-dithiobis(2-nitrobenzoic acid) (DTNB) in 10 mL solution of phosphate buffer 0.1 M at pH 7.4 and kept in a sealed vial under nitrogen atmosphere. 0.5

mL of the crude, initially containing 0.1-0.2 µmol of free thiols, were diluted with 0.9 mL of phosphate buffer (0.1 M pH 8) and mixed with 100 µL of DTNB solution. A blank was prepared with the same volume of DTNB dissolved in 1.5 mL.

Conjugation to azide -cyanine5

Peptides were obtained by manual Fmoc/*t*Bu solid-phase peptide synthesis as described previously, and *5*-hexynoic acid was coupled at the *N*-termini in solid-phase. After that, peptides were cleaved and purified. Two solutions were prepared prior to the reaction, the first one containing 25 mM ascorbate in water pH 7 and the second one mixing $CuSO_4$ (200 mM in water) and THPTA (200 mM in DMSO) 1:1. Conjugation to cyanine5-azide was performed in aqueous buffer with DMSO. The alkyne-peptide (1.2 μmol) was dissolved in 100 μL of NaP (50 mM, pH 8) and mixed with Cyanine5.5-maleimide (16 μmol, 16 μL DMSO), ascorbic acid (120 μL of 25 mM stock) and Cu-THPTA (3 μmol, 30 μL). The reaction mixture was degassed with N_2 steam. The mixture was allowed to react for 30 min and the reaction progression was monitored by UPLC and upon completion the crude mixture was purified by HPLC.

Desalination by GL tips

GL-GC and GL-SDB tips where inserted and washed by adding 50 µL of 80% v/v of ACN containing 0.1% TFA followed by a centrifugation step at 3000g for 3 minutes at 10ºC. After, 50 µL of 0.1% TFA were added and centrifuged as previous conditions. Samples were added containing 0.1% of TFA and centrifuged at the previous conditions. The order of tips was changed and add 50 µL of 0.1% TFA followed by a centrifugation step were performed. The tube was changed for a low-binding protein tube and add 50 µL of 80% v/v of ACN containing 0.1% TFA followed by another step of centrifugation. Repeat the last step once in order to increase the recovery.

Purification of peptides

Peptides were dissolved in H_2O/ACN (the percentage depending on the peptide), filtered through 0.45 µm filters and purified by semi-preparative RP-HPLC. The fractions containing the peptide were analyzed by UPLC or UPLC-MS, pooled together and lyophilized.

Two semi-preparative RP-HPLC systems were used. The first instrument was a Waters system with MassLynx 4.1 software, a 2545 binary gradient module, a 2767 manager collector, a SFO system fluid organiser, a 3100 mass detector, a 2998 photodiode array detector, and a 515 HPLC pump. A SunFire C_{18} column (150 x 10 mm x 3.5 µm, 100 A, Waters) was used, with ACN (0.1% TFA) and H_2O (0.1% TFA) as solvents and a flow rate of 6.6 mL/min. The second instrument was a Waters system with ChromScope software, a 2707 Autosampler, a Prep Degasser, a 2545 binary gradient module, a 2489 UV/Visible Detector, and a Fraction Collector III. A XBridge C_{18} column (150 x 19 mm

x 5 µm, Waters) or a Aeris Peptide XB C$_{18}$ column (250 x 21.1 mm x 5 µm, Phenomenex) was used, with ACN (0.1% TFA) and H$_2$O (0.1% TFA) as solvents and a flow rate of 15-20 mL/min.

Identification of peptides
UPLC-MS
Chromatograms and spectra were recorded on a Waters high class (PDA detector, sample manager FNT and Quaternary solvent manager) coupled to an electrospray ion source ESI-MS Micromass ZQ and using the MassLynx 4.1 software (Waters, Milford, MA). Using a BEH C$_{18}$ column (50 x 2.1 mm x 1.7 µm, Waters). The flow rate was 0.6 mL/min, and ACN (0.07% formic acid) and H$_2$O (0.1% formic acid) were used as solvents.

LTQ-FT MS
A high-resolution mass spectrometer was used to determine the exact mass of the peptides. The samples were diluted in H$_2$O/ACN (1:1) with 1% formic acid and analyzed with an LTQ-FT Ultra (Thermo Scientific). They were introduced by automated nanoelectrospray. A NanoMate (Advion BioSciences, Ithaca, NY) infused the samples through the nanoESI Chip (which consisted of 400 nozzles in a 20 x 20 array). The spray voltage was 1.70 kV, and the delivery pressure was 0.5 psi. MS conditions were as follows: Nano-ESI, positive ionization, capillary temperature 200°C, tube lens 100 V, ion spray voltage 2 kV, and *m/z* 200–2000 a.m.u.

Quantitative Targeted Absolute Proteomics (QTAP)
The absolute protein expression levels of target peptides were determined by QTAP analysis as described previously (Uchida *et al.*[159]). In the case of the calibration curve, peptides were mixed with internal standard peptides and a dilution series of non-labeled (standard) peptides. All the samples were desalted using GL-tip GC and SDB, and followed by the injection into the LC-MS/MS system.

Purity assessment
UPLC-PDA
UPLC chromatograms were obtained on an Acquity high class (PDA detector, sample manager FNT and Quaternary solvent manager), using an Acquity BEH C$_{18}$ (50 x 2.1 mm x 1.7 µm) column. The flow rate was 0.61 mL/min and ACN (0.036% TFA) and H$_2$O (0.045% TFA) were used as solvents. 2-min linear gradients were used in all cases. Detection was performed at 220 nm.

HPLC-PDA
HPLC chromatograms were obtained on a Waters Alliance 2695 with an automatic injector and a photodiode array detector 2998 Waters (Waters, Milford, MA) using a SunFire C$_{18}$ column (100 x 4.6 mm x 5 µm, 100 A, Waters) and software EmpowerPro 2,

solvents ACN (0.036% TFA) and H_2O (0.045% TFA), flow rate: 1 mL/min. 8-min linear gradients were used. Detection was performed at 220 nm.

Quantification by amino acid analysis

The content and ratio of amino acids present in a peptide sample were determined by ion exchange chromatographic analysis after acid hydrolysis. The hydrolysis is performed with 6M HCl at 110°C for 16 h. After that time, the sample was evaporated to dryness at reduced pressure. The residue was dissolved in 20 mM aqueous HCl, derivatized using the AccQ-Tag protocol from Waters, which uses *6*-aminoquinolyl-*N*-hydroxysuccinimidyl carbamate as a derivatization reagent, and finally analyzed by ion exchange HPLC.

Stability assays

Pepsin

Peptide samples were incubated at 220 µM in a solution 2:50 (pepsin:peptide) at pH 2 for different selected times. After, 50 µL of NaOH 0.01 M solution were added to stop pepsin action. Analysis were performed by UPLC.

Pancreatin

0.1 g of pancreatin were dissolved in 10 mL of potassium phosphate buffer 50 mM at pH 7.5. After, aliquots of 2 mL were centrifuged at 14,000 rpm for 30 minutes and combined supernatants were used to dissolve the compounds to a final concentration of 220 µM. The samples were incubated at 37°C with orbital agitation (120 rpm) for different times. At selected time points, HCl 0.1 M was added to stop pancreatin activity and analyzed at the UPLC-MS. The protein content of the supernatant was measured using the BCA assay obtaining a 5.92 ± 0.86 mg/mL (N = 3).

Rat plasma

Peptides at 220 µM were dissolved in mixture of plasma:PBS (1:1). The samples were incubated at 37°C with orbital agitation (50 rpm). At selected time points, 100 µL aliquots were extracted, precipitating on 300 µL of cold methanol. Samples were immediately cooled down to 4°C and kept at that temperature for 30 minutes. After which, samples were centrifuged at 3000 rpm at 4°C for 15 minutes. The supernatant was analyzed by UPLC.

Filtration dialysis

Peptides were dissolved in RH at 5 µM and centrifuged for 2 hours at 5400g through the membrane. The obtained solution was diluted 1/10 in H_2O with 0.1% FA and injected at the LC-MS/MS with previous desalination procedure in order to calculate the recovery percentage.

Nuclear magnetic resonance

NMR spectra were recorded at 25 °C on a Bruker 600 MHz spectrometer equipped with a cryoprobe. The NMR sample was prepared by dissolving the peptide in 90% H_2O/10% D_2O at a final concentration of 1 mM and pH 2-3. Chemical shifts were referenced to internal DSS (*4,4*-dimethyl-*4*-silapentane-*1*-sulfonic acid) at 0.0 ppm. Complete proton and carbon resonance assignment was obtained by the combined analysis of 2D homo- (TOCSY, NOESY) and hetero-nuclear (^{1}H ^{13}C HSQC) NMR experiments. The TOCSY and NOESY mixing times were 80 and 200 ms, respectively. Suppression of the water signal was achieved by excitation sculpting. Unless otherwise stated, the populations of both the *cis* and *trans* isomers were determined from the integration of amide protons in the 1D ^{1}H NMR spectra acquired at 25 °C for each peptide.

Saturation-Transfer Difference NMR (STD NMR)

NMR samples were prepared in D_2O containing 30 mM of sodium phosphate (pH 7.4) and 0.05% (w/v) NaN_3. The final concentrations were 3-5 µM for the peptides and 500-550 µM for the transferrin receptor. NMR spectra were recorded at 25 °C on a Bruker 600 MHz spectrometer equipped with a cryoprobe. The *on*-resonance frequency, to selectively irradiate protein signals, was set to -1.5 ppm whereas the *off*-resonance frequency was 50 ppm. The saturation time was 2 seconds.

Cell-based assays

Cell culture conditions

Murine brain endothelial cells

bEnd.3 cells were cultured in DMEM complete medium (glucose 4.5 g/L, 2 mM glutamine, 10% FBS and 0.5% Pen/Strep. Medium was changed 3 times per week and cells were detached using 0.05% trypsin/EDTA. The passage number was kept below 35 for all experiments.

Human brain capillary endothelial cells

hCMEC/D3 cells were cultured in EBM-2 medium supplemented with 5% fetal bovine serum, 1% penicillin-streptomycin (Gibco/Invitrogen, Carlsbad, CA, USA), 1.4 µM hydrocortisone (SIGMA-Aldrich), 5 µg/mL ascorbic acid, 1% Chemically Defined Concentrate, 10 mM HEPES, 1 ng/mL human basic fibroblast growth factor (bFGF) in an atmosphere of 95% air and 5% CO_2 at 37 °C for 3–4 days for routine culture. The passage number was kept below 35 for all experiments.

Internalization experiments

Analysis using flow cytometry

Two days before the experiment, 100.000 bEnd.3 cells/well were seeded in 24-well plates. On the day of the assay, the cells were washed with Ringer HEPES (RH) for 15 min and then treated for another 15 min with selected inhibitor, filipin III (10 µg/mL). After this pre-incubation, QD conjugated peptide was added to reach a final concentration of 50 µM. After 30 min of incubation at 37°C, the cells were washed 5 times with Ringer HEPES or Gly buffer at 4°C, trypsinised and kept on ice. Cells were immediately analyzed using a FACSAria Fusion flow cytometer with a 582 nm laser.

Analysis using confocal microscopy

Two days before the confocal microscopy experiments, the cells (5000 cells/dish) were seeded on collagen pre-coated MatTek glass-bottom culture dishes and incubated at different times at 37°C. After, cells were washed 3 times with 1 mL of media and immediately imaged. Fluorescence was detected on a Zeiss LSM 780 laser scanning confocal microscope equipped with temperature-controlled environmental chamber and CO_2 for live-cell imaging. Images were taken with a Zeiss Plan-Apochromat 63x/1.40 oil DIC M27 objective. Carboxyfluorescein or Alexa488, and Hoechst were excited with an Ar laser at 488 and 405 nm, and emission was recorded at 546 and 458 nm, respectively. Pinholes were set to equate optical slice thicknesses. The images were processed using the ImageJ 1.49b software.

dSTORM imaging

To perform direct STORM (dSTORM) imaging *in vitro*. STORM buffer contains PBS, an oxygen scavenging system (0.5 mg/mL glucose oxidase, 40 µg/mL catalase), 5% (w/v) glucose and 100 mM cysteamine. STORM images were acquired using a Nikon N-STORM system configured for total internal reflection fluorescence (TIRF) imaging. DiI-QSs were imaged by means of a 561nm laser (80 mW) and TetraSpeck™ Microspheres were imaged by means of a 488 nm (80 mW) (only in the case of in vitro QS). No activation UV light was employed. Measurements of 20,000 frames were acquired for the 561 nm channel and every 100 frames a frame for the 488 nm channel (drift correction) was acquired. Fluorescence was collected by means of a Nikon 100x, 1.49 NA oil immersion objective and passed through a quad-band pass dichroic filter (97335 Nikon). Images were acquired onto a 256x256 pixel region (pixel size 0.16 µm) of a Hamamatsu ORCA- Flash 4.0 camera at 10 ms integration time. STORM images were analyzed with the STORM module of the NIS element Nikon software. The NIS elements Nikon software generates a list of localizations by Gaussian fitting of blinking dyes in the acquired movie of conventional microscopic images. To avoid over counting blinkings detected in consecutive frames are counted as single by the software.

Permeability assays in the *in vitro* BBB cellular model

These experiments were performed using the model developed in Prof. R. Cecchelli's laboratory. In brief, endothelial cells derived from human pluripotent stem cells and bovine pericytes were defrosted in gelatin-coated Petri dishes (Corning). After 48 h, endothelial cells were seeded in 12-well Transwell inserts (80000 cell/well) and pericytes were plated in 12-well plates (50000 cells/well) previously coated with Matrigel and gelatin, respectively. The medium was changed every 2-3 days and the assays were performed 7-8 days after seeding.

Lucifer Yellow (50 µM) was added as a control of barrier integrity (Papp < 15 x 10^{-6} cm/s). To perform the assay, 500 µL of the compound in Ringer HEPES was added to the donor compartment and 1500 µL of Ringer HEPES was introduced into the acceptor compartment. The plates were incubated for 2 h at 37°C, and the solutions from both compartments were recovered and analyzed by UPLC. The samples were evaluated in triplicates. The apparent permeability was calculated using the following formula:

$$Papp = \frac{QA\,t \cdot VD}{t \cdot A \cdot QD(to)}$$

where *Papp* is obtained in cm/s, *QA(t)* is the amount of compound at the time *t* in the acceptor well, V_D is the volume in the donor well, *t* is time in seconds, *A* is the area of the membrane in cm and $QD(t_0)$ is the amount of compound in the donor compartment at the beginning of the experiment.

Biophysical methods

ITC experiments

ITC experiments were performed at 25°C using a low volume nano ITC calorimeter (TA instruments). Peptide and protein samples were dissolved in the same buffer (20 mM Tris, 150 mM NaCl pH 7,4) and degassed prior to the ITC experiments. For each titration, a concentrated peptide solution was injected into a cell containing 190 µL of protein solution at a concentration of 12-15 µM, measured in a NanoDrop™ 2000 spectrophotometer. We performed 17 injections of 3 µL per titration with a 4-min delay after each injection. Binding isotherms were analyzed using the software provided by TA instruments, assuming a single binding site for the independent domains. Baseline controls were acquired with buffer and pure peptide solutions.

SAW experiments

Affinity analyses were performed with a Sam5 Blue biosensor (SAWInstruments, Bonn, Germany), consisting of a biosensor unit, an autosampler, and a microchip module with a gold layer sensing surface on a quartz chip. The chip surface was prepared and cleaned before binding and affinity determinations by 45 min washing with a 1:1 mixture (v/v) of concentrated sulfuric acid and hydrogen peroxide (30%). Immobilization of TfR was

performed by covalent binding of a flat 16-mercaptohexadecanoic acid self-assembled monolayer (COOH-SAM), as previously described.

TfR was immobilized on the SAM by carboxyl-group activation with a 1:1 mixture (v/v) of 200 mM (*1*-ethyl-*3*-(*3*-dimethylaminopropyl)-carbodiimide (EDC) and 50 mM *N*-hydroxysuccinimide (NHS). A 12-15 µM solution of TfR in 150 µL PBS was used for coupling, followed by capping of unreacted carboxyl groups with 1 M ethanolamine, pH 8.5. Peptide affinities were determined at 25ºC by injecting a range of peptide concentrations (micro- to millimolar) selected to cover the equilibrium concentration. For the regeneration of the chip between injections, affinity bound ligands were eluted with 0.1 M HCl aqueous solution (pH 1). Binding curves were analyzed using the Origin Pro 7.5 software, and K_D values were calculated determined using the FitMaster software.

NP modification and characterization
Quantum dot modification
Quantum dots with carboxylic acid groups

The conjugation of the peptide onto carboxylated functionalized quantum dots was done following the indications of the manufacturer. For this purpose, 1 eq. of nanocrystals (1 µM) in borate buffer pH 7 (10 mM) was mixed with 40 eq. of peptide and 3 eq. of EDC in a total volume of 250 µL. The mixture was allowed to react for 1 h at room temperature. The sample was then dialyzed at 4°C against water, changing the solvent every 8 h over a course of 36 h. In order to assess the level of conjugation of the peptide, samples were analyzed by zeta potential and by amino acid analysis to determine the number of peptide copies per particle.

Quantum dots with amino groups

1 μL of 0.4 M *N*-(γ-maleimidobutyryloxy)succinimide in DMF (400 nmol, 1000 eq) was diluted with 79 μL of 50 mM borate buffer pH 8. pH was readjusted to 8 with 0.1 M NaOH. This solution was mixed with 50 μL of 8 μM Amino PEG QDot 605 (0.4 nmol, 1 eq). The mixture was incubated for 1h at room temperature under gentle shaking and was then separated with a NAP-5 column eluting with PBS. A 0.4 M solution of 80 μL of 0.4 M *tris*(*2*-carboxyethyl)phosphine (TCEP) was prepared in 100 mM phosphate buffer pH 8. 4 μL of this TCEP solution (1.6 μmol, 4000 eq) was preincubated with 80 μL of 5 mM Cys-MiniAp-4 in water (400 nmol, 1000 eq) to minimize the presence and further formation of peptide dimers linked through a disulfide bond. This solution was mixed with the functionalized QDots and stirred for 1h at room temperature being gently shaken. Most of the peptide was then removed through a NAP-5 column.

QD characterization and quantification
Transmission electron microscopy (TEM)

Electron micrographs were acquired using a Tecnai Spirit electron microscope, equipped for cryo and tomography or Jeol JEM 2010F, operating at 200 KV coupled, to an electron

energy loss spectrometer. TEM grid covered with Formvar were activated for 5 min under UV illumination and the sample was deposited and dried in a desiccator.

Nanodrop

Quantum dot concentration was measured using a NanoDrop spectrophotometer ND-1000.

Amino acid analysis

Amino acid analysis of the peptides coating NPs was performed as described in the *Peptide Synthesis* section but digestion with HCl 6 M was extended to 72 h.

Zeta potential

Nanoparticle surface charges were measured using a Malvern Zetasizer Nano-ZS from Malvern Instruments. Measurements were performed at 25ºC in a 3 mm light path cuvette.

Protein characterization

SDS-PAGE

SDS-PAGE electrophoresis was carried out using BioRad system (Miniprotean cell) (7.5 % Tris gel, 25 mM Tris, 192 mM glycine, 0.1% SDS running buffer). Protein molecular weights were approximated by comparison to a protein marker. Gels were visualized by silver staining.

Silver staining

The gel was incubated with fixing solution for 15 min, washed with 30% EtOH (3 x 3 min). Then, it was soaked with pre-treatment solution for 1 min and washed with miliQ H_2O (3 x 3 min). After, the gel was treated with impregnation solution for 20 min and washed twice with milliQ H_2O. Finally, the gel was revealed using revealing solution until bands were observed, followed by milliQ H_2O washings (2 x 2 min), and incubated for additional 10 min with stop solution.

> *Fixing solution:* 50 mL MeOH, 12 mL AcOH, milliQ H_2O up to 100 mL. 50 µL of 37 % formaldehyde are added at the last moment.
> *Pre-treatment solution:* 19.1 mg of $Na_2S_2O_3$ in 150 mL milliQ H_2O. I
> *Impregnation solution:* 0.2 g $AgNO_3$, milliQ H_2O up to 100 mL. Then, 74.8 µL of 37 % formaldehyde are added in the last place.
> *Revealing solution:* 6 g $NaCO_3$, 2 mL pre-treatment solution, milliQ H_2O up to 100 mL. 50 µL of 37 % formaldehyde are added at the last instant.
> *Stop solution:* 50 mL MeOH, 15 mL AcOH, milliQ H_2O up to 100 mL.

Western blot

Proteins bands obtained during SDS-PAGE were rinsed in blotting buffer and transferred to a nitrocellulose membrane at 350 mA for 1h in pre-cooled blotting buffer.

The nitrocellulose membrane was rinsed with PBST and then it was incubated with deffated powder milk (10% w/v) for 2 hours at room temperature. Membrane was rinsed with PBST (5 x 5 min) and incubated with streptavidin HRP (1:1000) for 1 h at room

temperature. After, the membrane was developed by luminescence with the ECL kit *Western Blotting Detection Quit.*

Conjugation of biotin-NHS to lysozyme

Lysozyme (1 mg, 7×10^{-5} mmol) was mixed with biotin-NHS (0.12 mg, 3.5×10^{-4} mmol) in DMF for 3 times every 20 minutes. The reaction was followed by UPLC-MS. Most of the unreacted starting materials were removed through a midiTrapG25 column.

N-Boc-L-4-Oxoproline synthesis

N-Boc-L-4-Hydroxyproline (5 g, 21.6 mmol) was dissolved in 400 ml acetone. Jones reagent (37 ml, 98.8 mmol) was added dropwise with cooling over 10 min and the reaction mixture was stirred for 2 h. Methanol (8.1 ml) was added dropwise and the reaction mixture was then filtered through celite and concentrated *in vacuo*. EtOAc (270 ml) was added and the solution was again filtered through celite. The filtrate was washed with brine (6×100 ml). The organic phase was dried over Na_2SO_4 and solvent removed *in vacuo*. The product crystallized from EtOAc.

^{1}H NMR (400 MHz, CDCl$_3$): δ (ppm) = 4.61 (m, 1H); 3.78-3.56 (m, 1H); 3.14-2.98 (m, 1H); 2.46-2.41 (m, 1H); 1.95 (m, 1H); 1.34, 1.31 ($2 \times$ s, 9H). ^{13}C NMR (100 MHz, CDCl$_3$): δ (ppm) = 205.25 (CO); 173.74 + 173.49 (COOH), 155.07 + 154.32 (NCOOR), 80.84 (OCR3), 56.22 + 55.60 (Cα), 52.51 + 52.12 (C5), 40.84 + 40.31 (C3), 27.54 + 27.46 (Me). ES-MS: m/z 228.0 [M-H^{1-}).

N-Boc-proline-4-spiro-3-(3H-diazirine) synthesis

N-Boc-L-4-oxoproline (3.08 g, 13.5 mmol) was charged into a three necked-flask (100 ml) and ammonia was slowly condensed into the flask. The solution was refluxed for 5 h with stirring. The solution was cooled with a dry-ice bath and a solution of hydroxylamine *O*-sulfonic acid in anhydrous methanol (8 ml, 1.84 M, 14.7 mmol) was added. The mixture was refluxed for a further 1.5 h. Anhydrous methanol (18 ml) was added while the reaction was cooled with a dry ice bath. The solution was stirred overnight to allow the ammonia to evaporate. The resulting slurry was filtered through a sintered glass funnel and the filter cake was washed twice with methanol (50 ml). The combined methanol phases were treated with triethylamine (1.88 ml, 13.6 mmol) and concentrated to <15 ml. Another equivalent of triethylamine (1.88 ml, 13.6 mmol) was added, the solution was cooled with an ice bath and titrated with a solution of I$_2$ in MeOH (0.1 M) until the solution remained an orange colour. The solvent was removed *in vacuo* and the resulting slurry was dissolved in water (50 ml). The solution was acidified to pH 2 and the product was extracted with ethyl acetate (4×50 ml). The organic phase was washed once with brine and dried over Na_2SO_4. The solvent was removed in vacuo and product was purified by flash silica chromatography (95:5, CH$_2$Cl$_2$:MeOH).

^{1}H NMR (400 MHz, CDCl$_3$): δ (ppm) = 4.67, 4.56 ($2 \times$ dd, J=9.8 Hz & J=2.5 Hz, 1H); 3.26-3.12 (m, 1H); 3.15-3.08 ($2 \times$ d, *J*=13.1 Hz, 1H); 2.41-2.32 (m, 1H); 1.71-1.64 ($2 \times$

dd, J=15.2 Hz & J=2.2 Hz, 1H); 1.47,1.46 (2 × s, 9H). ^{13}C NMR (100 MHz, CDCl$_3$): δ (ppm) = 176.63 + 174.91 (COOH); 153.56 + 152.36 (CO); 80.76 + 80.49 (OCR$_3$); 56.85 + 56.53 (Cα); 47.47 + 47.13 (CN$_2$); 32.52 + 31.42 (CH$_2$); 29.78 + 29.27 (CH$_2$); 27.27 + 27.18(Me). MS?

N-Fmoc-L-proline-4-spiro-3-(3H-diazirine) synthesis

N-Boc-L-4-Diazirinylproline (0.99 g, 4.11 mmol) was dissolved in dioxane (20 ml) and concentrated HCl (2 ml) was added dropwise. The reaction was stirred for 1.5 h and the solvent evaporated *in vacuo*. The sample was dissolved in water and lyophilized to remove excess acid. The residue was dissolved in aq. Na$_2$CO$_3$ (9% w/v, 17.5 ml) and 0.9 eq. *O*-Fmoc-*N*-hydroxysuccinimide (1.24 g) in DMF/dioxane was added. The reaction was shaken for 10 min and then water (150 ml) was added and unreacted *O*-Fmoc-*N*-hydroxysuccinimide was extracted with diethyl ether and EtOAc. The aqueous phase was acidified to pH 2 and the product was extracted with EtOAc (5 × 50 ml). The organic phase was dried with Na$_2$SO$_4$ and the solvent evaporated. The product was purified by flash chromatography first with silica using 94:5:1 CH$_2$Cl$_2$:MeOH:AcOH, and then using 90:10:0.25, EtOAc:n-hexane:AcOH as eluant. A white powder was obtained after lyophilization.

1H NMR (400 MHz, CDCl$_3$): δ (ppm) = 7.77-7.72 (m, 2H); 7.55-7.53 (m, 2H); 7.42-7.28 (m, 4H); 4.74- 4.71 (m, 1H); 4.58-4.41 (m, 2H); 4.27, 4.19 (2 × t, J=6.8 Hz, 1H); 3.28 (dd, J=20 & J=16 Hz, 1H); 3.13 (m, 1H); 2.49-2.34 (m, 1H); 1.73, 1.58 (2 × dd, J=16.0 Hz & J=2.4 Hz, 1H). ^{13}C NMR (100 MHz, CDCl$_3$): δ (ppm) = 171.19 (COOH), 154.64 (CO), 143.93 + 143.58, 141.23, 127.17, 125.00 + 124.95, 119.97, 68.21 + 67.68 (CH), 57.99 + 57.81 (Cα), 48.49 + 48.17 (CN2), 47.16 + 47.06 (CH$_2$O), 33.82 + 32.68 (CH$_2$), 31.60 + 30.95 (CH$_2$). m/z [M-H]$^-$ 358.26

Photocrosslinking experiment with bEnd.3

b.End3 cells were seeded on 100 mm dishes, which were cultured for 48 h (80−90% confluent). The cells were treated with 1 μM of photoMiniAp-4 for 15 min at 4 °C in RH buffer, and irradiated at 365 nm for different selected times at 4 °C. After washing with PBS, the cells were scraped while kept on ice. After centrifugation at 900 rpm, 1 mL of ice-cold lysis buffer was added and cells were left on ice for 20 minutes. The lysates were sonicated at M2 mode for 15 minutes and after centrifuged at 16000g x 3 times.

Streptavidin magnetic beads protocol

Dynabeads™ MyOne™ Streptavidin T1 were resuspended with the help of the vortex for 30 seconds. Then, the desired volume of beads were transferred to a tube and an equal volume of buffer was added. The tubes were placed on a magnet for 3 minute and supernatant was discarded followed by 3 washes with PBS.

Isolation of biotinylated fragments from streptavidin magnetic beads

Urea protocol

Cell lysates samples were incubated with 100 μL of Dynabeads™ MyOne™ Streptavidin T1 (Thermo Scientific) overnight at 4 °C. Washes were done according to Franco *et al.*[227]: 2× WB1, 3× WB2, 1× WB3, 3× WB4, × WB1, 1× WB5 and 3× WB6 (WB1: 8 M urea, 0.25% SDS in PBS; WB2: 6 M guanidine hydrochloride in PBS; WB3: 6.4 M urea, 1 M NaCl, 0.2% SDS in PBS (pre-warmed to 37 °C); WB4: 4 M urea, 1 M NaCl, 10% isopropanol, 10% ethanol, 0.2% SDS in PBS; WB5: 8 M urea, 1% SDS in PBS; WB6: 2% SDS in PBS). Samples were eluted with 100 μL of 4× Laemmli buffer with 100 mM DTT by two cycles of heating (95°C, 5 minutes), with vortexing in between.

Ethanol protocol

Cell lysates samples were incubated with 100 μL of Dynabeads™ MyOne™ Streptavidin T1 overnight at room temperature (RT) followed by an incubation of 30 minutes at room temperature in 50 μL 30% Ethanol, 1% TFA.

Glycin protocol

Cell lysates samples were incubated with 100 μL of Dynabeads™ MyOne™ Streptavidin T1 overnight at RT. After that 50 μL 0.1 M Glycin at pH 2.5 were added and the beads were incubated for 10 minutes at RT followed by the neutralization with 5 μL of a solution 1 M Tris at pH 8.8.

Biotin protocol

Cell lysates samples were incubated with 100 μL of Dynabeads™ MyOne™ Streptavidin T1 overnight at RT. After, the samples were incubated for 15 min at RT and 15 min at 96 °C with 50 μL of a solution of 30 mM biotin, 2% SDS, 160 mM NaCl, 6 M urea, 2 M thiourea.

Intact mass

Sample preparation

TfR and TfR-THR were analyzed upon deglycosylation with PNGaseF in 150mM ammonium acetate. Both samples were filtered through polyLC C_{14} reverse phase tip. Proteins were eluted with ACN:H_2O:FA (80:20:1) and dried in the speedVac. Samples were reconstituted with 50μL of H_2O:ACN:FA (90:10:1). 2μL were directly injected for LC-MS/MS analysis.

Sample analysis

The nano-LC-MS/MS set up was as follows. Samples were reconstituted with 50μL of H_2O:ACN:FA, 90:10:1). Sample was loaded to a trap column (Acquity UPLC M-Class BEH C4 Trap Column 300A, 5μm, 180μm x 20mm 2G V/M. Waters) at a flow rate of 5 μL/min. Proteins were separated using a polymeric analytical column (Acquity UPLC M-Class BioResolve mAb Column, 450Å, 2.7μm, 75μm x 250mm. Waters) with a flow rate

of 300 nl/min and a 150 min run, comprising three consecutive steps with linear gradients from 10 to 50% B in 120 min, from 50 to 85% B in 7 min, followed by isocratic elution at 85 % B in 7 min and stabilization to initial conditions (A= 0.1% FA in water, B= 0.1% FA in CH_3CN). The column outlet was directly connected to an Advion TriVersa NanoMate (Advion) fitted on an Orbitrap Fusion Lumos™ Tribrid (Thermo Scientific). The mass spectrometer was operated in a data-dependent acquisition (DDA) mode. In each data collection cycle, one full MS scan (500-1700 m/z) was acquired in the Orbitrap ($1.2x10^5$ resolution setting and automatic gain control (AGC) of 4.0e5). The most abundant ions were selected for fragmentation by Electron transfer dissociation (ETD). ETD was performed with a reaction time of 10 ms, 300 ms maximum injection time, a reagent target of 7.0 e^5, an AGC target of 5.0 e^5 and detected in the orbitrap at $1.2x10^5$ of resolution. Previously analyzed precursor ions were dynamically excluded for 30s. Spray voltage in the NanoMate source was set to 1.60 kV. RF Lens were tuned to 30%. The spectrometer was working in positive polarity mode and singly charge state precursors were rejected for fragmentation. Data was acquired with Xcalibur software vs 2.0SR2 (Thermo Scientific). An automatic deconvolution was performed with BioPharma Finder software v1.0.92.0 (Thermo) with Xtract node using TfR user sequence database.

In-gel digestion

Samples were tryptic digested directly in polyacrylamide gel. Briefly, stained electrophoretic protein bands were reduced with DTT 10mM for 45min at 56ºC and alkylated for 30 min in the dark with IAA 55 mM. Then, in-gel digestion was performed with trypsin (0.1 µg/µL) in 50mM NH_4HCO_3 at 37ºC overnight. The digestion was stopped by adding formic acid. Peptides were extracted with 100 % ACN and completely evaporated. Samples were reconstituted in 50 µL of 1% FA aqueous solution for MS analysis.

Identification of the binding site

The nano-LC-MS/MS set up was as follows. Digested peptides were diluted in 3% ACN/1% FA. Sample was loaded to a 300 µm × 5 mm PepMap100, 5 µm, 100 Å, C18 µ-precolumn (Thermo Scientific) at a flow rate of 15 µl/min using a Thermo Scientific Dionex Ultimate 3000 chromatographic system (Thermo Scientific). Peptides were separated using a C_{18} analytical column Acclaim PepMap® RSLC (75 µm × 50 cm, nanoViper, C_{18}, 2 µm, 100Å) (Thermo Scientific) with a 90 min run, comprising three consecutive steps with linear gradients from 3 to 35% B in 60 min, from 35 to 50% B in 5 min, and from 50 % to 85 % B in 2 min, followed by isocratic elution at 85 % B in 5 min and stabilization to initial conditions (A= 0.1% FA in water, B= 0.1% FA in CH_3CN). The column outlet was directly connected to an Advion Page 3/4 TriVersa NanoMate (Advion) fitted on an Orbitrap Fusion Lumos™ Tribrid (Thermo Scientific). The mass spectrometer was operated in a data-dependent acquisition (DDA) mode. Survey MS scans were acquired in the Orbitrap with the resolution (defined at 200 m/z) set to

120,000. The lock mass was user-defined at 445.12 m/z in each Orbitrap scan. The top speed (most intense) ions per scan were fragmented by HCD and detected in the orbitrap. The ion count target value was 400,000 and 10,000 for the survey scan and for the MS/MS scan respectively. Target ions already selected for MS/MS were dynamically excluded for 15s. Spray voltage in the NanoMate source was set to 1.60 kV. RF Lens were tuned to 30%. Minimal signal required to trigger MS to MS/MS switch was set to 25,000. The spectrometer was working in positive polarity mode and singly charge state precursors were rejected for fragmentation. A database search was performed with Proteome Discoverer software v2.3.0.480 (Thermo) using Sequest HT search engine and SwissProt Human canonical isoforms released 2018_11, contaminants database and user protein manually introduced. Search was run against targeted and decoy database to determine the false discovery rate (FDR). Search parameters included trypsin enzyme specificity, allowing for four missed cleavage sites, oxidation in M, carbamidomethylation in C, acetylation in protein *N*-terminus and THR(Bpa)/THR(Bpa-digested) in all residues (simulating crosslinks between transferrin and user's peptide) as dynamic modifications. Peptide mass tolerance was 10 ppm and the MS/MS tolerance was 0.02 Da. Peptides with a q-value lower than 0.1 and a FDR < 1% were considered as positive identifications with a high confidence level. Finally, the Percolator FDR node was used to estimate the number of falsely identified proteins among all the identified proteins.

PRODUCT CHARACTERIZATION

Peptides

Yields were calculated after purification and quantification by amino acid analysis or UPLC-PDA.

All the chromatograms are recorded at 220 nm in a UPLC with a 2-min linear gradient from 0 to 100% of ACN (0.036% TFA) in H_2O (0.045% TFA).

Chromatograms and mass spectra are shown for each synthesized peptide. For the nomenclature of cyclic peptides we followed the abbreviation rules proposed by Spengler *et al*[63].

Peptides	Molecular formula	Calc MW, Da	Found MW, Da	t_R UPLC, min	Purity, %	Sequence, cargoes and linkers
THR	$C_{71}H_{100}N_{20}O_{14}S$	1489.77	1489.7524	1.328	>98	THRPPMWSPVWP
THR scrambled	$C_{71}H_{100}N_{20}O_{14}S$	1489.77	1488.7419	1.258	>90	PWRPSHPVWMPT
THRre	$C_{71}H_{100}N_{20}O_{14}S$	1489,77	1489.7589	1.273	>98	pwvpswmpprht
THRre(Heavy)	$C_{71}H_{100}N_{20}O_{14}S$	1494.75	1493.7604	1.320	>95	pw*Vpswmpprht
G-THRre	$C_{73}H_{103}N_{21}O_{15}S$	1546,82	1545.7985	1.277	>90	Gpwvpswmpprht
biotin-GTHR(Bpa)1	$C_{88}H_{120}N_{22}O_{18}S_2$	1838.18	1838.8633	1.445	>98	Biotin-GTHRPPMWSPV(Bpa)P
biotin-GTHR(Bpa)2	$C_{88}H_{120}N_{22}O_{18}S_2$	1838.18	1838.8523	1.440	>98	Biotin-GTHRPPM(Bpa)SPVWP
biotin-GTHRre(Bpa)1	$C_{88}H_{120}N_{22}O_{18}S_2$	1838.18	1838.8565	1.453	>98	Biotin-Gpwvps(Bpa)mpprht
biotin-GTHRre(Bpa)2	$C_{88}H_{120}N_{22}O_{18}S_2$	1838.18	1838.9212	1.467	>98	Biotin-Gp(Bpa)vpswmpprht
THRre-G-DRG1	$C_{104}H_{149}N_{31}O_{23}S$	2233.59	2232.1133	1.298	>95	pwvpswmpprht-G-SPGARAF
THRre-G-DRG2	$C_{112}H_{160}N_{32}O_{25}S_2$	2418,83	2416.1821	1.307	>95	pwvpswmpprht-G-DGPWRKM
THRre(PEG)₃-DRG1	$C_{111}H_{162}N_{30}O_{27}S$	2380.76		1.121	>95	pwvpswmpprht-(PEG)₃-SPGARAF
THRre(PEG)₃-DRG2	$C_{119}H_{174}N_{32}O_{28}S_2$	2565.02	2565.52	1.088	>95	pwvpswmpprht-(PEG)₃-DGPWRKM
L-Dopa-G-THRre	$C_{80}H_{109}N_{21}O_{17}S$	1668.94	1667.7997	1.293	>95	L-Dopa-G-pwvpswmpprht
L-Dopa-(PEG)₃-THRre	$C_{87}H_{120}N_{22}O_{21}S$	1872.18	1870.9141	1.316	>95	L-Dopa-(PEG)₃-pwvpswmpprht
MiniAp-4	$C_{39}H_{66}N_{12}O_{13}$	911.03	911,4867	1,128	>98	Dap(&)KAPETALD(&)
MiniAp-4(Heavy)	$C_{39}H_{66}N_{12}O_{13}$	915.5	915.5022	1.135	>98	Dap(&)K*APETALD(&)
Cys-MiniAp-4	$C_{42}H_{70}N_{13}O_{14}S$	1013.16	1014.4256	1.189	>95	CDap(&)KAPETALD(&)

cyanine5-MiniAp-4		1	1773.7664	1.249	>95	Cy5- Dap(&)KAPETALD(&)
Analogue 1	$C_{39}H_{66}N_{12}O_{13}$	911.03	911,4925	1,151	>95	D(&)KAPETALDap(&)
Analogue 2	$C_{39}H_{66}N_{12}O_{13}$	911.03	911,0867	1,143	>95	Dap(&)KAPETALd(&)
Analogue 3	$C_{40}H_{68}N_{12}O_{13}$	925.06	925,4896	1,136	>95	Dab(&)KAPETALD(&)
Analogue 4	$C_{41}H_{70}N_{12}O_{13}$	939.08	939,5180	1,165	>95	Orn(&)KAPETALD(&)
Analogue 5	$C_{42}H_{72}N_{12}O_{13}$	953.10	953,5404	1,159	>95	K(&)KAPETALD(&)
Analogue 6	$C_{40}H_{68}N_{12}O_{13}$	925.06	925,5082	1,145	>95	Dap(&)KAPETALE(&)
Analogue 7	$C_{41}H_{70}N_{12}O_{13}$	939.08	939,5291	1,200	>95	Dap(&)KA(dmP)ETALD(&)
Conjugated 8	$C_{62}H_{79}N_{13}O_{20}$	1325.55	1325.651	1.380	>95	cF- Dap(&)KAPETALD(&)
Conjugated 9	$C_{62}H_{80}N_{12}O_{19}$	1297.39	1296.5652	1.384	>95	cF-Dap(&)KA(dmP)ETALD(&)
biotin-MiniAp-4*	$C_{49}H_{78}N_{16}O_{15}S$	1163.56	1163.5593	1.254	>98	Dap(&)KA*PETALD(&)
cyanine5-MiniAp-4*	$C_{82}H_{116}N_{20}O_{24}S_3^{2-}$	1862.17	1862.7809	1.244	>98	Dap(&)KA*PETALD(&)
Angiopep-2	$C_{104}H_{149}N_{29}O_{31}$	2301,51	2300.0932	1.185	>99	TFFYGGSRGKRNNFKEEY
Cys-Angiopep-2	$C_{107}H_{154}N_{30}O_{32}S$	2404.65	2403.1040	1.179	>98	CTFFYGGSRGKRNNFKEEY
Cys-ApoE	$C_{111}H_{215}N_{41}O_{20}S$	2476,27	2474.6762	1.225	>98	CLRKLRKRLLLRKLRKRLL
Cys-THRre	$C_{74}H_{104}N_{20}O_{16}S_2$	1593.89	1592.7443	1.305	>95	cpwvpswmpprht

Chromatogram

Spectrum

THR
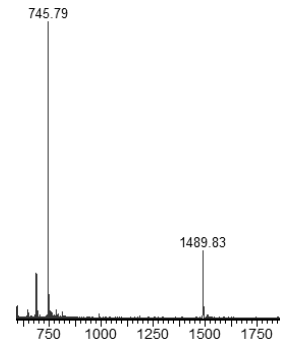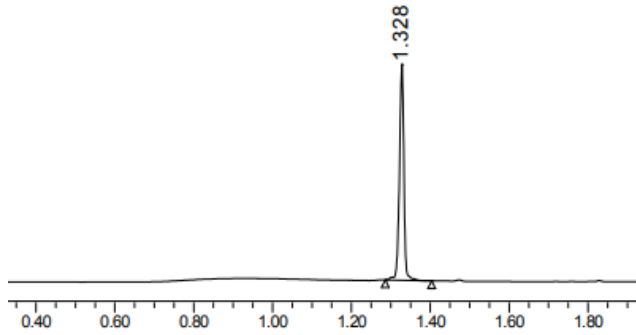
THRre
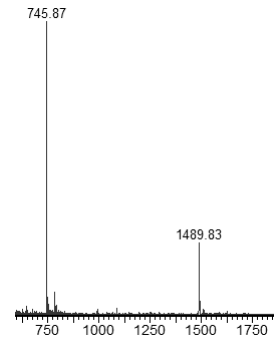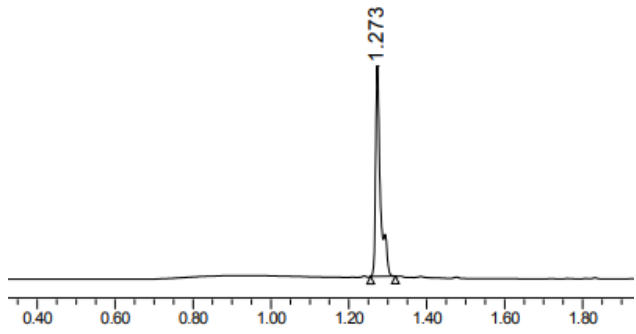
THRre-G-DRG1
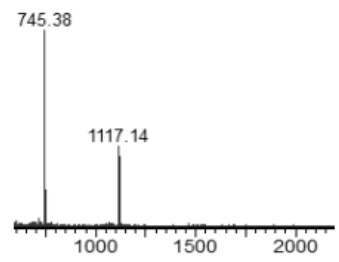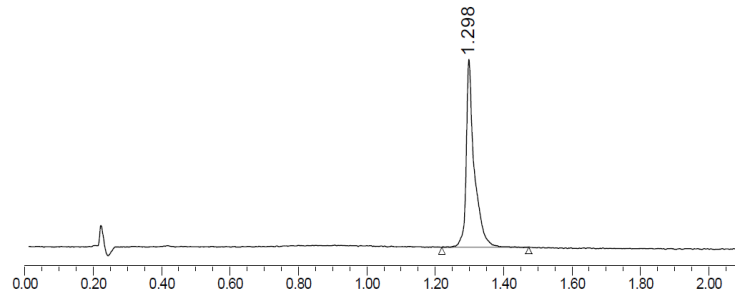
THRre-G-DRG2
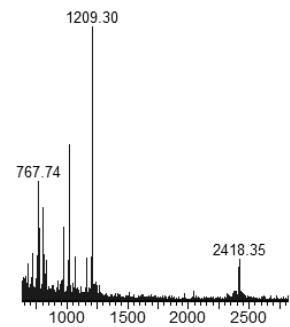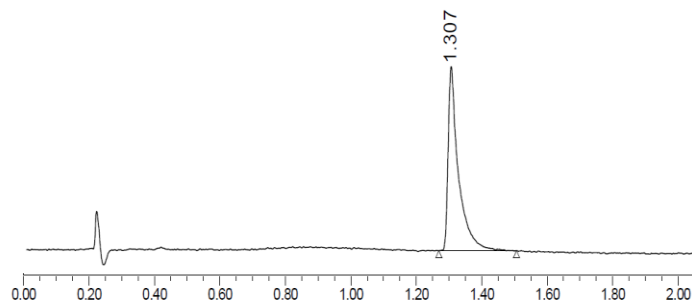
THRre-(PEG)₃-DRG2
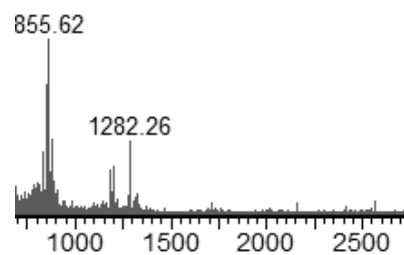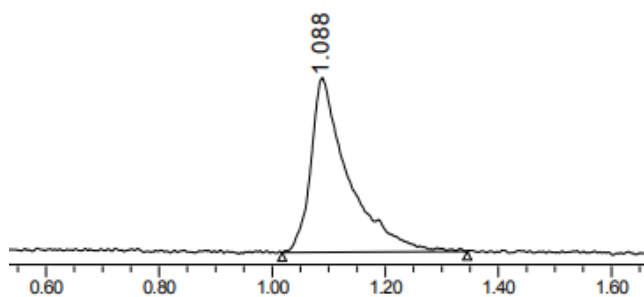
L-Dopa-THRre
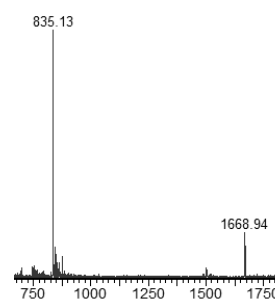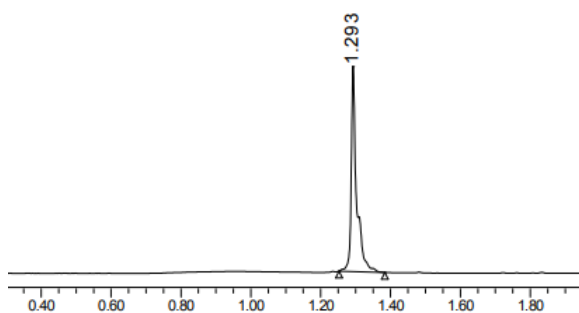
L-Dopa-(PEG)₃-THRre
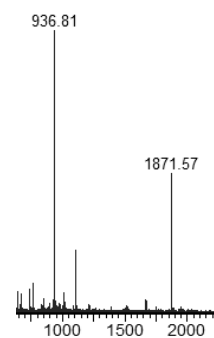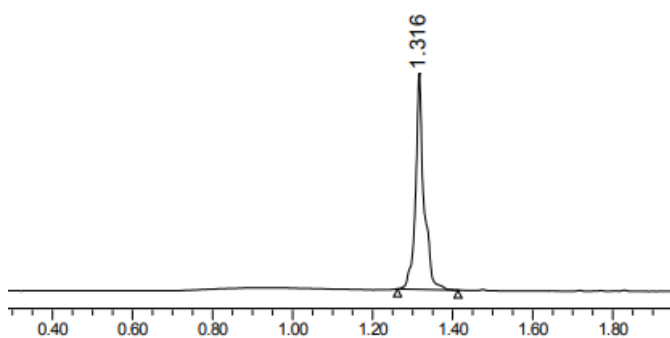
Fmoc-L-Dopa
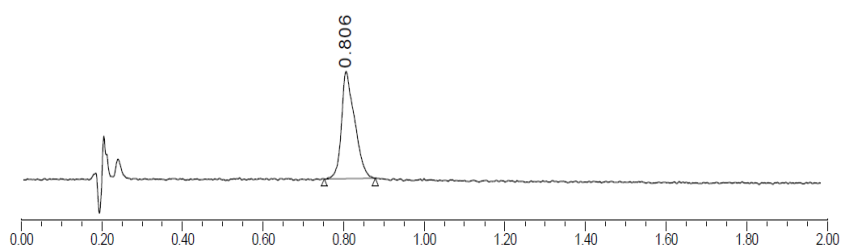
G-THRre
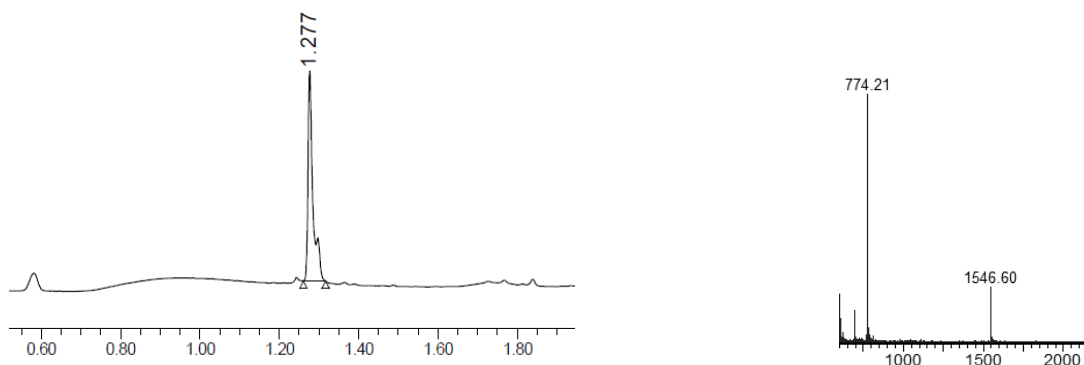
Cys-THRre
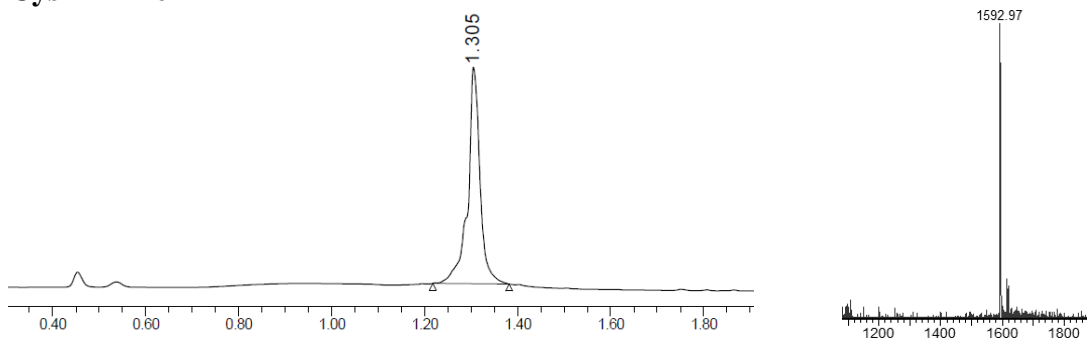
THR scrambled
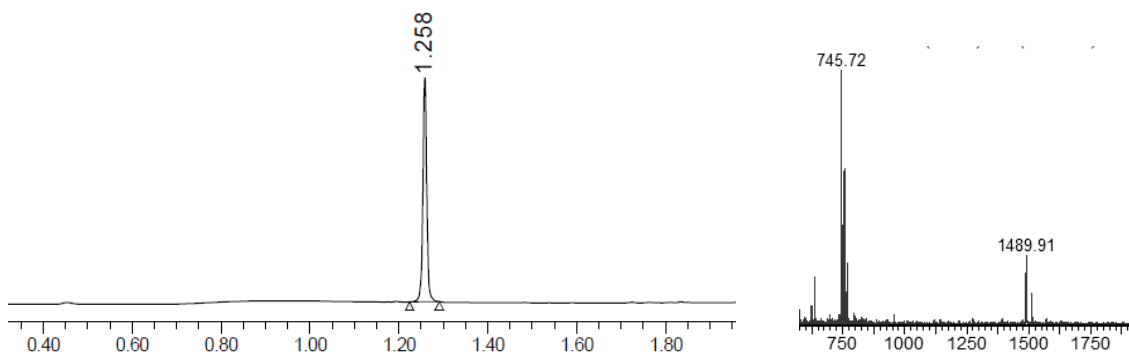
Biotin-THR(Bpa)-1
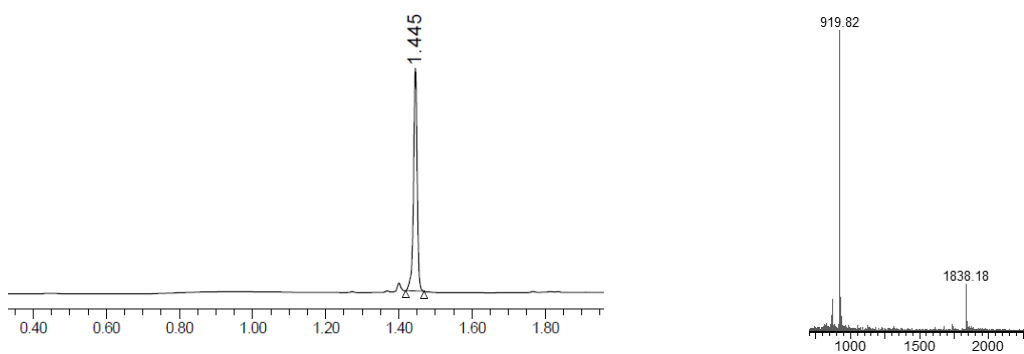
Biotin-THR(Bpa)-2
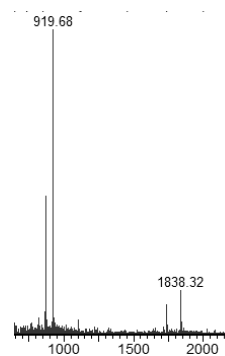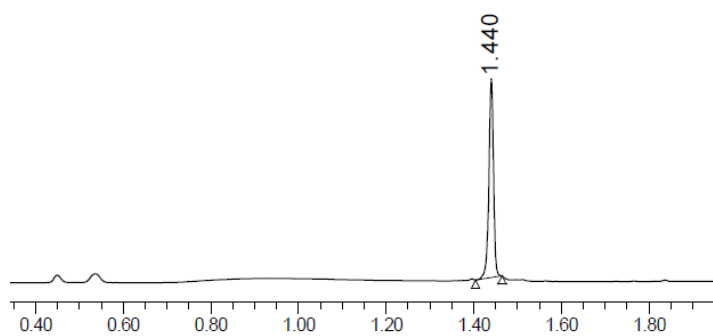
Biotin-THRre(Bpa)-1
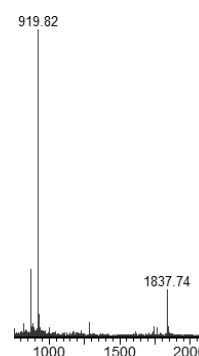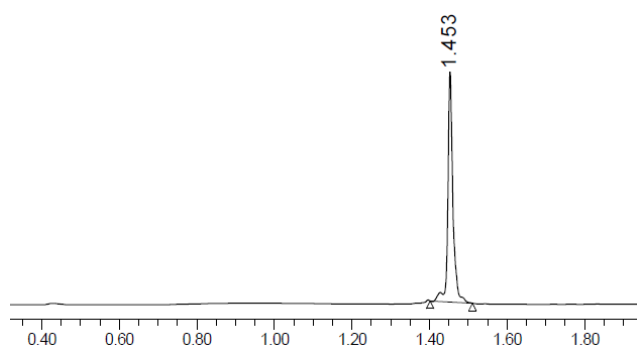
Biotin-THRre(Bpa)-2

MiniAp-4

152
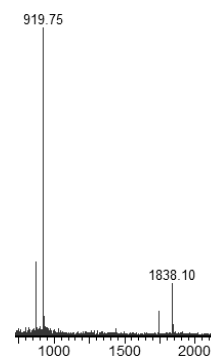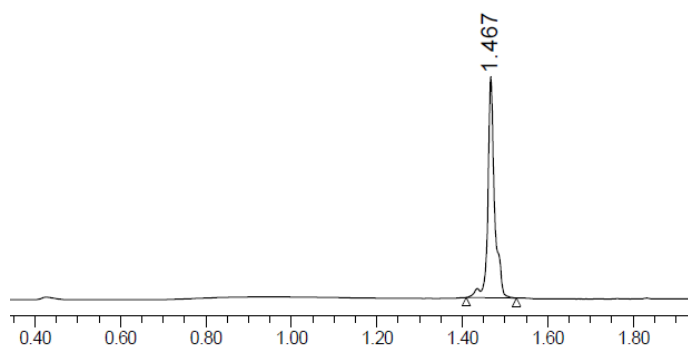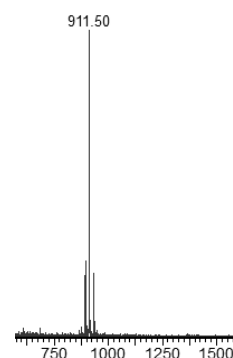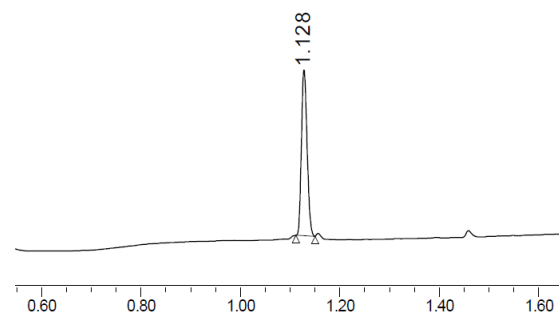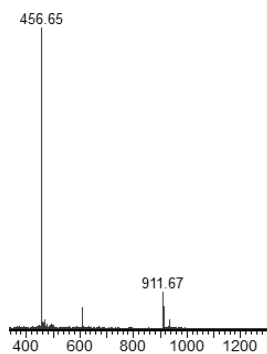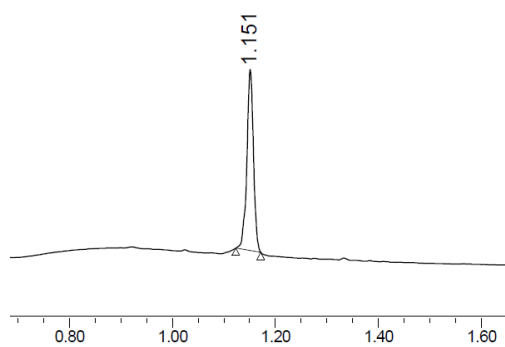
Analogue 1

Analogue 2
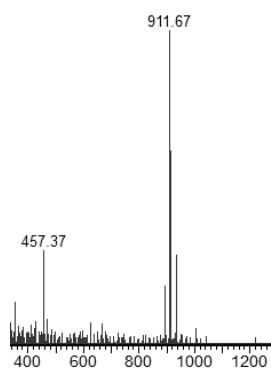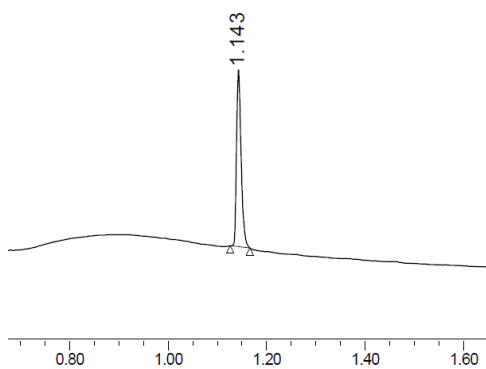
Analogue 3

Analogue 4

153
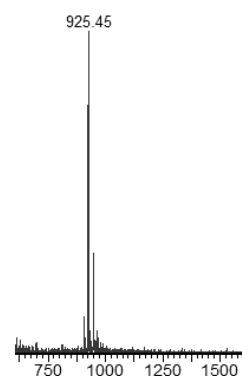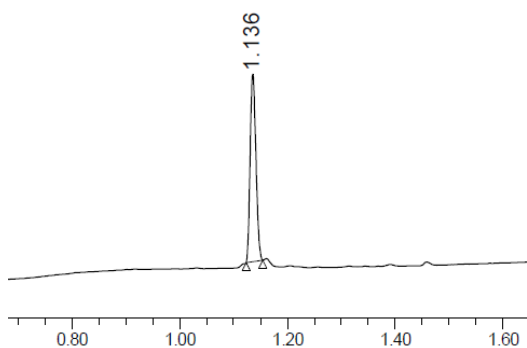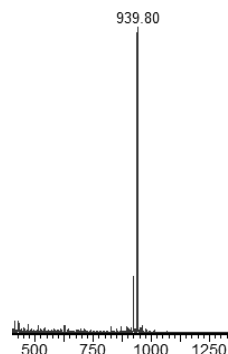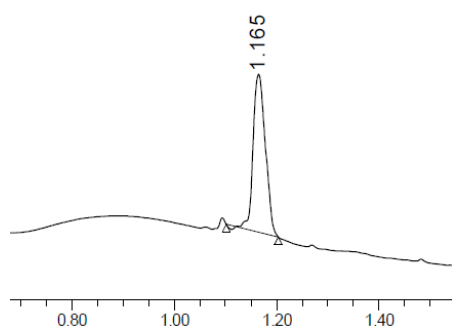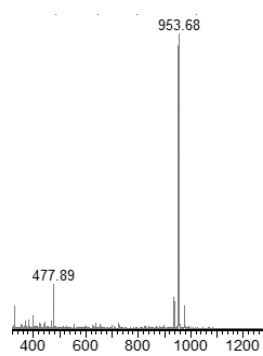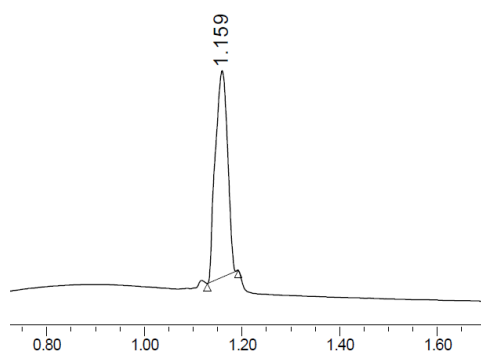
Analogue 5

Analogue 6
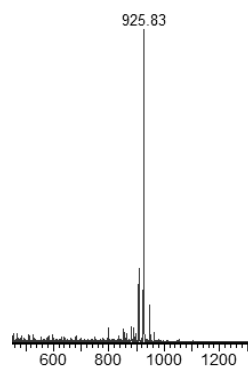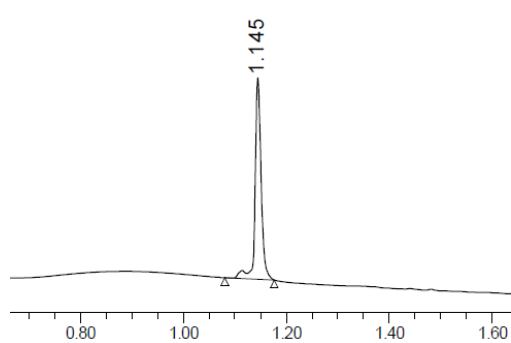
Analogue 7
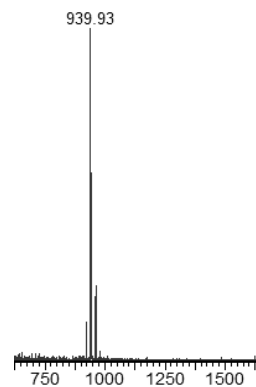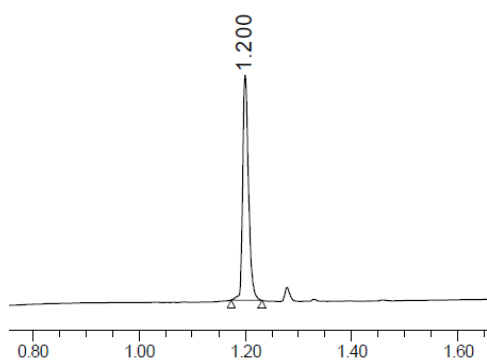
Conjugate 8
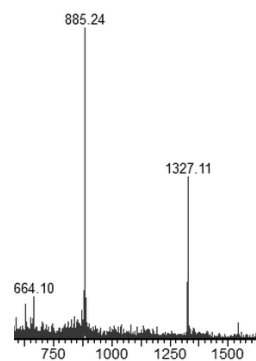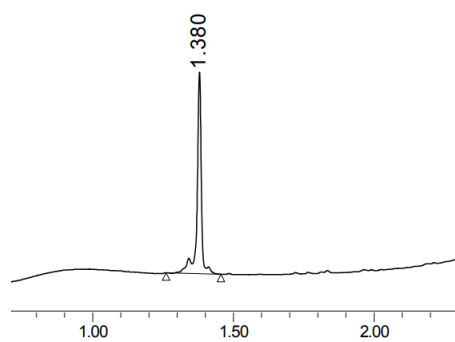
Conjugate 9
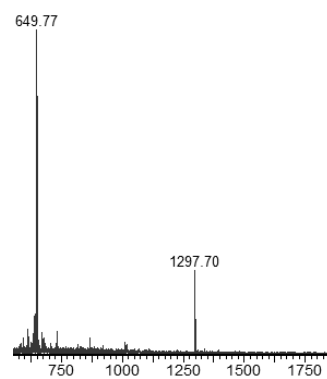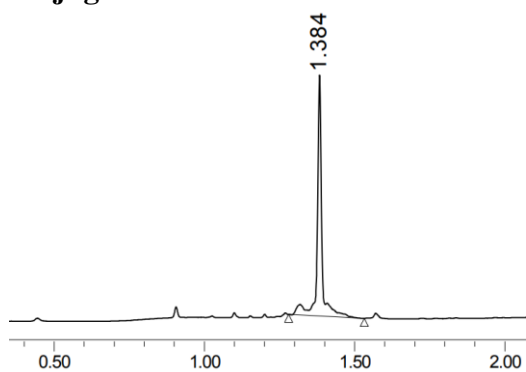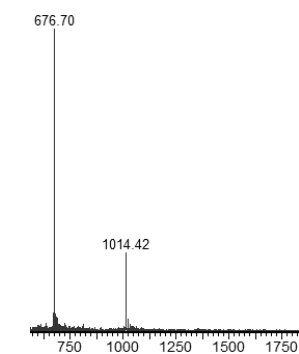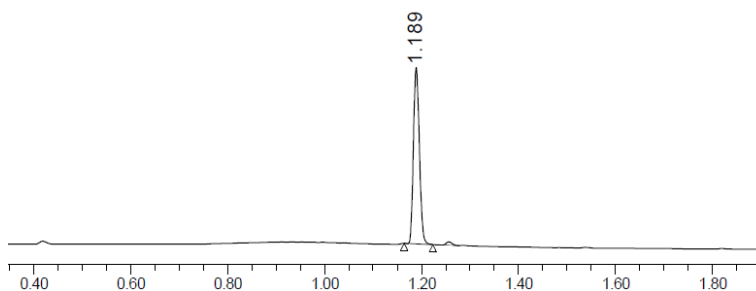

Cy5-MiniAp-4
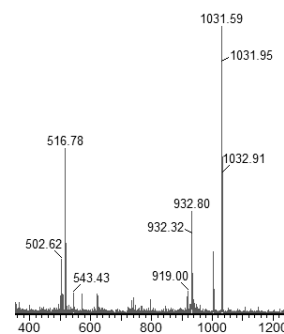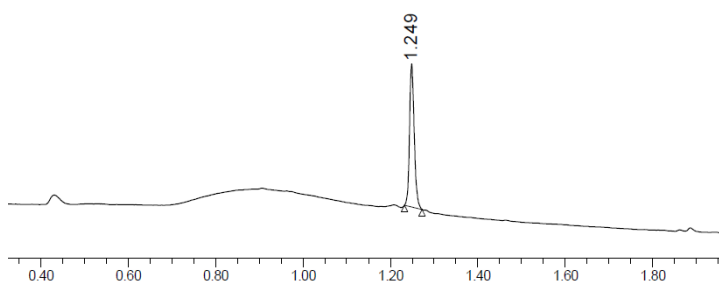
Biotin-photoMiniAp-4
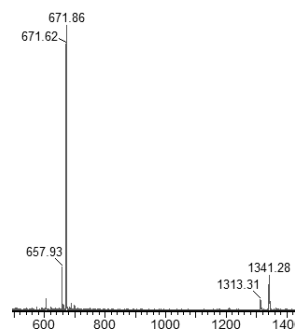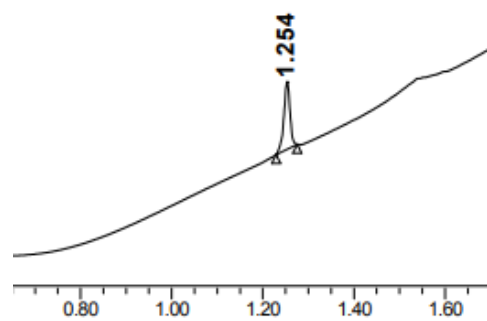
Cy5-PhotoMiniAp-4
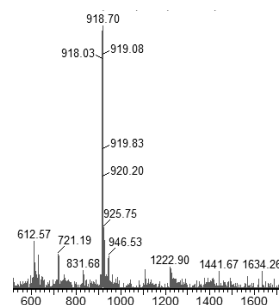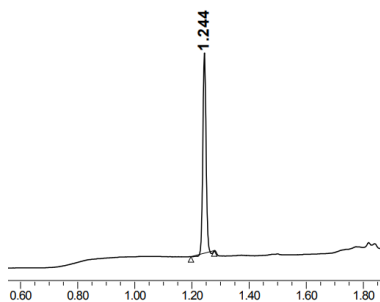
THRre(Heavy)
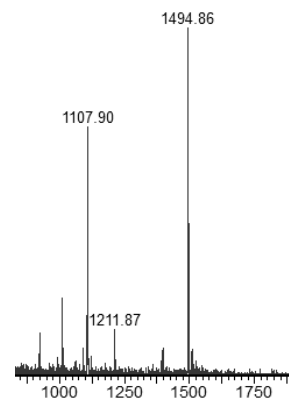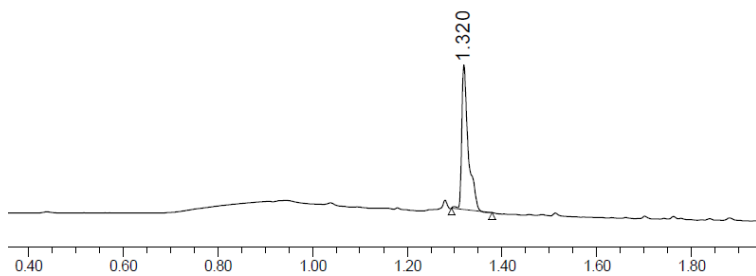
MiniAp-4(Heavy)
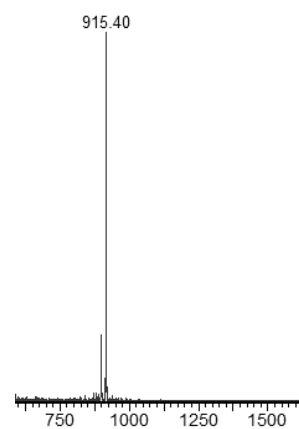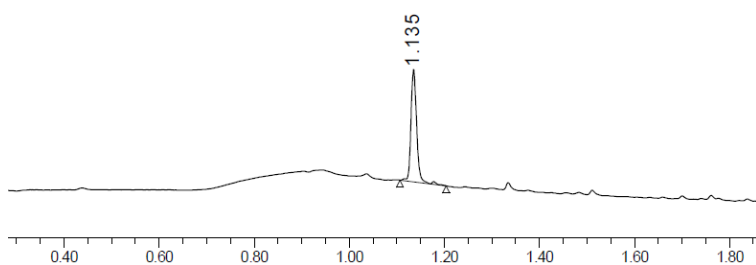
Cys-MiniAp-4

Cys-ApoE
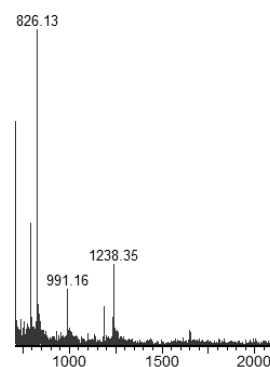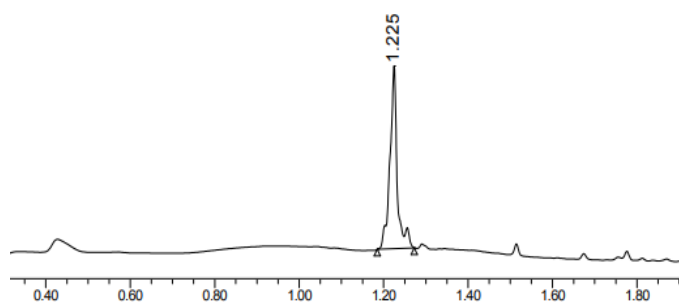
Cys-Angiopep-2
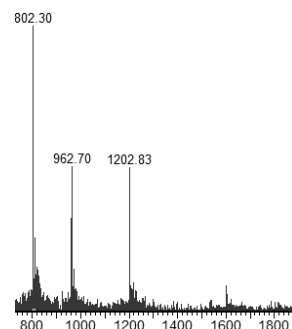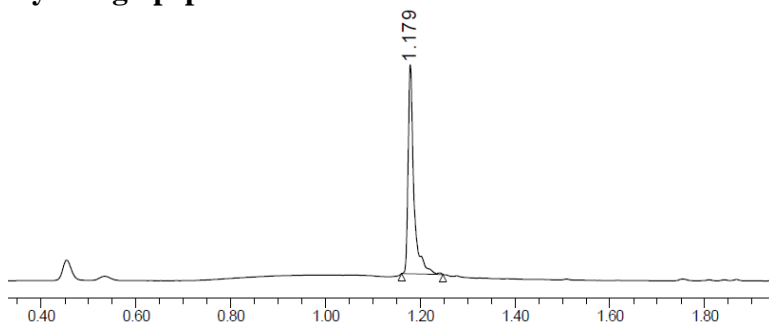
Angiopep-2
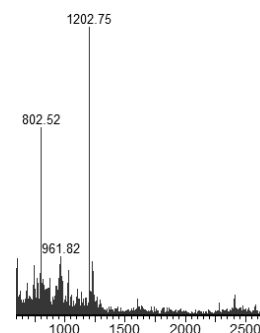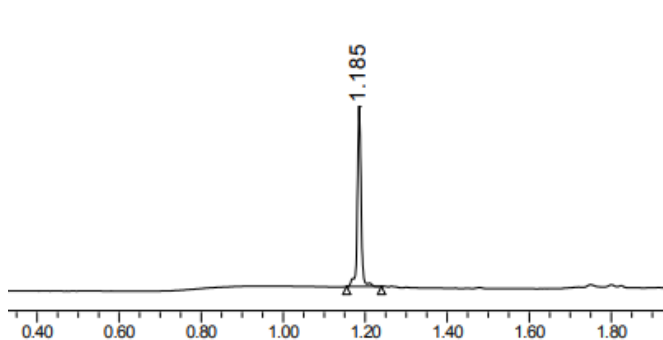
Compound 4

Compound 5

157
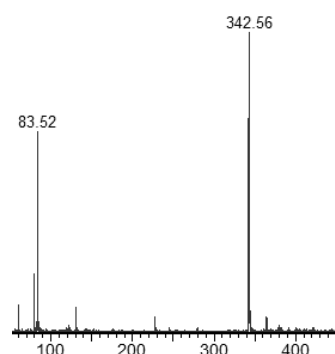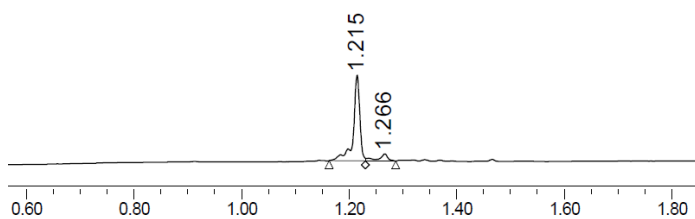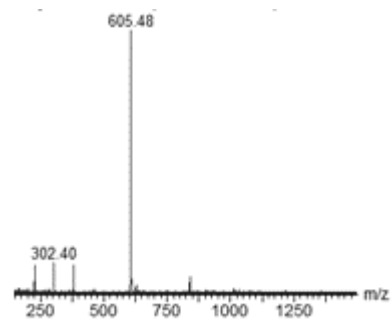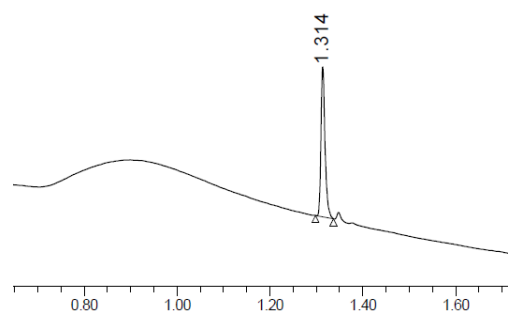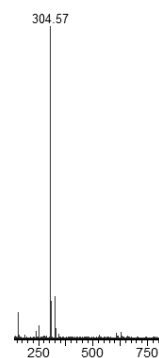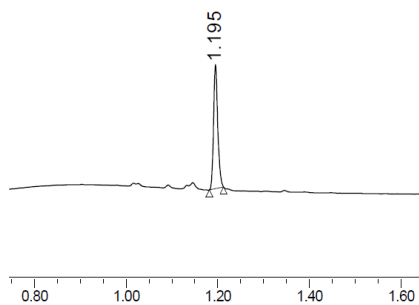
Compound 6

Compound 7
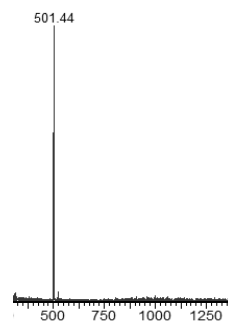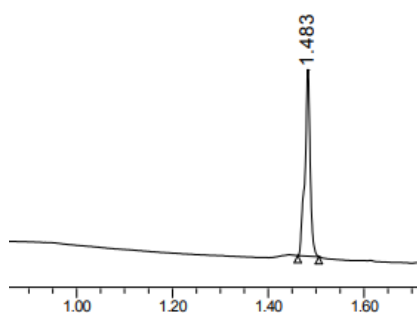
Compound 8
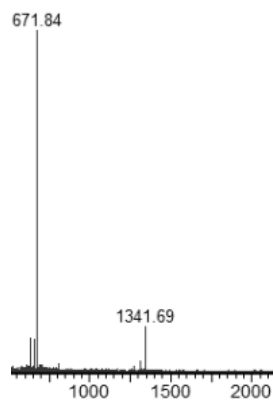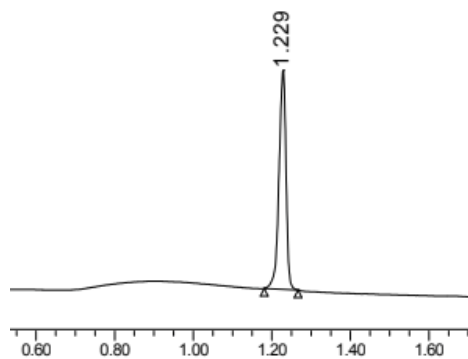
APPENDIX

2D homo-nuclear (TOCSY, ROESY) and hetero-nuclear (^{1}H ^{13}C HSQC) NMR experiments of all peptides of *Evaluation of proline cis-trans ratio as tool to fine-tune transport* section.

				Trans		
Residue	**Hα**	**Hβ**	**Cα**	**Cβ**	**NH**	**Others**
Lys2	4.34	1.94-1.59	55.07	32.54	8.89	Hγ= 1.46 Hδ= 1.69 Hε= 2.99 Cγ= 24.50 Cδ= 29.04 Cε= 42.07
Ala3	4.64	1.33	-	18.70	8.26	
Pro4	4.30	2.30-1.99	64.06	32.01	-	Hγ= 2.03 Hδ= 3.68 Cγ= 27.34 Cδ= 50.42
Glu5	4.40	2.42	54.94	33.46	8.09	Hγ= 2.23-2.05 Cγ=28.24
Thr6	4.19	4.29	62.22	70.09	8.07	Hγ= 1.20 Cγ=21.58
Ala7	4.32	1.36	51.51	17.36	8.59	
Leu8	4.31	1.67	55.26	41.94	7.74	Hγ= 1.51 Hδ= 0.92-0.86 Cγ= 27.04 Cδ=24.83-23.25
Dap9	4.41	3.76-3.52	55.53	42.85	8.13	

Table 18. ^{1}H-and ^{13}C-NMR chemical shifts (ppm) for analogue **1** (D(&)-KAPETAL-Dap(&)).
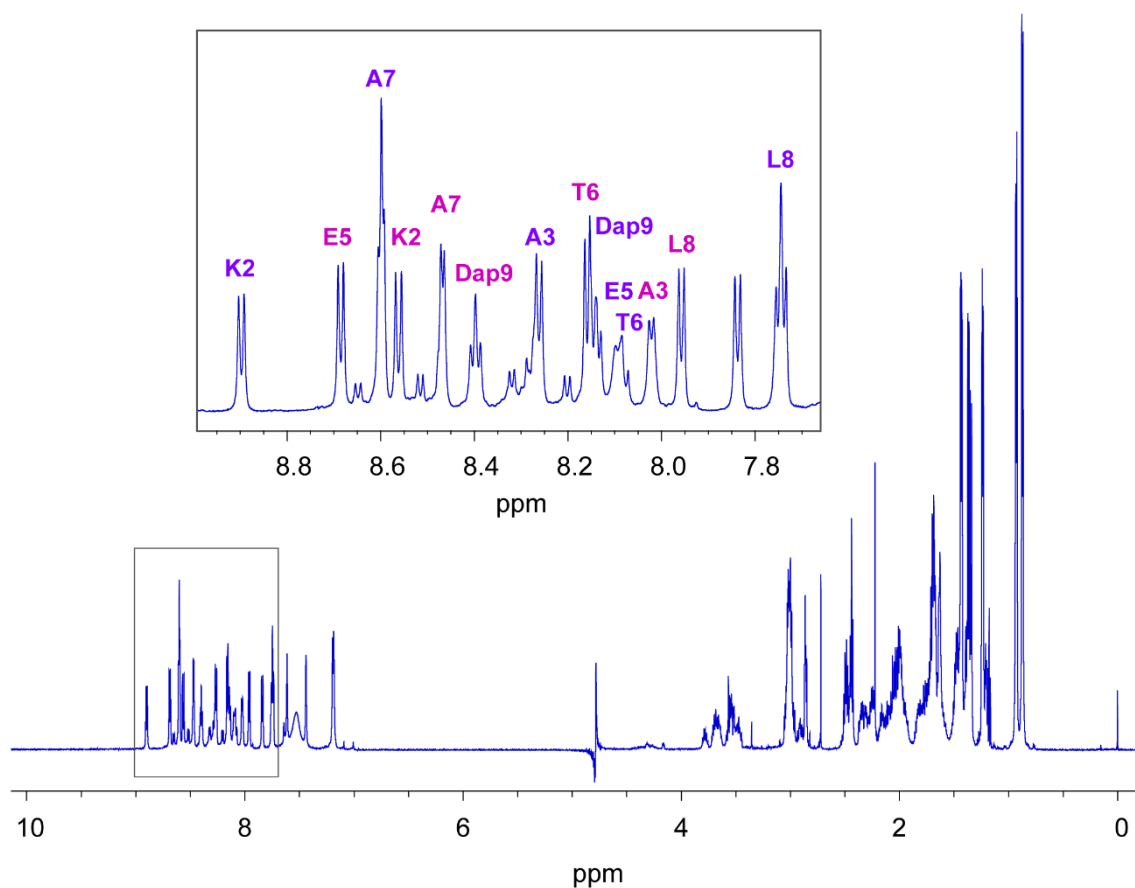
Figure 68. 1D ^{1}H-NMR spectra of analogue **1** at 298 K in aqueous solution. The NH amide resonances of the *trans* (purple) and *cis* (pink) conformers are labeled in the inset.

Figure 69. ^{1}H ^{13}C-HSQC NMR spectrum of analogue **1** in aqueous solution.

Figure 70. TOCSY contour map of the amidic region of analogue **1** in aqueous solution.

Figure 71. Selected regions of the ROESY spectrum of analogue **1** in aqueous solution.

			Trans			
Residue	**Hα**	**Hβ**	**Cα**	**Cβ**	**NH**	**Others**
Dap1	4.14	3.70-3.63	55.41	42.88	8.24	
Lys2	4.38	1.83-1.76	56.19	33.88	8.59	Hγ= 1.45 Hδ= 1.68 Hε= 3.00 Cγ= 24.39 Cδ= 29.07 Cε= 42.05
Ala3	4.37	1.34	50.93	18.17	8.36	
Pro4	4.40	2.31-1.95	64.01	31.90	-	Hγ= 1.95 Hδ= 3.75 Cγ= 27.41 Cδ= 50.56
Glu5	4.35	2.23-2.06	54.49	28.20	8.41	Hγ= 2.45 Cγ=33.49
Thr6	4.28	4.28	62.41	69.87	7.84	Hγ= 1.23 Cγ=21.73
Ala7	-	-	-	-	-	
Leu8	4.22	1.68	55.61	41.46	8.08	Hγ= 1.61 Hδ= 0.92-0.88 Cγ=27.03 Cδ=24.87-23.24
D-Asp9	4.64	2.84	53.29	39.40	7.87	
			Cis			
Residue	**Hα**	**Hβ**	**Cα**	**Cβ**	**NH**	**Others**
Dap1	4.14	3.70-3.63	55.41	42.88	8.24	
Lys2	4.31	1.88-1.76	57.16	32.78	8.81	Hγ= 1.43 Hδ= 1.68 Hε= 2.98 Cγ= 24.71 Cδ= 29.07

					Cε= 41.97
Ala3	4.71	1.38	-	18.85	8.18	
Pro4	4.63	2.30-2.24	63.10	33.87	-	Hγ= 1.82 Hδ= 3.54 Cγ= 24.60 Cδ= 50.16
Glu5	4.47	2.18-2.09	56.46	28.42	8.71	Hγ= 2.47 Cγ=33.49
Thr6	4.33	4.29	61.69	69.93	8.04	Hγ= 1.21 Cγ=21.72
Ala7	-	-	-	-	-	
Leu8	4.22	1.68	55.61	41.46	8.08	Hγ= 1.61 Hδ= 0.92-0.88 Cγ=27.03 Cδ=24.87-23.24
D-Asp9	4.61	2.91-2.72	53.26	39.06	7.99	

**Table 19.** ¹H-and ¹³C-NMR chemical shifts (ppm) for analogue **2** (Dap(&)KAPETALd(&)).
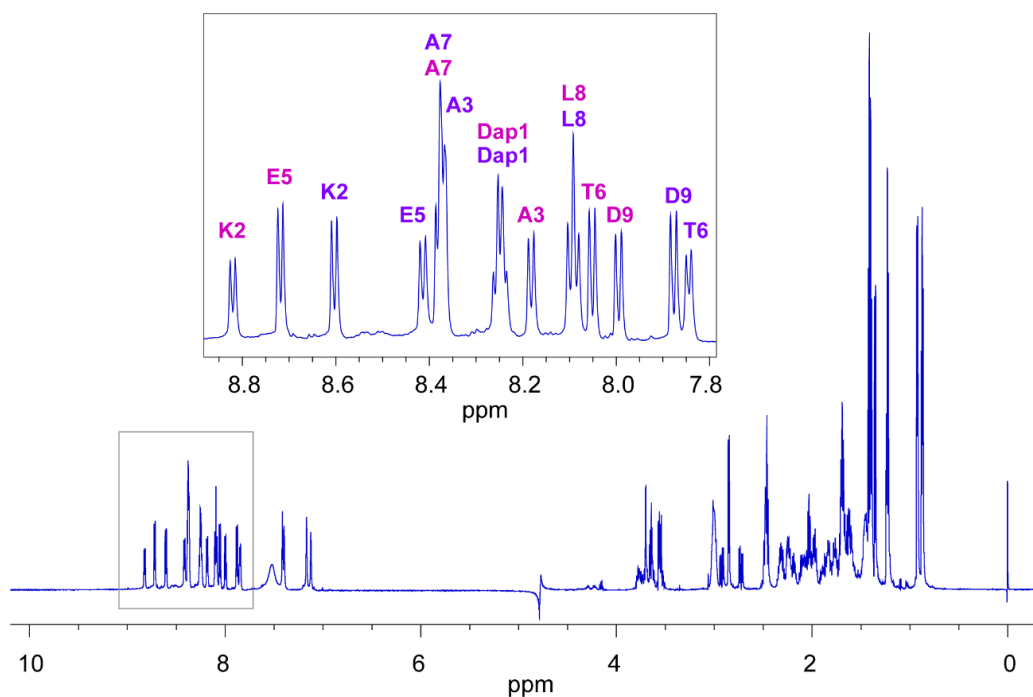
Figure 72. 1D ¹H-NMR spectra of analogue **2** at 298 K in aqueous solution. The NH amide resonances of the *trans* (purple) and *cis* (pink) conformers are labeled in the inset.
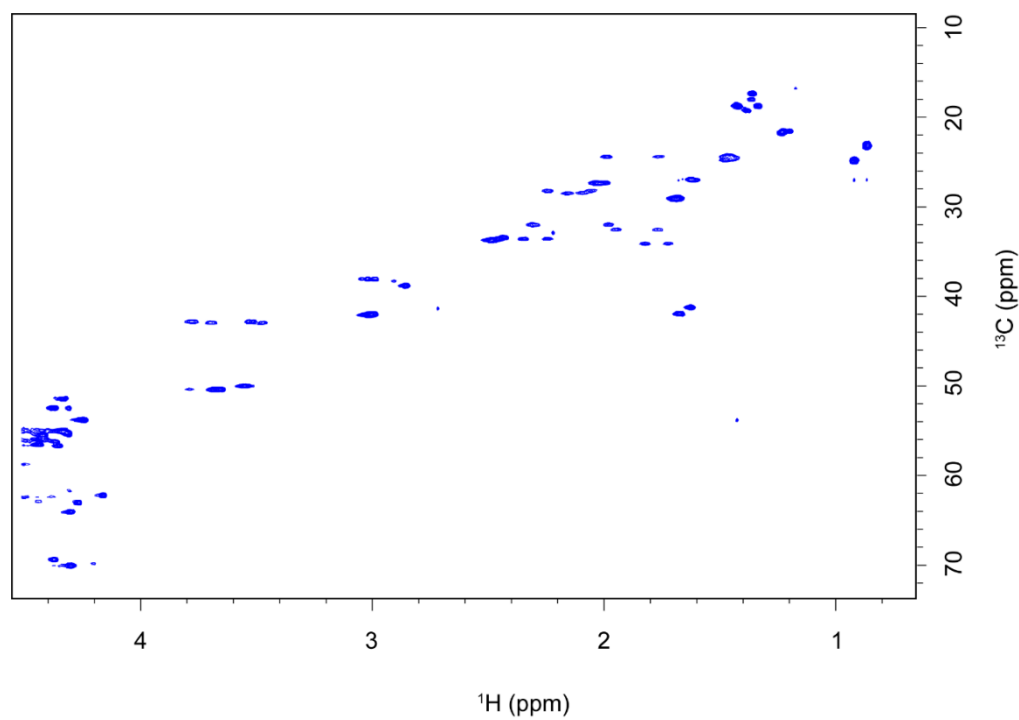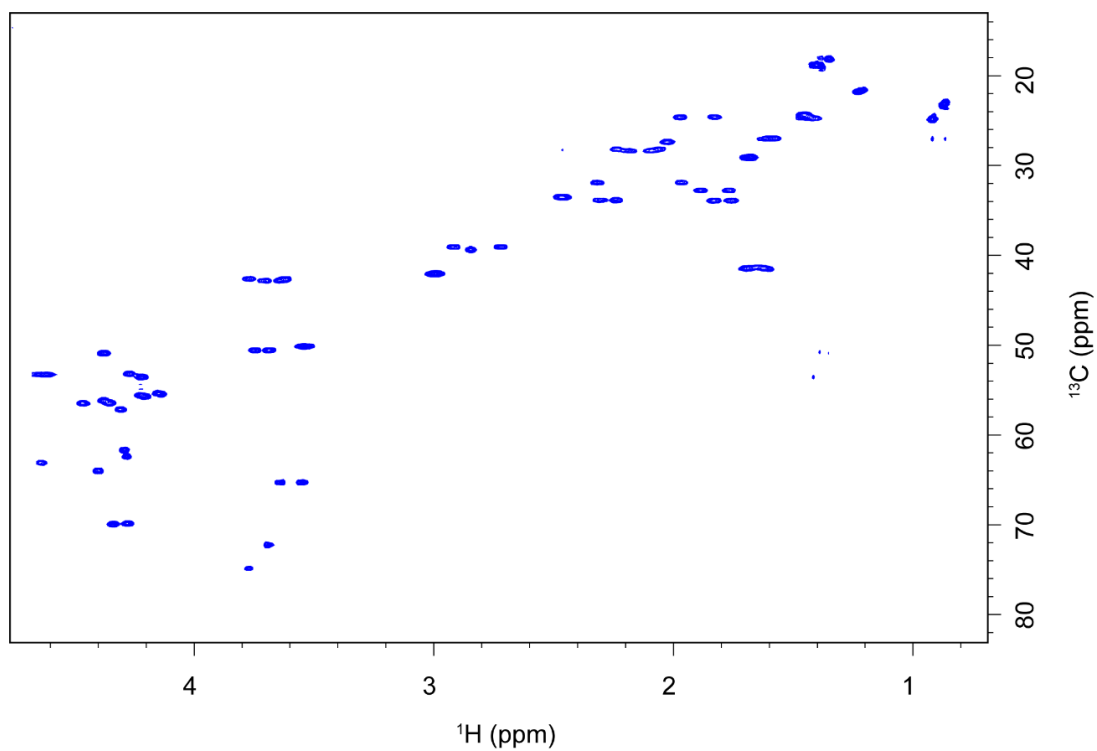
Figure 73. ^1H ^{13}C-HSQC NMR spectrum of analogue **2** in aqueous solution.
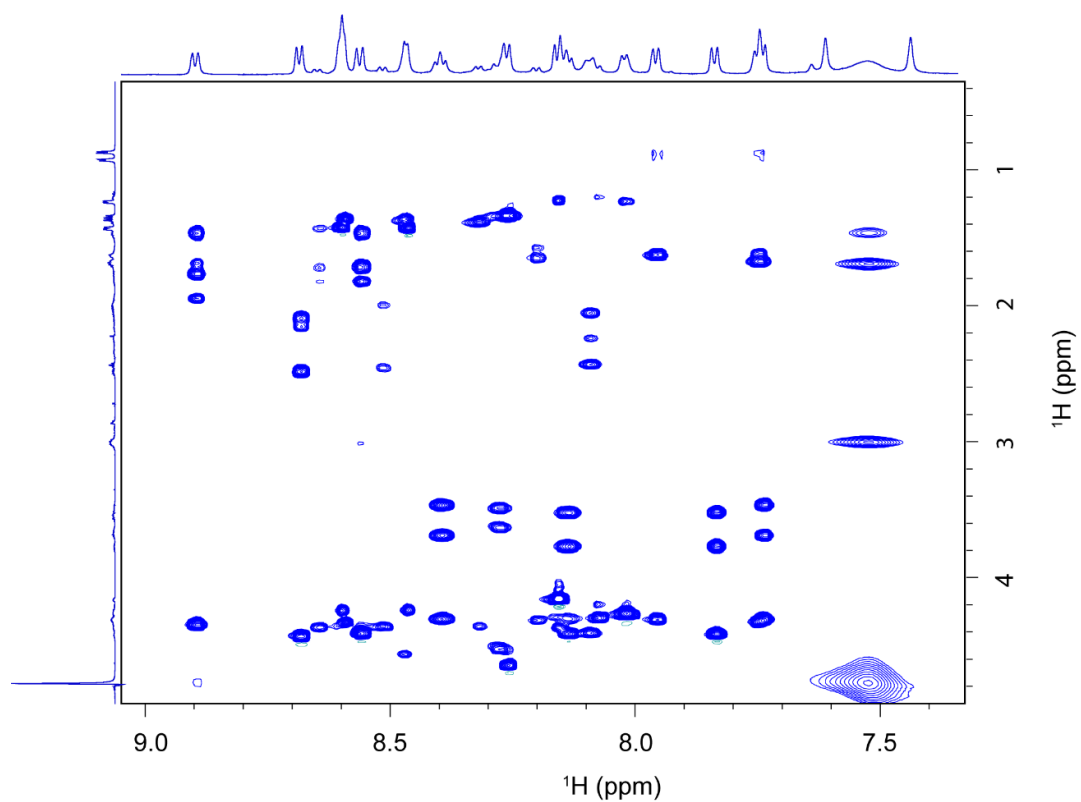

Figure 74. TOCSY contour map of the amidic region of analogue **2** in aqueous solution.
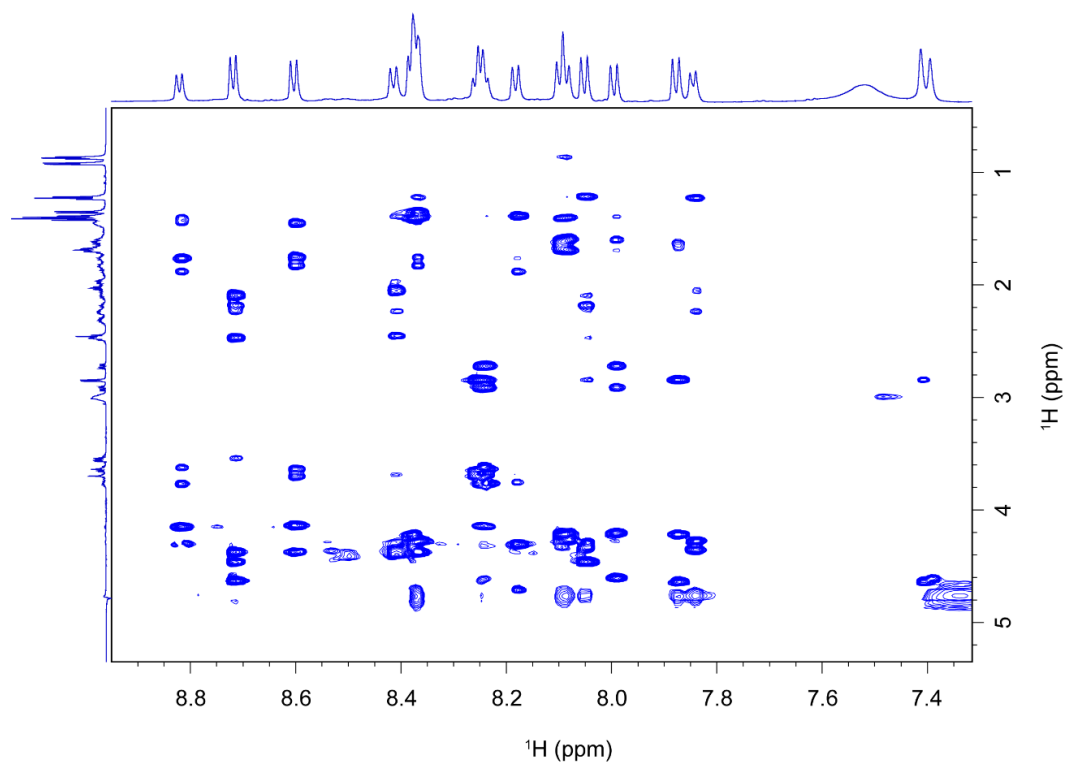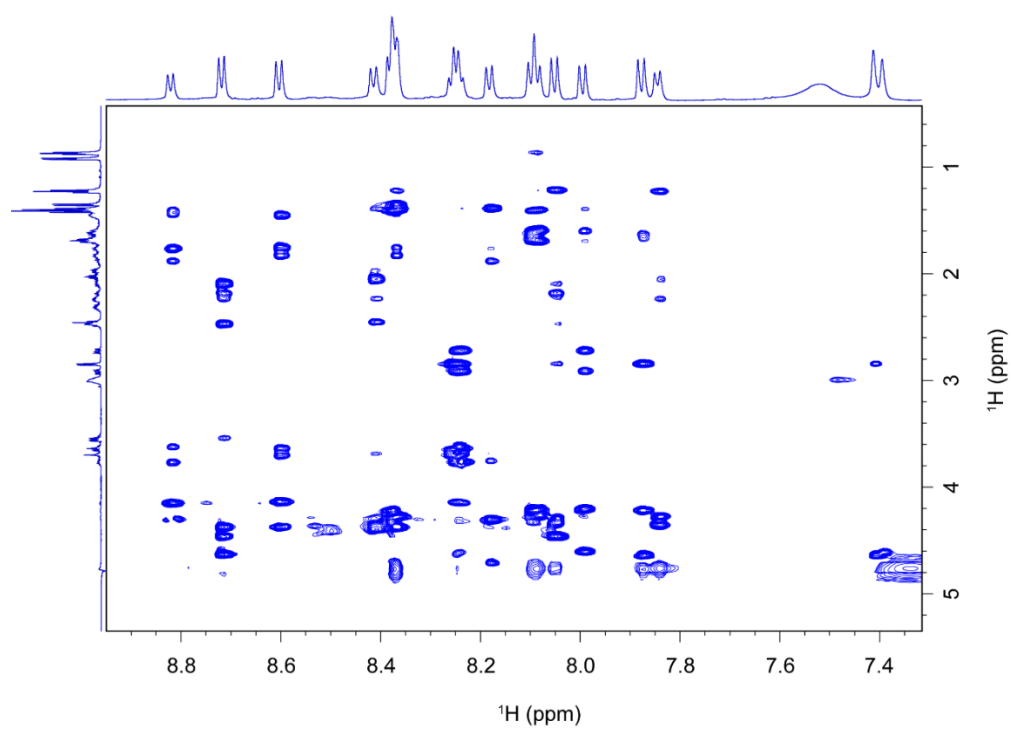
Figure 75. Selected regions of the ROESY spectrum of analogue **2** in aqueous solution.

			Trans			
Residue	Hα	Hβ	Cα	Cβ	NH	Others
Dab1	4.04	2.10	53.90	33.33	8.12	Hγ= 3.45-3.06 Cγ= 37.70
Lys2	4.32	1.88-1.80	55.19	33.21	8.86	Hγ= 1.48 Hδ= 1.69 Hε= 3.00 Cγ= 24.95 Cδ= 29.10 Cε= 42.07
Ala3	4.59	1.36	-	18.35	8.55	
Pro4	4.36	2.41-2.38	61.61	34.01	-	Hγ= 2.10-2.01 Hδ= 3.62 Cγ= 28.60 Cδ= 50.54
Glu5	4.36	2.09	57.23	28.64	8.72	Hγ= 2.42 Cγ=33.99
Thr6	4.37	4.36	64.14	70.18	8.04	Hγ= 1.20 Cγ=21.60
Ala7	4.20	1.43	53.96	18.68	8.33	
Leu8	4.31	1.62	55.17	41.44	7.97	Hδ= 0.92-0.89 Cδ=25.00-22.97
Asp9	4.65	2.85-2.78	-	39.49	7.78	

				Cis		
Residue	**Hα**	**Hβ**	**Cα**	**Cβ**	**NH**	**Others**
Dab1	4.01	2.02	53.85	33.79	8.24	Hγ= 3.47-3.25 Cγ= 38.70
Lys2	4.40	1.84-1.75	55.08	33.98	8.75	Hγ= 1.46 Hδ= 1.70 Hε= 3.10 Cγ= 24.47 Cδ= 29.08 Cε= 42.07
Ala3	4.39	1.35	50.65	18.35	8.35	
Pro4	4.62	2.31-2.23	-	33.88	-	Hγ= 1.96-1.86 Hδ= 3.56-3.52 Cγ= 24.60 Cδ= 50.13
Glu5	4.44	2.24-2.01	55.75	28.90	7.89	Hγ= 2.39 Cγ=33.92
Thr6	4.10	4.26	63.79	69.61	7.97	Hγ= 1.24 Cγ=21.73
Ala7	4.21	1.41	53.96	18.68	8.59	
Leu8	4.31	1.67	55.17	41.70	7.72	Hδ= 0.92-0.89 Cδ=25.00-22.97
Asp9	4.61	2.80	-	39.89	7.91	

Table 20. ^{1}H-and ^{13}C-NMR chemical shifts (ppm) for analogue **3** (Dab(&)KAPETALD(&)).

Figure 76. 1D ¹H-NMR spectra of analogue **3** at 298 K in aqueous solution. The NH amide resonances of the *trans* (purple) and *cis* (pink) conformers are labeled in the inset.

Figure 77. ¹H ¹³C-HSQC NMR spectrum of analogue **3** in aqueous solution.

Figure 78. TOCSY contour map of the amidic region of analogue **3** in aqueous solution.
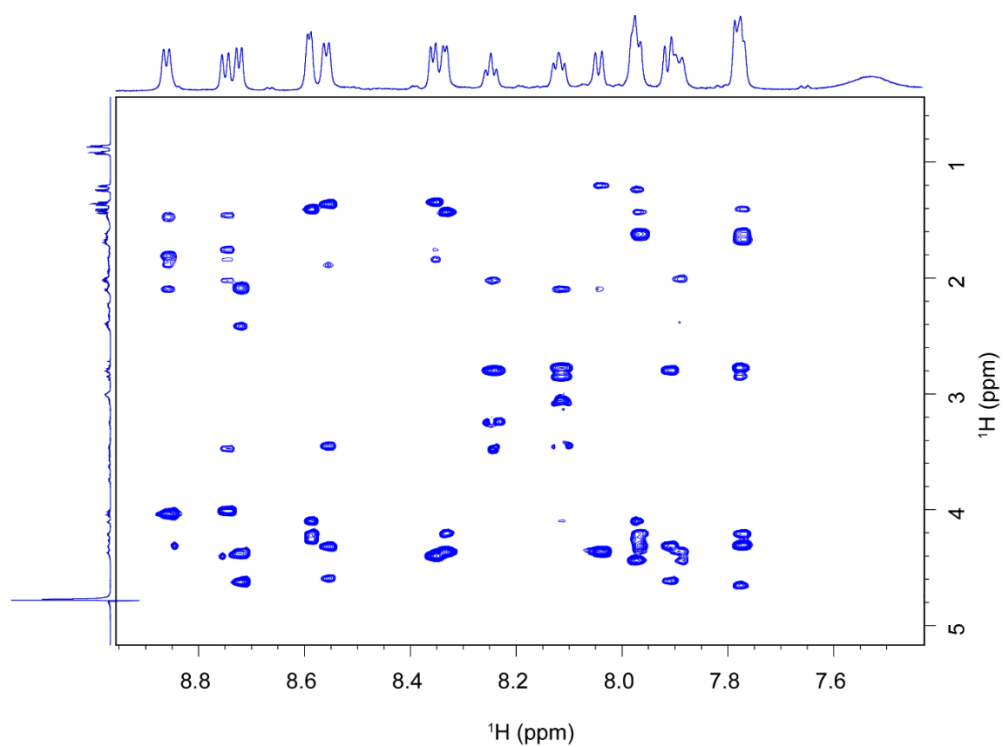
Figure 79. Selected regions of the ROESY spectrum of analogue **3** in aqueous solution.

Trans					
Residue	**Hα**	**Hβ**	**Cα**	**Cβ**	**NH**	**Others**
Lys2	4.32	1.68	56.81	29.11	8.75	Hγ= 1.44 Hδ= 1.89-1.76 Hε= 2.99 Cγ= 24.58 Cδ= 32.67 Cε= 42.05
Ala3	4.59	1.35	51.21	18.59	8.14	
Pro4	4.40	2.31-1.95	63.69	31.98	-	Hγ= 2.02 Hδ= 3.73-3.63 Cγ= 27.39 Cδ= 50.4

Cis					
Residue	**Hα**	**Hβ**	**Cα**	**Cβ**	**NH**	**Others**
Pro4	4.60	2.31-2.19	62.59	34.03	-	Hγ= 1.95-1.87 Hδ= 3.58-3.51 Cγ= 24.59 Cδ= 50.27

**Table 21.** ^{1}H-and ^{13}C-NMR chemical shifts (ppm) for analogue **4** (Orn(&)KAPETALD(&)).
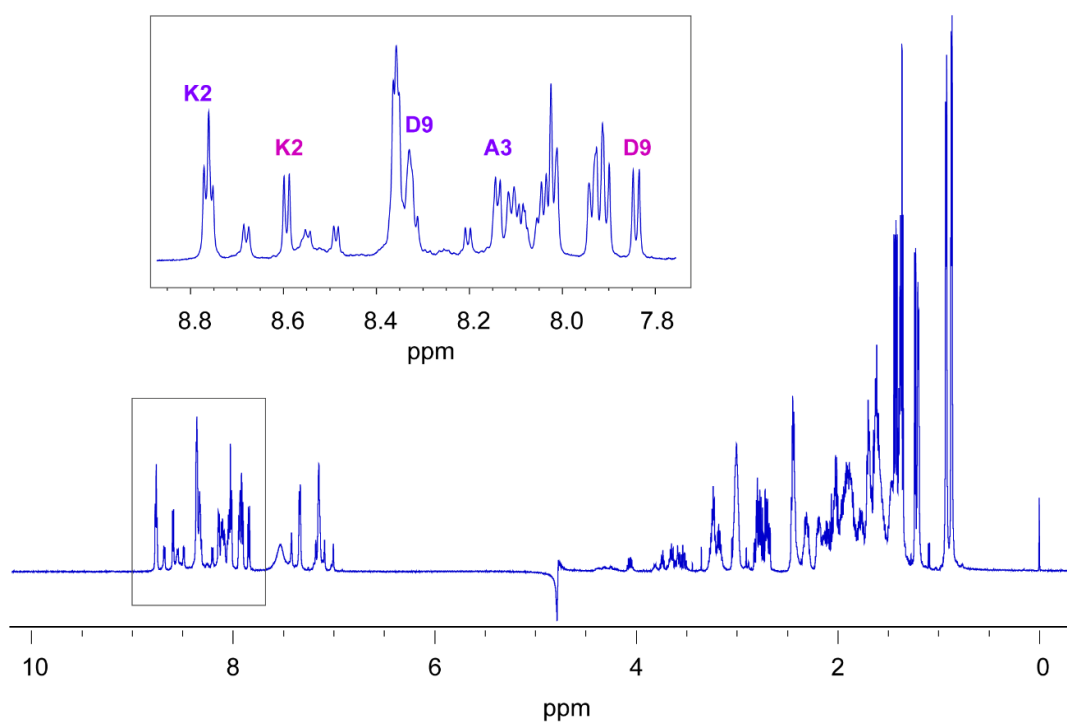
Figure 80. 1D ^{1}H-NMR spectra of analogue **4** at 298 K in aqueous solution. The NH amide resonances of the *trans* (purple) and *cis* (pink) conformers are labeled in the inset. Quantification of the *cis/trans* population ratio was based on the integration of the Leu methyl protons (0.86 and 0.92 ppm), due to the signal overlap in the amide region which prevent the integration of equivalent amide NH signals in both species

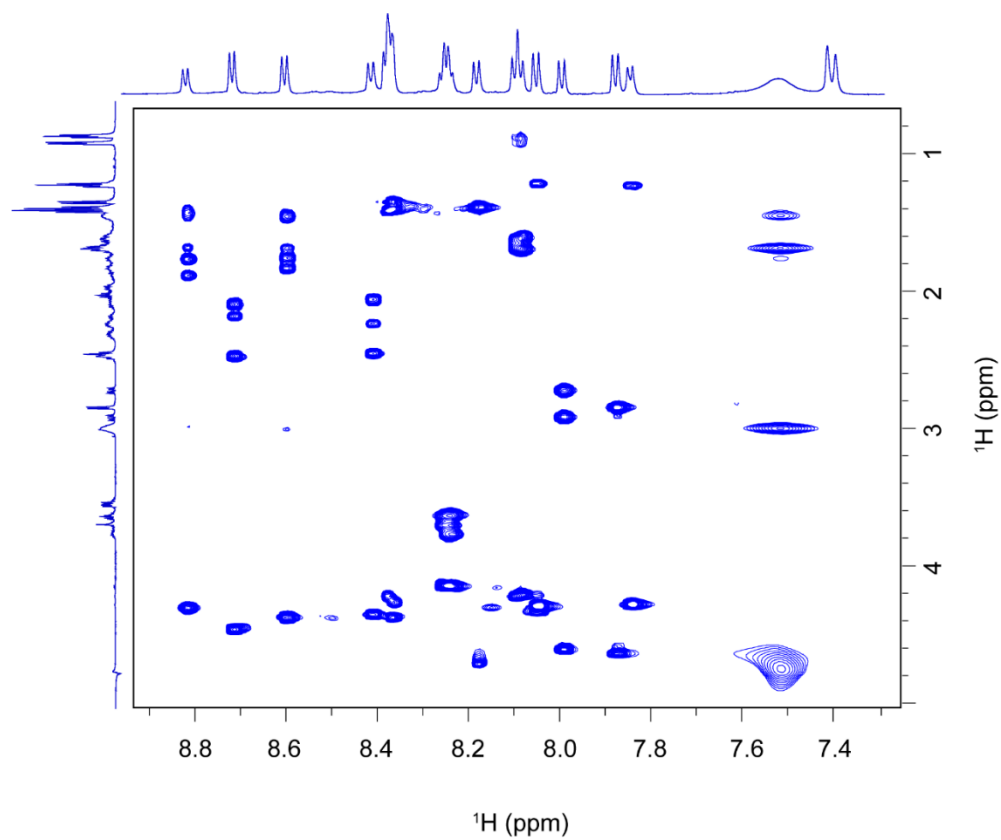**Figure 81.** ^{1}H ^{13}C-HSQC NMR spectrum of analogue **4** in aqueous solution.

**Figure 82.** TOCSY contour map of the amidic region of analogue **4** in aqueous solution.
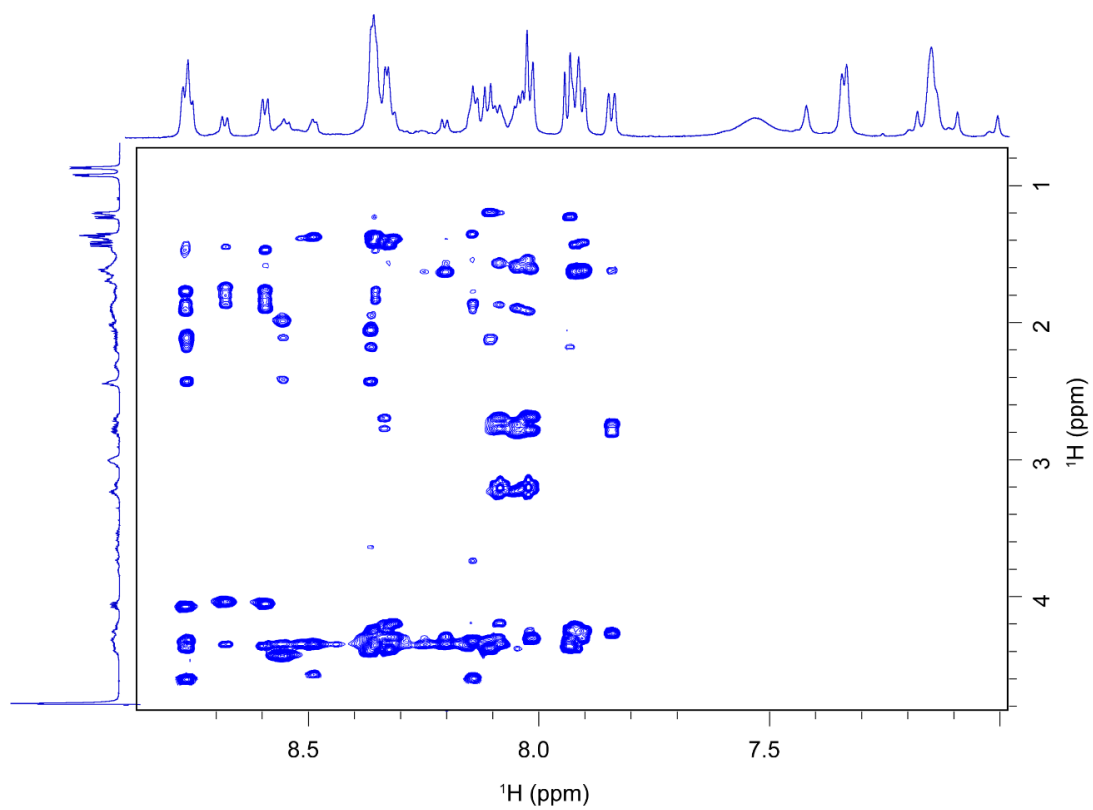
Figure 83. Selected regions of the ROESY spectrum of analogue **4** in aqueous solution.

			Trans			
Residue	**Hα**	**Hβ**	**Cα**	**Cβ**	**NH**	**Others**
Lys2	4.36	1.86-1.75	56.54	32.80	8.73	Hγ= 1.43 Hδ= 1.69 Hε= 2.98 Cγ= 24.79 Cδ= 29.11 Cε= 42.04
Ala3	4.55	1.38	51.66	18.42	8.16	
Pro4	4.40	2.31-1.91	61.61	31.90	-	Hγ= 2.02 Hδ= 3.61-3.77 Cγ= 27.57 Cδ= 50.47
Glu5	4.36	2.18-2.07	57.23	28.79	8.34	Hγ= 2.48 Cγ=33.62
Thr6	4.24	4.33	62.83	69.91	7.98	Hγ= 1.22 Cγ=21.70
Ala7	4.23	1.42	53.56	18.83	8.28	
Leu8	4.31	1.63	55.42	42.11	7.87	Hγ= 1.63 Hδ= 0.92-0.89 Cγ=27.01 Cδ=24.91-23.14
Asp9	4.67	2.76	53.43	39.62	7.94	

			Cis			
Residue	**Hα**	**Hβ**	**Cα**	**Cβ**	**NH**	**Others**
Lys2	4.40	1.74	56.55	32.80	8.55	Hγ= 1.45 Hδ= 1.84 Hε= 3.01 Cγ= 24.38

					Cδ= 33.74
					Cε= 42.04
Ala3	4.33	1.36	50.95	18.07	8.38
					Hγ= 1.96-1.83
					Hδ= 3.58-3.51
Pro4	4.62	2.30-2.23	-	34.04	-	Cγ= 24.47
					Cδ= 50.16
Glu5	4.35	2.13	57.28	28.51	8.70	Hγ= 2.47
					Cγ=33.62
Thr6	4.30	4.38	61.80	69.87	8.07	Hγ= 1.18
					Cγ=21.74
Ala7	4.26	1.43	53.54	18.83	8.21
					Hγ= 1.63
					Hδ= 0.92-0.89
Leu8	4.29	1.63	55.43	42.11	7.92	Cγ=27.01
					Cδ=24.91-23.14
Asp9	4.64	2.78	55.43	39.62	7.89

Table 22. ^{1}H-and ^{13}C-NMR chemical shifts (ppm) for analogue **5** (K(&)KAPETALD(&)).
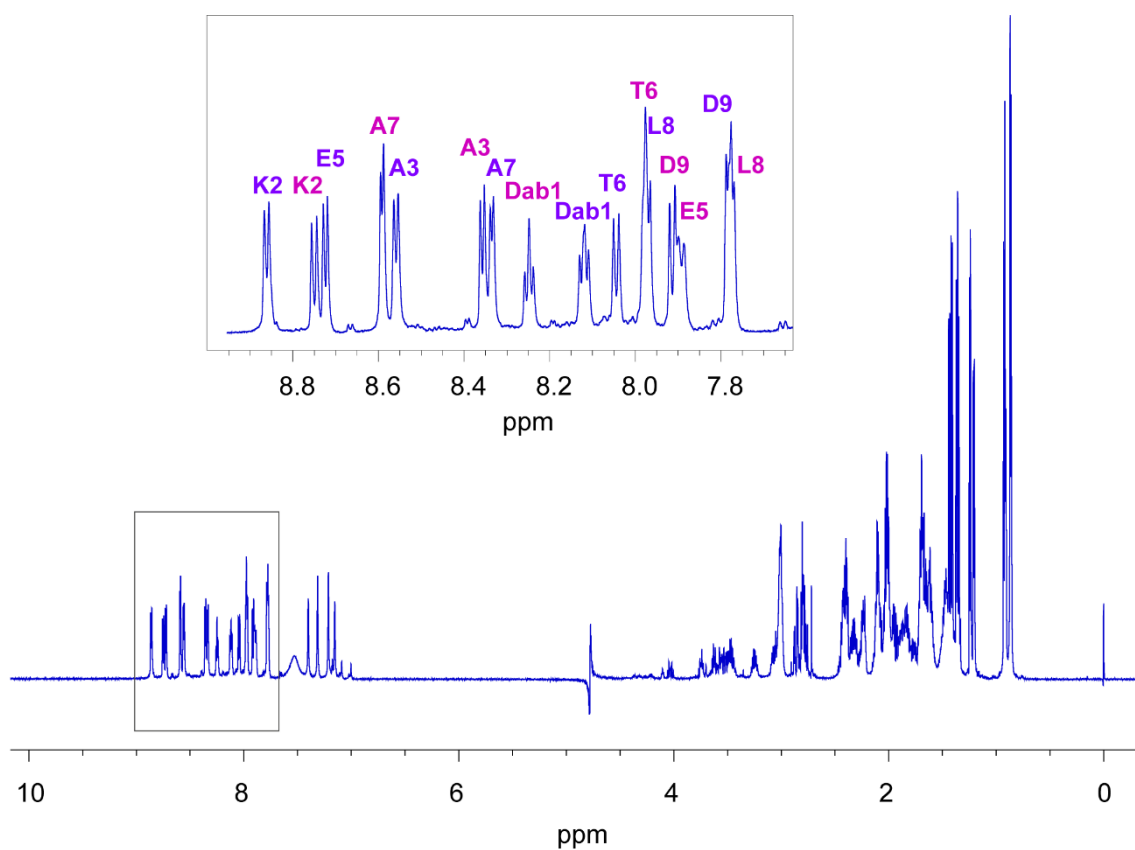
Figure 84. 1D ^{1}H-NMR spectra of analogue **5** at 298 K in aqueous solution. The NH amide resonances of the *trans* (purple) and *cis* (pink) conformers are labeled in the inset.
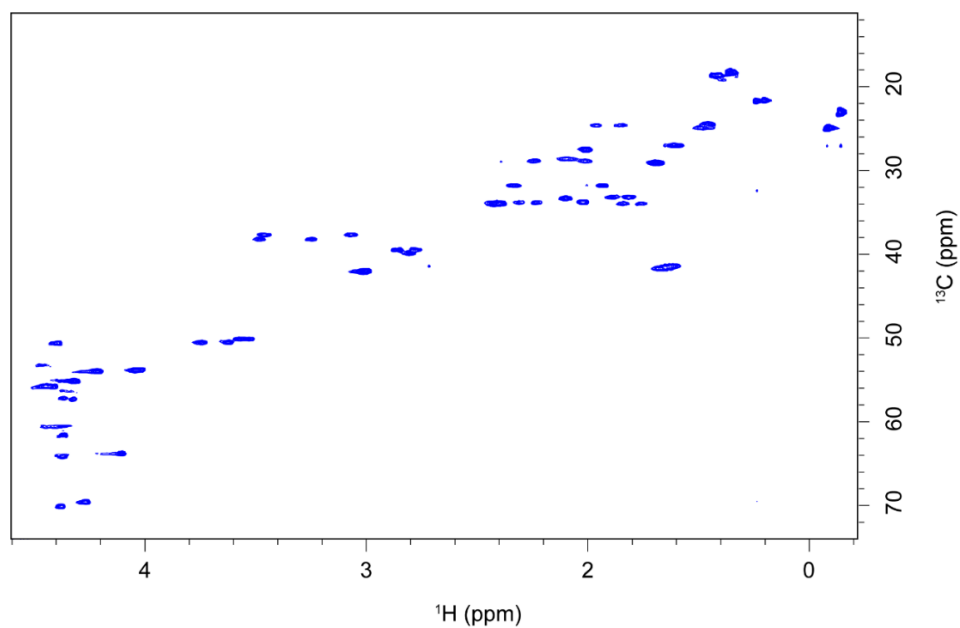

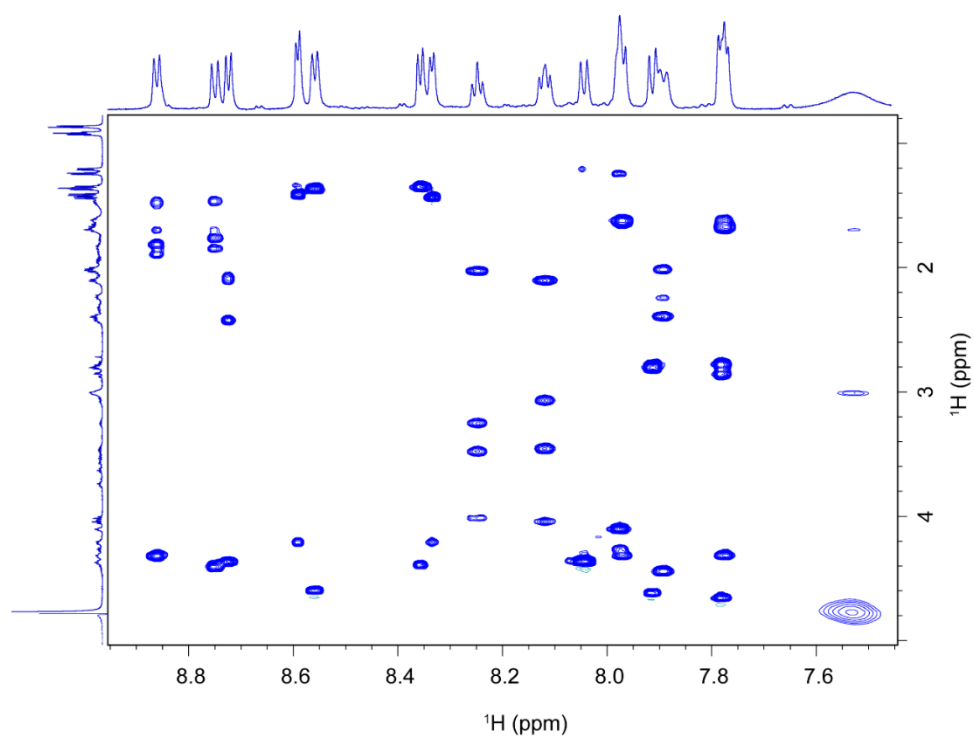**Figure 85.** ^{1}H ^{13}C-HSQC NMR spectrum of analogue **5** in aqueous solution.

**Figure 86.** TOCSY contour map of the amidic region of analogue **5** in aqueous solution.
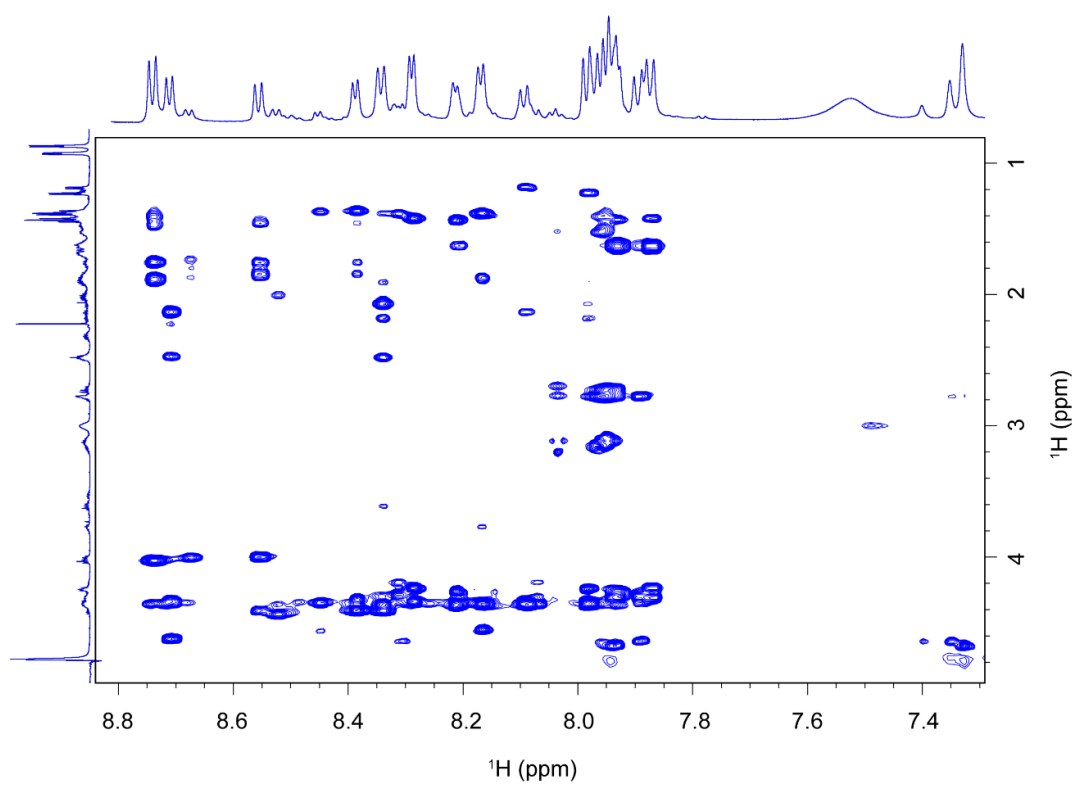
Figure 87. Selected regions of the ROESY spectrum of analogue **5** in aqueous solution.

					Trans	
Residue	**Hα**	**Hβ**	**Cα**	**Cβ**	**NH**	**Others**
Lys2	4.33	1.88-1.74	56.79	32.86	8.83	Hγ= 1.41 Hδ= 1.68 Hε= 2.98 Cγ= 24.69 Cδ= 29.10 Cε= 42.08
Ala3	4.63	1.38	50.60	18.62	8.27	
Pro4	4.41	2.30-1.96	63.79	31.86		Hγ= 2.02-1.96 Hδ= 3.79-3.67 Cγ= 27.36 Cδ= 50.52
Glu5	4.39	2.13	56.97	28.42	8.68	Hγ= 2.47 Cγ=33.66
Thr6	4.31	4.36	61.60	69.94	8.15	Hγ= 1.20 Cγ=21.60
Ala7	4.24	1.42	53.53	18.98	8.29	
Leu8	4.33	1.69	55.42	41.66	7.83	Hγ= 1.64 Hδ= 0.92-0.88 Cγ= 27.04 Cδ=24.83-23.28
Glu9	4.25	2.14-2.00	55.45	28.65	8.02	Hγ= 2.39 Cγ= 33.53

				Cis		
Residue	**Hα**	**Hβ**	**Cα**	**Cβ**	**NH**	**Others**
Lys2	4.40	1.85-1.75	55.93	32.86	8.64	Hγ= 1. 45 Hδ= 1.70 Hε= 3.03 Cγ= 23.31 Cδ= 29.10 Cε= 42.06
Ala3	4.32	1.35	51.04	18.91	8.42	
Pro4	4.61	2.25	63.79	33.86		Hγ= 1.96-1.82 Hδ= 3.55 Cγ= 24.50 Cδ= 50.52
Glu5	-	2.45-2.20	-	28.68	8.07	Hγ= 2.04 Cγ=33.66
Thr6	4.40	4.23-4.16	56.92	69.39	8.06	Hγ= 1.22 Cγ=21.75
Ala7	4.27	1.40	53.33	19.09	8.39	
Leu8	4.28	1.66	55.42	42.24	8.01	Hγ= 1.61 Hδ= 0.92-0.88 Cγ= 26.04 Cδ=24.83-23.28
Glu9	-	-	-	-	-	-

Table 23. ^{1}H-and ^{13}C-NMR chemical shifts (ppm) for analogue **6** (Dap(&)KAPETALE(&)).
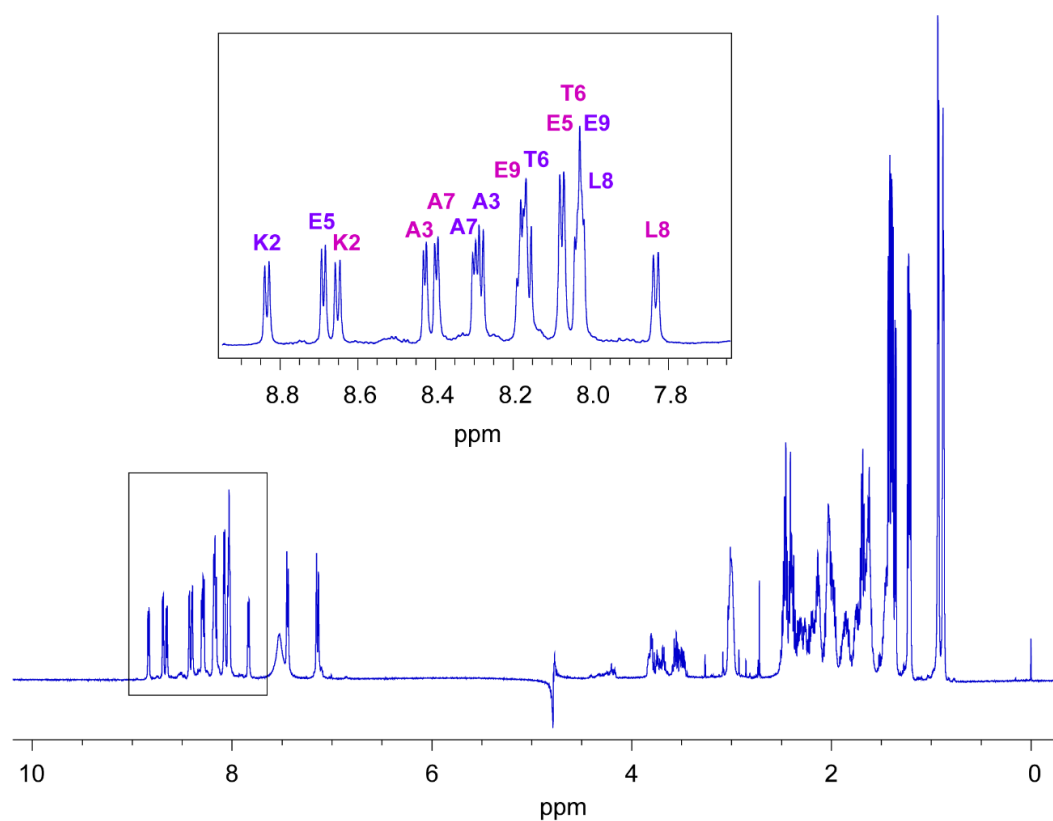
Figure 88. 1D ^{1}H-NMR spectra of analogue **6** at 298 K in aqueous solution. The NH amide resonances of the *trans* (purple) and *cis* (pink) conformers are labeled in the inset.
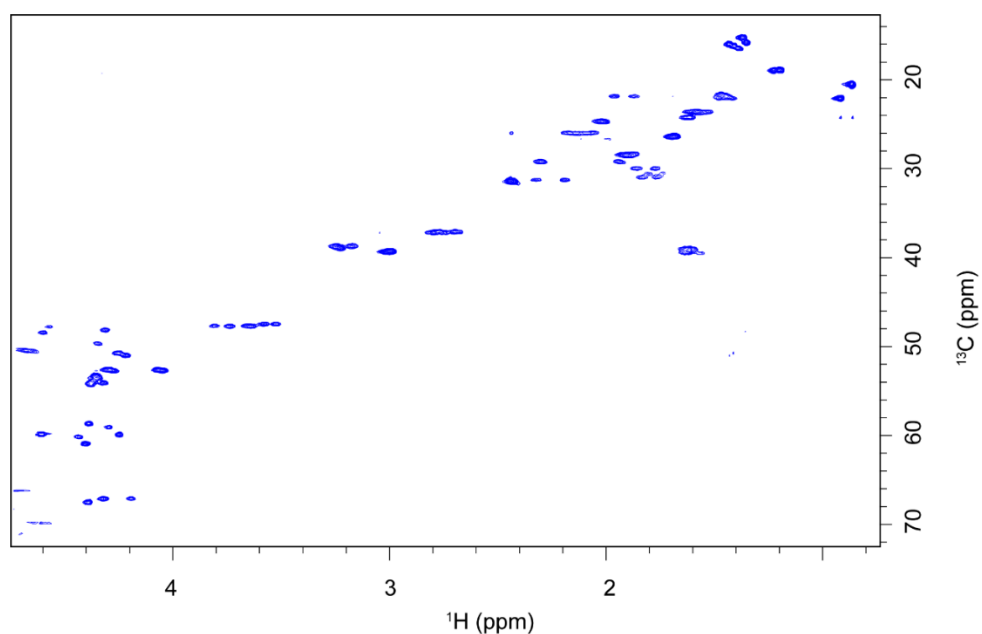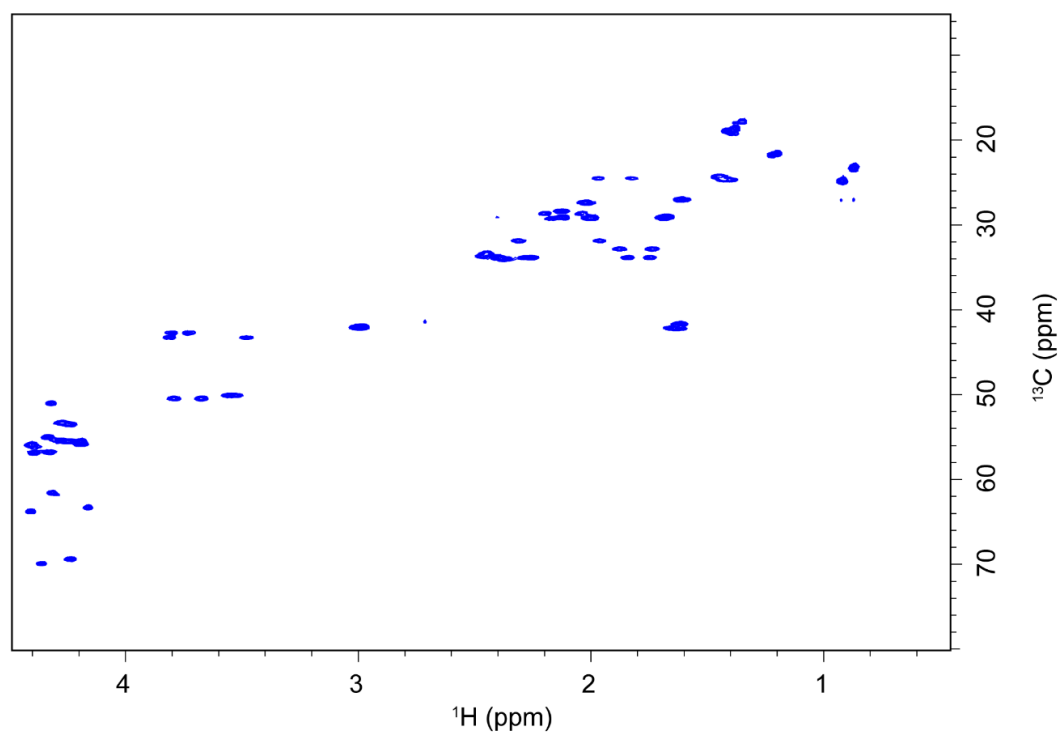

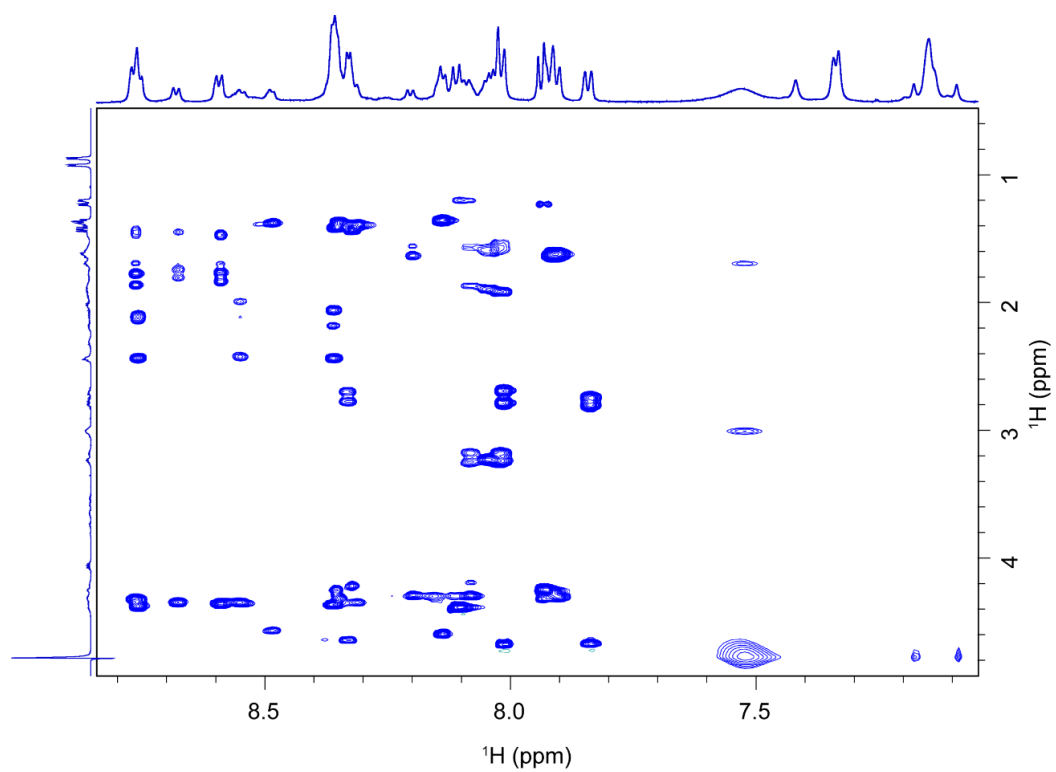**Figure 89.** ^{1}H ^{13}C-HSQC NMR spectrum of analogue **6** in aqueous solution.
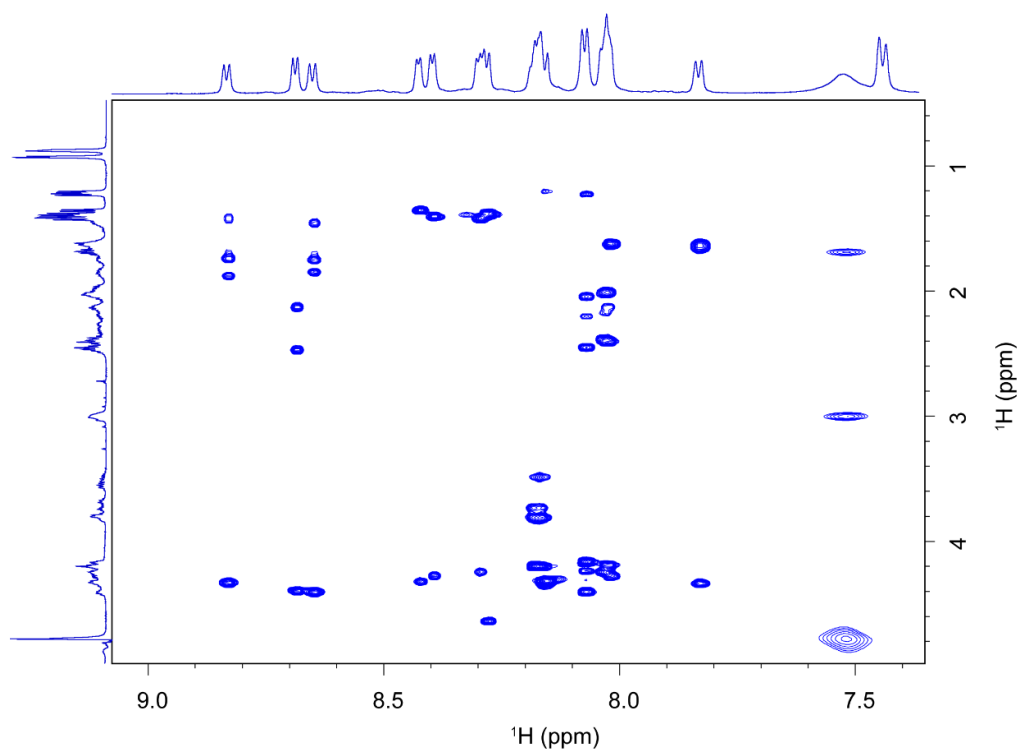
**Figure 90.** TOCSY contour map of the amidic region of analogue **6** in aqueous solution.
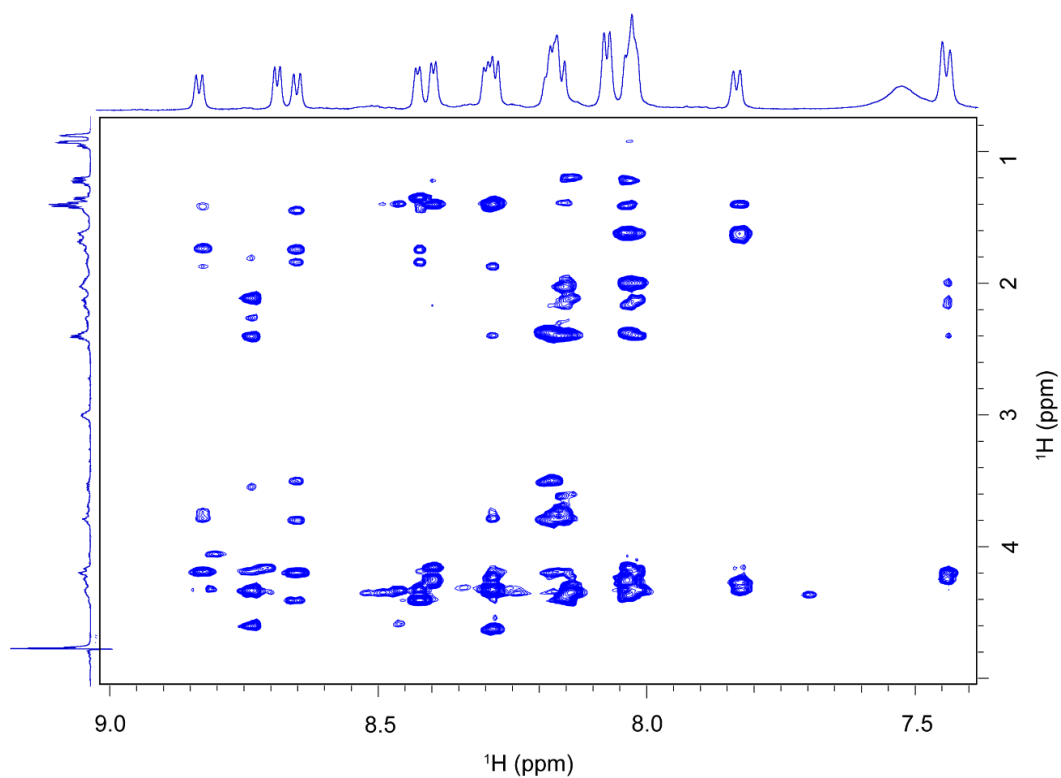
Figure 91. Selected regions of the ROESY spectrum of analogue **5** in aqueous solution.

Trans					
Residue	**Hα**	**Hβ**	**Cα**	**Cβ**	**NH**	**Others**
Lys2	4.36	1.72-1.63	54.55	35.26	8.58	Hγ= 1.41 Hε= 2.96 Cγ= 24.49 Cε= 42.09
Thr6	4.30	4.19	61.75	69.95	8.11	Hγ= 1.20 Cγ=21.61

Cis					
Residue	**Hα**	**Hβ**	**Cα**	**Cβ**	**NH**	**Others**
Dap 1	4.25	3.86-3.48	55.44	43.14	8.21	
Lys2	4.41	1.86-1.75	55.80	33.81	8.63	Hγ= 1.48 Hδ= 1.67 Hε= 3.01 Cγ= 24.44 Cδ= 29.19 Cε= 42.08
Ala3	4.17	1.33	51.88	17.79	8.37	
dmP4	4.58	2.29-2.21	65.21	30.48	-	Hγ= 1.84-1.76 Hδ= 3.68 Hε= 1.51-1.38 Cγ= 41.67 Cδ= 50.42 Cε= 28.97-26.24
Glu5	4.48	2.2-2.11	56.47	28.14	8.69	Hγ= 2.48 Cγ=33.36
Thr6	4.24	4.31	62.09	69.55	8.00	Hγ= 1.17 Cγ=21.73
Ala7	4.24	1.40	53.27	19.00	8.20	
Leu8	4.27	1.62	55.51	41.57	8.06	Hγ= 1.61 Hδ= 0.92-0.86 Cγ= 26.98 Cδ=24.78-23.35
Asp9	4.72	2.86-2.73	58.72	39.90	8.07	

Table 24. ^{1}H-and ^{13}C-NMR chemical shifts (ppm) for analogue **7** (Dap(&)KA(dmP)PETALD(&)). The complete assignation of the *trans* rotamer was not possible due to the low peaks intensity.
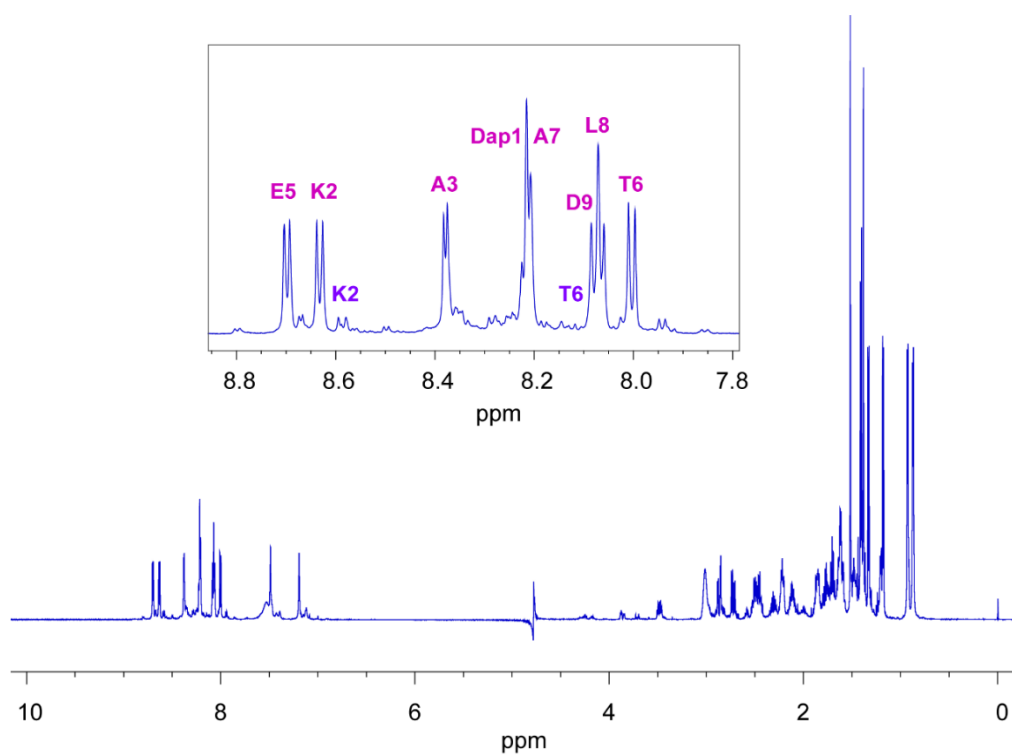
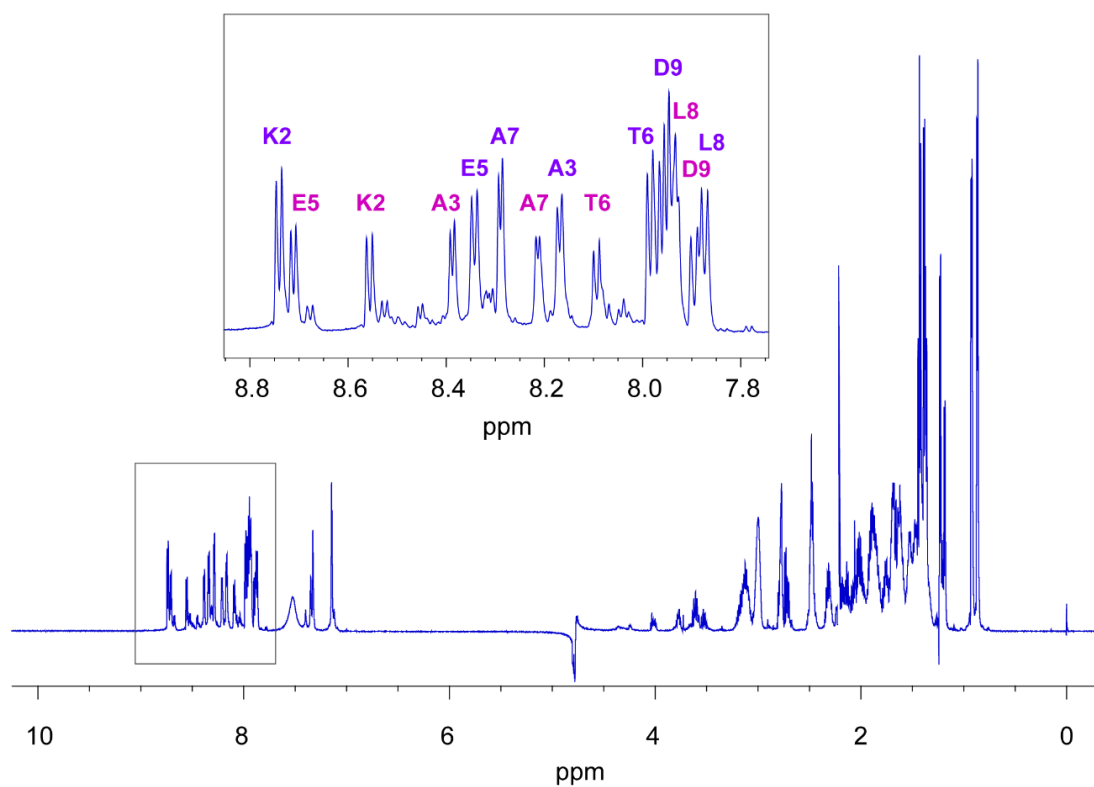**Figure 92.** 1D ^{1}H-NMR spectra of analogue **7** at 298 K in aqueous solution. The NH amide resonances of the *cis* (pink) conformers are labeled in the inset.
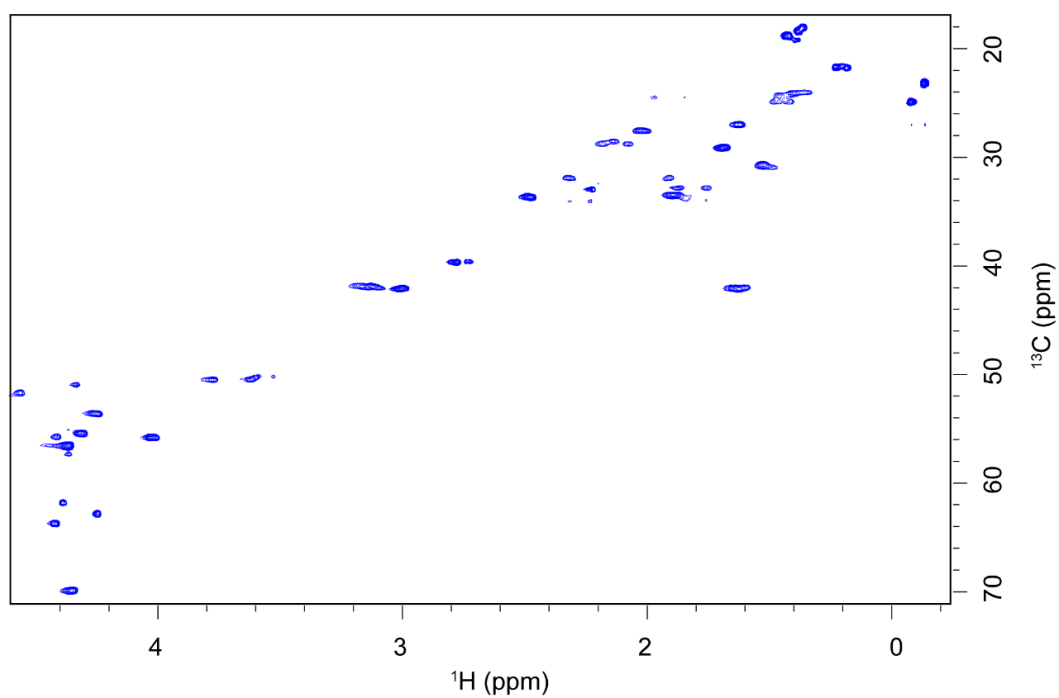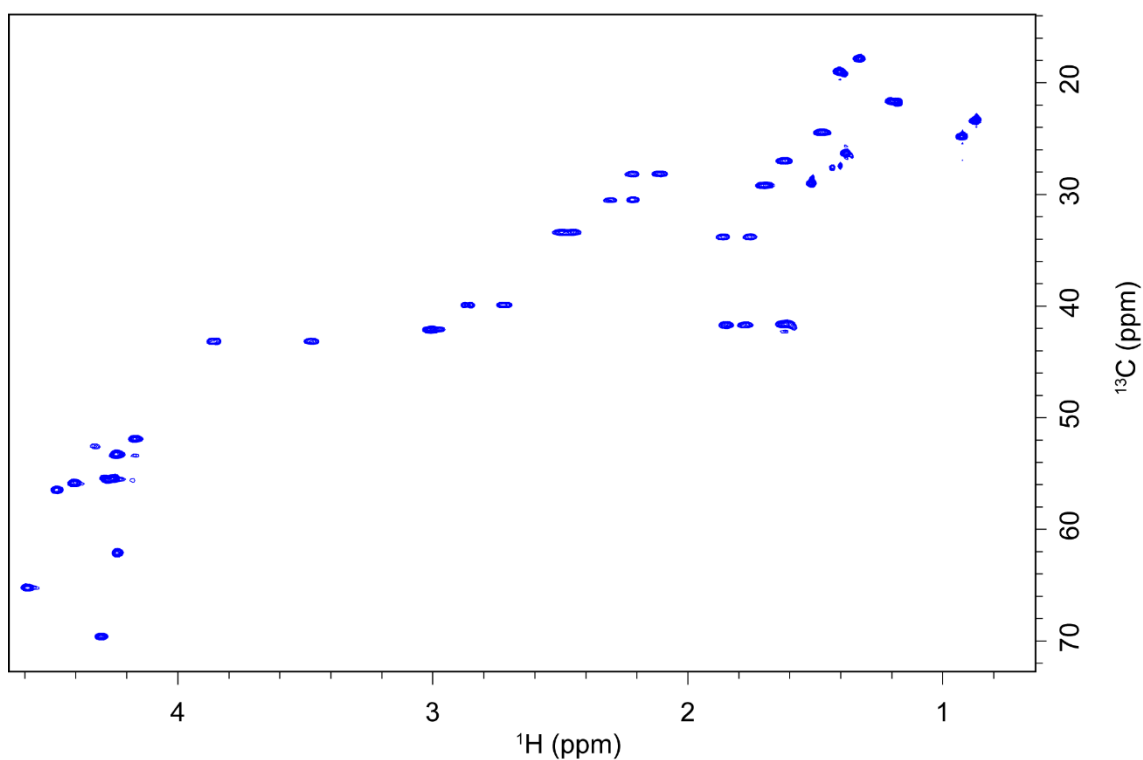

Figure 93. ^{1}H ^{13}C-HSQC NMR spectrum of analogue **7** in aqueous solution.
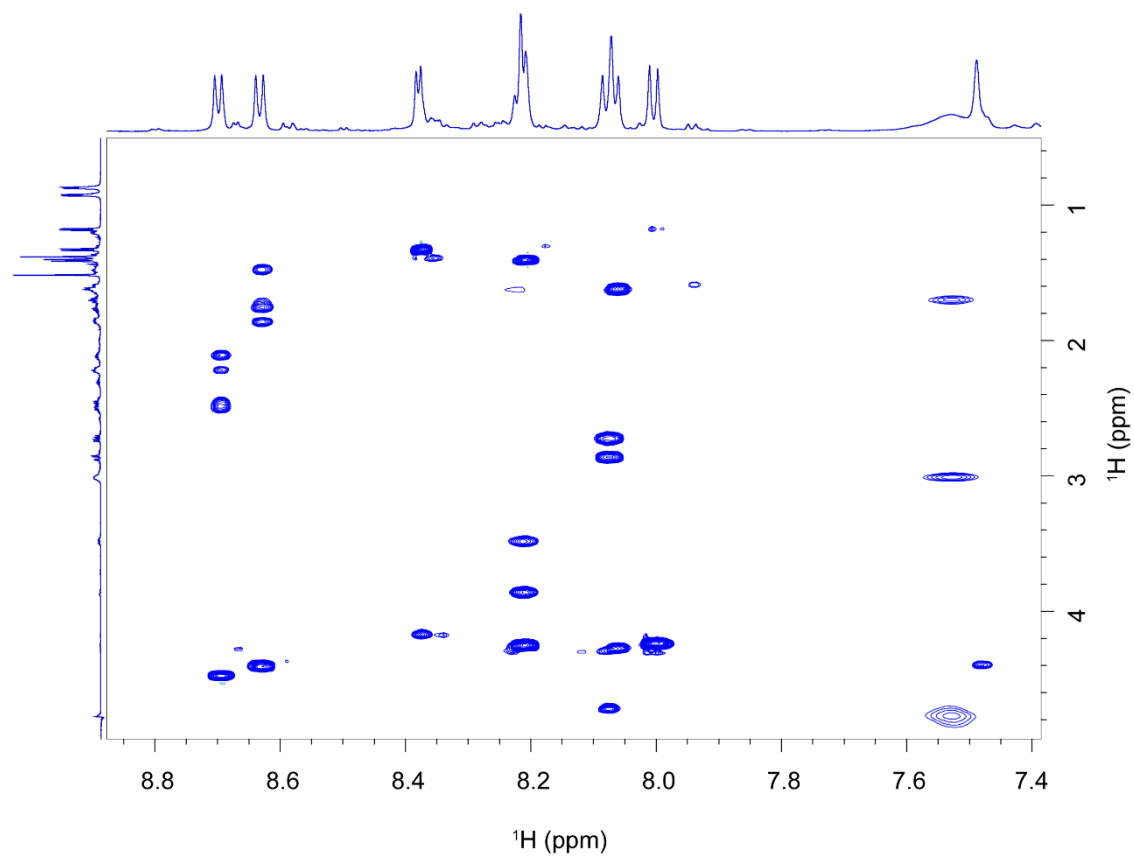
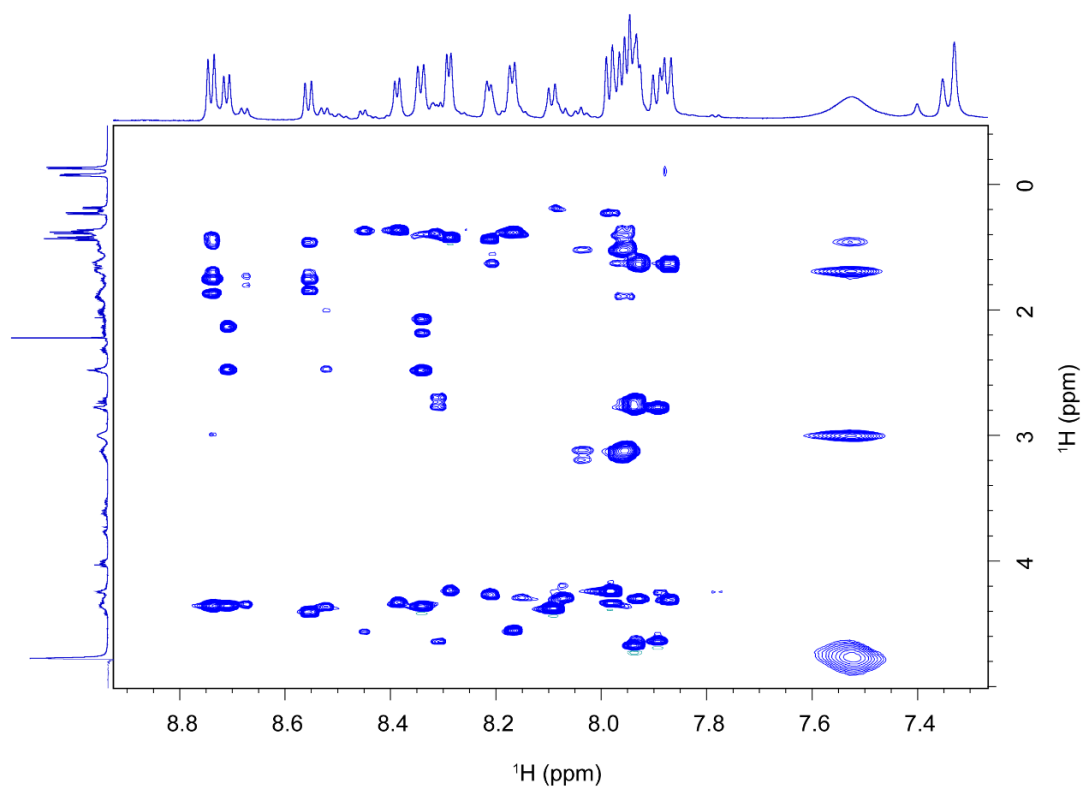**Figure 94.** TOCSY contour map of the amidic region of analogue **7** in aqueous solution.
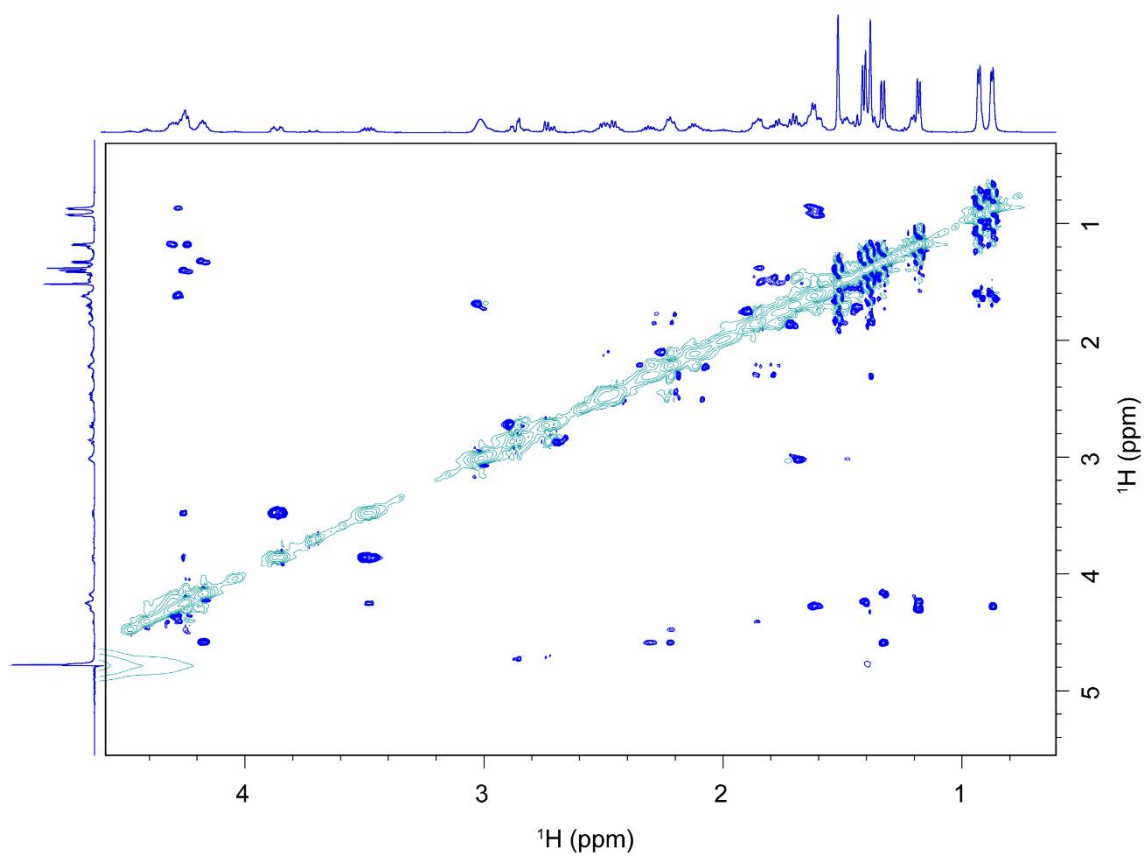
Figure 95. Selected regions of the ROESY spectrum of analogue **7** in aqueous solution.

REFERENCES

[1] Pardridge WM. Drug Transport across the Blood-Brain Barrier. *J. Cereb. Blood Flow Metab.* 2012; **32**: 1959–1972.

[2] Pardridge WM. The Blood-Brain Barrier: Bottleneck in Brain Drug Development. *NeuroRx* 2005; **2**: 3–14.

[3] Pardridge WM. Drug and Gene Targeting to the Brain with Molecular Trojan Horses. *Nat. Rev. Drug Discov.* 2002; **1**: 131.

[4] Engelhardt B, Sorokin L. The Blood–brain and the Blood–cerebrospinal Fluid Barriers: Function and Dysfunction. *Semin. Immunopathol.* 2009; **31**: 497–511.

[5] McCully M, Sanchez-Navarro M, Teixido M, Giralt E. Peptide Mediated Brain Delivery of Nano- and Submicroparticles: A Synergistic Approach. *Curr. Pharm. Des.* 2018; **24**: 1366–1376.

[6] Dohrmann GJ. The Choroid Plexus: A Historical Review. *Brain Res.* 1970; **18**: 197–218.

[7] Omidi Y, Barar J. Impacts of Blood-Brain Barrier in Drug Delivery and Targeting of Brain Tumors. *Bioimpacts* 2012; **2**: 5–22.

[8] Abbott NJ. Blood–brain Barrier Structure and Function and the Challenges for CNS Drug Delivery. *J. Inherit. Metab. Dis.* 2013; **36**: 437–449.

[9] Pardridge WM. Blood–brain Barrier Delivery. *Drug Discov. Today* 2007; **12**: 54–61.

[10] Reese TS, Karnovsky MJ. Fine Structural Localization of a Blood-Brain Barrier to Exogenous Peroxidase. *J. Cell Biol.* 1967; **34**: 207 LP-217.

[11] Abbott NJ, Rönnbäck L, Hansson E. Astrocyte–endothelial Interactions at the Blood–brain Barrier. *Nat. Rev. Neurosci.* 2006; **7**: 41.

[12] Jefferies WA, Brandon MR, Hunt S V, Williams AF, Gatter KC, Mason DY. Transferrin Receptor on Endothelium of Brain Capillaries. *Nature* 1984; **312**: 162–163.

[13] Krewson CE, Klarman ML, Saltzman WM. Distribution of Nerve Growth Factor Following Direct Delivery to Brain Interstitium. *Brain Res.* 1995; **680**: 196–206.

[14] Ai Y, Markesbery W, Zhang Z, Grondin R, Elseberry D, Gerhardt GA, Gash DM. Intraputamenal Infusion of GDNF in Aged Rhesus Monkeys: Distribution and Dopaminergic Effects. *J. Comp. Neurol.* 2003; **461**: 250–261.

[15] Mehta AM, Sonabend AM, Bruce JN. Convection-Enhanced Delivery. *Neurotherapeutics* 2017; **14**: 358–371.

[16] Lu C-T, Zhao Y-Z, Wong HL, Cai J, Peng L, Tian X-Q. Current Approaches to Enhance CNS Delivery of Drugs across the Brain Barriers. *Int. J. Nanomedicine* 2014; **9**: 2241–2257.

[17] Hanig JP, Morrison JM, Krop S. Ethanol Enhancement of Blood-Brain Barrier Permeability to Catecholamines in Chicks. *Eur. J. Pharmacol.* 1972; **18**: 79–82.

[18] Broadwell RD, Salcman M, Kaplan RS. Morphologic Effect of Dimethyl Sulfoxide on the Blood-Brain Barrier. *Science* 1982; **217**: 164-166.

[19] Saija A, Princi P, Trombetta D, Lanza M, De Pasquale A. Changes in the Permeability of the Blood-Brain Barrier Following Sodium Dodecyl Sulphate Administration in the Rat. *Exp. Brain. Res.* 1997; **115**: 564-551.

[20] Sztriha L, Betz AL. Oleic Acid Reversibly Opens the Blood-Brain Barrier. *Brain Res.*

1991; **550**: 257–262.

[21] Öztaş B, Küçük M. Intracarotid Hypothermic Saline Infusion: A New Method for Reversible Blood-Brain Barrier Disruption in Anesthetized Rats. *Neurosci. Lett.* 1995; **190**: 203–206.

[22] Liu H-L, Hua M-Y, Chen P-Y, Chu P-C, Pan C-H, Yang H-W, Huang C-Y, Wang J-J, Yen T-C, Wei K-C. Blood-Brain Barrier Disruption with Focused Ultrasound Enhances Delivery of Chemotherapeutic Drugs for Glioblastoma Treatment. *Radiology* 2010; **255**: 415–425.

[23] Hynynen K, McDannold N, Sheikov NA, Jolesz FA, Vykhodtseva N. Local and Reversible Blood–brain Barrier Disruption by Noninvasive Focused Ultrasound at Frequencies Suitable for Trans-Skull Sonications. *Neuroimage* 2005; **24**: 12–20.

[24] Cecchelli R, Berezowski V, Lundquist S, Culot M, Renftel M, Dehouck M-P, Fenart L. Modelling of the Blood–brain Barrier in Drug Discovery and Development. *Nat. Rev. Drug Discov.* 2007; **6**: 650.

[25] Malakoutikhah M, Teixidó M, Giralt E. Shuttle-Mediated Drug Delivery to the Brain. *Angew. Chemie Int. Ed.* 2011; **50**: 7998–8014.

[26] Pardridge WM. Drug Targeting to the Brain. *Pharm. Res.* 2007; **24**: 1733–1744.

[27] Pardridge WM. Receptor-Mediated Peptide Transport through the Blood-Brain Barrier. *Endocr. Rev.* 1986; **7**: 314–330.

[28] Kumagai A, B Eisenberg J, Pardridge W. Absorptive-Mediated Endocytosis of Cationized Albumin and a Beta-Endorphin-Cationized Albumin Chimeric Peptide by Isolated Brain Capillaries. *J. Biol. Chem.* 1987; **262**: 15214-15219.

[29] Friden PM, Walus LR, Musso GF, Taylor MA, Malfroy B, Starzyk RM. Anti-Transferrin Receptor Antibody and Antibody-Drug Conjugates Cross the Blood-Brain Barrier. *Proc. Natl. Acad. Sci. U. S. A.* 1991; **88**: 4771–4775.

[30] Uhlig T, Kyprianou T, Martinelli FG, Oppici CA, Heiligers D, Hills D, Calvo XR, Verhaert P. The Emergence of Peptides in the Pharmaceutical Business: From Exploration to Exploitation. *EuPA Open Proteomics* 2014; **4**: 58–69.

[31] Schwarze SR, Ho A, Vocero-Akbani A, Dowdy SF. In Vivo Protein Transduction: Delivery of a Biologically Active Protein into the Mouse. *Science.* 1999; **285**: 1569-1572.

[32] Demeule M, Currie J-C, Bertrand Y, Ché C, Nguyen T, Régina A, Gabathuler R, Castaigne J-P, Béliveau R. Involvement of the Low-Density Lipoprotein Receptor-Related Protein in the Transcytosis of the Brain Delivery Vector Angiopep-2. *J. Neurochem.* 2008; **106**: 1534–1544.

[33] Régina A, Demeule M, Ché C, Lavallée I, Poirier J, Gabathuler R, Béliveau R, Castaigne J-P. Antitumour Activity of ANG1005, a Conjugate between Paclitaxel and the New Brain Delivery Vector Angiopep-2. *Br. J. Pharmacol.* 2008; **155**: 185–197.

[34] Ché C, Yang G, Thiot C, Lacoste M-C, Currie J-C, Demeule M, Régina A, Béliveau R, Castaigne J-P. New Angiopep-Modified Doxorubicin (ANG1007) and Etoposide (ANG1009) Chemotherapeutics With Increased Brain Penetration. *J. Med. Chem.* 2010; **53**: 2814–2824.

[35] Malakoutikhah M, Guixer B, Arranz-Gibert P, Teixidó M, Giralt E. 'À La Carte' Peptide Shuttles: Tools to Increase Their Passage across the Blood–Brain Barrier. *Chemmedchem* 2014; **9**: 1594–1601.

[36] Malakoutikhah M, Prades R, Teixidó M, Giralt E. N-Methyl Phenylalanine-Rich Peptides

as Highly Versatile Blood−Brain Barrier Shuttles. *J. Med. Chem.* 2010; **53**: 2354–2363.

[37] Teixidó M, Zurita E, Malakoutikhah M, Tarragó T, Giralt E. Diketopiperazines as a Tool for the Study of Transport across the Blood−Brain Barrier (BBB) and Their Potential Use as BBB-Shuttles. *J. Am. Chem. Soc.* 2007; **129**: 11802–11813.

[38] Kansy M, Senner F, Gubernator K. Physicochemical High Throughput Screening: Parallel Artificial Membrane Permeation Assay in the Description of Passive Absorption Processes. *J. Med. Chem.* 1998; **41**: 1007–1010.

[39] Arranz-Gibert P, Guixer B, Malakoutikhah M, Muttenthaler M, Guzmán F, Teixidó M, Giralt E. Lipid Bilayer Crossing—The Gate of Symmetry. Water-Soluble Phenylproline-Based Blood-Brain Barrier Shuttles. *J. Am. Chem. Soc.* 2015; **137**: 7357–7364.

[40] Kiptoo P, Sinaga E, Calcagno AM, Zhao H, Kobayashi N, Tambunan USF, Siahaan TJ. Enhancement of Drug Absorption through the Blood-Brain Barrier and Inhibition of Intercellular Tight Junction Resealing by E-Cadherin Peptides. *Mol. Pharm.* 2011; **8**: 239–249.

[41] Tabanor K, Lee P, Kiptoo P, Choi I-Y, Sherry EB, Eagle CS, Williams TD, Siahaan TJ. Brain Delivery of Drug and MRI Contrast Agent: Detection and Quantitative Determination of Brain Deposition of CPT-Glu Using LC-MS/MS and Gd-DTPA Using Magnetic Resonance Imaging. *Mol. Pharm.* 2016; **13**: 379–390.

[42] Lee JH, Okuno Y, Cavagnero S. Sensitivity Enhancement in Solution NMR: Emerging Ideas and New Frontiers. *J. Magn. Reson.* 2014; **241**: 18–31.

[43] Bonina FP, Arenare L, Palagiano F, Saija A, Nava F, Trombetta D, Caprariis P De. Synthesis, Stability, and Pharmacological Evaluation of Nipecotic Acid Prodrugs. *J. Pharm. Sci.* 1999; **88**: 561–567.

[44] Gynther M, Laine K, Ropponen J, Leppänen J, Mannila A, Nevalainen T, Savolainen J, Järvinen T, Rautio J. Large Neutral Amino Acid Transporter Enables Brain Drug Delivery via Prodrugs. *J. Med. Chem.* 2008; **51**: 932–936.

[45] Gynther M, Ropponen J, Laine K, Leppänen J, Haapakoski P, Peura L, Järvinen T, Rautio J. Glucose Promoiety Enables Glucose Transporter Mediated Brain Uptake of Ketoprofen and Indomethacin Prodrugs in Rats. *J. Med. Chem.* 2009; **52**: 3348–3353.

[46] Frankel AD, Pabo CO. Cellular Uptake of the Tat Protein from Human Immunodeficiency Virus. *Cell.* 1988; **55**: 1189–1193.

[47] Derossi D, Gerard C, Prochiantz A. Trojan Peptide: The Penetratin System for Intracellular Delivery. *Trends Cell. Biol.* 1998; **8**: 84-87.

[48] Arginine-Rich Peptides. An Abundant Source of Membrane-Permeable Peptides Having Potential as Carriers for Intracellular Protein Delivery. *J. Biol. Chem.* 2000; **276**: 5836–5840.

[49] Pardridge WM, Triguero D, Buciak J. Transport of Histone through the Blood-Brain Barrier. *J. Pharmacol. Exp. Ther.* 1989; **251**: 821-826.

[50] Vorbrodt AW. Ultracytochemical Characterization of Anionic Sites in the Wall of Brain Capillaries. *J. Neurocytol.* 1989; **18**: 359–368.

[51] Rao KS, Reddy MK, Horning JL, Labhasetwar V. TAT-Conjugated Nanoparticles for the CNS Delivery of Anti-HIV Drugs. *Biomaterials* 2008; **29**: 4429–4438.

[52] Jeon H, Blacklow SC. Structure and Physiologic Function of the Low-Density Lipoprotein receptor. *Annu. Rev. Biochem.* 2005; **74**: 535–562.

[53] Jones AR, Shusta E V. Blood–Brain Barrier Transport of Therapeutics via Receptor-Mediation. *Pharm. Res.* 2007; **24**: 1759–1771.

[54] Wang D, El-Amouri SS, Dai M, Kuan C-Y, Hui DY, Brady RO, Pan D. Engineering a Lysosomal Enzyme with a Derivative of Receptor-Binding Domain of ApoE Enables Delivery across the Blood–brain Barrier. *Proc. Natl. Acad. Sci.* 2013; **110**: 2999-3004.

[55] Spencer BJ, Verma IM. Targeted Delivery of Proteins across the Blood-Brain Barrier. *Proc. Natl. Acad. Sci. U. S. A.* 2007; **104**: 7594–7599.

[56] Demeule M, Régina A, Ché C, Poirier J, Nguyen T, Gabathuler R, Castaigne J-P, Béliveau R. Identification and Design of Peptides as a New Drug Delivery System for the Brain. *J. Pharmacol. Exp. Ther.* 2008; **324**: 1064-1072.

[57] Sun X, Pang Z, Ye H, Qiu B, Guo L, Li J, Ren J, Qian Y, Zhang Q, Chen J, Jiang X. Co-Delivery of PEGFP-HTRAIL and Paclitaxel to Brain Glioma Mediated by an Angiopep-Conjugated Liposome. *Biomaterials* 2012; **33**: 916–924.

[58] Shen J, Zhan C, Xie C, Meng Q, Gu B, Li C, Zhang Y, Lu W. Poly(Ethylene Glycol)-Block-Poly(D,L-Lactide Acid) Micelles Anchored with Angiopep-2 for Brain-Targeting Delivery. *J. Drug Target.* 2010; **19**: 197-203.

[59] Huang R, Ma H, Guo Y, Liu S, Kuang Y, Shao K, Li J, Liu Y, Han L, Huang S, An S, Ye L, Lou J, Jiang C. Angiopep-Conjugated Nanoparticles for Targeted Long-Term Gene Therapy of Parkinson's Disease. *Pharm. Res.* 2013; **30**: 2549–2559.

[60] Prades R, Guerrero S, Araya E, Molina C, Salas E, Zurita E, Selva J, Egea G, López-Iglesias C, Teixidó M, Kogan MJ, Giralt E. Delivery of Gold Nanoparticles to the Brain by Conjugation with a Peptide That Recognizes the Transferrin Receptor. *Biomaterials* 2012; **33**: 7194–7205.

[61] Malcor J-D, Payrot N, David M, Faucon A, Abouzid K, Jacquot G, Floquet N, Debarbieux F, Rougon G, Martinez J, Khrestchatisky M, Vlieghe P, Lisowski V. Chemical Optimization of New Ligands of the Low-Density Lipoprotein Receptor as Potential Vectors for Central Nervous System Targeting. *J. Med. Chem.* 2012; **55**: 2227–2241.

[62] Zhang B, Sun X, Mei H, Wang Y, Liao Z, Chen J, Zhang Q, Hu Y, Pang Z, Jiang X. LDLR-Mediated Peptide-22-Conjugated Nanoparticles for Dual-Targeting Therapy of Brain Glioma. *Biomaterials* 2013; **34**: 9171–9182.

[63] Spengler J, Jiménez JC, Burger K, Giralt E, Albericio F. Abbreviated Nomenclature for Cyclic and Branched Homo- and Hetero-Detic Peptides. *J. Pept. Res.* 2005; **65**: 550–555.

[64] Ponka P, Lok CN. The Transferrin Receptor: Role in Health and Disease. *Int. J. Biochem. Cell Biol.* 1999; **31**: 1111–1137.

[65] Andrews NC. Iron Homeostasis: Insights from Genetics and Animal Models. *Nat. Rev. Genet.* 2000; **1**: 208–217.

[66] Qian ZM, Li H, Sun H, Ho K. Targeted Drug Delivery via the Transferrin Receptor-Mediated Endocytosis Pathway. *Pharmacol. Rev.* 2002; **54**: 561-587.

[67] Skarlatos S, Yoshikawa T, Pardridge WM. Transport of [125I]Transferrin through the Rat Blood-Brain Barrier. *Brain Res.* 1995; **683**: 164–171.

[68] Miyamoto T, Tanaka N, Eishi Y, Amagasa T. Transferrin Receptor in Oral Tumors. *Int. J. Oral Maxillofac. Surg.* 1994; **23**: 430–433.

[69] Keer HN, Kozlowski JM, Tsai YC, Lee C, McEwan RN, Grayhack JT. Elevated Transferrin Receptor Content in Human Prostate Cancer Cell Lines Assessed in Vitro and in Vivo. *J. Urol.* 1990; **143**: 381–385.

[70] Visser C, Stevanović S, Heleen Voorwinden L, Gaillard P, Crommelin D, Danhof M, Boer A. Validation of the Transferrin Receptor for Drug Targeting to Brain Capillary Endothelial Cells In Vitro. *J. Drug Target.* 2004; **12**: 145-150.

[71] Aktaş Y, Yemisci M, Andrieux K, Gürsoy RN, Alonso MJ, Fernandez-Megia E, Novoa-Carballal R, Quiñoá E, Riguera R, Sargon MF, Çelik HH, Demir AS, Hıncal AA, Dalkara T, Çapan Y, Couvreur P. Development and Brain Delivery of Chitosan−PEG Nanoparticles Functionalized with the Monoclonal Antibody OX26. *Bioconjug. Chem.* 2005; **16**: 1503–1511.

[72] Saito Y, Buciak J, Yang J, Pardridge WM. Vector-Mediated Delivery of 125I-Labeled Beta-Amyloid Peptide A Beta 1-40 through the Blood-Brain Barrier and Binding to Alzheimer Disease Amyloid of the A Beta 1-40/Vector Complex. *Proc. Natl. Acad. Sci. U. S. A.* 1995; **92**: 10227–10231.

[73] Kurihara A, Deguchi Y, Pardridge WM. Epidermal Growth Factor Radiopharmaceuticals: 111In Chelation, Conjugation to a Blood-Brain Barrier Delivery Vector via a Biotin-Polyethylene Linker, Pharacokinetics, and in Vivo Imaging of Experimental Brain Tumors. *Bioconjug. Chem.* 1999; **10**: 502–511.

[74] Bickel U, Yoshikawa T, Landaw EM, Faull KF, Pardridge WM. Pharmacologic Effects in Vivo in Brain by Vector-Mediated Peptide Drug Delivery. *Proc. Natl. Acad. Sci. U. S. A.* 1993; **90**: 2618–2622.

[75] Zhang Y, Pardridge WM. Delivery of β-Galactosidase to Mouse Brain via the Blood-Brain Barrier Transferrin Receptor. *J. Pharmacol. Exp. Ther.* 2005; **313**: 1075-1081.

[76] Zhu C, Zhang Y, Zhang Y, Yi Li J, Boado RJ, Pardridge WM. Organ-Specific Expression of the LacZ Gene Controlled by the Opsin Promoter after Intravenous Gene Administration in Adult Mice. *J. Gene Med.* 2004; **6**: 906–912.

[77] Pardridge WM. Brain Drug Targeting: The Future of Brain Drug Development. *J. Clin. Pathol.* 2002; **55**: 158.

[78] Niewoehner J, Bohrmann B, Collin L, Urich E, Sade H, Maier P, Rueger P, Stracke JO, Lau W, Tissot AC, Loetscher H, Ghosh A, Freskgård P-O. Increased Brain Penetration and Potency of a Therapeutic Antibody Using a Monovalent Molecular Shuttle. *Neuron* 2014; **81**: 49–60.

[79] Lo SL, Wang S. An Endosomolytic Tat Peptide Produced by Incorporation of Histidine and Cysteine Residues as a Nonviral Vector for DNA Transfection. *Biomaterials* 2008; **29**: 2408–2414.

[80] Xia H, Anderson B, Mao Q, Davidson BL. Recombinant Human Adenovirus: Targeting to the Human Transferrin Receptor Improves Gene Transfer to Brain Microcapillary Endothelium. *J. Virol.* 2000; **74**: 11359–11366.

[81] Lee JH, Engler JA, Collawn JF, Moore BA. Receptor Mediated Uptake of Peptides That Bind the Human Transferrin Receptor. *Eur. J. Biochem.* 2001; **268**: 2004–2012.

[82] Staquicini FI, Ozawa MG, Moya CA, Driessen WHP, Barbu EM, Nishimori H, Soghomonyan S, Flores 2nd LG, Liang X, Paolillo V, Alauddin MM, Basilion JP, Furnari FB, Bogler O, Lang FF, Aldape KD, Fuller GN, Höök M, Gelovani JG, Sidman RL, Cavenee WK, Pasqualini R, Arap W. Systemic Combinatorial Peptide Selection Yields a Non-Canonical Iron-Mimicry Mechanism for Targeting Tumors in a Mouse Model of Human Glioblastoma. *J. Clin. Invest.* 2011; **121**: 161–173.

[83] Prades R, Oller-Salvia B, Schwarzmaier SM, Selva J, Moros M, Balbi M, Grazú V, de La Fuente JM, Egea G, Plesnila N, Teixidó M, Giralt E. Applying the Retro-Enantio Approach To Obtain a Peptide Capable of Overcoming the Blood–Brain Barrier. *Angew.*

Chemie Int. Ed. 2015; **54**: 3967–3972.

[84]   Lee J, Pilch PF. The Insulin Receptor: Structure, Function, and Signaling. *Am. J. Physiol. Physiol.* 1994; **266**: C319–C334.

[85]   Boado RJ, Zhang Y, Zhang Y, Pardridge WM. Genetic Engineering, Expression, and Activity of a Fusion Protein of a Human Neurotrophin and a Molecular Trojan Horse for Delivery across the Human Blood–brain Barrier. *Biotechnol. Bioeng.* 2007; **97**: 1376–1386.

[86]   Boado RJ, Zhang Y, Zhang Y, Xia C, Wang Y, Pardridge WM. Genetic Engineering of a Lysosomal Enzyme Fusion Protein for Targeted Delivery across the Human Blood-Brain Barrier. *Biotechnol. Bioeng.* 2008; **99**: 475–484.

[87]   Wu J, Lukas RJ. Naturally-Expressed Nicotinic Acetylcholine Receptor Subtypes. *Biochem. Pharmacol.* 2011; **82**: 800–807.

[88]   L. Lentz T. Rabies Virus Binding to an Acetylcholine Receptor Alpha-Subunit Peptide. *J. Mol. Recognit.* 1990; **3**: 82-88.

[89]   Kumar P, Wu H, McBride JL, Jung K-E, Hee Kim M, Davidson BL, Kyung Lee S, Shankar P, Manjunath N. Transvascular Delivery of Small Interfering RNA to the Central Nervous System. *Nature* 2007; **448**: 39-45.

[90]   Liu Y, Hu Y, Guo Y, Ma H, Li J, Jiang C. Targeted Imaging of Activated Caspase-3 in the Central Nervous System by a Dual Functional Nano-Device. *J. Control. Release* 2012; **163**: 203–210.

[91]   Hwang DW, Son S, Jang J, Youn H, Lee S, Lee D, Lee Y-S, Jeong JM, Kim WJ, Lee DS. A Brain-Targeted Rabies Virus Glycoprotein-Disulfide Linked PEI Nanocarrier for Delivery of Neurogenic MicroRNA. *Biomaterials* 2011; **32**: 4968–4975.

[92]   Son S, Hwang DW, Singha K, Jeong JH, Park TG, Lee DS, Kim WJ. RVG Peptide Tethered Bioreducible Polyethylenimine for Gene Delivery to Brain. *J. Control. Release* 2011; **155**: 18–25.

[93]   Liu Y, Huang R, Han L, Ke W, Shao K, Ye L, Lou J, Jiang C. Brain-Targeting Gene Delivery and Cellular Internalization Mechanisms for Modified Rabies Virus Glycoprotein RVG29 Nanoparticles. *Biomaterials* 2009; **30**: 4195–4202.

[94]   Fu A, Wang Y, Zhan L, Zhou R. Targeted Delivery of Proteins into the Central Nervous System Mediated by Rabies Virus Glycoprotein-Derived Peptide. *Pharm. Res.* 2012; **29**: 1562–1569.

[95]   Zhan C, Yan Z, Xie C, Lu W. Loop 2 of Ophiophagus Hannah Toxin b Binds with Neuronal Nicotinic Acetylcholine Receptors and Enhances Intracranial Drug Delivery. *Mol. Pharm.* 2010; **7**: 1940–1947.

[96]   Zhan C, Li B, Hu L, Wei X, Feng L, Fu W, Lu W. Micelle-Based Brain-Targeted Drug Delivery Enabled by a Nicotine Acetylcholine Receptor Ligand. *Angew. Chemie Int. Ed.* 2011; **50**: 5482–5485.

[97]   Wei X, Zhan C, Shen Q, Fu W, Xie C, Gao J, Peng C, Zheng P, Lu W. A D-Peptide Ligand of Nicotine Acetylcholine Receptors for Brain-Targeted Drug Delivery. *Angew. Chemie Int. Ed.* 2015; **54**: 3023–3027.

[98]   Barrett GL, Trieu J, Naim T. The Identification of Leptin-Derived Peptides That Are Taken up by the Brain. *Regul. Pept.* 2009; **155**: 55–61.

[99]   Liu Y, Li J, Shao K, Huang R, Ye L, Lou J, Jiang C. A Leptin Derived 30-Amino-Acid Peptide Modified Pegylated Poly-l-Lysine Dendrigraft for Brain Targeted Gene Delivery.

Biomaterials 2010; **31**: 5246–5257.

[100] Pinnen F, Cacciatore I, Cornacchia C, Sozio P, Iannitelli A, Costa M, Pecci L, Nasuti C, Cantalamessa F, Di Stefano A. Synthesis and Study of L-Dopa−Glutathione Codrugs as New Anti-Parkinson Agents with Free Radical Scavenging Properties. *J. Med. Chem.* 2007; **50**: 2506–2515.

[101] More SS, Vince R. Design, Synthesis and Biological Evaluation of Glutathione Peptidomimetics as Components of Anti-Parkinson Prodrugs. *J. Med. Chem.* 2008; **51**: 4581–4588.

[102] Gaillard PJ, Appeldoorn CCM, Rip J, Dorland R, van der Pol SMA, Kooij G, de Vries HE, Reijerkerk A. Enhanced Brain Delivery of Liposomal Methylprednisolone Improved Therapeutic Efficacy in a Model of Neuroinflammation. *J. Control. Release* 2012; **164**: 364–369.

[103] Rotman M, Welling MM, Bunschoten A, de Backer ME, Rip J, Nabuurs RJA, Gaillard PJ, van Buchem MA, van der Maarel SM, van der Weerd L. Enhanced Glutathione PEGylated Liposomal Brain Delivery of an Anti-Amyloid Single Domain Antibody Fragment in a Mouse Model for Alzheimer's Disease. *J. Control. Release* 2015; **203**: 40–50.

[104] Tettamanti G, Bassi R, Viani P, Riboni L. Salvage Pathways in Glycosphingolipid Metabolism. *Biochimie* 2003; **85**: 423–437.

[105] Daniotti JL, Iglesias-Bartolomé R. Metabolic Pathways and Intracellular Trafficking of Gangliosides. *IUBMB Life* 2011; **63**: 513–520.

[106] Georgieva J V, Brinkhuis RP, Stojanov K, Weijers CAGM, Zuilhof H, Rutjes FPJT, Hoekstra D, van Hest JCM, Zuhorn IS. Peptide-Mediated Blood–Brain Barrier Transport of Polymersomes. *Angew. Chemie Int. Ed.* 2012; **51**: 8339–8342.

[107] Stojanov K, Georgieva J V, Brinkhuis RP, van Hest JC, Rutjes FP, Dierckx RAJO, de Vries EFJ, Zuhorn IS. In Vivo Biodistribution of Prion- and GM1-Targeted Polymersomes Following Intravenous Administration in Mice. *Mol. Pharm.* 2012; **9**: 1620–1627.

[108] Nagpal K, Singh SK, Mishra DN. Drug Targeting to Brain: A Systematic Approach to Study the Factors, Parameters and Approaches for Prediction of Permeability of Drugs across BBB. *Expert Opin. Drug Deliv.* 2013; **10**: 927–955.

[109] He Y, Yao Y, Tsirka SE, Cao Y. Cell-Culture Models of the Blood-Brain Barrier. *Stroke* 2014; **45**: 2514–2526.

[110] Brown RC, Morris AP, O'Neil RG. Tight Junction Protein Expression and Barrier Properties of Immortalized Mouse Brain Microvessel Endothelial Cells. *Brain Res.* 2007; **1130**: 17–30.

[111] Weksler B, Romero I, Couraud P-O. The HCMEC/D3 Cell Line as a Model of the Human Blood Brain Barrier. *Fluids Barriers CNS*. 2013; **10**: 16.

[112] Mayor S, Pagano RE. Pathways of Clathrin-Independent Endocytosis. *Nat. Rev. Mol. Cell Biol.* 2007; **8**: 603.

[113] Bitsikas V, Corrêa Jr IR, Nichols BJ. Clathrin-Independent Pathways Do Not Contribute Significantly to Endocytic Flux. *Elife* 2014; **3**: e03970.

[114] Pearse BM. Clathrin: A Unique Protein Associated with Intracellular Transfer of Membrane by Coated Vesicles. *Proc. Natl. Acad. Sci. U. S. A.* 1976; **73**: 1255–1259.

[115] Traub LM. Regarding the Amazing Choreography of Clathrin Coats. *PLOS Biol.* 2011; **9**: e1001037.

[116] Weinberg J, Drubin DG. Clathrin-Mediated Endocytosis in Budding Yeast. *Trends Cell Biol.* 2012; **22**: 1–13.

[117] Perry MM, Gilbert AB. Yolk Transport in the Ovarian Follicle of the Hen (Gallus Domesticus): Lipoprotein-like Particles at the Periphery of the Oocyte in the Rapid Growth Phase. *J. Cell Sci.* 1979; **39**: 257-272.

[118] Koenig JH, Ikeda K. Disappearance and Reformation of Synaptic Vesicle Membrane upon Transmitter Release Observed under Reversible Blockage of Membrane Retrieval. *J. Neurosci.* 1989; **9**: 3844-3860.

[119] Mayle KM, Le AM, Kamei DT. The Intracellular Trafficking Pathway of Transferrin. *Biochim. Biophys. Acta.* 2012; **1820**: 264–281.

[120] Lakadamyali M, Rust MJ, Zhuang X. Ligands for Clathrin-Mediated Endocytosis Are Differentially Sorted into Distinct Populations of Early Endosomes. *Cell.* 2006; **124**: 997–1009.

[121] Rink J, Ghigo E, Kalaidzidis Y, Zerial M. *Rab Conversion as a Mechanism of Progression from Early to Late Endosomes*, Vol. 122. 2005.

[122] Inoue H, Ha VL, Prekeris R, Randazzo PA. Arf GTPase-Activating Protein ASAP1 Interacts with Rab11 Effector FIP3 and Regulates Pericentrosomal Localization of Transferrin Receptor-Positive Recycling Endosome. *Mol. Biol. Cell* 2008; **19**: 4224–4237.

[123] Traer CJ, Rutherford AC, Palmer KJ, Wassmer T, Oakley J, Attar N, Carlton JG, Kremerskothen J, Stephens DJ, Cullen PJ. SNX4 Coordinates Endosomal Sorting of TfnR with Dynein-Mediated Transport into the Endocytic Recycling Compartment. *Nat. Cell Biol.* 2007; **9**: 1370.

[124] Tomas A, Futter CE, Eden ER. EGF Receptor Trafficking: Consequences for Signaling and Cancer. *Trends Cell Biol.* 2014; **24**: 26–34.

[125] Simons K, Ikonen E. Functional Rafts in Cell Membranes. *Nature* 1997; **387**: 569–572.

[126] Parton RG, Simons K. The Multiple Faces of Caveolae. *Nat. Rev. Mol. Cell Biol.* 2007; **8**: 185.

[127] Parton RG. Caveolae - from Ultrastructure to Molecular Mechanisms. *Nat. Rev. Mol. Cell Biol.* 2003; **4**: 162.

[128] Rothberg KG, Heuser JE, Donzell WC, Ying Y-S, Glenney JR, Anderson RGW. Caveolin, a Protein Component of Caveolae Membrane Coats. *Cell* 1992; **68**: 673–682.

[129] Wilhelm I, Krizbai IA. In Vitro Models of the Blood–Brain Barrier for the Study of Drug Delivery to the Brain. *Mol. Pharm.* 2014; **11**: 1949–1963.

[130] Cecchelli R, Aday S, Sevin E, Almeida C, Culot M, Dehouck L, Coisne C, Engelhardt B, Dehouck M-P, Ferreira L. A Stable and Reproducible Human Blood-Brain Barrier Model Derived from Hematopoietic Stem Cells. *PLoS One* 2014; **9**: e99733.

[131] Deli MA, Ábrahám CS, Kataoka Y, Niwa M. Permeability Studies on In Vitro Blood–Brain Barrier Models:Physiology, Pathology, and Pharmacology. *Cell. Mol. Neurobiol.* 2005; **25**: 59–127.

[132] Oller-Salvia B, Sánchez-Navarro M, Ciudad S, Guiu M, Arranz-Gibert P, Garcia C, Gomis RR, Cecchelli R, García J, Giralt E, Teixidó M. MiniAp-4: A Venom-Inspired Peptidomimetic for Brain Delivery. *Angew. Chem. Int. Ed.* 2016; **55**: 572–575.

[133] Díaz-Perlas C, Varese M, Guardiola S, García J, Sánchez-Navarro M, Giralt E, Teixidó M. From Venoms to BBB-Shuttles. MiniCTX3: A Molecular Vector Derived from

Scorpion Venom. *Chem. Commun.* 2018; **54**: 12738–12741.

[134] Díaz-Perlas C, Sánchez-Navarro M, Oller-Salvia B, Moreno M, Teixidó M, Giralt E. Phage Display as a Tool to Discover Blood–brain Barrier (BBB)-Shuttle Peptides: Panning against a Human BBB Cellular Model. *Pept. Sci.* 2017; **108**: e22928.

[135] Smith GP. Filamentous Fusion Phage: Novel Expression Vectors That Display Cloned Antigens on the Virion Surface. *Science.* 1985; **228**: 1315-1317.

[136] Smith GP, Petrenko VA. Phage Display. *Chem. Rev.* 1997; **97**: 391–410.

[137] Burdo JR, Simpson IA, Menzies S, Beard J, Connor JR. Regulation of the Profile of Iron-Management Proteins in Brain Microvasculature. *J. Cereb. Blood Flow Metab.* 2004; **24**: 67–74.

[138] Ohtsuki S, Ikeda C, Uchida Y, Sakamoto Y, Miller F, Glacial F, Decleves X, Scherrmann J-M, Couraud P-O, Kubo Y, Tachikawa M, Terasaki T. Quantitative Targeted Absolute Proteomic Analysis of Transporters, Receptors and Junction Proteins for Validation of Human Cerebral Microvascular Endothelial Cell Line HCMEC/D3 as a Human Blood–Brain Barrier Model. *Mol. Pharm.* 2013; **10**: 289–296.

[139] Oller-Salvia B, Sánchez-Navarro M, Giralt E, Teixidó M. Blood–brain Barrier Shuttle Peptides: An Emerging Paradigm for Brain Delivery. *Chem. Soc. Rev.* 2016; **45**: 4690–4707.

[140] Goldflam M, Tarragó T, Gairí M, Giralt E. NMR Studies of Protein–Ligand Interactions BT - Protein NMR Techniques. In, Shekhtman A, Burz DS (eds). Humana Press: Totowa, NJ, 2012; 233–259.

[141] Dalvit C. NMR Methods in Fragment Screening: Theory and a Comparison with Other Biophysical Techniques. *Drug Discov. Today* 2009; **14**: 1051–1057.

[142] Viegas A, Manso J, Nobrega FL, Cabrita EJ. Saturation-Transfer Difference (STD) NMR: A Simple and Fast Method for Ligand Screening and Characterization of Protein Binding. *J. Chem. Educ.* 2011; **88**: 990–994.

[143] Schwenke KD. K. Wüthrich: NMR in Biological Research: Peptides and Proteins. XII *Die Nahrung* 1978; **22**: 439-451.

[144] Krishnan V V. Ligand Screening by Saturation-Transfer Difference (STD) NMR Spectroscopy. *Current Analytical Chemistry*, 2005, **1**: 307–320.

[145] Arranz-Gibert P, Ciudad S, Seco J, García J, Giralt E, Teixidó M. Immunosilencing Peptides by Stereochemical Inversion and Sequence Reversal: Retro-D-Peptides. *Sci. Rep.* 2018; **8**: 6446.

[146] Wiseman T, Williston S, Brandts JF, Lin L-N. Rapid Measurement of Binding Constants and Heats of Binding Using a New Titration Calorimeter. *Anal. Biochem.* 1989; **179**: 131–137.

[147] Bou-Abdallah F, Terpstra TR. The Thermodynamic and Binding Properties of the Transferrins as Studied by Isothermal Titration Calorimetry. *Biochim. Biophys. Acta - Gen. Subj.* 2012; **1820**: 318–325.

[148] Fischer M, P Leech A, E Hubbard R. Comparative Assessment of Different Histidine-Tags for Immobilization of Protein onto Surface Plasmon Resonance Sensorchips. *Anal. Chem.* 2011; **83**: 1800-1807.

[149] Oi J, Terashima T, Kojima H, Fujimiya M, Maeda K, Arai R, Chan L, Yasuda H, Kashiwagi A, Kimura H. Isolation of Specific Peptides That Home to Dorsal Root Ganglion Neurons in Mice. *Neurosci. Lett.* 2008; **434**: 266–272.

[150] Wei X, Zhan C, Chen X, Hou J, Xie C, Lu W. Retro-Inverso Isomer of Angiopep-2: A Stable d-Peptide Ligand Inspires Brain-Targeted Drug Delivery. *Mol. Pharm.* 2014; **11**: 3261–3268.

[151] Singh A, Thornton ER, Westheimer FH. The Photolysis of Diazoacetylchymotrypsin. *J. Biol. Chem.* 1962; **237**: PC3006-PC3008.

[152] Das J. Aliphatic Diazirines as Photoaffinity Probes for Proteins: Recent Developments. *Chem. Rev.* 2011; **111**: 4405–4417.

[153] Dubinsky L, Krom BP, Meijler MM. Diazirine Based Photoaffinity Labeling. *Bioorg. Med. Chem.* 2012; **20**: 554–570.

[154] Prestwich GD, Dormán G, Elliott JT, Marecak DM, Chaudhary A. Benzophenone Photoprobes for Phosphoinositides, Peptides and Drugs. *Photochem. Photobiol.* 1997; **65**: 222–234.

[155] Baldwin MA. Mass Spectrometers for the Analysis of Biomolecules. *Methods Enzymol.* 2005; **402**: 3–48.

[156] Welsh MJ, Smith AE. Molecular Mechanisms of CFTR Chloride Channel Dysfunction in Cystic Fibrosis. *Cell.* 1993; **73**: 1251–1254.

[157] Nezu J, Tamai I, Oku A, Ohashi R, Yabuuchi H, Hashimoto N, Nikaido H, Sai Y, Koizumi A, Shoji Y, Takada G, Matsuishi T, Yoshino M, Kato H, Ohura T, Tsujimoto G, Hayakawa J, Shimane M, Tsuji A. Primary Systemic Carnitine Deficiency Is Caused by Mutations in a Gene Encoding Sodium Ion-Dependent Carnitine Transporter. *Nat. Genet.* 1999; **21**: 91-94.

[158] Kartenbeck J, Leuschner U, Mayer R, Keppler D. Absence of the Canalicular Isoform of the MRP Gene-Encoded Conjugate Export Pump from the Hepatocytes in Dubin-Johnson Syndrome. *Hepatology* 1996; **23**: 1061–1066.

[159] Uchida Y, Tachikawa M, Obuchi W, Hoshi Y, Tomioka Y, Ohtsuki S, Terasaki T. A Study Protocol for Quantitative Targeted Absolute Proteomics (QTAP) by LC-MS/MS: Application for Inter-Strain Differences in Protein Expression Levels of Transporters, Receptors, Claudin-5, and Marker Proteins at the Blood-Brain Barrier in DdY, FVB and C57BL/6J mice. *Fluids Barriers CNS.* 2013; **10**: 21.

[160] Godfrey K. Compartmental Models and Their Application. 1985; **74**: 806.

[161] Yamaoka K, Tanigawara Y, Nakagawa T, Uno T. A Pharmacokinetic Analysis Program (MULTI) for Microcomputer. J Pharmacobiodyn. 1951; 4: 879-885.

[162] Sato H, Tsuji A, HIRAI KI, Kang Y-S. Application of HPLC in Disposition Study of A14-125I-Labeled Insulin in Mice. *Diabetes.* 1990; **39**: 563-569.

[163] Lee HJ, Engelhardt B, Lesley J, Bickel U, Pardridge WM. Targeting Rat Anti-Mouse Transferrin Receptor Monoclonal Antibodies through Blood-Brain Barrier in Mouse. *J. Pharmacol. Exp. Ther.* 2000; **292**: 1048-1052.

[164] Bickel U, Yoshikawa T, Pardridge W. Delivery of Peptides and Proteins through the Blood-Brain Barrier. *Adv. Drug Deliv. Rev.* 2001; **46**: 247-279.

[165] Banks WA, Kastin AJ, Durham DA. Bidirectional Transport of Interleukin-1 Alpha across the Blood-Brain Barrier. *Brain Res. Bull.* 1989; **23**: 433–437.

[166] Barbeau A. L-Dopa Therapy in Parkinson's Disease: A Critical Review of Nine Years' Experience. *Can. Med. Assoc. J.* 1969; **101**: 59–68.

[167] Hawkins RA, Mokashi A, Simpson IA. An Active Transport System in the Blood-Brain

Barrier May Reduce Levodopa Availability. *Exp. Neurol.* 2005; **195**: 267–271.

[168] Lee KC, Moon SC, Park MO, Lee JT, Na DH, Yoo SD, Lee HS, DeLuca PP. Isolation, Characterization, and Stability of Positional Isomers of Mono-PEGylated Salmon Calcitonins. *Pharm. Res.* 1999; **16**: 813–818.

[169] Kameyama S, Horie M, Kikuchi T, Omura T, Tadokoro A, Takeuchi T, Nakase I, Sugiura Y, Futaki S. Acid Wash in Determining Cellular Uptake of Fab/Cell-Permeating Peptide Conjugates. *Biopolymers.* 2007; **88**: 98-107.

[170] Parrish-Novak J, Byrnes-Blake K, Lalayeva N, Burleson S, Fidel J, Gilmore R, Gayheart-Walsten P, Bricker GA, William J. Crumb J, Tarlo KS, Hansen S, Wiss V, Malta E, Dernell WS, Olson JM, Miller DM. Nonclinical Profile of BLZ-100, a Tumor-Targeting Fluorescent Imaging Agent. *Int. J. Toxicol.* 2017; **36**: 104–112.

[171] Pennington MW, Czerwinski A, Norton RS. Peptide Therapeutics from Venom: Current Status and Potential. *Bioorg. Med. Chem.* 2018; **26**: 2738–2758.

[172] Bernardoni JL, Sousa LF, Wermelinger LS, Lopes AS, Prezoto BC, Serrano SMT, Zingali RB, Moura-da-Silva AM, Casewell NR, Wüster W, Vonk FJ, Harrison RA, Fry BG, Osipov A, Utkin Y, Fry BG, Näreoja K, Näsman J. Effects of Snake Venom Polypeptides on Central Nervous System. *PLoS One* 2012; **12**: 186–201.

[173] Labbé-Jullié C, Granier C, Albericio F, Defendini M-L, Ceard B, Rochat H, Van Rietschoten J. Binding and Toxicity of Apamin Characterization of the Active Site. *Eur. J. Biochem.* 1991; **196**: 639–645.

[174] Oller-Salvia B, Sánchez-Navarro M, Ciudad S, Guiu M, Arranz-Gibert P, Garcia C, Gomis RR, Cecchelli R, García J, Giralt E, Teixidó M. MiniAp-4: A Venom-Inspired Peptidomimetic for Brain Delivery. *Angew. Chem. Int. Ed. Engl.* 2016; **55**: 572–575.

[175] Shi T, Spain SM, Rabenstein DL. A Striking Periodicity of the Cis/Trans Isomerization of Proline Imide Bonds in-Cyclic Disulfide-Bridged Peptides. *Angew. Chemie - Int. Ed.* 2006; **45**: 1780–1783.

[176] Buckton LK, McAlpine SR. Improving the Cell Permeability of Polar Cyclic Peptides by Replacing Residues with Alkylated Amino Acids, Asparagines, and d-Amino Acids. *Org. Lett.* 2018; **20**: 506–509.

[177] An SSA, Lester CC, Peng J-L, Li Y-J, Rothwarf DM, Welker E, Thannhauser TW, Zhang LS, Tam JP, Scheraga HA. Retention of the Cis Proline Conformation in Tripeptide Fragments of Bovine Pancreatic Ribonuclease A Containing a Non-Natural Proline Analogue, 5,5-Dimethylproline. *J. Am. Chem. Soc.* 1999; **121**: 11558–11566.

[178] Isidro-Llobet A, Álvarez M, Albericio F. Amino Acid-Protecting Groups. *Chem. Rev.* 2009; **109**: 2455–2504.

[179] Schubert M, Labudde D, Oschkinat H, Schmieder P. A Software Tool for the Prediction of Xaa-Pro Peptide Bond Conformations in Proteins Based On13C Chemical Shift Statistics. *J. Biomol. NMR.* 2002; **24**: 149–154.

[180] Rudakova E V, Boltneva NP, Makhaeva GF. Comparative Analysis of Esterase Activities of Human, Mouse, and Rat Blood. *Bull. Exp. Biol. Med.* 2011; **152**: 73–75.

[181] Wang J, Yadav V, Smart AL, Tajiri S, Basit AW. Toward Oral Delivery of Biopharmaceuticals: An Assessment of the Gastrointestinal Stability of 17 Peptide Drugs. *Mol. Pharm.* 2015; **12**: 966–973.

[182] Wang CK, Swedberg JE, Harvey PJ, Kaas Q, Craik DJ. Conformational Flexibility Is a Determinant of Permeability for Cyclosporin. *J. Phys. Chem. B* 2018; **122**: 2261–2276.

[183] Cai W, Hsu AR, Li Z-B, Chen X. Are Quantum Dots Ready for in Vivo Imaging in Human Subjects? *Nanoscale Res. Lett.* 2007; **2**: 265-281.

[184] Michalet X, Pinaud FF, Bentolila LA, Tsay JM, Doose S, Li JJ, Sundaresan G, Wu AM, Gambhir SS, Weiss S. Quantum Dots for Live Cells, in Vivo Imaging, and Diagnostics. *Science.* 2005; **307**: 538-544.

[185] Reshma VG, Mohanan P V. Quantum Dots: Applications and Safety Consequences. *J. Lumin.* 2019; **205**: 287–298.

[186] Nozik AJ. SPECTROSCOPY AND HOT ELECTRON RELAXATION DYNAMICS IN SEMICONDUCTOR QUANTUM WELLS AND QUANTUM DOTS. *Annu. Rev. Phys. Chem.* 2001; **52**: 193–231.

[187] Hermanson GT. Bioconjugate techniques. 2008; 1041–1132.

[188] Watanabe T, Dohgu S, Takata F, Nishioku T, Nakashima A, Futagami K, Yamauchi A, Kataoka Y. Paracellular Barrier and Tight Junction Protein Expression in the Immortalized Brain Endothelial Cell Lines BEND.3, BEND.5 and Mouse Brain Endothelial Cell 4. *Biol. Pharm. Bull.* 2013; **36**: 492–495.

[189] Dutta NK, Panse M V, Kulkarni DR. Role of Cholera a Toxin in Experimental Cholera. *J. Bacteriol.* 1959; **78**: 594–595.

[190] De SN. Enterotoxicity of Bacteria-Free Culture-Filtrate of Vibrio Cholerae. *Nature* 1959; **183**: 1533–1534.

[191] K Ganguly N, Kaur T. Mechanism of Action of Cholera Toxin & Other Toxins. *Indian J. Med. Res.* 1996; **104**: 28-37.

[192] Capitan F, Robu AC, Popescu L, Flangea C, Vukelić Ž, Zamfir A. B Subunit Monomers of Cholera Toxin Bind G1 Ganglioside Class as Revealed by Chip-Nanoelectrospray Multistage Mass Spectrometry. *J. Carbohydr. Chem.* 2015; **34**: 388-408.

[193] Spangler BD. Structure and Function of Cholera Toxin and the Related Escherichia Coli Heat-Labile Enterotoxin. *Microbiol. Rev.* 1992; **56**: 622–647.

[194] M Dawson R. Characterization of the Binding of Cholera Toxin to Ganglioside G M1 Immobilized onto Microtitre Plates. *J. Appl. Toxicol.* 2005; **25**: 30-38.

[195] Parton RG. Ultrastructural Localization of Gangliosides; GM1 Is Concentrated in Caveolae. *J. Histochem. Cytochem.* 1994; **42**: 155–166.

[196] Torgersen ML, Skretting G, van Deurs B, Sandvig K. Internalization of Cholera Toxin by Different Endocytic Mechanisms. *J. Cell Sci.* 2001; **114**: 3737-3747.

[197] Hansen GH, Dalskov S-M, Rasmussen CR, Immerdal L, Niels-Christiansen L-L, Danielsen EM. Cholera Toxin Entry into Pig Enterocytes Occurs via a Lipid Raft- and Clathrin-Dependent Mechanism. *Biochemistry* 2005; **44**: 873–882.

[198] Massol RH, Larsen JE, Fujinaga Y, Lencer WI, Kirchhausen T. Cholera Toxin Toxicity Does Not Require Functional Arf6- and Dynamin-Dependent Endocytic Pathways. *Mol. Biol. Cell* 2004; **15**: 3631–3641.

[199] Pearse BMF, Robinson MS. Clathrin, Adaptors, and Sorting. *Annu. Rev. Cell Biol.* 1990; **6**: 151–171.

[200] Macia E, Ehrlich M, Massol R, Boucrot E, Brunner C, Kirchhausen T. Dynasore, a Cell-Permeable Inhibitor of Dynamin. *Dev. Cell* 2006; **10**: 839–850.

[201] Manders EM, Stap J, Brakenhoff GJ, van Driel R, Aten JA. Dynamics of Three-

Dimensional Replication Patterns during the S-Phase, Analysed by Double Labelling of DNA and Confocal Microscopy. *J. Cell Sci.* 1992; **103**: 857-862.

[202] MANDERS EMM, VERBEEK FJ, ATEN JA. Measurement of Co-Localization of Objects in Dual-Colour Confocal Images. *J. Microsc.* 1993; **169**: 375–382.

[203] Pujals S, Fernández-Carneado J, Ludevid MD, Giralt E. D-SAP: A New, Noncytotoxic, and Fully Protease Resistant Cell-Penetrating Peptide. *ChemMedChem* 2008; **3**: 296–301.

[204] Endesfelder U, Heilemann M. Direct Stochastic Optical Reconstruction Microscopy (DSTORM) BT - Advanced Fluorescence Microscopy: Methods and Protocols. In, Verveer PJ (ed). Springer New York: New York, NY, 2015; 263–276.

[205] Jensen E, Crossman DJ. Technical Review: Types of Imaging—Direct STORM. *Anat. Rec.* 2014; **297**: 2227–2231.

[206] van de Linde S, Aufmkolk S, Franke C, Holm T, Klein T, Löschberger A, Proppert S, Wolter S, Sauer M. Investigating Cellular Structures at the Nanoscale with Organic Fluorophores. *Chem. Biol.* 2013; **20**: 8–18.

[207] Rasnik I, McKinney SA, Ha T. Nonblinking and Long-Lasting Single-Molecule Fluorescence Imaging. *Nat. Methods* 2006; **3**: 891.

[208] Sinz A. Investigation of Protein–Ligand Interactions by Mass Spectrometry. *ChemMedChem* 2007; **2**: 425–431.

[209] Suchanek M, Radzikowska A, Thiele C. Photo-Leucine and Photo-Methionine Allow Identification of Protein-Protein Interactions in Living Cells. *Nat. Methods* 2005; **2**: 261.

[210] Van der Meijden B, Robinson JA. Synthesis and Application of Photoproline -a Photoactivatable Derivative of Proline. Arkivoc. 2011; **6**: 130-136.

[211] Moss RA. Diazirines: Carbene Precursors Par Excellence. *Acc. Chem. Res.* 2006; **39**: 267–272.

[212] Blencowe A, Hayes W. Development and Application of Diazirines in Biological and Synthetic Macromolecular Systems. *Soft Matter* 2005; **1**: 178–205.

[213] Kotzyba-Hibert F, Kapfer I, Goeldner M. Recent Trends in Photoaffinity Labeling. *Angew. Chemie Int. Ed. English* 1995; **34**: 1296–1312.

[214] Hashimoto M, Hatanaka Y. Recent Progress in Diazirine-Based Photoaffinity Labeling. *European J. Org. Chem.* 2008; **2008**: 2513–2523.

[215] Green NM. Thermodynamics of the Binding of Biotin and Some Analogues by Avidin. *Biochem. J.* 1966; **101**: 774–780.

[216] Green NM. Avidin 1. The Use of (14-C) Biotin for Kinetic Studies and for Assay. *Biochem. J.* 1963; **89**: 585–591.

[217] Rybak J-N, Scheurer SB, Neri D, Elia G. Purification of Biotinylated Proteins on Streptavidin Resin: A Protocol for Quantitative Elution. *Proteomics* 2004; **4**: 2296–2299.

[218] Hesketh GG, Youn J-Y, Samavarchi-Tehrani P, Raught B, Gingras A-C. Parallel Exploration of Interaction Space by BioID and Affinity Purification Coupled to Mass Spectrometry BT - Proteomics: Methods and Protocols. In, Comai L, Katz JE, Mallick P (eds). Springer New York: New York, NY, 2017; 115–136.

[219] Pirone L, Xolalpa W, Sigurðsson JO, Ramirez J, Pérez C, González M, de Sabando AR, Elortza F, Rodriguez MS, Mayor U, Olsen J V, Barrio R, Sutherland JD. A Comprehensive Platform for the Analysis of Ubiquitin-like Protein Modifications Using in Vivo

Biotinylation. *Sci. Rep.* 2017; **7**: 40756.

[220] Fukuyama H, Ndiaye S, Hoffmann J, Rossier J, Liuu S, Vinh J, Verdier Y. On-Bead Tryptic Proteolysis: An Attractive Procedure for LC-MS/MS Analysis of the Drosophila Caspase 8 Protein Complex during Immune Response against Bacteria. *J. Proteomics* 2012; **75**: 4610–4619.

[221] Leriche G, Chisholm L, Wagner A. Cleavable Linkers in Chemical Biology. *Bioorg. Med. Chem.* 2012; **20**: 571–582.

[222] Gemeay AH. Kinetics and Mechanism of the Reduction of Some Azo-Dyes by Inorganic Oxysulfur Compounds. *Dye. Pigment.* 2002; **54**: 201–212.

[223] Yang Y-Y, Grammel M, Raghavan AS, Charron G, Hang HC. Comparative Analysis of Cleavable Azobenzene-Based Affinity Tags for Bioorthogonal Chemical Proteomics. *Chem. Biol.* 2010; **17**: 1212–1222.

[224] Szklarczyk D, Gable AL, Lyon D, Junge A, Wyder S, Huerta-Cepas J, Simonovic M, Doncheva NT, Morris JH, Bork P, Jensen LJ, Mering C von. STRING V11: Protein-Protein Association Networks with Increased Coverage, Supporting Functional Discovery in Genome-Wide Experimental Datasets. *Nucleic Acids Res.* 2019; **47**: D607–D613.

[225] H Lundgren D, Hwang S, Wu L, Han D. Role of Spectral Counting in Quantitative Proteomics. Expert. Rev. Proteomics. 2010; **7**: 39-53.

[226] Kaiser E, Colescott RL, Bossinger CD, Cook PI. Color Test for Detection of Free Terminal Amino Groups in the Solid-Phase Synthesis of Peptides. *Anal. Biochem.* 1970; **34**: 595–598.

[227] Franco M, Seyfried NT, Brand AH, Peng J, Mayor U. A Novel Strategy to Isolate Ubiquitin Conjugates Reveals Wide Role for Ubiquitination during Neural Development. *Mol. &amp; Cell. Proteomics* 2011; **10**: M110.002188.